Ruthenium Polypyridyl Complexes for Biological Applications in Imaging and as Anti-Cancer Agents

Bjørn la Cour Poulsen, M.Sc.

November 2017

University of Dublin
Trinity College Dublin

Based on research carried out under the direction of
Prof. Thorfinnur Gunnlaugsson and John M. Kelly

A thesis submitted to the School of Chemistry,
Trinity College Dublin, The University of Dublin, for the degree of
Doctor of Philosophy

Declaration

This thesis is submitted for the degree of Doctor of Philosophy to the University of Dublin, Trinity College and has not been submitted before for any degree or examination to this or any other university. Other than where acknowledged, all work described herein is original and carried out by the author alone. Permission is granted so that the library may lend or copy this thesis upon request. This permission covers only single copies made for study purposes, subject to normal conditions of acknowledgement.

Bjørn la Cour Poulsen

Bjørn la Cour Poulsen

Acknowledgements

I will first of all thank Prof. Thorfinnur Gunnlaugsson for your fantastic supervision and the great opportunity you gave me when you welcomed me into your amazing group. I will miss your inspirational pep-talks and very helpful guidance. I expect to have a good collaboration with you in the future. I will also thank John M. Kelly for your guidance in the amazing world of ruthenium chemistry and DNA. I feel very privileged to have two such skilful and encouraging mentors to support me in my project.

I would also like to thank Clive Williams for your guidance in the cellular world. I'm very grateful for getting the opportunity to work with living subjects rather than just dead chemistry. A huge thank you to Dr Sandra Bright and Dr Kim Orange for your good collaborations and instruction in how to kill cancer cells. I would also like to express my sincere thank you to Dr Gavin McManus for your guidance in doing confocal microscopy and for your patience when an ignorant chemist like me brought some strange molecular species. I would like to thank all of the staff members in the School of Chemistry, especially Dr Manuel Reuther, Dr John O'Brien, Dr Martin Feeney and Dr Gary Hessman for your assistance with NMR spectroscopy and mass spectrometry. I will thank Dr Pancham Singh Kandiyal for guiding me in my NMR studies. I'm very thankful to Dr Viola Previtali and Dr Cristina Trujillo for allowing me to pick their brains in the world of computational chemistry.

I owe a massive thank you to all of the postdocs within the group during my PhD time. Thanks to Dr Salvador Blasco and Dr Miguel Martínez-Calvo for good and close collaboration and constructive discussion about different subjects. Also thanks to collaborators Raju, Chris and Dawn. Thanks to Oxana for making the lab running. Thanks to Sachi and Ester for helping me out with the nanoparticles. To all current and former PhD and visiting students (Jason *et al.*). I can't thank your people enough for your friendship, our pub crawls, exploring Dublin and Ireland with me, and for all the good memories. My PhD time would have been very different and much more lonely without you; I will miss our weekly drinky pooh. Thanks to Sandra Estalayo-Adrían and Fergus Poynton for a very good collaboration in the ruthenium world - I will miss your positive spirits! And a special thanks to Eoin, my 4th year buddy and flat mate for putting a roof over my head twice, protecting me in the traffic, and keeping me out of trouble. If you had not found me on Talbot Street

four years ago I don’t know where I would be in my life. You are a great friend, and I hope you will be happy. Also thank you to all members of the group for proof reading and practical and mental support, especially here in the last couple of weeks where thing became a little bit tough.

Without the generous financial support from the Irish Research Council it would not have been possible to do my PhD. Thanks to the Irish Centre for High-End Computing for funding of computational resources. I would like to thank Trinity College Dublin for support during my scholarship. Thanks to my family and friends abroad for making me feel home when I’m in Denmark. A special thanks to my mother, PhD, for her careful chemical proofreading of my report. And of course thanks to my girlfriend Susanne, I look forward to getting home to you!

Abstract

Ruthenium-polypyridyl complexes containing extended aromatic ring systems exhibit attractive photophysical properties and have been shown to bind strongly to DNA. Such properties make complexes like these suitable for a broad range of biological applications. This thesis, entitled "Ruthenium Polypyridyl Complexes for Biological Applications in Imaging and as Anti-Cancer Agents", is focusing on DNA binding and treatment of cancer and aims to develop novel Ru(II) polypyridyl complexes, which can be used as luminescence dyes for imaging or as photodynamic therapeutic (PDT) agents in cancer treatments.

Chapter 1 gives a basic introduction to the background of the problem treated in the thesis by, firstly, providing an overview of DNA and its structure and a brief description of the various binding modes, by which molecular species can interact with DNA. Following this overview, relevant Ru(II) polypyridyl complexes are described, including their application as DNA binding, cellular imaging, or anti-cancer agents. A critical literature review of multivalent binding is given to help with a conceptual understanding. New, more accurate methods to calculate binding parameters are also introduced. This chapter then concludes by outlining recent examples of similar Ru(II) polypyridyl complexes and other biologically relevant molecules developed in the Gunnlaugsson group.

In Chapter 2, synthesis, characterisation and photophysical properties of two Ru(II) polypyridyl complexes are explored with a new, extended aromatic moiety as one of the ligands. The photophysical properties of the compounds show promising features for use in imaging by being emissive in aqueous and/or organic solvents. The DNA binding properties of the two new Ru(II) complexes are investigated. Their binding interactions with DNA are evaluated using various spectroscopic techniques and both complexes are seen to bind strongly to DNA ($K_b > 10^6$ M^{-1}) through intercalation. The potential use as imaging probes of one of the complexes is demonstrated by a dramatic enhancement of the emission by the compound in aqueous environment upon binding to DNA.

In Chapter 3 the synthesis and characterisation of compounds based on 1,10-phenanthroline-5,6-dione are described. In Chapter 4 the activity at the cellular level for these and the two new DNA binding complexes is evaluated. The behaviour of the complexes in HeLa cervical cancer cells has been studied, their cytotoxicity has been described, and their ability to act as luminescent dyes and PDT agents has been explored.

One of the two new complexes showed great potential for use in PDT with a large increase in toxicity at photoactivation. Further, Ru(II) complexes with naphthalimide based Tröger's bases as bridging ligands are evaluated for use in PDT. The naphthalimide based Tröger's bases that are tested do not show potential for use in PDT, however some of them show anti-cancer activity or potential for use in cellular imaging.

Chapter 5 describes the investigation into the site specific and cooperative binding of the two enantiomers of $[Ru(TAP)_2dppz]^{2+}$. This includes studies of the binding to oligomeric and polymeric DNA. Both enantiomers show strong selectivity, with preferential binding to AT-rich DNA. Investigations of the delta enantiomer show positive cooperativity for binding to natural DNA.

In Chapter 6 the possibility of functionalising gold nanoparticles with ruthenium-polypyridyl complexes has been explored, an approach that may, among other things, help in cellular uptake. The aims of this project are the development of new Ru(II) polypyridyl complexes that can conjugate to the surface of gold for application as biological imaging agents and cancer therapeutics due to their high Ru(II) complex loading and rapid cellular uptake.

Finally, Chapter 7 outlines the experimental procedures, and presents the synthesis and characterisation of the compounds discussed within this thesis. Following this, literature references and Appendices are provided, the latter containing supplementary experimental data to support the work described in the main text.

Abbreviations

A	absorbance
A	adenine
aq	aqueous
Ar	aromatic
a.u.	arbitrary unit
AuNP	gold nanoparticle
BET	back electron transfer
bp/Ru	DNA base pairs to ruthenium complex ratio
bpy	2,2'-bipyridine
bs	broad singlet
C	cytosine
Cq	quaternary carbon
ca.	circa
CD	circular dichroism
cod	cycloocta-l,5-diene
conc.	concentrated
CPF	canonical partition function
CT	computed tomography or charge transfer
ct-DNA	calf thymus DNA
D	deuterium
d	doublet
DAPI	4',6-diamidino-2-phenylindole
DCM	dichloromethane
DFT	Density Functional Theory
DLS	dynamic light scattering
DMF	dimethylformamide
DMSO	dimethyl sulfoxide
DNA	deoxyribonucleic acid
dppz	dipyrido[3,2-*a*:2',3'-*c*]phenazine
dtp	dipyrido[3,2-*a*:2’,3’-*c*][1,2,5]thiadiazolo[3,4-

	4,3]phenazine
duplex/Ru	DNA duplex to ruthenium complex ratio
E_a	molar emission
EDCI	*N*-(2-dimethylaminopropyl)-*N'*-ethylcarbodiimide
EPR	Enhanced Permeability and Retention
eq	equivalent
ESI	electrospray ionization
ESMS	electrospray mass spectrometry
ET	energy transfer
FACS	fluorescence-activated cell sorting
FET	forward electron transfer
FRET	Förster resonance energy transfer
FTIR	Fourier transform infrared
G	guanine
GPF	grand partition function
h	hour or Planck constant (6.626×10^{-34} J s)
HRMS	high resolution mass spectrometry
hν	energy of a photon with frequency υ
I	inosine
I	intensity
IC_{50}	half maximal inhibitory concentration
ICD	induced circular dichroism
IR	infrared
ISC	intersystem crossing
J	coupling constant
k	site binding constant
K_b	binding constant
K_N	association constant
K_N'	step-wise binding constant
L	ligand
LD	linear dichroism
litt.	literature
Ln	lanthanide

logP	logarithmic value of partition coefficient
M	molecular ion, metal or molar
m	multiplet
M06	Minnesota 06 (functional in DFT)
M06/6-311G(d,p)	used the functional M06 and the basis set 6-311G(d,p)
MALDI	matrix-assisted laser desorption/ionisation
Max UE	maximum unsigned error
MC	metal-centred
mdeg	millidegrees
MGVH	McGhee-von Hippel
min	minute
MLCT	metal to ligand charge transfer
m.p.	melting point
mpdppz	3-methylpyrazino[2,3-*h*]dipyrido[3,2-*a*:2',3'-*c*]phenazine
MRI	magnetic resonance imaging
MS	mass spectrometry
MUE	mean unsigned error
m/*z*	mass-to-charge ratio
n	binding site size in DNA helix (number of base pairs)
NAC	*N*-acetyl cysteine
naph	naphthalimide
naphTB	naphthalimide based Tröger's base
NIR	near infrared
NMR	nuclear magnetic resonance
PBS	phosphate buffered saline
Pd/C	palladium on carbon
pdppz	pyrazino[2,3-*h*]dipyrido[3,2-*a*:2',3'-*c*]phenazine
PDT	photodynamic therapy
PET	photoinduced electron transfer
phen	1,10-phenanthroline
phendione	1,10-phenanthroline-5,6-dione
ROS	reactive oxygen species
PCM	Polarizable Continuum Model

ppm	parts per million
PTT	photothermal therapy
q	quadruplet
rac	racemic
ref.	reference
R_f	Retardation factor
RNA	ribonucleic acid
rt	room temperature
s	singlet
sat.	saturated
SEM	standard error of the mean
SMD	Solvation Model based on Density
SPECT	single-photon emission computed tomography
SPR	surface plasmon resonance
st-DNA	salmon testes DNA
SVD	singular-value decomposition
T	thymine
t	triplet
TAP	1,4,5,8-tetraazaphenanthrene
TB	Tröger's base
TBACl	tetrabutylammonium chloride
TCD	Trinity College Dublin
TEM	transmission electron microscopy
T_m	melting temperature for DNA
TOAB	tetraoctylammonium bromide
TFA	trifluoroacetic acid
TLC	thin layer chromatography
UCD	University College Dublin
UE	unsigned error
UV	ultraviolet
Vis	visible
w/w	weight per weight
Å	Ångström

α	slope
Δ	heat, increase or delta enantiomer
ε	molar extinction coefficient
ε_a	apparent molar extinction coefficient
ε_b	molar extinction coefficient for bound compound
ε_f	molar extinction coefficient for free compound
η	viscosity
Λ	lambda enantiomer
λ	wavelength or absolute activity
λ_{em}	emission wavelength
λ_{ex}	excitation wavelength
λ_{max}	wavelength of maximum absorbance/intensity
ν	frequency
$\tilde{\nu}$	wavenumber
Φ_{em}	emission quantum yield
Φ_{Δ}	quantum yield of singlet oxygen production

Table of Contents

Chapter 1

Introduction

1.1 Introduction

DNA contains our genetic information, and defects in DNA can result in changes in the expression of key proteins leading to loss of cell division control, the hallmark of cancer. Molecular species that bind to deoxyribonucleic acid (DNA) and possess photophysical properties sensitive to the microenvironment at the binding site have great promise as nucleic acid probes, diagnostic markers, and therapeutic agents.[7]

The work presented in this thesis concerns studies of Ru(II) complexes and their biological applications, with the primary goal being to develop imaging probes and cancer therapeutic agents. This chapter will begin with a short description of the structure of DNA and of how DNA interacts with small molecules. The DNA binding and photophysical properties of new and classic literature examples of Ru(II) polypyridyl complexes and of complexes synthesised within the Gunnlaugsson group will be described. It will be discussed how these compounds can be used as imaging agent in cells and in treatment of cancer. Further, an introduction to gold nanoparticles and their potential applications in development of drugs and imaging agents will be given.[8] Finally, the work presented in Chapters 2 to 7 of this PhD thesis will be outlined.

1.2 The Structure of Deoxyribonucleic Acid

Much effort in biomolecular chemistry, and in this project in particular, focusses on the development of molecules that bind to DNA and have chemical or photophysical properties useful in sensing, gene delivery, or cancer treatment.[9-11] DNA is composed of four types of nucleotides as shown in Figure 1.1, which consist of two purine bases, adenine (A) and guanine (G), and two pyrimidine bases, cytosine (C) and thymine (T). Each of these planar

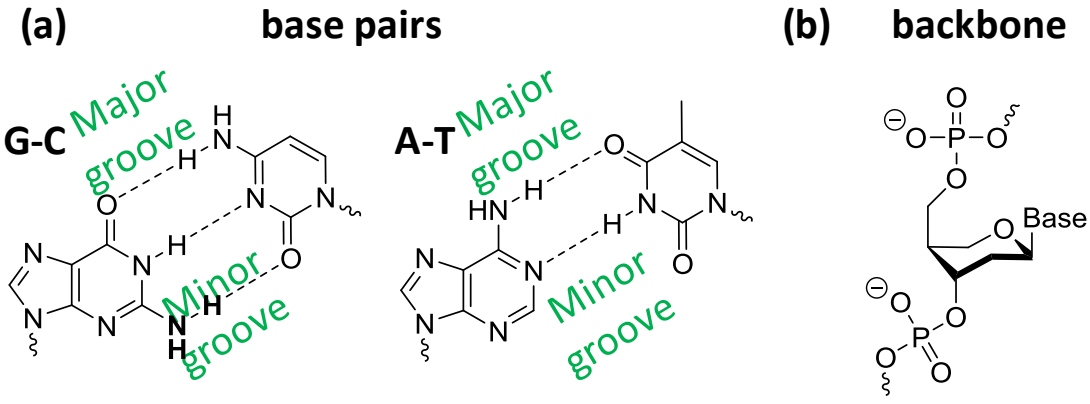

Figure 1.1: *(a) Structure of the DNA base pairs showing the Watson-Crick base pairs of double stranded DNA with the position of the major and minor grooves. (b) One monomeric unit of the sugar-phosphate backbone.*

aromatic heterocyclic bases is linked to a deoxyribose sugar and forms a linear strand through phosphate groups attached to the 3' and 5' positions of the sugar.[12] Two of these strands can arrange into an antiparallel double helix, which is held together by specific intermolecular hydrogen bonds between the bases of each strand and by stacking of the base pairs.[13] The bases are typically held together by Watson-Crick base pairing (Figure 1.1). Hoogsteen base pairing is an alternative version of interactions between the bases which can lead to the formation of a triple stranded DNA where a single strand binds in one of the grooves of a duplex.[14] Quadruplexes of DNA can also be formed for guanine rich sequences (G-quadruplex).

There are three main types of double stranded DNA,[14] where B-DNA is the primary form at low ionic strength in aqueous solution and the most common conformation under physiological conditions, Figure 1.2 and Table 1.1. The helical structure of B-DNA is right-handed. The anti-parallel orientation of the sugar backbone and the pairing between two non-identical heteroaromatic bases result in asymmetry in the helical structure and the formation of two parallel grooves in the DNA strand; the wide and deep major groove and the narrow and shallow minor groove.[12] A conformational change to the A-form happens when the hydration of B-DNA is decreased to 75%. A-DNA is wider and flatter than B-DNA with a narrow major groove and a wide minor groove. At high salt concentration, DNA can adopt a left-handed helical structure in the form of Z-DNA. Z-DNA is longer than B-DNA and has a "zig-zag" backbone compared to the smooth backbone of B-DNA. Structural features of all three forms are found in Table 1.1.

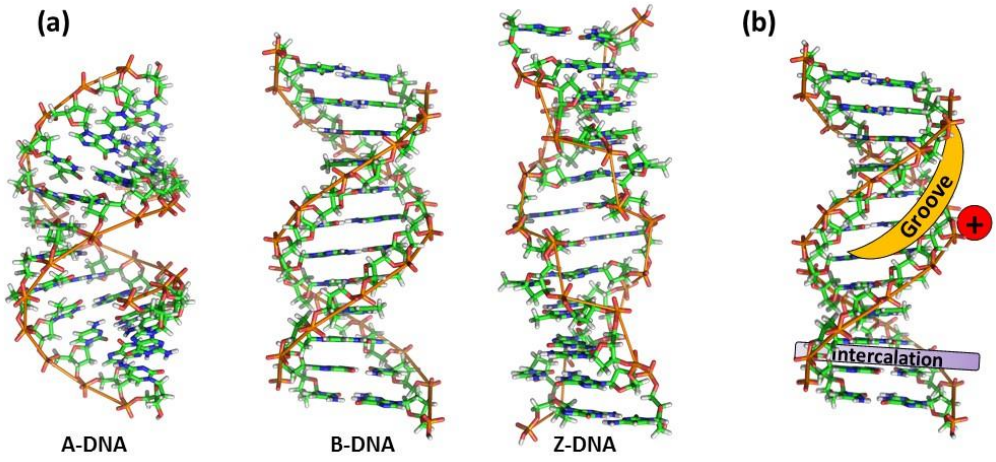

Figure 1.2: *(a) Structures of A-DNA, B-DNA and Z-DNA.*[15] *(b) Schematic representation of the non-covalent binding modes possible for double helical B-DNA.*

Table 1.1: *Average helix parameters for A-DNA, B-DNA and Z-DNA.*[12]

	A	B	Z
Helix	Right-handed	Right-handed	Left-handed
Diameter	~26 Å	~20 Å	~18 Å
bp per helical turn	11	10	12
Helical twist per bp	32.7°	36°	-9°, -51°
Helix rise per bp	2.56 Å	3.4 Å	3.7 Å
Base tilt to the helix axes	20°	-6°	-7°
Major groove	Narrow/deep	Wide/deep	Flat
Minor groove	Wide/shallow	Narrow/deep	Narrow/deep
Glycosidic bond	Anti	Anti	Anti for pyrimidines, syn for purines
Sugar pucker	C3'-endo	C2'-endo	C2'-endo for pyrimidines, C3'-endo for purines

1.3 DNA Binding Interactions

Binding to DNA can be either covalent binding with formation of proper chemical bonds, or it can be non-covalent with weaker intermolecular interactions. Non-covalent binding is described as electrostatic binding, groove binding or intercalation.

1.3.1 Covalent Binding

Covalent binding to DNA involves strong chemical bonds to DNA and is generally considered to be irreversible.[16] Many cancer drugs act at the genomic level by covalent attachment to DNA which disturbs the gene transcription and DNA replication. This may result in cell death by apoptosis (programmed cell death). One of the most famous examples is cisplatin and analogous compounds that induce cell death by crosslinking two guanine bases as shown in Figure 1.3.[17]

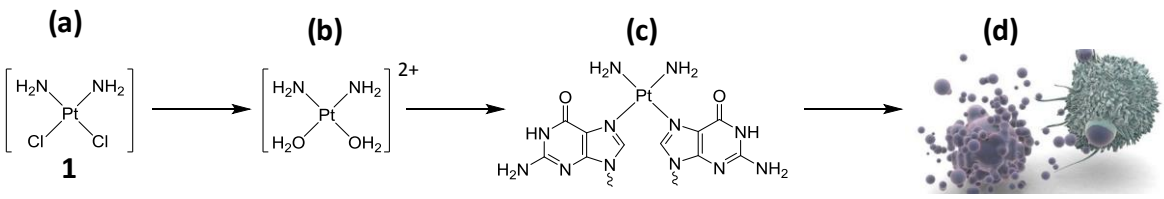

Figure 1.3: *The structure of cisplatin and its effect on cancer cells: (a) cisplatin (**1**). (b) Hydrated form of cisplatin after cellular uptake. (c) Cross-linking of guanine in the nuclei of cells. (d) Induced apoptosis of cancer cells.*[17]

1.3.2 Electrostatic Binding

Electrostatic binding refers to binding of a cationic species with coulombic attractions to the negatively charged phosphate backbone of DNA.[18] Small ionic species such as Na^+ and K^+ bind to DNA with electrostatic binding with binding constants (K_b) in the order of $10^4\ M^{-1}$. Protonated polyamines, such as spermine (**2**), also bind to DNA with electrostatic interactions.[19] Electrostatic binding to DNA is non-specific with little variation in the binding constants for different base pairs and with no specific orientation of the compound at binding. Usually for cationic compounds with other types of binding modes, such as groove binders and intercalators, the electrostatic interaction will also have a strong contribution to the binding.

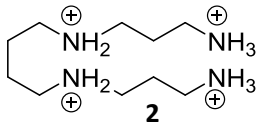

2

Figure 1.4: *Structure of spermine.*

1.3.3 Groove Binding

The base pairs are exposed to the surroundings from the grooves, and groove binders are often selective with large variations in the binding strength for different base pair sequences. The ability to form hydrogen bonds in the groove will depend on the base pairs as well as possible steric clash (Figure 1.1 and Table 1.2). For molecules that bind in the grooves, one distinguishes between *major* and *minor* groove binders. Major groove binders will typically be large molecular species.[20] This includes most DNA binding proteins such as transcription factors that make the major groove an important structural feature with respect to gene regulation. Formation of triple stranded DNA is a result of major groove binding of a single strand of DNA through Hoogsteen base pairing.[14] Methyl green (**3**) is an example of a synthetic molecule that binds exclusively in the major groove.[20] Large synthetic molecules such as oligonucleotides and peptide nucleic acids (PNA)[21] have been shown to bind selectively to DNA and to prevent transcription of specific genes (gene silencing).[22-27]

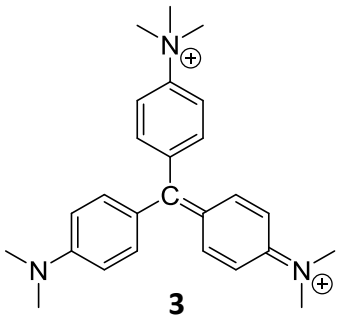

3

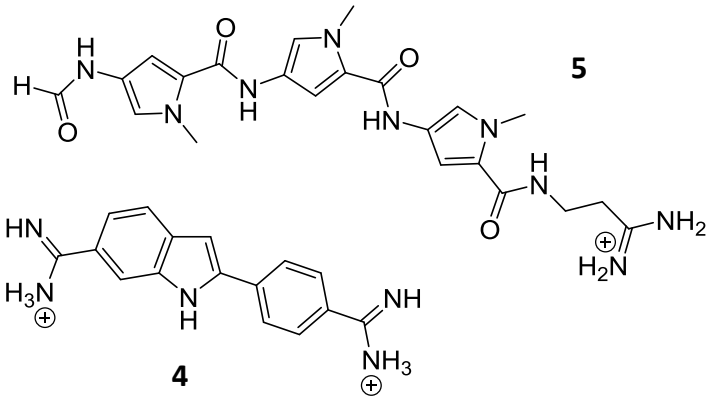

4

5

Figure 1.5 *Major groove binder methyl green (**3**) and minor groove binders 4',6-diamidino-2-phenylindole (DAPI, **4**) and Distamycin A (**5**).*

Table 1.2: *The hydrogen bond donating and accepting functional groups of the nucleobases, which are exposed in the major and minor grooves of the DNA double helix.*

Hydrogen Bond Site	Major Groove	Minor Groove
Donor	A (NH_2), C (NH_2)	G (NH_2)
Acceptor	A (N), T (O), G (N and O)	A (N), T (O), G (N), C (O)

Minor groove binders are typically small cationic compounds which are able to adopt a "half-moon" structure.[28] They tend to be composed of several aromatic rings connected by bonds that allow torsional freedom. 4',6-Diamidino-2-phenylindole (DAPI, **4**) is an example of a minor groove binder with high selectivity for AT-rich DNA. It is used as a fluorescence dye of DNA for the nucleus in cells since the compound becomes strongly luminescent upon binding to DNA. Also, the chemotherapeutic drug Distamycin A (**5**) binds to DNA in the minor groove.[29]

1.3.4 Intercalation

Fused aromatic ring systems can often bind to DNA through stacking between the base pairs due to van der Waals forces and hydrophobic interactions.[30] Ethidium bromide (EtBr, **6**) is an example of an intercalator that is used as a fluorescence imaging dye for DNA, for example in agarose gel electrophoresis and in ethidium bromide binding assays. Intercalation has a strong impact on the structure of DNA with a lengthening of the double strand of approximately 3.4 Å and unwinding of the helix. This can lead to both positive and negative cooperativity in an allosteric manner. It is known to prevent the binding of an intercalator in the binding pocket next to another intercalator, an effect called "nearest neighbour exclusion principle" (Figure 1.6b).[4,31] On the other hand intercalators introduce a global disturbance of the helical structure that can make it energetically more favourable for another intercalator to bind to DNA[32], and many studies do indeed reveal positive cooperativity in case of

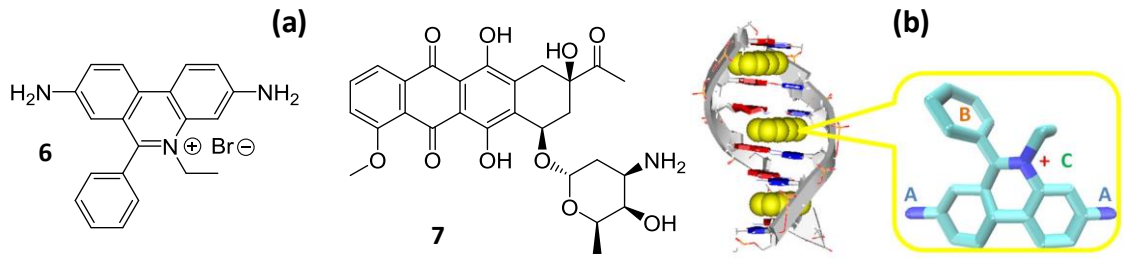

Figure 1.6: *(a) Structure of ethidium bromide (EtBr, **6**) and Daunomycin (**7**). (b) Schematic representation of intercalation of EtBr between the base pairs in double stranded DNA.*[4]

intercalation.[33] Intercalators often possess structural features that interact with the bases from the minor groove, increasing their sequence selectivity. The chemotherapeutic drug Daunomycin (**7**) intercalates between the base pairs with its large fused ring system, while the amino sugar ring results in attractive van der Waals forces and hydrogen bonds from the minor groove.[34]

1.4 The Theory of Multivalent Binding to DNA

Studies of binding to DNA involve measuring and calculation of binding parameters to quantify binding strengths, structural features, site selectivity and cooperativity. In the study of macromolecular binding equilibria focus can be either on simple quantification of binding strength and stoichiometry[35] or on exploration of microscopic features of the system, including structural features and interactions between bound ligands.[31] Several binding models have been developed to treat both types of questions differing with respect to their assumptions about the binding events.

Ideally, the model used includes a microscopic description of the binding event that accurately corresponds to the system under study. However, in most cases, simplified binding models are used because of limited knowledge of the system of interest, or to reduce the number of parameters that must be estimated.[36] In the following sections, a critical review of some of the most important concepts in the study of multivalent binding to DNA will be introduced. This includes a historical and practical literature review of the field of multivalent binding as well as an introduction of new concepts and methods to calculate binding parameters from spectroscopic data. Examples from experiments reported in Chapter 2 and 5 are included for illustrate purposes and to demonstrate how binding parameters can be calculated from spectroscopic data in practice. A detailed discussion of the experiment and the significance of the obtained results will be treated in the respective chapters.

1.4.1 Macroscopic Description of Binding

In the most cases in the literature, multivalent binding refers to the binding of several identical and non-interacting ligands to one molecular species, which will be called the macromolecule.[35,37-41] If a macromolecule (M) has the capacity of binding *N* number of ligands (L) there are *N* binding equilibria:

$$L + M \rightleftharpoons LM \qquad K_1 = \frac{[LM]}{[L][M]}, \quad K_1{}' = \frac{[LM]}{[L][M]} \tag{1.1}$$

$$iL + M \rightleftharpoons L_iM \qquad K_i = \frac{[L_iM]}{[L]^i[M]}, \quad K_i{}' = \frac{[L_iM]}{[L][L_{i-1}M]} \tag{1.2}$$

$$NL + M \rightleftharpoons L_N M \qquad K_N = \frac{[L_N M]}{[L]^N [M]}, \quad K_N{}' = \frac{[L_N M]}{[L][L_{N-1} M]} \tag{1.3}$$

Here, K_i and $K_i{}'$ represent the association constant and the stepwise binding constant, respectively. It is presumed that no interactions between individual macromolecules and ligands are present. In non-ideal systems, the activity of the ligand should be considered rather than the concentration, in which case this will be an exact description.

This description is often used to describe non-idealised cases including the one presented in the next chapter where the binding of a racemic mixture of Ru(II) polypyridyl complexes to DNA is studied. Sometimes multivalent binding will also refer to the case where the same DNA binding ligand has several DNA binding groups,[42] which is the case in Chapter 6 where the binding of gold nanoparticles to DNA is described.[2,43] Many sophisticated descriptions of how to describe more complex situations are included in the literature.[41,44,45] However, these methods are often difficult to use in practice, especially because they involve calculation of many binding parameters, which demand high quality data. In the following treatment of multivalent binding, descriptions of more complex situations will be excluded.

The equilibria are phenomenological or empirical by nature since they involve no description of the system under study and give poor insight into the binding event.[46] A phenomenological description is not always a useful concept since it does not give a proper quantification of the binding affinity for a specific site, as will be described in the next and subsequent sections. Furthermore, it does not give any insight into how the binding occurs nor any information about sequence specificity and cooperativity.

A useful concept in relation to multivalent binding is the binding polynomial (P)[37,41,46] that is defined by the association constant and free ligand concentration as:

$$P = 1 + K_1[L] + \cdots + K_i[L]^i + \cdots + K_N[L]^N \tag{1.4}$$

This equation corresponds to the grand partition function (*GPF*) in statistical mechanics, see Section 1.4.2.[38] In the simple case, with only one binding site, it will be given as:

$$P = 1 + K_1[L] \tag{1.5}$$

A binding isotherm is a relation between different species in an equilibrium system.[37] The binding isotherm corresponding to the degree of saturation of the macromolecule (number of ligands bound per macromolecule) as a function of free ligand concentration, is related to the binding polynomial as:[47]

$$Y = \theta N = \frac{\partial ln(P)}{\partial ln[L]} = \frac{[L]}{P}\frac{\partial P}{\partial [L]} \tag{1.6}$$

$$Y = \frac{K_1[L]+\cdots+iK_i[L]^i+\cdots+N\cdot K_N[L]^N}{1+K_1[L]+\cdots+K_i[L]^i+\cdots+K_N[L]^N} \quad (1.7)$$

Here Y is the average number of ligands bound per macromolecule and θ is the degree of saturation (Y/N). In the special case where N is equal to one, the equation is reduced to:

$$Y = N\theta = N\frac{K[L]}{1+K[L]} \quad (1.8)$$

$$\theta = \frac{K[L]}{1+K[L]} \quad (1.9)$$

Where K is substituted for K_1. This equation has the same form as Langmuir's binding isotherm that can be used for multivalent binding when all binding sites are independent (no cooperativity). [36,47]

1.4.2 Microscopic Description of Binding

Multivalent macromolecular binding is poorly understood at a pure phenomenological level, and a brief introduction to statistical mechanics is necessary in order to discuss binding strength, specificity and cooperativity.[38] Often, interest is in binding to individual sites (including differences in affinity for the sites, *i.e.* specific binding) and about interactions between ligands bound to different sites (*i.e.* cooperativity).

Statistical Nature of Binding

The macroscopic binding constants presented earlier give a poor background for a discussion at the binding site level. In the case of multivalent binding, where a macromolecule has the capacity of binding multiple ligands, it will be preferential to discuss the affinity of a ligand for the individual sites in the form of microscopic binding constants.[37,40,48] Without any statistical consideration concerning the nature of the binding, there will be no obvious connection between the microscopic and the macroscopic binding constants. A simple example of a molecule with two identical and well separated binding sites emphasises this, as shown in Figure 1.7.

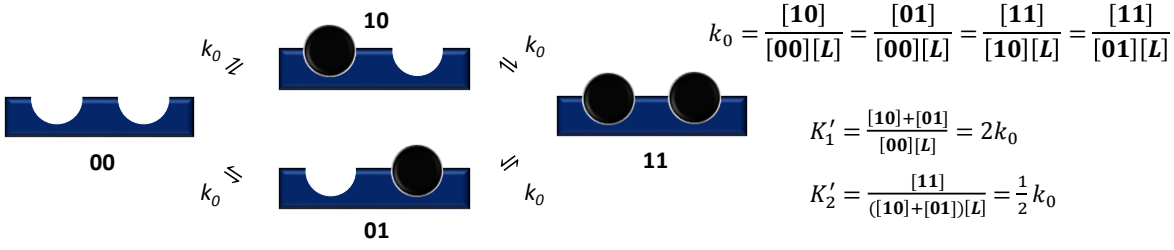

Figure 1.7: *Non-cooperative binding where a species (blue rectangle) has two non-interacting binding sites. Each site can bind a ligand (black circle) with the same microscopic binding constant k_0. "0" and "1" represent free and occupied binding sites, respectively (e.g. "**10**" means first site occupied and second site free).*

In the absence of cooperativity, it is tempting to assume that the two stepwise binding constants are of the same size. However, it can be shown using simple statistical considerations that this is not the case,[40] and that the binding constants are related to a microscopic binding constant *k* by the relation:

$$K_1' = 2k, \qquad K_2' = \frac{1}{2}k \tag{1.10}$$

This is a consequence of a reduction of accessible sites when forming LM, which results in a decrease of the stepwise binding constant. The enthalpic contribution at each step will be the same. In the general case, with *N* identical and independent sites, it can be shown that the *i*'th association and stepwise binding constant are given as:[48]

$$K_i = \binom{N}{i} k^i, \qquad K_i' = \frac{N-i+1}{i}k, \qquad \binom{N}{i} = \frac{N!}{i!(N-i)!} \tag{1.11}$$

The quantity $\binom{N}{i}$ is the binomial coefficient and represents the number of combinations of how *i* numbers of ligands can bind *N* different sites.[38]

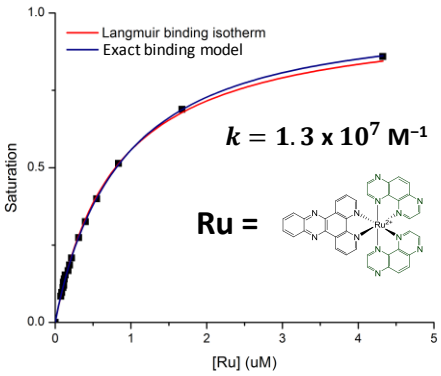

i	K_i' (10^7 M^{-1})	$\frac{N-i+1}{i}k$ (10^7 M^{-1})
1	4.1	3.8
2	0.9	1.3
3	0.7	0.4

$$\boldsymbol{Ru + I9 \rightleftharpoons Ru_1I9}$$
$$\boldsymbol{Ru + Ru_1I9 \rightleftharpoons Ru_2I9}$$
$$\boldsymbol{Ru + Ru_2I9 \rightleftharpoons Ru_3I9}$$

Figure 1.8: *Example of an equilibrium system with weak cooperativity. Binding of a Ru(II) polypyridyl complex (Λ-**9b**) to a self-complementary decamer of DNA with inosine at position nine (will be discussed in Chapter 5).*

Combined with equation (1.4) the binding polynomial will be given as:

$$P = 1 + Nk[L] + \cdots + \binom{N}{i} k^i[L]^i + \cdots + k^N[L]^N \tag{1.12}$$

$$k = \frac{K_1}{N}, \qquad k = K_N^{1/N}$$

In the general case where Q_i' is the number of ways *i* ligands can bind to DNA, all corresponding to the same energy, the macroscopic binding constants and the binding polynomial can be written as:[38]

$$P = 1 + Q_1'k[L] + \cdots + Q_i'k^i[L]^i + \cdots + k^N[L]^N \tag{1.13}$$

$$K_i = Q_i'k^i, \qquad K_i' = \frac{Q_i'}{Q_{i-1}'}k \tag{1.14}$$

It is presumed that there is only one way in which *N* ligands can bind to the macromolecule ($Q_N' = 1$). The constant *k* is related to K_1 and K_N as:

$$k = \frac{K_1}{Q_1'} \qquad k = K_N^{1/N} \tag{1.15}$$

The free energy change for binding of a ligand are related to the step-wise binding constant in the usual way:

$$\Delta G_i' = -RTln(K_i') = -RTln(k') - RT\ln(Q_i'/Q_{i-1}') = \Delta G_0 - T\Delta S_i' \tag{1.16}$$

$$\Delta G_0 = -RTln(k) = \Delta H_0 - T\Delta S_0 \tag{1.17}$$

$$\Delta S_i' = R \cdot ln(Q_i'/Q_{i-1}') \tag{1.18}$$

It can be seen from this relation that the variation in K_i' and the free energy for binding of a ligand (ΔG_i') for different *i's* is an entropic effect while the change in enthalpy is always the same.

The Canonical and the Grand Partition Function

A central entity in statistical thermodynamics is the partition function. A partition function for an equilibrium system can be used to derive all thermodynamic parameters including internal energy, enthalpy and entropy.[38] In this sense, the partition function has the same status in statistical mechanics as the wave function has in quantum mechanics.[49]

The partition function for a system can be expressed in different forms. One form is the canonical partition function (*CPF*) that, for a system with a fixed number of components, is a sum of states weighted with respect to their energy by a Boltzman's distribution. This form of the partition function is the natural choice to describe a single macromolecule with *i* ligands bound:

$$Q_i(T) = \sum_{j \in all\ states} g_j\, e^{-Ej/kT} \tag{1.19}$$

This expression represents the partition function for L_iM where g_j is the degeneracy of states with energy E_j. If all states have the same energy ($E_j = 0$), Q_i will simply be the number of combinations in which *i* ligands can bind to M [*cf.* Q_i' in equation (1.13)].

In cases of multivalent binding, with an equilibrium system containing a variable number of bound ligands, the natural choice will be the grand partition function (*GPF*). The GPF is a sum of states weighted with respect to the number of components in the system. In case of a macromolecule that can bind a maximum of *N* ligands, the *GPF* is given as:[38]

$$GPF(T) = \sum_{i=0}^{N} Q_i\,(T) e^{-\frac{i\mu}{kT}} = \sum_{i=0}^{N} Q_i\,\lambda^i \tag{1.20}$$

This equation represents the partition function for the whole equilibrium system where Q_i is the canonical partition function for L_iM, and μ is the total chemical potential of the system.

λ is called the absolute activity, because it can be shown to be proportional to the free ligand concentration or activity.

Q_i and λ are non-familiar theoretical entities. Fortunately, it can be shown that *GPF* is directly related to experimental and familiar properties in the form of the binding polynomial P [equation (1.4)]:

$$GPF = 1 + K_1[L] + \cdots + K_i[L]^i + \cdots + K_N[L]^N \quad (1.21)$$

In this way, *GPF* and *P* can be used interchangeably in case of multivalent binding to a single macromolecule.

This relates *GPF* to the binding isotherm in the same way as *P*:

$$\theta N = \frac{\partial \ln(GPF)}{\partial \ln[L]} = \frac{[L]}{GPF}\frac{\partial GPF}{\partial [L]} \quad (1.22)$$

$$\ln(GPF) = N \int_0^{\ln[L]} \theta \, d\ln[L] \quad (1.23)$$

These expressions introduce a method to derive the *GPF* from the binding isotherm, either by fitting a parameterised expression for the *GPF* to the data, like the binding polynomial [equation (1.22)], or numerically by integration [equation (1.23)].[46] The derived expression for the *GPF* may be model independent, without any assumption of how the binding occurs. Examples are use of the binding polynomial and the numeric integrations. To gain insight into the binding event and to reduce the number of parameters that must be calculated, an explicit binding model can be used, like the Langmuir or the Hill model.

As mentioned, it is possible to derive all thermodynamic parameters from a partition function.[38] The canonical and the grand partition function are related to the Helmholtz free energy (A) and the grand potential (Φ) by the relation:

$$A = U - TS = -RTln(CPF) \quad (1.24)$$

$$\Phi = \langle U \rangle - T\langle S \rangle - \langle i \rangle \mu = -RTln(GPF) \quad (1.25)$$

$\langle i \rangle$ represents the average number of ligands bound to the macromolecule. The two parameters (*A* and Φ) are related to all other thermodynamic parameters (*e.g. G*, *H* and *S*), which can be found if the dependence of the partition function (*GPF* or *CPF*) on all thermodynamic variables are known (*e.g.* temperature, volume and pressure).

Non-cooperative and Cooperative Binding

If the *GPF* is used the relation between the microscopic and macroscopic case is well understood if there is no cooperativity. It is an important property of any partition function (*CPF* or *GPF*) that it is given as the product of the partition functions for all independent

sub-systems. For a single site, *GPF* can be written as 1+*k*[L] [equation (1.5)] in the non-cooperative case. This means that for *N* independent binding sites *GPF* can be written as:

$$GPF = (1 + k[L])^N \tag{1.26}$$

$$GPF = \prod_{i=1}^{N}(1 + k_i[L]) \tag{1.27}$$

Equation (1.26) describes binding to *N* number of identical sites each with the site binding constant *k*, while (1.27) describes binding to *N* non-identical binding sites each with a site binding constant k_i.[41,46,50] Expansion of equation (1.26) will result in the polynomial form of equation (1.12). It can also be shown by use of equation (1.22) that:

$$\theta N = \frac{\partial \ln((1+k[L])^N)}{\partial \ln[L]} = N\frac{\partial \ln(1+k[L])}{\partial \ln[L]} = N\frac{[L]}{1+k[L]}\frac{\partial(1+k[L])}{\partial[L]} \tag{1.28}$$

$$\theta = \frac{k[L]}{1+k[L]} \tag{1.29}$$

This equation corresponds to Langmuir's binding isotherm [equation (1.9)]. It reduces the number of parameters that must be determined from *N* macroscopic binding constants to only one microscopic binding constant and makes it possible to discuss binding at the site level.

In cases where a macromolecule consists of *N'* number of identical, however, interacting sub-units a less explicit form of (1.26) is sometimes used:[51]

$$GPF = x^{N'} \tag{1.30}$$

$$x = GPF^{1/N'} \tag{1.31}$$

This definition relates *x* to all thermodynamic properties of the grand potential by the relation:

$$\Phi = -RTln\left(x^{N'}\right) = -N' \times RTln(x) \tag{1.32}$$

In this sense, *x* represents the contribution of each sub-unit to the thermodynamic parameters of the system. As usual, the *GPF* can be related to the binding isotherm by the use of equation (1.22):

$$\theta N = \frac{\partial \ln(x^M)}{\partial \ln[L]} = M\frac{[L]}{x}\frac{\partial x}{\partial[L]} \tag{1.33}$$

$$\theta = \frac{M}{N}\frac{[L]}{x}\frac{\partial x}{\partial[L]} \tag{1.34}$$

An example of the practical use of this relatively abstract concept is found in so-called generating functions that are used to derive different binding models for the binding to a homogenous DNA string.[39,51]

1.4.3 Spectroscopic Titrations

In a typical spectroscopic titration experiment for study of multivalent binding, the change in the spectrum will be measured, while the concentration of macromolecule or ligand is varied. In the following, focus will be on the case where the spectroscopic signal originates from the ligand, and the concentration of macromolecule is increased gradually.[52-54] The amount of ligand is constant through the titration, and change in concentration is only a consequence of dilution when a solution of the macromolecule is added. Common practice is to continue increasing the concentration of the macromolecule to the point at which "almost" all ligand is bound to the macromolecule and then assume that the molar signal from the bound ligand (S_B) is equal to the apparent molar signal (S_a) of the ligand at this point. By assuming a linear relationship between the relative change in the apparent molar response and the relative amount of bound ligand, the amount of bound ([B]) and free ligand ([L]) can be calculated:

$$[B] = \frac{S_a - S_L}{S_B - S_L} C_L \tag{1.35}$$

$$[L] = C_L - [B] \tag{1.36}$$

$$Y = \frac{[B]}{C_M} \tag{1.37}$$

The values C_L and C_M are the total concentration DNA binding ligand and DNA molecules, respectively, while Y as mentioned previously is the saturation of DNA with bound ligand. One problem with this approach is that an approximated value of S_B is used. By using the last point in the titration curve as an estimate of S_B, the amount of bound ligand will be overestimated [equation (1.35)], and the amount of free ligand will be underestimated [equation (1.36)]. Even a small error in S_B can be shown to give a very large error in the binding constant.[54,55] Another problem is the assumption that there is a linear dependence between the fraction of bound compound and the change in the apparent molar signal.[39] In general, the molar response of bound ligands will be the average of several different binding modes with different molecular environments. Unfortunately, the distribution between the different binding modes and binding sites will vary through the titration when cooperativity and site-specific binding come into play, and accordingly S_B will also change. Sometimes, deviation from linearity will also be a result of non-static interactions, corresponding to collision between solutes,[56] or non-ideal behaviour (such as binding between macromolecules or between ligands).

The spectroscopic molar response, *e.g.* expressed by the extinction coefficient, from a macromolecule is a function of the degree of saturation.[39,57] It is possible to calculate the

degree of saturation from the molar signal, even in cases where the response is not linearly dependent on the concentration. This has been demonstrated by Bujalowski *et al.* It is possible, also, to calculate the binding isotherm from spectroscopic data, in which case the response comes from the ligand or from the macromolecule itself.[39,57]

Another strategy for calculation of the binding parameters from spectroscopic data is to fit the molar response of bound ligands directly to the desired binding model.[45,54,55] In the situation where the signal originates from the ligand, and macromolecules without any bound ligands are spectroscopically silent, the total signal will be the sum of the signal from free ligand and ligand in different binding modes:

$$S_{obs} = [L]S_L + \sum[B]_j S_{Lj} \quad (1.38)$$

Here, the spectroscopic response is not considered to be an intrinsic property of the macromolecule, but a sum of the signals from the individual ligands, distributed among different binding modes in a microscopic binding model. The disadvantages of such a model dependent consideration is that knowledge of the binding behaviour is required. Alternatively, it becomes necessary to make certain conservative assumptions, like those given for the McGhee-von Hippel model where some simple rules for the distribution among different binding modes are defined. [45] It is an advantage, however, that the model gives a unique opportunity to distinguish between different binding modes in solution, an opportunity not available from simple examination of the binding isotherm. This will often make it easier to fit many parameters simultaneously and to obtain knowledge of the different binding modes, including binding strength, type of binding, and spectral properties. Global analysis, where changes in the spectrum at several wavelengths are considered, can be useful when many binding parameters must be fitted.[45,55,58]

1.4.4 Microscopic Description with an Explicit Binding Model

The complexity of multivalent binding will often be so great that it will be impossible to obtain an exact description of the binding event. Take, for example, natural DNA that consists typically of a heterogeneous sequence of bases which can bind hundreds or thousands of ligands. If a thousand ligands can be bound it will be necessary to fit a thousand binding constants in equation (1.7) to the binding isotherm. This will, in practice, be impossible. To reduce the number of parameters that need to be fitted, a simplified binding model will often be used to calculate a small set of microscopic binding constant that can describe the strength of the binding to the individual binding sites and, in some cases, also the stoichiometry (size of binding site), sequence specificity, and cooperativity. The chosen

binding model is usually an approximation and selected on the bases of the level of description it will be possible to obtain using the applied experimental method.

Furthermore a microscopic description of the binding is necessary, to gain insight into the binding at the site level, where the macroscopic binding constant, or the *GPF* itself, gives poor insight into the binding. To explore how the binding occurs, *e.g.* to determine positive or negative cooperativity, it is advised to expose data to more than one binding model and to choose the model that makes the best fit.[55] However, this approach can rarely stand-alone since an inaccurate model often is able to give a good quality of the fit with an R^2 value close to unity.[42]

The Scatchard Model

The Scatchard model was introduced to treat cases where an unknown number of ligands binds to a macromolecule with low, or no, cooperativity. [35] As in the Langmuir's binding model, the individual binding sites will be treated as non-interacting species. However, the number of binding sites per macromolecule (*N*) is an unknown parameter that must be fitted:

$$Y = N\frac{k[L]}{1+k[L]} \quad (1.39a)$$

$$Y = \theta N = [B]/C_M \quad (1.39b)$$

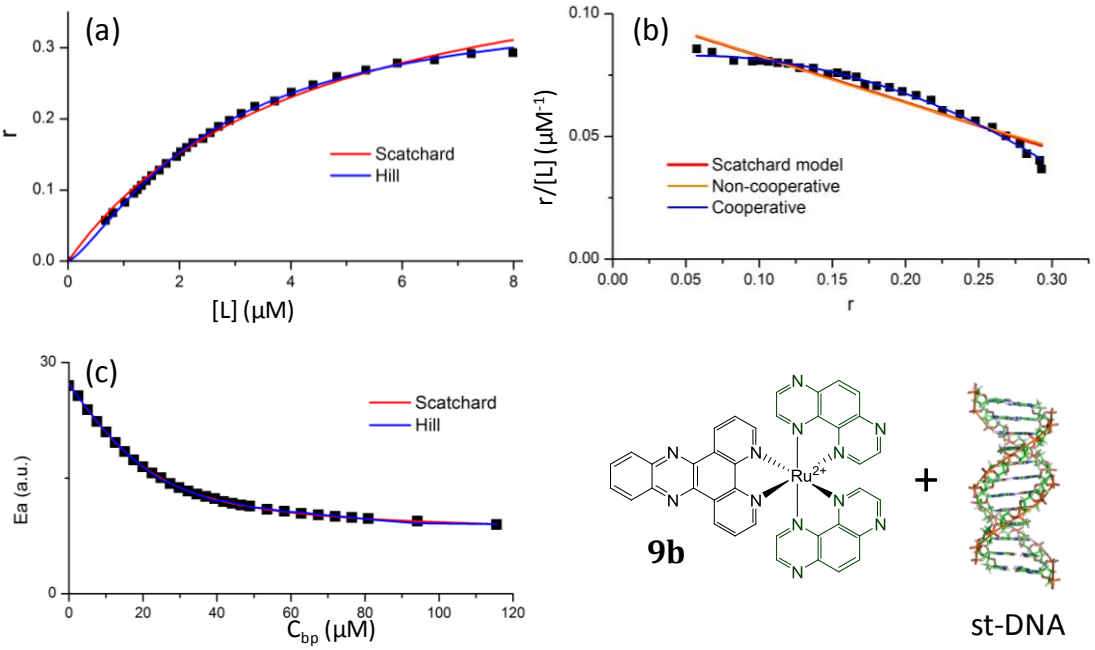

Figure 1.9: *Binding isotherms obtained from luminescence titration of ruthenium complex Δ-[Ru(dppz)TAP$_2$]$^{2+}$ (Δ-**9b**) with salmon testes DNA (st-DNA), 50 mM potassium phosphate buffer with 50 mM KCl (Chapter 5). (a) Fit of the Scatchard and the Hill models to a r-plot. (b) Fit of the Scatchard and the McGhee-von Hippel (MGVH, cooperative and non-cooperative) equations to a Scatchard plot. (c) Fit to the molar emission of the Scatchard and Hill models.*

$$\frac{Y}{[L]} = k(N - Y) \tag{1.40}$$

As mentioned previously θ is the degree of saturation. There is no principal difference between the Scatchard and the Langmuir binding model. However, Scatchard introduced the maximum of bound ligands (*N*) as a fitting parameter. Furthermore, the non-linear equation (1.39) is transformed into the linear Scatchard equation (1.40). This transformation was important in the past where a fit of a non-linear equation was a complicated matter.[55] Today the transformation is less important since a non-linear equation like (1.39) can easily be fitted using modern computer software.

When the concentration of monomers is known, rather than the macromolecular concentration, an alternative formulation will be used:[31,59]

$$r = n^{-1}\frac{k[L]}{1+k[L]} \tag{1.41a}$$

$$r = [B]/C_{bp} \tag{1.41b}$$

$$\frac{r}{[L]} = k(n^{-1} - r) \tag{1.42}$$

wherein *r* represents the ratio between the total concentration of bound ligands and the total concentration of monomers C_{bp} (here nucleic acid base pairs); *n* corresponds to the size of the binding site with the number of bp as the unit. The concentration of monomers is represented as the concentration of base pairs because the focus in this thesis is on binding to double stranded DNA.

Another version of the Scatchard equation, with the same binding description, was introduced by Carter, Rodriguez and Bard into the analysis of binding of a ligand to DNA.[59] Here, equation (1.43) is fitted to a plot with [B] as the dependent variable and C_{bp} and C_L as independent variables:

$$[B] = \frac{b-(b^2-4\cdot k^2 C_L C_{bp}/n)^{0.5}}{2k} \tag{1.43}$$

$$b = 1 + kC_L + kC_{bp}/n \tag{1.44}$$

C_{bp} and [B] are related more directly to the spectroscopic data than *r* and [L] [equation (1.39)]. By using equation (1.35) the following relation can be obtained:

$$\frac{S_a - S_L}{S_B - S_L} = \frac{b-(b^2-4\cdot k^2 C_L C_{bp}/n)^{0.5}}{2kC_L} \tag{1.45}$$

A small modification makes it possible to fit the binding constant and binding site size directly to the molar spectroscopic signal: [54]

$$S_a = \frac{b-(b^2-4\cdot k^2 C_L C_{bp}/n)^{0.5}}{2kC_L} \times (S_B - S_L) + S_L \tag{1.46}$$

In this equation S_a is the dependent variable and S_L and S_B can be considered either as fixed constants if they are known, or they can be fitted together with k and n (Figure 1.9c). It has been demonstrated that equation (1.46) gives much more accurate values for the binding constant when S_B was fitted to the data rather than using S_a in the end of the titrations as an estimate which is the traditional method. For the spectroscopic titrations in Chapter 2 the value of k using equation (1.43) with an estimated value of S_B was *ca*. twice the value obtained using equation (1.46).

Model Independent Method

One method to calculate k from spectroscopic data without consideration of the binding behaviour and binding site size has been developed by Schmechel and Crothers.[60,61] In this method, it is presumed that the saturation of the macromolecule is zero, and for that reason only data points that correspond to a very low saturation can be used to calculate the binding constant. Given these criterion, k can be written as a simple mass action equation of the form:

$$k = \frac{[LM]}{[L][M]N'} \approx \frac{[B]}{[L]C_{bp}} \qquad (1.47)$$

It is presumed that not more than one ligand is bound to each macromolecule ([B] = [L_1M]), and that an infinitesimal fraction of all macromolecules has bound a ligand ([M]N' = C_{bp}). In cases in which the macromolecule is very large hundreds of ligands can bind, and this presumption will, in practice, never be fulfilled. However, in case of very low cooperativity the number of bound ligands will not affect the value obtained for k, since the affinity of a ligand for the macromolecule will be unchanged in the presence of bound ligands. The problem is more serious if there is strong positive cooperativity, or if allosteric effects lead to global change in the affinity of the macromolecule for ligands at all sites.

In contrast to the Scatchard model, the size of the binding constant will depend on the choice of monomeric unit. In the Scatchard model, the size of k will be unchanged if the concentration of DNA is reported in single bases rather than in base pairs. However, in this approach the magnitude of k will be halved if the concentration of DNA is measured in single bases (C_{base}) rather than in base pairs, since the magnitude of the denominator in (1.47) will be doubled ($C_{base} = 2 \times C_{bp}$). In this case, k can be interpreted as the affinity of the ligand for a single monomeric unit.

With [B] and [L] expressed using the spectroscopic signals [equations (1.35) and (1.36)] equation (1.47) can be transformed into:

$$\Delta S_a{}^{-1} = \Delta S_B{}^{-1} + \Delta S_B{}^{-1} \cdot k^{-1} \cdot C_{bp}{}^{-1} \qquad (1.48)$$

$$\Delta S_a = S_a - S_L, \quad \Delta S_B = S_B - S_L, \qquad S_B = S_L + \Delta S_B \tag{1.49}$$

From linear regression to a plot of ΔS_a^{-1} as a function of C_{bp}^{-1}, k can be found as the ratio between the intercept (ΔS_B^{-1}) with the ΔS_a^{-1}-axis and the slope ($\Delta S_B^{-1} \cdot k^{-1}$, Figure 1.10). The intercept with the y-axis is the reciprocal value of the difference in the molar signal between bound (S_B) and free ligand (S_L). Unlike the case in the Scatchard model, n does not exist as a fitting parameter. This is convenient for weakly binding ligands where it is difficult to reach the high saturation necessary to derive n. Only the linear part of the plot can be used, the part based on data points for which the standard assumption in equation (1.47) are fulfilled (*i.e.* low saturation).

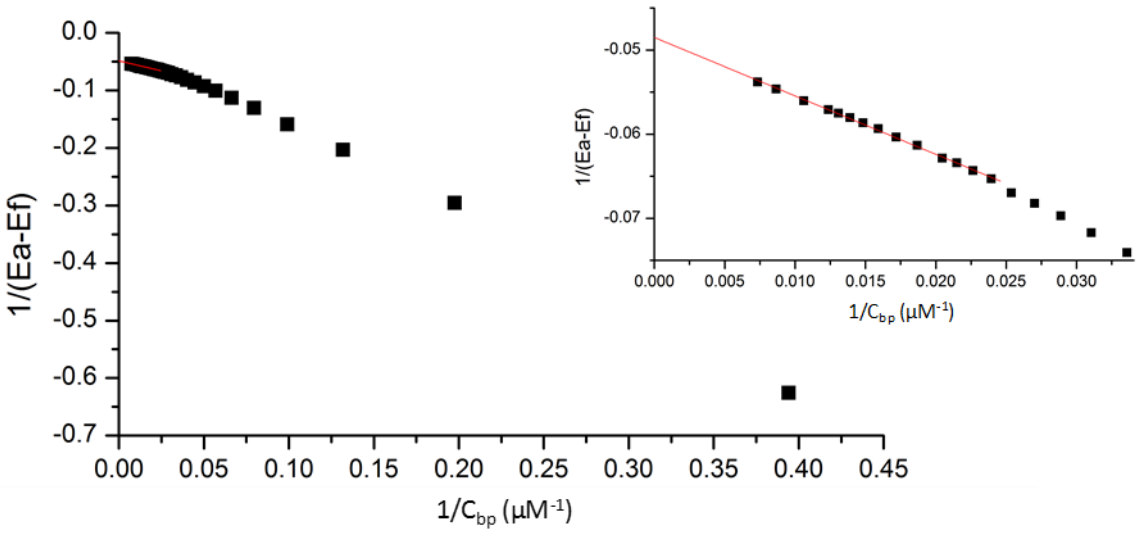

Figure 1.10: *Double-reciprocal plot with ΔS_a^{-1} as a function of C_{bp}^{-1} for the titration of Δ-[Ru(TAP)$_2$dppz]$^{2+}$ (Δ-**9b**) with st-DNA (will be described Chapter 6). Inset: Fitting of the linear region of the plot.*

A very useful application of equation (1.48) is the construction of a binding isotherm to which miscellaneous binding models can be fitted.[60] It was demonstrated in equation (1.46) how S_B can be fitted directly to the experimental data using the Scatchard binding model. Alternatively, S_B can be derived from the model independent approach where ΔS_B can be calculated from the y-intercept of the double reciprocial plot. This can be used to construction a Scatchard plot or similar and, finally, to fit the model of interest to the respective plot. The r and Scatchard plots in Figure 1.9b are constructed using this approach.

The Hill Model

A more general version of the Langmuir binding model, which gives a better description in cases of positive cooperativity, is the Hill model.[36] Instead of the assumption that one ligand

and one binding site form a one-to-one equilibrium, this model presumes that several ligands bind to a cluster of interacting sites (M'):

$$aL + M' \rightleftharpoons L_aM' \qquad K_a = k^a = \frac{[L_aM']}{[L]^a[M']} \qquad (1.50)$$

a is called the Hill coefficient and is, for $a > 1$, a measure of positive cooperativity. The model is referred to as "all-or-nothing" since a certain number of ligands, and only this exact number of ligands, will be able to bind at the same time.[62]

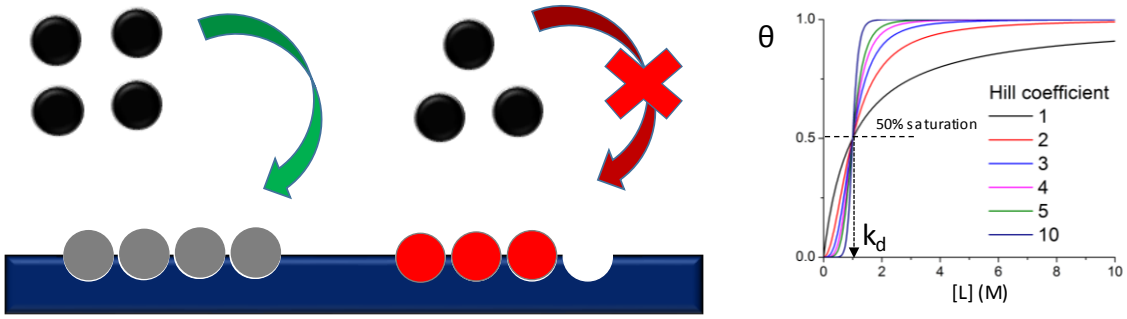

Figure 1.11: *Cooperative binding to a macromolecule as described in the Hill model. All sites are organised in clusters of interacting binding sites. The dissociation constant k_d (k^{-1}) is equal to the concentration at 50% saturation.*[37]

The binding polynomial for a cluster of sites will simply be:

$$P = 1 + k^a[L]^a \qquad (1.51)$$

Equation (1.22) gives:

$$Y = \frac{Nk^a[L]^a}{1+k^a[L]^a} \qquad (1.52)$$

$$\theta = \frac{k^a[L]^a}{1+k^a[L]^a} \qquad (1.53)$$

$$r = \frac{1}{n}\frac{k^a[L]^a}{1+k^a[L]^a} \qquad (1.54)$$

The Scatchard binding model is the special case where a = 1. In these equations, the Hill coefficient and the maximum number of bound ligands (N) or binding site size (n) are both fitting parameters. The equations give a measure of the total number of ligands, N, that can bind, and the number of interacting ligand binding sites ("cluster of sites"). A cluster of sites can, for example, be a domain on DNA. If all binding sites on the macromolecule are interacting, the Hill coefficient will be N. For that reason the Hill model is often used in a similar way as the Scatchard model to quantify the number of ligands that can bind to a macromolecule.[63] Equation (1.54), with r as a function of [L], should be used only if it is possible to calculate the total concentration of bound ligand, and if the size of the

macromolecule is unknown. Sometimes, the degree of saturation, θ, can be measured directly, and *a* can be calculated without any consideration of *N* or *n*.[62]

By use of equation (1.36) and (1.35) an expression can be obtained where the spectroscopic signals for bound and free ligand can be fitted:

$$S_a = \frac{1}{n} \cdot \frac{k_{sat}{}^a \left(C_L - \frac{S_a - S_L}{S_B - S_L} C_L\right)^a}{1 + k_{sat}{}^a \left(C_L - \frac{S_a - S_L}{S_B - S_L} C_L\right)^a} \cdot \frac{C_{bp}}{C_L} \cdot (S_B - S_L) + S_L \qquad (1.55)$$

In this equation *k*, *n*, *a*, S_L and S_B can be fitted to a plot with S_a as a function of C_{bp}, C_L and S_a (S_a is the dependent as well as an independent variable, Figure 1.9).

A Hill coefficient less than one indicates negative cooperativity; however, in this case the coefficient has no real physical meaning. It is normal to get non-integer Hill coefficients, because few systems can be described as "all-or-nothing" as assumed in equation (1.50) or due to varying cluster sizes. For example, the reported value for the association of oxygen with haemoglobin is 2.6 and not four, the number of oxygen binding sites.[37]

The McGhee-von Hippel Model

The McGhee-von Hippel (MGVH) model is a cooperative model specially designed to describe the binding of a number of ligands to a polymer of nucleic acids of an infinite length, or to any other linear polymer consisting of identical sub-units (Figure 1.12).[31] For a DNA duplex, this could, for example, be poly(dA)poly(dT) in which each AT base pair corresponds to one sub-unit. Two different versions of the model are referred to as the cooperative model and the non-cooperative model, respectively. However, both models are cooperative, in practice, in the sense that it is not possible to treat the individual sub-units or sites as independent species such as it is done in the Scatchard model.

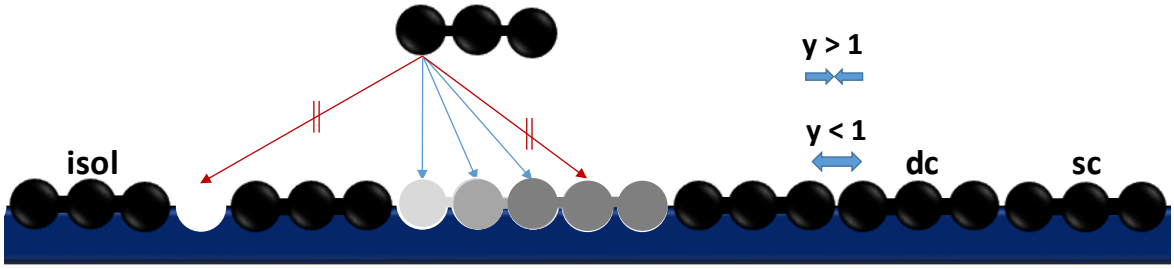

Figure 1.12: *Accessible sites on a linear lattice given by the McGhee-von Hippel (MGVH) model for a ligand that can occupy three sub-units. Three consecutive sub-units must be unoccupied to bind a ligand. The cooperativity parameter, y, describes attraction (>1) or repulsion (<1) between neighbouring bound ligands. Isolated, single continuers and double continuers refer to bound ligands that have no neighbours (isol), one neighbour (sc) and two neighbours (dc), respectively.*

In the non-cooperative version, the affinity of a ligand will be the same for all parts of the lattice, and a simple mass-action equation can be used to describe the affinity for a sub-unit:

$$k = \frac{[B]}{[L][site]} \tag{1.56}$$

In this equation, [site] refer to the total concentration of sub-unit that can, potentially, be the starting point of the binding of a ligand. The value of the binding constant depends on "the choice" of the smallest sub-unit, something that must be taken into consideration when results from different systems are compared. In this thesis, the smallest subunit for double stranded DNA is defined as a single base pair. For single stranded DNA or RNA the smallest subunit is defined as a single base.

It can be shown that the following expression describes the binding isotherm:

$$\frac{r}{[L]} = k(1-nr)\left(\frac{n-nr}{1-nr+r}\right)^{n-1} \tag{1.57}$$

This expression was derived by McGhee and von Hippel using conditional probabilities.[31] Before then, Zasedatelev, Gurskii and Vol'kenshtein published a very similar expression for the same problem.[64] They discussed, also, the binding to a heterogeneous lattice consisting of a random sequence of nucleic bases.[65]

The cooperative MGVH model includes interactions between neighbouring ligands where the end of one ligand corresponds to the start of a new one (Figure 1.12). It is presumed that the total cooperativity energy is proportional to the number of interactions. This gives three mass-action equations that describe the binding constant for an isolated bound ligand without any neighbours (isolated), a ligand with a single neighbour (single continuer) and a ligand with two neighbours (double continuer):

$$k_{isol} = \frac{[B]_{isol}}{[L][site]_{isol}} \tag{1.58}$$

$$k_{sc} = \frac{[B]_{sc}}{[L][site]_{sc}} = yk \tag{1.59}$$

$$k_{dc} = \frac{[B]_{dc}}{[L][site]_{dc}} = y^2k \tag{1.60}$$

In these equations, y is a cooperativity constant that describes the explicit energetic interactions that occur between neighbouring ligands.

It can be shown that:[i]

$$\frac{r}{[L]} = k(1-nr)\left(\frac{(2y-1)(1-nr)+r-R}{2(y-1)(1-nr)}\right)^{n-1}\left(\frac{1-(n+1)r+R}{2(1-nr)}\right)^2 \tag{1.61}$$

[i] Corrections are made for a typographical error in the original McGhee-von Hippel paper.

$$R = ((1-(n+1)r)^2 + 4yr(1-nr))^{1/2} \quad (1.62)$$

Zasedatelev *et al.* derived a similar expression, and included interactions between non-neighbouring ligands;[64] however, the expression derived by McGhee and von Hippel is more elegant and easier to use in practice.[31]

One problem with the McGhee-von Hippel equation is that the term (*y*-1) occurs as a factor in the denominator. This prevent the use of the expression in cases where *y* is one since this would result in division by zero. Also, in cases with weak cooperativity this can lead to computational problems. An alternative expression[37] that does not have this problem is:

$$\frac{r}{[L]} = k_{isol}(1-nr)\left(\frac{2y(1-nr)}{(2y-1)(1-nr)+r+R}\right)^{n-1}\left(\frac{1-(n+1)r+R}{2(1-nr)}\right)^2 \quad (1.63)$$

Here the result for $y = 1$ corresponds to the result you will obtain in the non-cooperative case.

1.4.5 Global Fitting with Non-linear Regression

In Section 1.4.3 it was described how binding isotherms can be constructed from spectroscopic data using the relative change in the spectroscopic signal, while in Section 1.4.4 examples were given of how the spectroscopic signal can be fitted to specific binding models. These considerations all involved the change of a single value, such as the absorbance at a specific wavelength or the integrated emission intensity. Global fits of spectroscopic changes are simultaneous fits to more than one wavelength. One advance is that more data points are used. In general, more data will always give more precise measurements and result in more precise values of the binding parameters. It will be easier, also, to fit more binding parameters, such as cooperativity constants.[55] Lincoln *et al.* has used MatLab to calculate MGVH binding parameters for spectroscopic data obtained from titrations of Ru(II) polypyridyl complexes with polymeric DNA.[45]

In this thesis, the program ReactLab EQUILIBRIA will be used for non-linear fitting of binding constants for binding to DNA. The program is usually restricted to describe simple binding equilibria, such as metal complex formation, where it can calculate the binding constants for all equilibria and the molar spectra for all species present (*c.f.* Experimental, Section 6.3). The main interest of the following section has been to calculate binding constants for the binding of ligands to polymeric DNA using some of the binding models introduced in the previous sections. In accordance with the assumptions made in the described models, the strategy has been to treat the individual sites (S) as "independent"

species so that the site binding constants can be calculated as the equilibrium constants for simple 1:1 equilibria:

$$L + S \rightleftharpoons LS, \qquad k_{isol} = \frac{[LS]}{[L][S]} \tag{1.64}$$

The Scatchard model has been relatively simple to implement, since the total concentration of binding sites is given as:

$$C_S = \frac{C_{bp}}{n} \tag{1.65}$$

On the other hand, fitting of one binding equilibrium cannot describe possible cooperativity. Neither can this simple method contribute to the solution of problems, which involve non-linear behaviour arising from the presence of more binding modes with different molar signals. Such problems can be handled by introducing more equilibria into the program:

$$L + D \rightleftharpoons LD, \qquad K_1 = \frac{[LD]}{[L][D]} = \binom{N}{1} k_1 = N k_1 \tag{1.66}$$

$$2L + D \rightleftharpoons L_2D, \qquad K_2 = \frac{[L_2D]}{[L]^2[D]} = \binom{N}{2} {k_2}^2 \tag{1.67}$$

$$NL + D \rightleftharpoons L_ND, \qquad K_2 = \frac{[L_2D]}{[L]^2[D]} = \binom{N}{N} {k_N}^N = {k_N}^N \tag{1.68}$$

In these equations, D represents a part of DNA that can bind a maximum of *N* ligands. With this definition, the total concentration of "cluster of sites" is given as:

$$C_D = \frac{C_{bp}}{N \cdot n} \tag{1.69}$$

The binding constants and *n* can be fitted in a similar way as it is done for just one equilibrium.

The "association constants" K_1, K_2, … are not easy to interpret. However, in the non-cooperative case used to define the Scatchard model, the constants are related to the site binding constants according to equation (1.11), which is the background for the defined "site binding constants" k_1, k_2, … in equation (1.67). For simple multivalent binding, where *N* ligands can bind one "macromolecule", the differences between the different k_i are sometimes used to define cooperativity.[55,66] Consequently, the interaction parameter for step *i* (α_i) will be defined as:

$$\alpha_i = \frac{k_i}{k_1} \tag{1.70}$$

In the case described here, where *N* is a defined quantity, α_i is an approximation to the actual interaction parameter for *i/N* fractional saturation of DNA.

If there is low cooperativity, or if a fit of more than one binding constant results in over-parametrisation, it can be suitable to fit one common binding constant by restraining all k_i's in equation (1.67) to the same value (*c.f.* Section 7.3.2). This procedure will not help to calculate the interaction parameters, however, it will make it possible to handle problems that involve non-linear behaviour in the spectroscopic changes. The approach described here will rarely give a perfect description of the binding event. However, in all cases where the equilibrium system is described according to equation (1.2) by increasing the number of included binding equilibria, the calculated binding parameters will converge towards well-defined values. This includes site binding constant k_1 (average binding constant for the first ligand bound) and interaction parameters for different degrees of saturation, as well as the molar signal for the bound ligands.

ReactLab EQUILIBRIA can also be used to treat other binding models. Use of the Hill model would correspond to the fitting of one equilibrium with a numbers of ligands (L) bound to one cluster of sites (D) as described by equation (1.50). It is less obvious how to fit the MGVH model in the program. However, Mårtensson and Lincoln have shown how global fitting to the MGVH model can be done with MATLAB.[45] In the following section it will be explained how the same method can be used in ReactLab EQUILIBRIA. The concentration of free ligand binding sites was calculated by McGhee and von Hippel from conditional probability to be:

$$[free\ sites] = C_{bp}(1-nr)\left(\frac{1-nr}{1-(n-1)r}\right)^{n-1}, \qquad r = [B]/C_{bp} \tag{1.71}$$

The concentration of occupied sites is the same as the concentration of bound ligand ([B]), so the total concentration of free and occupied binding sites will be:

$$C_{sites} = C_{bp}\left(1-n[B]/C_{bp}\right)\left(\frac{1-n[B]/C_{bp}}{1-(n-1)[B]/C_{bp}}\right)^{n-1} + [B] \tag{1.72}$$

This expression is somewhat more complicated to implement in the program than equation (1.65). The main problem is that the expression is recursive in the sense that in order to be able to calculate C_{site} it is necessary to know [B] for each recorded spectrum. All [B]s are values that have to be calculated by the program, and it is, consequently, necessary to have at least an estimate of a starting value of [B] to be able to start fitting of the data. For the titrations presented in this chapter the Scatchard model has been used to give a first estimate of the concentration profile of B. Afterwards, [B] values for each data point have been recalculated iteratively to fit *k* and *n* (Chapter 7).

The situation becomes even more complicated when the program is used to fit the cooperative MGVH model. Here you need not only to redefine the total concentration of sites; it is also necessary to redefine what is meant by the total concentration of ligands. The strategy is to fit one of the three equilibria in (1.59). In the following it will be explained how *k*, *n* and *y* can be fitted to the equilibrium:

$$L + Site_{isol} \rightleftharpoons B_{isol} \qquad k_{isol} = \frac{[B]_{isol}}{[L][site]_{isol}} \tag{1.73}$$

The concentration of isolated free binding sites was, according to McGhee and von Hippel, given from conditional probabilities as:

$$[free\ sites]_{isol} = \frac{(bf)(ff)^{n+1}}{(fb)}[B] \tag{1.74}$$

The factors (bf), (ff) and (fb) are conditional probabilities, and they express for a lattice point, such as a base pair, the probability that the next lattice point will be free or occupied by a bound ligand. Factor (bf) is the probability that a base pair next to a bound ligand is free. Factor (ff) is the probability that a base pair next to an unoccupied base pair is free. Factor (fb) is the probability that a base pair next to an unoccupied base pair is occupied. Expressions for each probability are given as functions of *r* ([B]/C_{bp}) and involve the parameters *k*, *n* and *y*, as shown in the footnote.[ii] The concentration of B_{isol} will be given as the total concentration of bound ligand times the square of the probability that each side of a bound ligand is unoccupied:

$$[B]_{isol} = (bf)^2[B] \tag{1.75}$$

The background for this expression is that the probability that a specific bound ligand is isolated is given as the product of the probabilities that each side of the ligand is non-occupied [(bf)×(bf)].

The program needs as input the total concentration of binding sites and of free and bound ligands. Since the interest is only about the fitting of *k* in equation (1.73) the total concentration must, in both cases, be defined as:

$$\tilde{C}_{bp} = [free\ sites]_{isol} + [B]_{isol} = \left(\frac{(bf)(ff)^{n+1}}{(fb)} + (bf)^2\right)[B] \tag{1.76}$$

$$\tilde{C}_L = [L] + [B]_{isol} = [L] + (bf)^2[B] \tag{1.77}$$

$$[B] = C_L - [L] \tag{1.78}$$

The only thing left to be solved is the 'corrections' of the recorded spectra since they represent the signals for all bound and free ligands. It is necessary to subtract the signal

[ii] $(bf) = \frac{(n-1)r-1+R}{2r(y-1)}$, $(ff) = \frac{(2y-1)(1-nr)+r-R}{2(y-1)(2-nr)}$, $(fb) = \frac{(n-1)r-1+R}{2(y-1)(1-nr)}$

corresponding to bound ligands that are single and double continuers (B_{sc} and B_{dc}). In the simple case, it is presumed that the molar signal is the same for all bound ligands (B_{isol}, B_{sc} and B_{dc}). For the absorption the corrected spectra will be:

$$\widetilde{\boldsymbol{A}} = \boldsymbol{A_{exp}} - \overline{\boldsymbol{C}}_{\boldsymbol{B}} \times \bar{\boldsymbol{\varepsilon}}_{\boldsymbol{B}} \tag{1.79}$$

The parameters $\widetilde{\boldsymbol{A}}$ and $\boldsymbol{A_{exp}}$ are here the corrected and experimental spectra, respectively, in form of $M\times\lambda$ matrices where λ is the number of wavelengths and M is the number of recorded spectra. $\overline{\boldsymbol{\varepsilon}_{\boldsymbol{B}}}$ is a row vector of the molar absorbance at the different wavelengths of the bound ligand. $\overline{\boldsymbol{C}}_{\boldsymbol{B}}$ is a column vector with the sum of the concentration of single continuer ($[B]_{sc}$) and double continuer ($[B]_{dc}$) bound ligands for each recorded spectrum.

It is also possible to handle the situation where B_{isol}, B_{sc} and B_{dc} have different molar spectra. By using matrix algebra it is possible to calculate the molar spectra for B_{isol}, B_{sc}, B_{dc} and free ligand (L) as an $\lambda\times4$ vector:

$$\boldsymbol{\varepsilon} = (\boldsymbol{C}^{\boldsymbol{T}}\boldsymbol{C})^{-\mathbf{1}}\boldsymbol{C}^{\boldsymbol{T}}\boldsymbol{A_{exp}} \tag{1.80}$$

$\boldsymbol{\varepsilon}$ is here a $4\times\lambda$ matrix with the molar spectra for all four species, and $\boldsymbol{C}$ is the concentration matrix in the form of a $M\times4$ matrix. Afterwards, the absorption can be corrected similarly to the correction of equation (1.79):

$$\widetilde{\boldsymbol{A}} = \boldsymbol{A_{exp}} - \boldsymbol{C}_{\boldsymbol{B}} \times \boldsymbol{\varepsilon}_{\boldsymbol{B}} \tag{1.81}$$

$\boldsymbol{\varepsilon}_{\boldsymbol{B}}$ is here the molar spectrum and $\boldsymbol{C}_{\boldsymbol{B}}$ is the concentration matrix for B_{sc} and B_{dc}. A fit of the cooperative MGVH model with ReactLab EQUILIBRIA depends on the presence of an initial estimate for the total concentration of bound and free ligand [equation (1.77)] and also for the molar spectra of bound species [equations (1.79) and (1.81)]. As for the non-cooperative model this can be obtained by an initial fit by the Scatchard model, as described previously. The basis of using ReactLab EQULIBRIA in this thesis is that it is designed to treat this type of problems, which makes it more convenient to use in practice with reliable results.

1.5 Ruthenium(II) Polypyridyl Complexes

Ruthenium(II) polypyridyl complexes have received considerable attention during the past 30 years, especially due to their strong DNA binding and photophysical properties making these compounds useful as luminescence dyes and photocatalysts.[45,67] In this class of ruthenium complexes the ligands involved are derivatives of connected pyridine rings.[67]

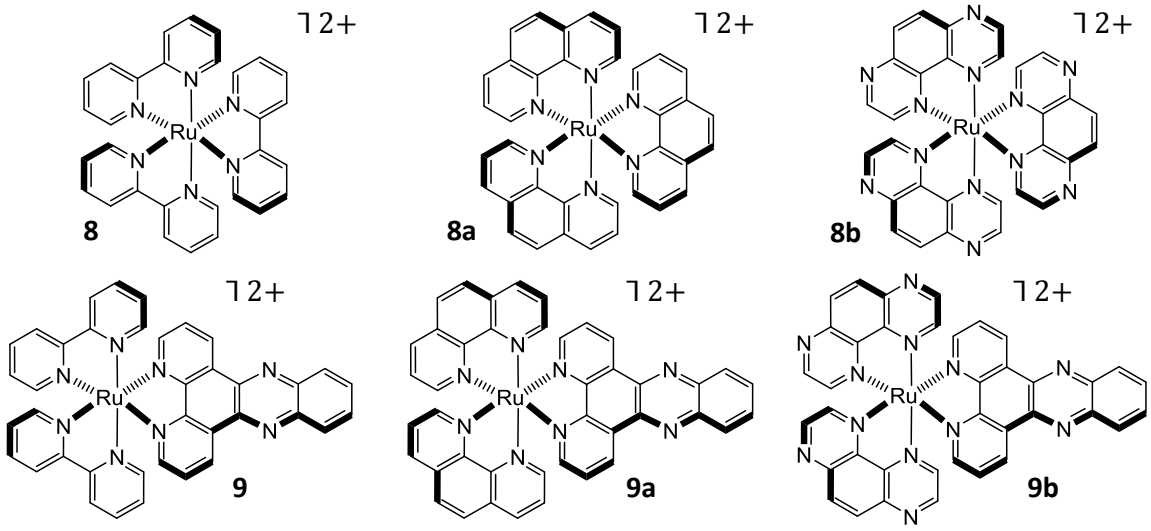

Figure 1.13: *Litterature examples of Ru(II) polypyridyl complexes.*

1.5.1 Photophysical Properties

The photophysical properties of Ru(II) polypyridyl complexes make them promising candidates in a range of applications, such as development of solar cells, probes for cellular imaging or as drug in photodynamic therapy (PDT).[67] In the following section, a brief introduction of the photophysics of this class of compounds will be outlined.

A schematic energy diagram for the well-studied complex $[Ru(bpy)_3]^{2+}$ (**8**), with three 2,2'-bipyridine (**bpy**) ligands, with the metal to ligand charge transfer (MLCT) absorption and the resulting radiative and non-radiative decays is shown in Figure 1.14.[67,68] After excitation, the described system will undergo a rapid spin-forbidden intersystem crossing (ISC) from a singlet to a triplet state, allowed as a consequence of spin-orbit coupling due to the high orbital angular momentum of the heavy atom ruthenium.[69] As decay to the singlet ground state is spin-forbidden, the result is a long-lived excited state. The decay from the excited triplet state can occur through three major pathways:

1) Radiative deactivation which results in emission with a maximum at *ca*. 600 nm.
2) Non-Radiative decay to the ground state (^{1}MLCT) with the release of heat is the main mechanism at which most Ru(II) polypyridyl complexes are deactivated.
3) Conversion to the triplet metal-centred state (^{3}MC) by thermal activation with possible loss of ligands as a consequence of electronic population of anti-bonding orbitals.

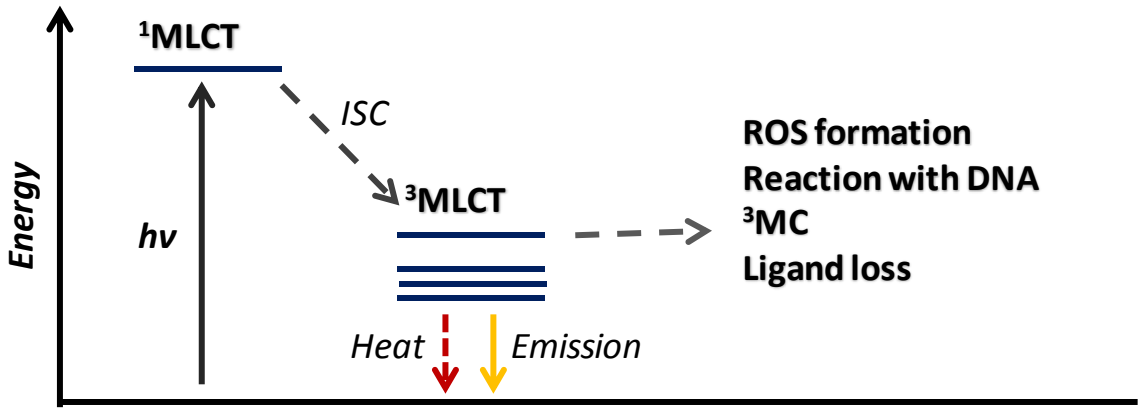

Figure 1.14: *Schematic representation of the energy level diagram for the electronic transitions following MLCT in many Ru(II) polypyridyl complexes.*[72]

Similar spectroscopic properties are known for other Ru(II) polypyridyl complexes and may permit this class of compounds to act as imaging and photochemical reagents. One of the requirements for a photochemical reaction is that the lifetime of the excited state is long enough for the occurrence of an energy transfer and a resulting chemical transformation (*e.g.* damage of DNA).[70,71]

The photophysical properties of Ru(II) complexes with **dppz** or similar aromatic moieties as ligands have also been studied extensively, including by the Gunnlaugsson group and collaborators.[9,73] Many studies of complexes **9** and **9a** have shown modulation in the photophysical properties in aqueous and aprotic environment as shown in Figure 1.15. The complexes are non-emissive in water since the hydrogen bonds to the non-coordinated *N*-atoms in **dppz** quench the emission. However, in aprotic solvents such as acetonitrile, the complexes become strongly emissive. This modulation in the photophysical properties are sometimes referred to as the "light-switch" effect, and has shown promising with respect to imaging of biomolecular structures, such as DNA, which will be described in the next section.

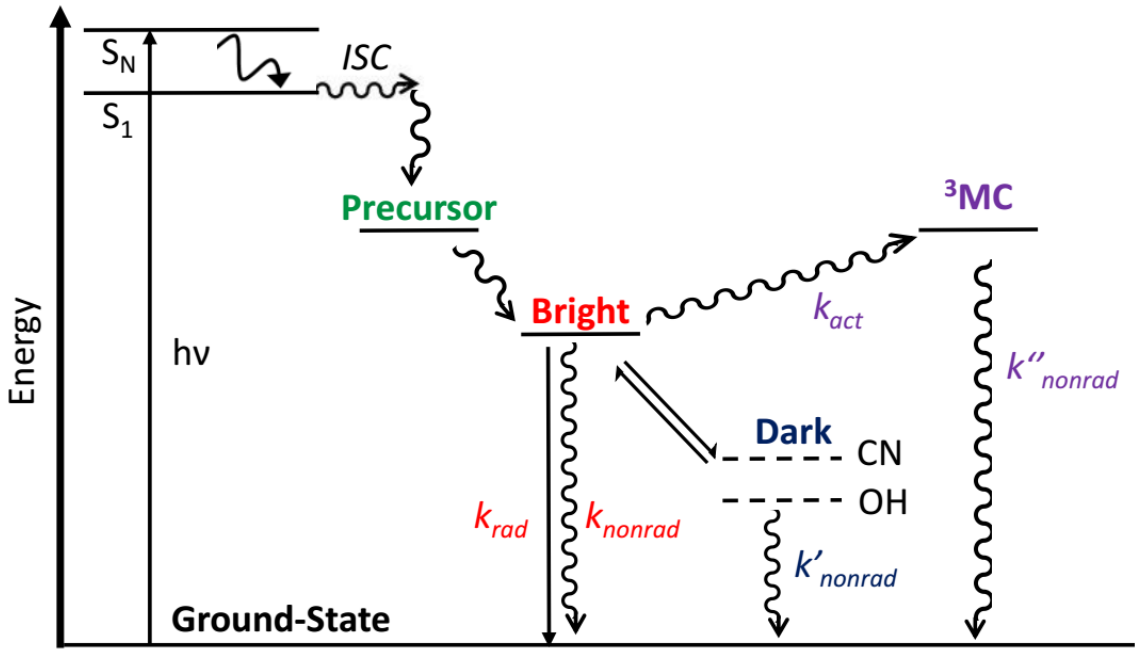

Figure 1.15: *Schematic representation of the energy level diagram for the electronic transitions following MLCT in complexes **9** and **9a**.*[74] *OH and CN refer to different energies of the excited states depending on whether the solvent is protic (OH) or non-protic (CN).*

1.5.2 Ru(II) Complexes as DNA Binding Agents

The positive charge of the ruthenium ion results in a relatively strong electrostatic binding between $[Ru(bpy)_3]^{2+}$ (**8**) and the negatively charged phosphate backbone of DNA.[71] By extending the ring system of one or more of the **bpy** ligands, the binding constant can be increased dramatically, since the increased van der Waals interactions result in groove binding or intercalation.[67] While **8** has a relatively weak binding to DNA ($K_b < 10^3$ M^{-1}, 50 mM NaCl), the corresponding complex **8a** with 1,10-phenanthroline (**phen**) replacing **bpy** ($[Ru(phen)_3]^{2+}$) will have a stronger binding due to the increased ring systems that can interact with DNA through van der Waals interactions ($K_b = 6.2\times10^3$ M^{-1}, 50 mM NaCl).[75] Complex **8** binds to DNA primarily through electrostatic interactions, while **8a** has been shown to bind to DNA through semi-intercalation (Figure 1.16a). Friedman *et al.* showed that further extension of the aromatic ring system increased the affinity for DNA.[76] Complex **9** with dipyrido[3,2-a:2'3'-c]phenazine (**dppz**) as a ligand shows a binding constant for DNA, which is increased by three orders of magnitude ($K_b > 10^6$ M^{-1}).[9,77] Several studies have shown that complexes in which one of the ligands is a derivative of **dppz** will intercalate between the base pairs of DNA (Figure 1.16b and c).[6,67,78]

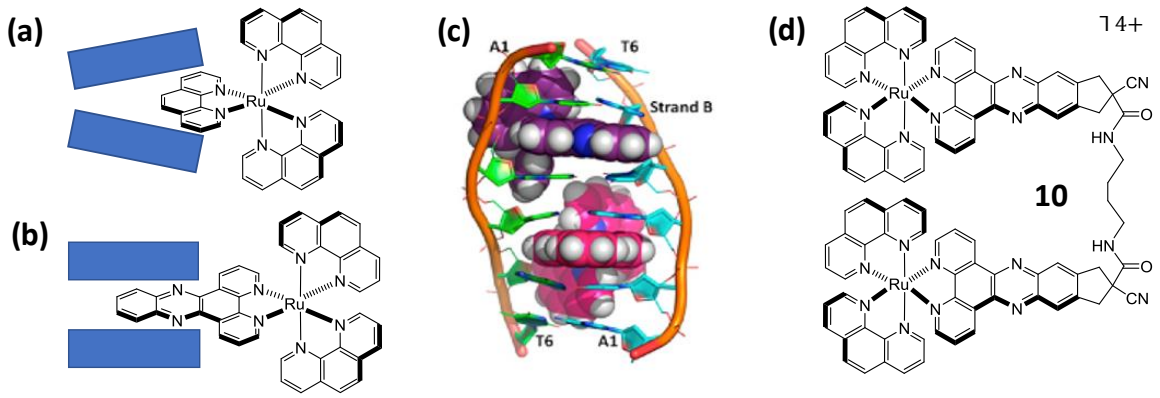

Figure 1.16: *Schematic presentation of (a) semi-intercalation of **8a** and (b) intercalation of **9a**. (c) X-ray crystal structure of intercalations of an enantiomer pair of **9a**.[79] (d) Bimetallic Ru(II) polypyridyl complex **10**, which has an extremely high binding affinity for DNA ($K_b \approx 10^{10}\ M^{-1}$).*

As mentioned in the previous section, complexes **9** and **9a** act as "light switches" by displaying no luminescence in aqueous solution whereas the luminescence was "switched on" in aprotic solvents.[9] The lack of luminescence in aqueous environments is expected to be a consequence of hydrogen bonding between the phenazine nitrogen atoms and water resulting in quenching of the excited state by non-radiative deactivation (luminescence "switched off").[71,77] After intercalation of DNA, the **dppz** nitrogen atoms are protected from the aqueous medium resulting in luminescence (*i.e.* luminescence is "switched on").

Ortmans *et al.* have synthesised and studied the photophysical properties of complex **9b**.[80] Substitution of **phen** in complex **9a** with 1,4,5,8-tetraazaphenanthrene (**TAP**) gives a complex with fundamentally different properties. Complex **9b** is, in contrast to **9a**, luminescent in water since the MLCT excited state corresponds to an electron transfer to **TAP** rather than to **dppz**. Resulting interactions of **dppz** with H_2O will not quench the excited state. An emission enhancement for **9a** in solution is observed upon binding of the complex to poly(dA)poly(dT), which might be explained by protection from molecular oxygen. On the other hand, upon binding to guanine rich DNA the luminescence is quenched dramatically. The quenching of the emission upon binding to DNA is sometimes referred to as an inverse "light-switch" effect. Several studies have confirmed that the quenching results from an electron transfer from guanine to **9b** as a result of the electron deficient **TAP** ligands and an increased reduction potential after excitation. In most cases, a back electron transfer recovers the neutral form of guanine. However, it is observed that light activation can lead to photo-cleavage of DNA in the presence of **9b**, and one suggested mechanism of action involves the electron transfer between **9b** and guanine.

1.5.3 Ru(II) Complexes in Cellular Imaging

The emissive properties of Ru(II) polypyridyl complexes and the modulation of their photo-physical properties upon binding to biomolecules such as DNA make them interesting candidates for cellular imaging.[6,67,81] The first challenge for use in cellular imaging is to achieve cellular uptake. Because of the positive charge of Ru(II) polypyridyl complexes with neutral ligands these compounds will, in general, preferentially be taken up by cells, as mammalian cells have a negative membrane potential, and the interior of cells are more negatively charged than the extracellular medium. Ru(II) polypyridyl complexes are, in the vast majority of cases, taken up by the cells *via* passive diffusion through the lipid cell membrane.[81] This makes lipophilicity an important physico-chemical property of the complexes. Lipophilicity is often quantified using the logarithmic value of the partition coefficient, *logP*, between an organic solvent, such as *n*-octanol, and water. Examples of complexes with different lipophilicity and cellular uptake are seen in Figure 1.17. Some uptake is observed for **9b**, which has two hydrophilic **TAP** units and the extended aromatic ring system **dppz** as ligands. In Chapter 3 in this thesis, *logP* values of *ca*. -8 are found for a similar **TAP** complex, which exhibit similarly low uptake.[6] A very good cellular uptake is observed for complex **11** (logP = +1.30), which has several features in common with **9b.** In complex **9b** the ligand **TAP** has been substituted with the very lipophilic ligand 4,7-diphenyl-1,10-phenanthroline (**dip**).[82]

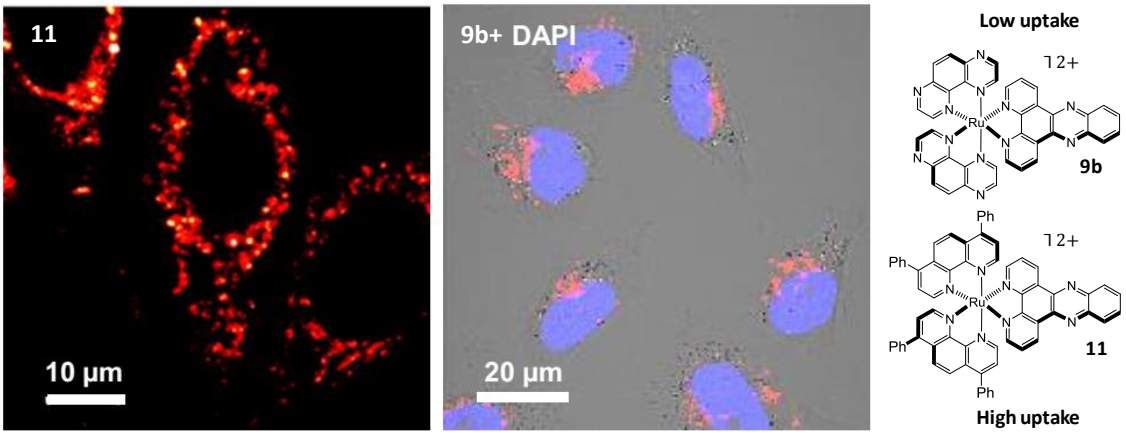

Figure 1.17: *Confocal fluorescence microscopy images of Ru(II) polypyridyl complexes with different degrees of cellular uptake in HeLa cervical cancer cells. Nuclei are stained blue with DAPI in case of* ***9b****. Images are reproduced from Pucket et al.*[3] *and Cloonen et al.*[6]

The next challenge in cellular imaging is to localise the imaging agent at or within a certain target region of the cell. The "light-switch effect" property of many Ru(II) complexes with **dppz** derived ligands make these compounds excellent candidates for imaging the nuclei of cells. The nuclei are also a central therapeutic target as described in the next section. However, the nuclei in cells are protected by a membrane, and only a fraction of all Ru(II) polypyridyl complexes reported in the literature localises in the nuclei after cellular uptake.[6,81] However, the bimetallic complex **12a** with tetrapyrido[3,2-a:2',3'-c:3'',2''-h:2''',3'''-j]phenazine (**tpphz)** as bridging ligand and **phen** units as ancillary ligands does show effective localisation in the nuclei after cellular uptake.[83] Substitution of **phen** with **dip** shows, as seen for **9a** and **11**, increased cellular uptake; however, the complex localises in the membrane of endoplasmic reticulum as a consequence of the increased lipophilicity.[84] Many Ru(II) polypyridyl complexes are also shown to be taken up by mitochondria, among these the bimetallic complex **13**. [85]

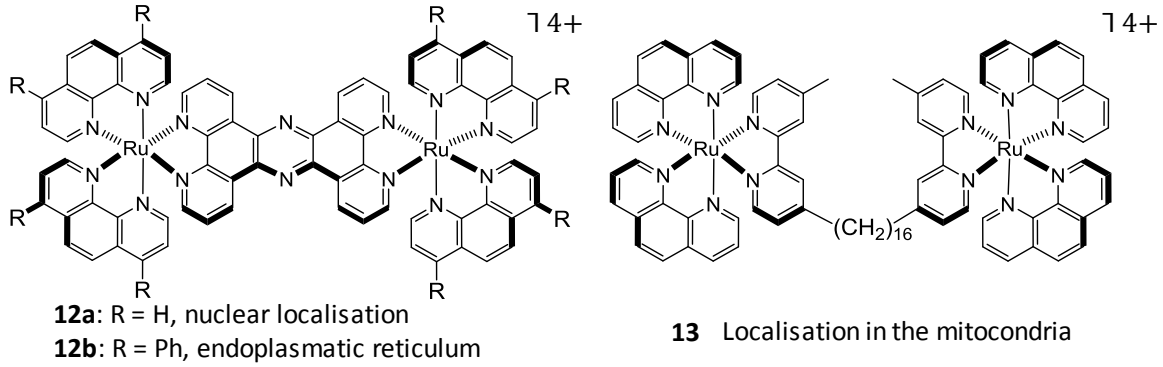

12a: R = H, nuclear localisation
12b: R = Ph, endoplasmatic reticulum

13 Localisation in the mitocondria

Figure 1.18: *Ru(II) polypyridyl complexes with different cellulur localisation.*

1.5.4 Ru(II) Complexes for Treatment of Cancer

Cancer is a disease with one of the highest mortality rates worldwide responsible for an annual mortality of *ca*. 200 million.[86] It is a complex group of diseases with *ca*. 200 different forms making the development of cancer drugs one of the most intense research areas in the biomedical sciences. The development of the structurally simple compound, cisplatin, for treatment of cancer has motivated the development of many metal-based anti-cancer drugs, including complexes with ruthenium as the metal centre (Figure 1.19).[7] Three ruthenium complexes have, to date, been tested for treatment of cancer in clinical trials, including NAMI A (**14**) that reached phase II out of three required clinical phases. TLD1433 (**16**) is the first Ru(II) polypyridyl complex to be tested in humans, and this complex has been tested for use in photodynamic therapy.[81]

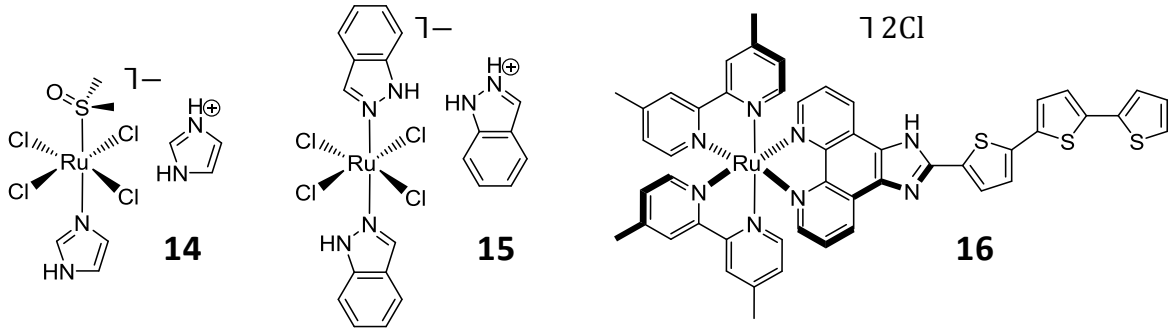

Figure 1.19: *Ruthenium complexes that have been [NAMI A (**14**) and KP1019 (**15**)] or are in clinical trials. [TLD1433 (**16**)].*

An important characteristic of ruthenium complexes is their metal centre that, usually, makes these compounds positively charged and water soluble.[81] Like lipophilicity, solubility is one of the most important physico-chemical properties of a compound, as water solubility is essential for the administration of a drug.[87] A sufficient solubility is required if a drug is to reach the target, such as a cancer tumour. Further, as mentioned in the previous section, a positive charge on a compound favours cellular uptake as long the compound can pass through the cell membrane. Cellular uptake of a neutral compound will be driven mainly by the concentration gradient, however, often a similar concentration of a compound is observed both inside and outside the cells. A Ru(II) polypyridyl complex with two positive charges will, over time, usually accumulate inside the cells. A simple statistical consideration using a Boltzmann distribution predicts that, at equilibrium, the concentration will be almost 100 times higher inside the cell than outside (Appendix 1). Very few negatively charged compounds show any significant uptake in mammalian cells. NAMI A (**14**) and KP1019 (**15**) are examples of ruthenium complexes that are negatively charged due to negatively charged ligands. Apparently, these compounds were not taken up by cells, and the reported anti-cancer activity *in cellulo* and *in vivo* is expected to be a result of interactions with the cell membrane.

As mentioned, many Ru(II) polypyridyl complexes show a high affinity for DNA, which has made DNA a central target in the effort to target cancer cells using these compounds.[81] As for Cisplatin, binding to DNA might induce apoptosis in cancer cells (Figure 1.3). Cancer cells are highly sensitive to disturbance at the genomic level because of their high proliferation. Disturbance of the genome can either slow down the cell cycle or induce cell death, because cells are in general extraordinarily sensitive to DNA damage in the mitotic phase. However, even though DNA is a popular target for the development of

anti-cancer compounds, it has only rarely been confirmed that attacks on DNA by Ru(II) polypyridyl complexes result in cellular death. As described in the previous section, few Ru(II) polypyridyl complexes localise in the nuclei after cellular uptake, which is the primary target for DNA binding agents. Mechanistic studies indicate that cellular death occurs by apoptosis as a result of mitochondrial stress.[6] It cannot be excluded that DNA is still a useful target for binding in some cases, especially as cell death can be induced by mitochondrial stress, since the mitochondria also contain DNA. *In vivo* studies have also shown that necrosis can induce death of cancer cells after treatment with Ru(II) polypyridyl complexes, in which case the immune system attacks the cells.[88]

1.5.5 Ru(II) Complexes for use in Photochemotherapy

The photochemical properties of ruthenium polypyridyl complexes also make these compounds suitable for causing photoinduced damage to cancer cells and to act as photodynamic therapeutic agents.[5,7,71] Photochemotherapy involves the administration of a photoactive drug which is subsequently taken up by the cells. Once locally irradiated with localised light, the drug is activated and induces irreversible cytotoxic damage to tumour cells (Figure 1.20).[89] The Ru(II) polypyridyl complex TLD1433 (**16**) seen in Figure 1.19 is a drug candidate that is currently in phase I of clinical trials and with potential application in photochemotherapy. The term photodynamic therapy (PDT) is reserved for cases where

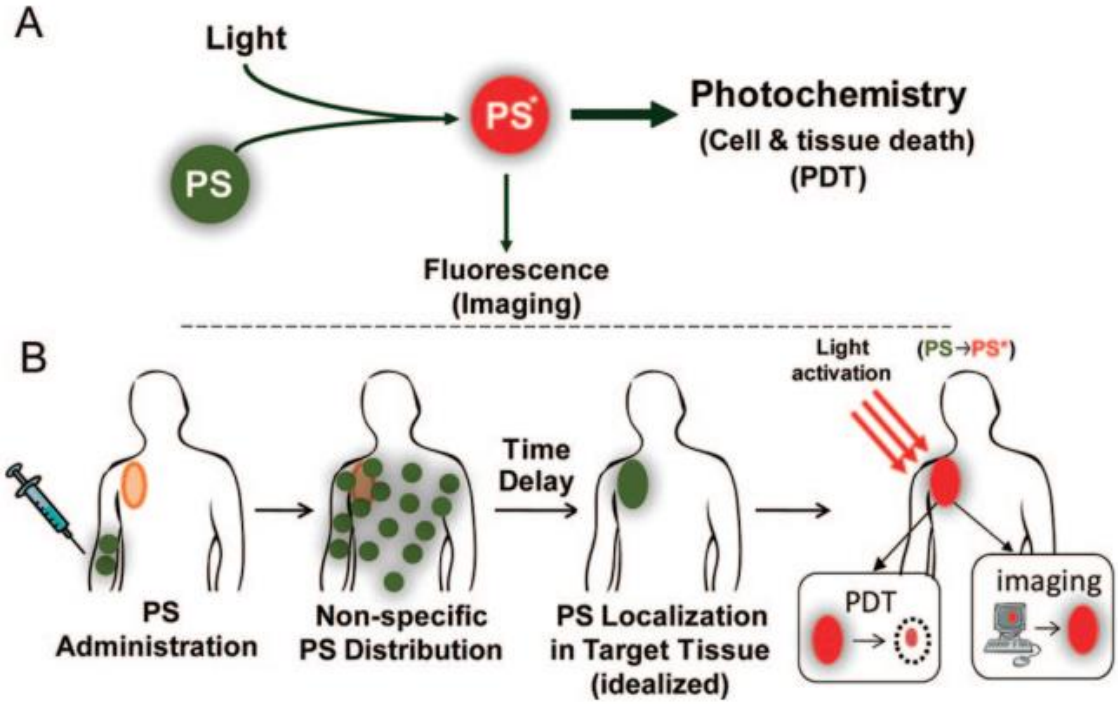

Figure 1.20: *Schematic presentation of the principle behind PDT.*[5]

the damage arises from reactions with oxygen upon exposure to light, typically a consequence of the formation of a reactive oxygen species (ROS).[90] The more general term, photochemotherapy, should be used in cases where other mechanisms are involved.[6] Most clinically approved and potentially PDT agents cause damage through the formation of singlet oxygen ($^1O_2$). The adverse effect to healthy cells in the rest of the body is limited since the drug needs photoactivation, and the therapeutic effect is localised to the area of the body exposed to light. Photodynamical agents have also shown potential in treatment of other types of disease such as infection. An example of a compound that have shown promising for the eye disease age-related macular degeneration (AMD) is 2-(1-methoxyethyl)-2-devinylpyropheophorbide-a (MEP).[91]

First-generation PDT agents are porphyrin based (Figure 1.21)[92] and exhibit poor light absorption, some dark toxicity, low water solubility, and they cause patients to experience prolonged skin photosensitivity due to poor clearance from the body.[93] An ideal photosensitiser should be water-soluble and non-mutagenic. It should also possess very low dark toxicity and induce apoptosis.[92] Therefore, there is still a great need for the development of new PDT agents to address these issues. A number of ruthenium polypyridyl complexes have shown high photo-induced toxicity to cancer cells, probably as a consequence of formation of ROS, such as singlet dioxygen ($^1O_2$), or because of direct reaction with DNA.[7,67,71,83] Furthermore, the combination of the characteristic photostability, water solubility, effective DNA binding, and the useful photochemical and photophysical properties[83] make this class of compounds excellent candidates for potential cancer therapeutics and diagnostic agents, which also is referred to as theranostics.[10]

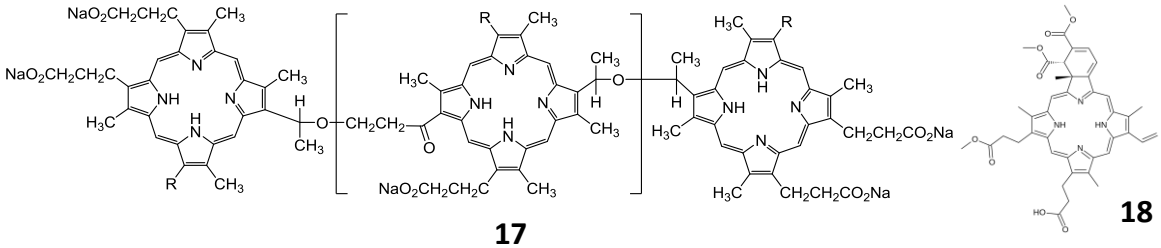

Figure 1.21: *The clinical approved PDT agents Photofrin® (**17**) and Visudyne® (**18**).*[94,95]

The effect of a toxic or growth-inhibitory compound on the viability of a cell culture is usually quantified by an IC_{50} value. This is the concentration that, after a certain incubation time with the compound, will result in a 50% reduction in live cells compared to untreated cells.[96] The lower the IC_{50} value, the more toxic the compound for a certain cell type. The

photoindex (*PI*) is the ratio between the IC_{50} value in the dark and the IC_{50} value after the cells have been exposed to light, and the *PI*-value represents the increase in toxicity.[97]

Howerton *et al.* showed that complex **19** had an increase in toxicity in the presence of light expressed by a *PI*-value of 42 for HL60 leukemia cells.[7,98] Even larger increases have been reported by Hidayatullah *et al.* for complex **20** which showed a *PI*-value of 1880 for HeLa cervical cancer cells.[99] Albani *et al.* have shown that the complex **21** with an extended aromatic ring system as ligand, has a *PI*-value for HL60 cells of 282.

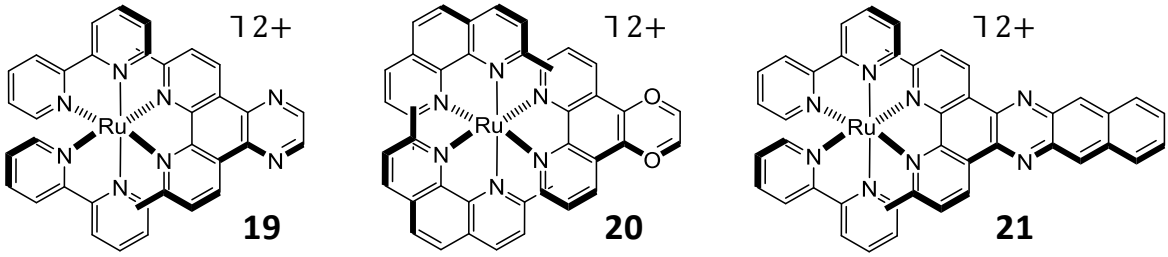

Figure 1.22: *Ru(II) polypyridyl complexes with high increase in toxicity upon photo-activation.*

Singlet oxygen formation is one way in which Ru(II) polypyridyl complexes are expected to cause damage after light activation. However, more direct reactions with biomolecular structures inside the cells have also been suggested as a possible mechanism of action. As mentioned in section 1.5.2, complex **9b** can oxidise guanine directly upon excitation. It has also has been reported that complex **8b** can form a photo-adduct with GMP. A similar reaction with nuclear DNA may induce cell death by apoptosis. This is an oxygen independent mechanism and thus the term PDT does not apply. However, since supply of oxygen is a bottleneck for PDT treatment, the mechanism may be suitable for treatment of cancer.

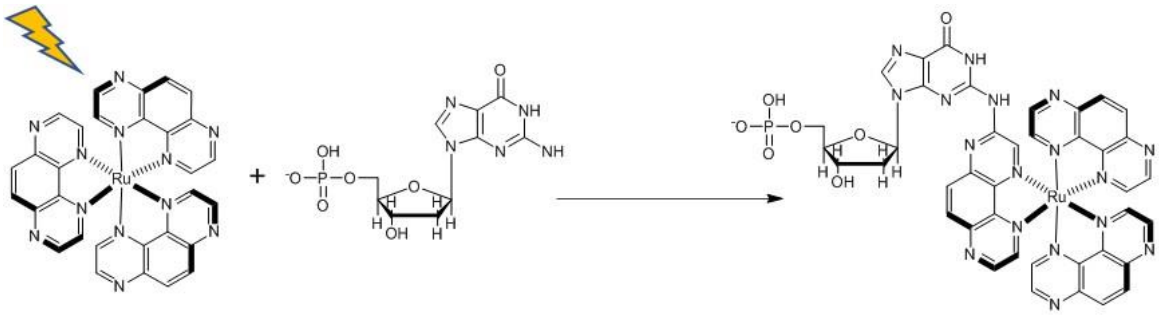

Scheme 1.1: *Formation of photo-adduct between **8b** and GMP after light activation.*

In Section 1.5 a background for study of Ru(II) polypyridyl complexes has been given, including a study of their photophysical properties and some possible biological applications. It has been shown how some Ru(II) polypyridyl complexes can act as "light-

switches" for imaging DNA, by being non-luminescent in water and becoming strongly emissive upon binding to DNA. A general introduction to the uptake and localisation in cells has been given. It has been shown that there is a large variation in the cellular uptake of different Ru(II) polypyridyl complexes and that there is a strong correlation between lipophilicity and degree of cellular uptake. With respect to the use of this class of complexes as imaging dyes for genomic DNA it has been explained that a major challenge is to achieve nuclear localisation since few Ru(II) complexes enter the nuclei of cells. It has been described how many Ru(II) polypyridyl complexes have potential in photochemotherapy with a high increase in the toxicity for cancer cells at light activation.

1.6 Naphthalimide-based Trögers's bases

The unique V-shaped framework and chirality of Tröger's bases have been the motivation for the preparation of a range of receptor systems since their discovery in 1887 (Figure 1.23).[100] Tröger's base (**22**) was structurally characterised half a century later when Spielman established the correct structure[101] and Wilcox reported its X-ray crystal structure in 1985.[102] In the late 1980s, interest in functionalised analogues of Tröger's bases emerged. In these compounds the central bicyclic framework results in fusion of the two aromatic rings nearly perpendicular to each other. Hence, the Tröger's base was seen to offer itself as a unique, nanometer-sized building block for molecular designs and, since then, it has been heavily utilised within molecular recognition and supramolecular chemistry.[103,104] Furthermore, due to the locked conformation of the two nitrogen atoms, the molecule is chiral with a C_2 symmetry-axis, thus giving it the potential for enantiospecific recognition of molecules.

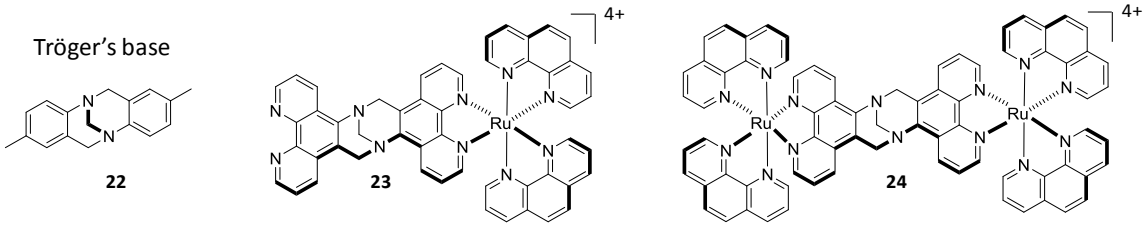

Figure 1.23: *Literature examples of Tröger's bases derivatives.*

Nucleic acids, which are chiral, have been targeted using Tröger's base analogues as DNA-binding motifs.[105] Yashima *et al.* reported the synthesis of a racemic bis-(1,10-phenanthroline)-containing Tröger's base, and, using CD spectroscopy, they showed that a racemic mixture could interact with DNA.[106] Kirsch De Mesmaeker *et al*. have studied Ru(II) complexes with polypyridyl based Tröger's bases (**23**), including their interactions

with DNA.[107,108] The work of Thomas *et al.* has led to the development of **24**, which has shown potential as an *in cellulo* nuclear DNA stain.[83]

The Tröger's base structure has been exploited in our group by Veale *et al.* for use as theranostic agents. In these studies organic derivatives, *e.g.* compound **28**, were shown to localise within the nucleus of cancer cells.[109,110] These bis-1,8-naphthalimide containing Tröger's base species also exhibited many other advantageous properties, such as the ability to bind strongly to DNA. On binding, changes were observed both in their ground state and excited state properties. Furthermore, these species were shown to induce apoptosis within the K562 Leukaemia cells with IC_{50} values as low as 5.53 μM (for compound **28**) making these compounds potential candidates for anti-cancer therapeutic agents. Similarly, Banerjee *et al*. studied compound **29** and other pyridine-based Tröger's bases as racemic mixtures, and also for the two isolated enantiomers with *R,R* or *S,S* configuration at the two chiral nitrogen atoms.[111] Strong binding to DNA and good cellular uptake were demonstrated as well as low cytotoxicity making these compounds suitable candidates for cellular imaging.

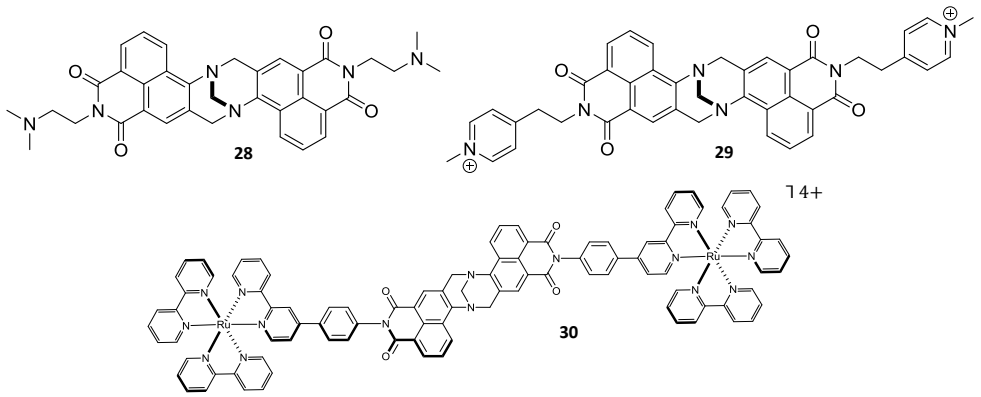

Figure 1.24: *Examples of naphthalimide based Tröger's bases, which has been synthesised and studied in the Gunnlaugsson group.*

As an extension to the work concerning naphthalimide-based Tröger's bases reported by Ryan *et al.*, Elmes *et al.* synthesised bimetallic Ru(II) complexes with naphthalimide-based Tröger's base as bridging ligands, among these compound **30**.[112] It was found that the compounds were readily taken up by HeLa cells and showed emission in the cytoplasm. No dark toxicity was observed at the applied concentration (15 μM), making these compounds well suited for use in cellular imaging. The light toxicity of the compounds has not yet been tested.

1.7 Functionalised Gold Nanoparticles and Medical Applications

Gold nanoparticles (AuNPs) have shown to be promising in biomedical applications due to their special physical and chemical properties and due to their high biocompatibility. This includes high water solubility and low toxicity of the nanoparticles themselves because of the inert nature of metallic gold.[113] Nanoparticles are defined as structures with sizes between one and 100 nm in at least one dimension. Included herein are spherical nanoparticles, nanorods, nanoshells and nanocages. AuNPs absorb strongly at long wavelengths, corresponding to excitation of the conductive electrons at the surface of the gold. This phenomenon is known as surface plasmon resonance (SPR). The opportunity to functionalise AuNPs by attaching molecules to the surface has resulted in a range of potential uses of AuNPs in medical applications such as treatment of cancer or as contrast agents in different types of imaging.[114] All of these properties make AuNPs promising candidates for use in therapeutic and medical applications.[114] For the time being, silica-gold nanoparticles with the trade name AuroLase are being tested in clinical trials for photo-thermal therapy of different types of cancer.[115] However, the applications of AuNPs in medicine are still pending.

1.7.1 Gold Nanoparticles for Treatment of Cancer

A lot of research has focused on the use of AuNPs in the treatment of cancer.[113] The water solubility of AuNPs makes it possible to use these particles as carriers of surfactants with suitable anti-cancer activity. The opportunity to introduce multiple functionality by attaching other surfactants can, for example, help to increase the stability or the selectivity of certain targets by improving localisation in certain areas of the body or strengthen the relative toxicity for certain cells.[114] A property of AuNPs that has made these particles particularly interesting for cancer treatment is their tendency to accumulate in cancer tumours as a result of the Enhanced Permeability and Retention (EPR) effect.[116,117] When cancer tumours grow new blood vessels are formed, and these are of an abnormal nature. They are less suitable for filtering large macromolecular structures, thus making it easier for nanoparticles to enter a tumour than healthy tissues. It was demonstrated *in vivo* that the EPR effect resulted in a high accumulation in cancer tumours. Clearance of nanoparticles are also less efficient because of problems with removal from the tumour. Ayala-Orozco *et al.* developed stabilised silica-gold nanoparticles coated with polyethylene glycol (PEG).[118] PEG coating of nanoparticles is known to increase the lifetime in the body due to less accumulation in the liver, lung and spleen. The phenomenon is referred to as ‘stealth coating’.

AuNPs have also been shown to be taken up by cells better than many small lipophobic molecules through endocytosis.[114] AuNPs can thus be used as vehicles for cellular uptake of small molecules. By attaching such molecules onto the surface of the nanoparticles the molecules can be transported through the cell membrane and achieve biological activity inside the cells. Attachment of molecules with high affinities for specific receptors on the surface of cells makes it possible to target specific cell-types such as certain cancer cells. It has been demonstrated that polyethyleneimine-capped AuNPs (Au-PEI) could target PC-3 prostate cancer cells when functionalised with anisamide (AA).[119] PC-3 cells are known to overexpress the sigma receptor, which has a high affinity for AA. It was shown that siRNA can be internalised in the cells when it was attached to the AA functionalised AuNPs (AuNP-PEI-AA) and efficiently downregulated a target oncogene.

The opportunity to include multiple functionalities on AuNPs makes these particles well suited for development as PDT agents. Hone *et al.* have demonstrated how AuNPs can be used for delivery of molecules with PDT activity to cancer cells.[120,121] The hydrophobic photosensitiser was attached to the surface of AuNPs together with the hydrophilic phase transfer agent phthalocyanine with a diameter of *ca*. 3 nm. This resulted in good solubility in water for the AuNPs and enabled the delivery of the drug candidate to the cells. The photosensitiser absorbs radiation at 695 nm with singlet oxygen quantum yields *ca*. 50% higher than the free dye alone. The AuNPs were readily internalised in HeLa cervical cancer cell lines and enabled the photosensitiser to carry out its biological activity inside the cells. The toxicity upon photoactivation was *ca.* twice the value obtained for the free photosensitiser, which is in accordance with the observed increase in the singlet oxygen quantum yield. The results demonstrated that AuNPs have good potential as a transport vehicle for the delivery of photosensitisers in PDT.

1.7.2 Gold Nanoparticles for Imaging

A significant amount of work has been invested in the evaluation of AuNPs in imaging, both for use *in vivo* for diagnostics and *in cellulo* for studies of intracellular structures.[2,113,122] It has been demonstrated that the optical properties of gold itself can be used in the diagnosis of cancer. The SPR band can absorb strongly in the NIR region, making it possible to use absorption spectroscopy of the AuNPs in diagnostic imaging, since tissue absorbs weakly at wavelengths above the visible region, and for photothermal therapy (PTT).[113] Sokolov *et al.* functionalised AuNPs with an antibody for an epidermal growth factor receptor, which is overexpressed in many cancer cell lines.[123] Using a scanning confocal microscope in

reflectance mode with excitation wavelength at 647 nm it was demonstrated that the AuNPs were able to detect cancer cells. The cells were clearly imaged on a dark background as a result of absorbance of the SPR band.

Functionalised AuNPs can extend the potential applications to other types of imaging such as MRI, CT, SPECT or luminescence imaging. The properties of AuNPs make it possible to use the same contrast agent for several imaging techniques simultaneously. Zhao *et al.* doped gold nanospheres with ^{199}Au, which is a radioactive isotope of gold.[124] This enabled the use of the AuNPs in SPECT scanning, which is a technique that uses radioactive species as contrast agents. Further attachment of a peptide enabled targeting of a C-C chemokine receptor, which is overexpressed in many breast cancer cells. Combined with the ability of gold to attenuate X-rays, breast cancer cells were detected accurately *in vivo* by using SPECT and X-ray CT scanning.

1.7.3 Gold Nanoparticles for Use in Theranostics

The properties of gold itself and the opportunity for functionalisation of AuNPs with different molecular species simultaneously is very relevant in theranostics, which is the field in which the same treatment has a therapeutic as well as a diagnostic purpose, making the treatment suitable for a personalised medicine.[113,125] For example, AuNPs can be functionalised with compounds with anti-cancer activity and labelled with contrast agents making it possible to follow the accumulation of the drug in a tumour. Consequently, the efficiency of the treatment can be evaluated at an early stage of the treatment, and increased insight into the physiological effects can help to find the optimal dose of the drug.

Gao *et al.* synthesised graphene oxide (GO) seeded with AuNPs (GA) for use in PTT and NIR fluorescence imaging.[126] The NIR fluorescence dye Cy5.5 was labelled on the surface of GA with a biodegradable linker. The fluorescence of Cy5.5 was quenched by the SPR capacity of both GO and Au. However, after successful internalisation in cancer cells Cy5.5 was released and became fluorescent. The absorbance of the SPR band of gold itself resulted in a strong increase in the temperature at exposure to NIR light resulting in ablation of the tumour. It was demonstrated *in vivo* using a mouse model that it was possible to simultaneously image the tumours due to release of Cy5.5 after cellular uptake and to induce destruction of the tumour by light activation as a result of photothermal heating.

1.7.4 Gold Nanoparticles Functionalised with Luminescent Metal Complexes

There are some examples of functionalised AuNPs with metal complexes as the surfactant, including some systems synthesised and studied in the Gunnlaugsson group.[2,122] Complex

25 is an example of Ru(II) polypyridyl functionalised AuNPs. The complex has been shown to stabilise AuNPs in solution having a strong affinity for the gold surface through the nitrogen atoms in one end of the rigid bridging ligand.[127] Compared to the free complex, the AuNP conjugate shows a 33% quenching of the emission which is an important feature in many cases of functionalisation of AuNPs with luminescent metal complexes.[2] This is usually a result of Förster energy transfer to gold[128] or of immediate absorbance of the emitted photon by the SPR band.[129] The degree of quenching depends on different factors including the length and nature of the spacer between the gold surface and the fluorophore. In rare cases a luminescence increase can be observed. For AuNP-**25** the authors expected the quenching to be a result of an electron transfer to the gold surface through the conjugated π-electron system of the spacer.[127]

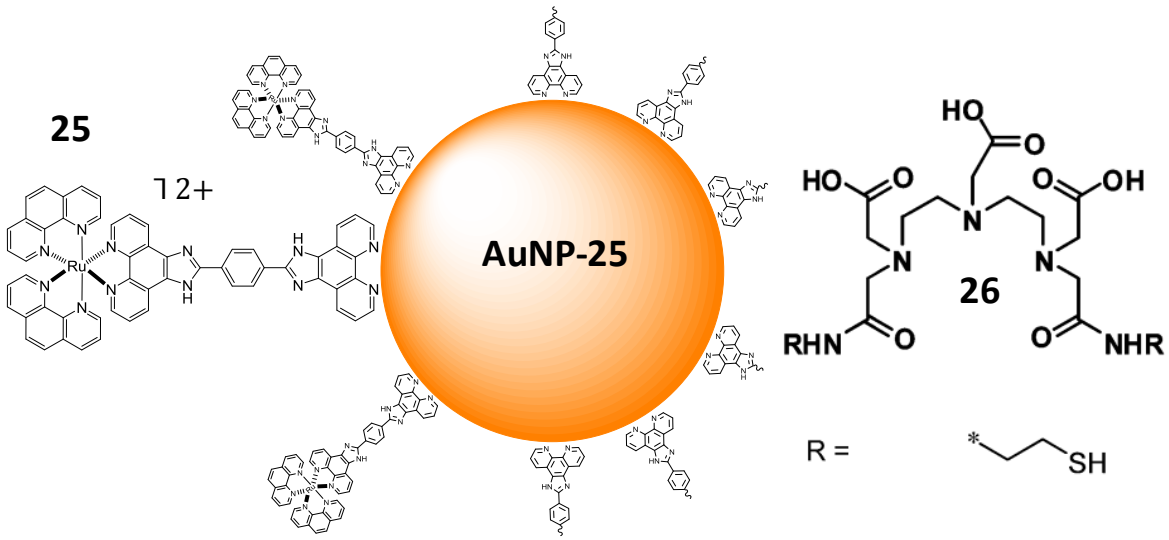

Figure 1.25: *Literature examples of AuNPs functionalised with luminescent metal complexes.*

Debouttière *et al*. synthesised Gd(III) functionalised AuNPs with ligand **26** as spacer.[130] Gadolinium is applied intensively as contrast agent in Magnetic Resonance Imaging (MRI) because of its magnetic properties. It was demonstrated that functionalisation of AuNPs with the Gd(III) complex resulted in a 200-fold gain in the relaxivity compared to the Gd(III)·**26** complex alone with a corresponding increase in the MRI activity. The use of the AuNPs for MRI *in vivo* was demonstrated successfully together with X-ray CT.

Inspired by the novel biological properties of Ru(II)-polypyridyl complexes and AuNPs, Elmes and Gunnlaugsson *et al.* synthesised a series of AuNPs with a diameter of *ca.* 5 nm and functionalised with luminescent Ru(II)-complexes. The Ru(II)-complexes were adsorbed at the surface of gold *via* a **phen** ligand with a long aliphatic linker attached

through an amide bond (Figure 1.26).[2] The AuNPs were characterised with respect to size, stability and photophysical properties. A biological profiling of the AuNPs was carried out to give an insight into the cellular uptake, the localisation, the cytotoxicity and the DNA binding behaviour. The AuNPs were found to be very stable in aqueous media. For all surfactants, the emission quantum yields were reduced significantly. This is often observed upon functionalisation, were the excited state is usually quenched by Förster energy transfer to the gold surface[128] or by immediate absorbance of emitted light by the SPR band corresponding to excitation of the conductive electrons in the gold surface.[129] However, the AuNPs showed some emission which enabled the use of confocal microscopy to confirm the cellular uptake of the AuNPs. The photophysical properties were modulated upon binding to DNA, and from ethidium bromide assays the site binding constant was estimated to be in the order of 10^7 M^{-1}. In Chapter 6, work with this and similar AuNPs will be described.

Surender, Gunnlaugsson *et al.* functionalised gold nanoparticles (AuNPs) with luminescent europium complexes and demonstrated how these particles could be used for imaging of micro-damage in bones.[122] The europium complex acted as a calcium ion sensor with strong NIR emission upon binding of Ca^{2+}. Microdamage is characterised by the release of Ca^{2+} resulting in strong emission in damaged tissue. By using two-photon excitation (TPE) microscopy it was possible to use excitation wavelengths in the NIR region which has optimal tissue penetration. This makes the technique well-suited *in vivo*.

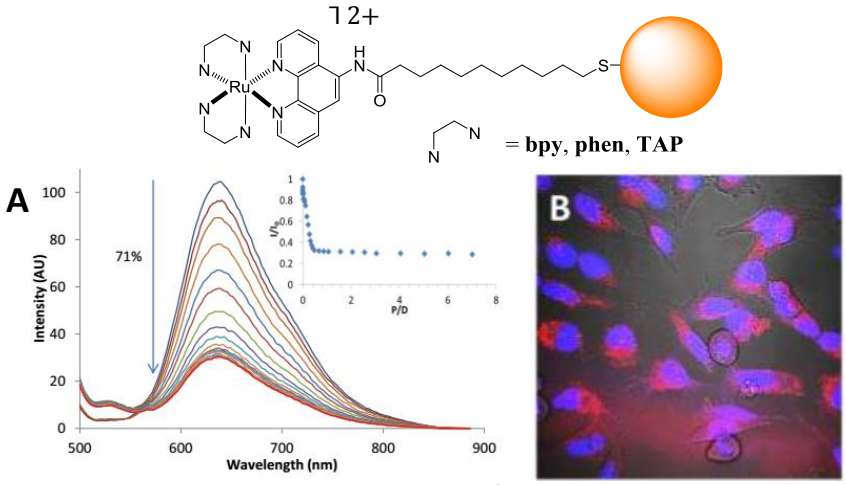

Figure 1.26: *AuNPs studied by Elmes et al.[2] The particles have* ***bpy*** *(**AuNP1**),* ***phen*** *(**AuNP2**) or* ***TAP*** *(**AuNP3**) as ancillary ligands. A: Modulation in the emission spectrum at increasing concentration of st-DNA with AuNPs where* ***TAP*** *is the ancillary ligands. B: Cellular uptake and localisation of the AuNPs with* ***bpy*** *as ancillary ligand followed by confocal microscopy.*

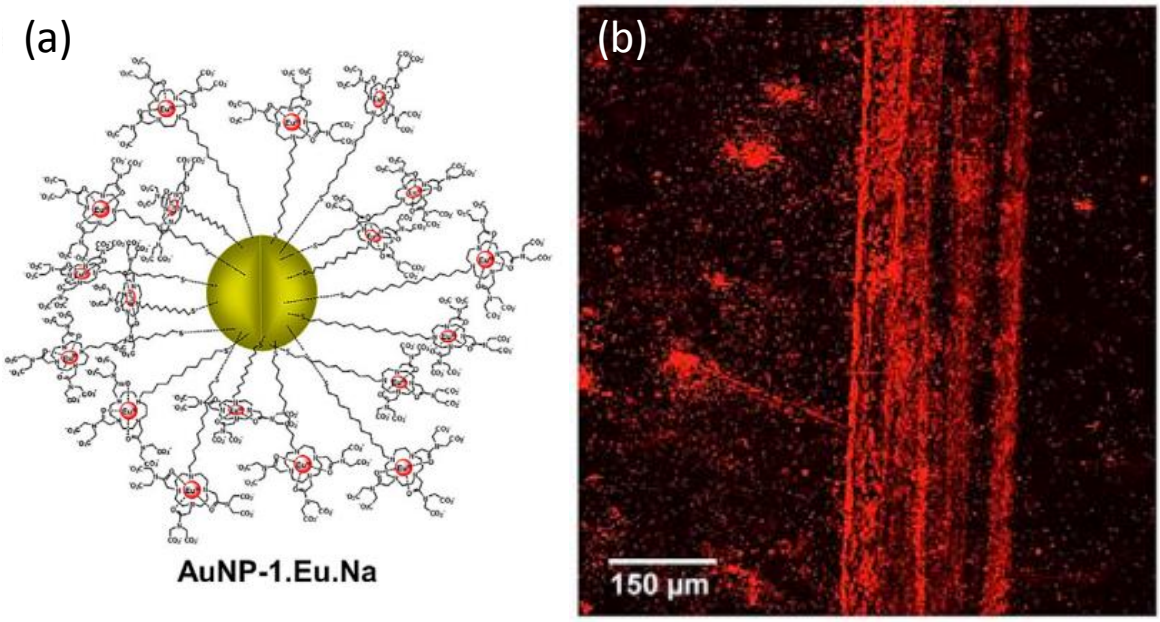

Figure 1.27: *(a) The surface-functionalised AuNP synthesised and studied by Surender et al.; (b) the image shows microdamaged bovine bone structure after being immersed for 24 hours in an aqueous solution of the AuNPs.*

The examples of AuNPs presented in this section demonstrate the great potential for the use of AuNPs in biomedical applications. It is expected that in the future AuNPs will have a major role to play in development of new therapeutic and diagnostic agents. The opportunity for introducing multiple functionalities make AuNPs the perfect template for development of theranostics and more personalised medicine.

1.8 Recent Advances within the Gunnlaugsson Group

Work with Ru(II) polypyridyl complexes, gold nanoparticles and other types of biologically relevant topics has been undertaken in the Gunnlaugsson laboratory over the past several years with the aim to develop DNA binding agents, probes for imaging, and new cancer therapeutic drugs.

Ryan *et al.* developed Ru(II) polypyridyl complexes with one or two 1,8-naphthalimide groups attached. It was the goal to develop new DNA binding agents with diagnostic and therapeutic potential.[131,132] Naphthalimides are shown to bind strongly to DNA through intercalation, with modulation of the photophysical properties. Some naphthalimide-based compounds have shown high anti-cancer activity with IC_{50} as low as 4 µM. It was shown that attachment of a naphthalimide group resulted in a very strong affinity for st-DNA with a binding constant in the order 10^7 M^{-1} (10 mM sodium phosphate buffer, pH 7). Compounds **27a** and **27b** showed a binding site size (*n*) of only *ca.* 0.5 base

pairs. Such a small *n* has been reported for many naphthalimide based compounds. **27c** and **27d**, with a flexible linker between the ruthenium centres and one or two naphthalimide moieties, showed a site size of *ca*. 2.2 base pairs. This is normal in case of an intercalator as described in section 1.3.4. K_b for **27d** (1.5×10^7 M^{-1}) was almost twice as high as for **27c** (0.9×10^7 M^{-1}) in accordance with the presence of two naphthalimide groups rather than just one.[42]

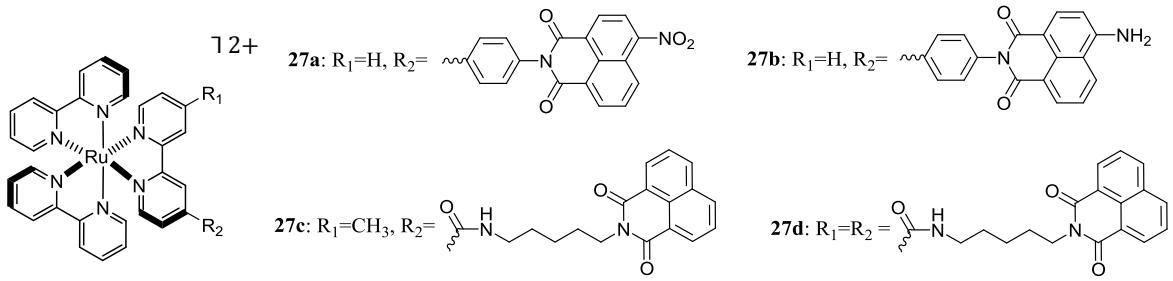

Figure 1.28: *Examples of naphthalimide functionalised Ru(II) polypyridyl complexes, which has been synthesised and studied in the Gunnlaugsson group.*

The photophysical properties of Ru(II) polypyridyl complexes bound to DNA have also been studied extensively in the Gunnlaugsson group in collaboration with the Kelly, Cardin and Quinn laboratories. Hall *et al.* studied the proton coupled electron transfer (PCET) between complex **9b** and the guanine bases in DNA in the solid state using transient spectroscopy.[52] These studies were combined with the X-ray structure to get insights into the mechanism for the electron transfer and the relation of the mechanism with the binding geometry. Poynton *et al*. evaluated the "bright" and "dark" excited state of **9a** (Figure 1.29).[73] As described earlier, **phen** complex **9a** will be emissive in an aprotic solvent such as acetonitrile; however, the emission is quenched in water. The excited state in acetonitrile is referred to as the "bright" excited state (τ = 660 ns). In water, this state is also present. It

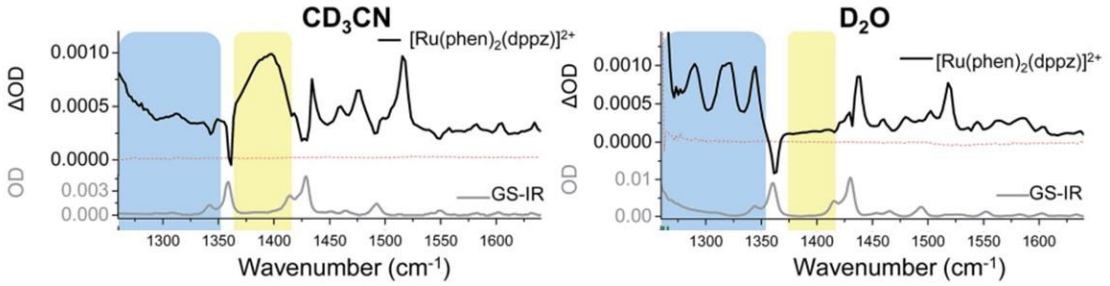

Figure 1.29: *Time-resolved infrared (TRIR) spectra recorded 35 ps after 400 nm excitation of* ***9a*** *CD_3CN (left column) and in D_2O (right column) and their corresponding ground state FTIR (GS-IR) spectra. The blue and yellow coloured regions highlight the characteristic transient bands for the "bright" and "dark" excited states, respectively.*

will, however, immediately decay to another excited state referred to as the "dark" state which will afterwards decay non-radiatively to the ground state (τ = 250 ps). Using time-resolved infrared (TRIR) spectroscopy it was possible to obtain spectra of both the "bright" state in CD_3CN and the "dark" state in D_2O, yielding important insight for use in further studies of the transitions in similar complexes.

The work in this thesis is inspired by the previous work in the Gunnlaugsson group concerning the biological application of a range of compounds, including use of Ru(II) polypyridyl complexes, functionalised AuNPs and naphthalimide based Tröger's bases for imaging and as anti-cancer agents. The following section will give a brief overview of the work presented in the individual chapters.

1.9 Work Described in this Thesis

This research project has been concerned primarily with the studies of Ru(II) complexes for various biological applications. The aim of the work has been to contribute to the development of new therapeutic and diagnostic agents for use against cancer as well as for use as analytic tools in biological studies. In Chapter 1, some important concepts have been introduced which will be used throughout the thesis, and an overview of the current state-of-the-art was given. An extensive introduction to DNA binding was also given.

Chapter 2 is based on previous work in our group. The syntheses of structurally similar complexes prepared with the intention of developing and improving DNA binding and therapeutic properties are described. Their binding to st-DNA is studied.

In Chapter 3 the syntheses and characterisation of compounds based on 1,10-phenanthroline-5,6-dione are described.

In Chapter 4 the potential of the compounds for treatment of cancer and their use in PDT are evaluated. Cellular studies of naphthalimide based Tröger's bases, including examples that involve bimetallic ruthenium complexes, will also be described.

In Chapter 5 the site-specific and cooperative binding of **9b** to DNA will be evaluated to gain an insight into the binding geometry of these novel compounds and to evaluate the possible use of the compound in the targeting of specific sequences of DNA.

Chapter 6 will focus on the syntheses of gold nanoparticles functionalised with Ru(II) polypyridyl complexes for biological applications. The characterisation and study of their binding to DNA will be described.

Finally, in Chapter 7, the general experimental procedures are outlined, and the syntheses of the compounds discussed in this thesis are described.

Chapter 2

Photophysical Studies of Binding of Ru(II) Polypyridyl Complexes to DNA

2.1 Introduction

Motivated by the potential application of Ru(II) polypyridyl complexes to act as imaging and therapeutic agents in photodynamic or photochemotherapeutic treatment of cancer, a significant effort has been made by the Gunnlaugsson group to develop the theranostic applications of this class of compounds.[125] Dr Robert Elmes developed ruthenium complexes with pyrazino[2,3-h]dipyrido[3,2-a:2',3'-c]phenazine (**pdppz**), an extended version of **dppz**, as ligand. [6,72] The design of **pdppz** was based on the well-known properties of Ru(II) complexes with **dppz** as a ligand, such as a strong affinity for DNA with concomitant modulation of the photo-physical properties as described in Section 1.5.2. The increased conjugation of **dppz** was expected to yield a stronger binding to DNA through intercalation, where the half-moon shaped structure of the ligand was presumed to fit in between the base pairs with an ideal stacking with the DNA base pairs because of the curved structure of the ligand that was expected to act as a "hook". Complexes **31a** and **31b** displayed high affinity for salmon testes DNA (st-DNA), with site binding constants (K_b) of 12×10^6 M^{-1} and 5.4×10^6 M^{-1}, respectively, in 10 mM sodium phosphate buffered aqueous solution at pH 7.4.

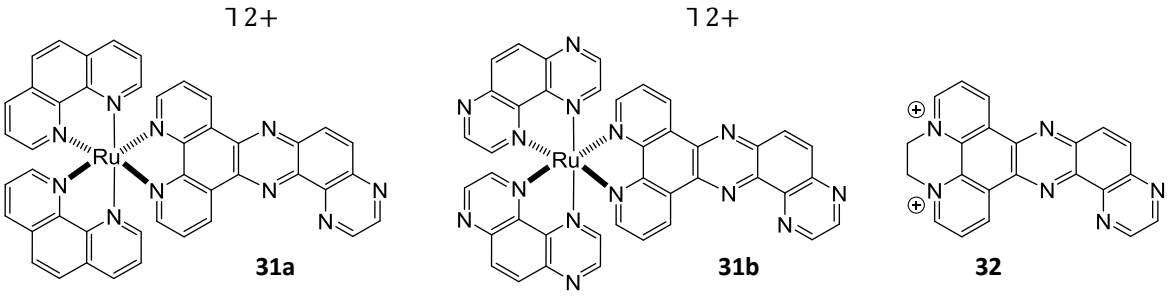

Figure 2.1: *Ru(II) polypyridyl complexes and diquaternised polypyridyl ligand previously synthesised and studied in the Gunnlaugsson group.*[6]

Both complexes exhibited photophysical responses similar to their **dppz** analogue upon interaction with DNA.[72] Complex **31a**, with 1,10-phenanthroline (**phen**) as ancillary ligands was non-emissive in water. However, upon binding to DNA the complex became emissive, which was referred to as the *"light-switch"* effect. This property enabled the compound to act as a luminescent probe for imaging of DNA, with potential applications such as in cellular stains.

Evidence of photo-oxidative quenching of the excited state of complex **31b** by the nucleic acid base guanine was obtained through DNA emission studies.[6] Binding of **31b** to poly(dA)poly(dT) induced an emission enhancement due to protection of the complex from water and oxygen. Meanwhile, binding to the guanine containing sequence poly(dG)poly(dC) resulted in a dramatic quenching of the emission. Complex **31b** exhibited

limited cellular toxicity towards HeLa cervical cancer cells in absence of light irradiation. However, irradiation of cells with 18 J/cm^2 of visible light after treatment with 100 μM of complex **31b** resulted in a more than 80% reduction in the cell viability. Fluorescence activated cell sorting (FACS) showed cell death to be occurring by apoptosis which may have been induced by mitochondrial stress. Co-localisation studies indicated that *ca*. 30% of the compounds entered the mitochondria, where there was no indication of nuclear localisation. Studies employing incubation of cells with the reactive oxygen species (ROS) quencher *N*-acetyl cysteine (NAC) implied inhibition of photo-induced cell death after treatment with complex **31b**, indicating that ROS production was involved in the initiation of cell death.[72]

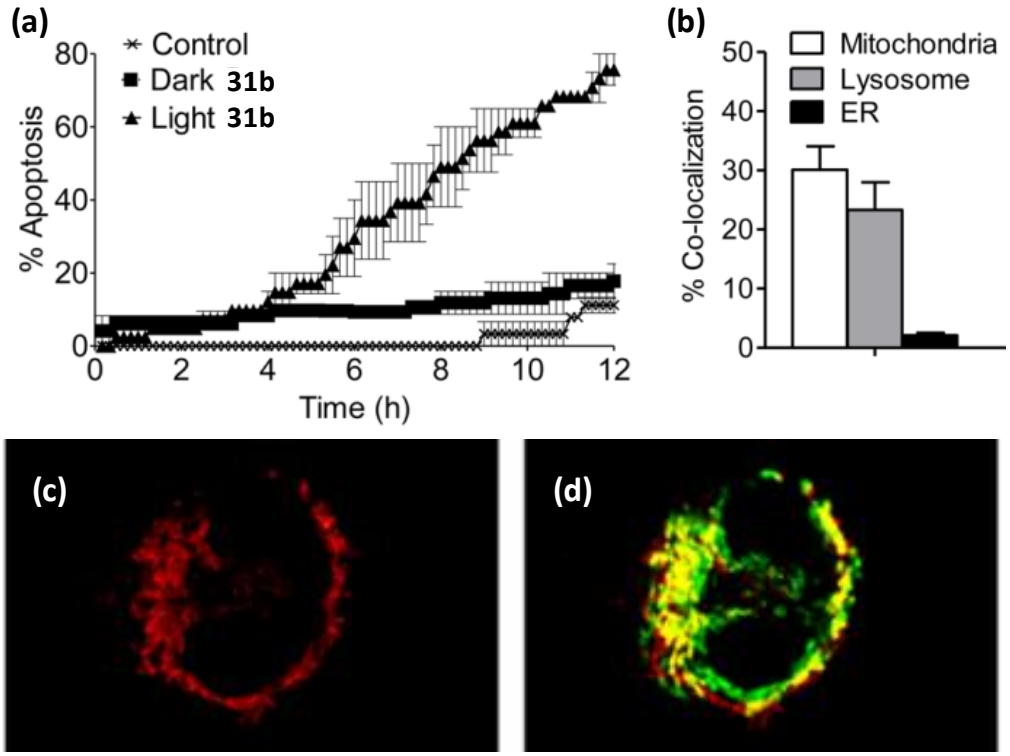

Figure 2.2: *Data obtained from confocal microscopy of HeLa cells with compound* ***31b****. (a) Assessment of the appearance of apoptotic cells and (b) co-localisation of the compound in different organelles. (c) Image of luminescence of* ***31b*** *in a HeLa cell and (d) together with luminescence of tagged mitocondria. Images are reproduced from Cloonen et al.*[6]

Compound **32**, a diquaternerised version of **pdppz**, was also synthesised by Dr Robert Elmes (Figure 2.1).[133] In this compound, both of the coordinating nitrogen atoms were alkylated with an ethylene bridge. The compound showed binding to st-DNA with a binding constant of 6.5×10^5 M^{-1} (10 mM sodium phosphate buffer, pH 7.4), and it photo-cleaved DNA upon light activation. Furthermore, it was taken up by cells, and some increase in the toxicity upon exposure to light was observed.

This project continues the previous research carried out within the Gunnlaugsson group concerning the development of new Ru(II) polypyridyl complexes. The objective was to prepare two new Ru(II) polypyridyl complexes, **33a** and **33b** (Figure 2.3), differing from **31a** and **31b** (Figure 2.1) by containing the ligand 3-methylpyrazino[2,3-*h*]dipyrido-[3,2-*a*:2',3'-*c*]phenazine (**mpdppz**) instead of **pdppz.** It was the purpose to facilitate the investigation of their biological effect, including the interactions with DNA and their effect on cancer cells. It was anticipated that the extension of the **pdppz** moiety would increase the binding affinity to DNA.[134] It was also planned to convert the methyl group to a functional group as a step towards the attachment of the complex to gold nanoparticles (AuNPs) *via* an aliphatic chain. One strategy was to oxidise the methyl group into a carboxylic acid, which afterwards could be used to attach a long aliphatic linker with a terminal primary amine group through an amide coupling. Biological studies have also been carried out for complexes synthesised by Dr Salvador Blasco (**33c**) and PhD student Sandra Estalayo-Adrián (**33d**).[54] Instead of **pdppz**, these complexes bear as a ligand dipyrido-[3,2-*a*:2'.3'-*c*][1,2,5]thiadiazolo[3,4-*h*]phenazine (**dtp**), a sulphur-containing derivative of **dppz**, however, this work will not be discussed here.

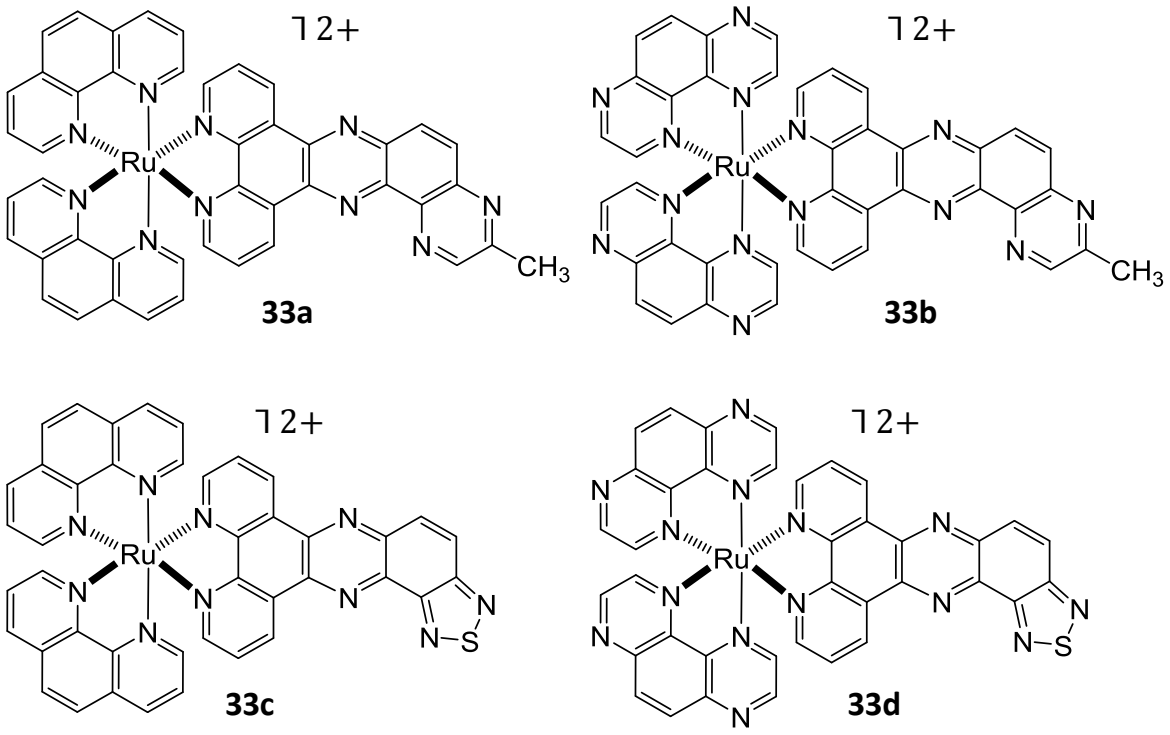

Figure 2.3: *Ru(II) polypyridyl complexes (structural similar to **31a** and **31b**), which have been synthesised and studied.*[54]

The binding of the compounds to DNA was explored using a variety of techniques, including absorption, emission, and circular and linear dichroism spectroscopies. HeLa cervical cancer cells were used for biological investigations, including cytotoxicity studies and evaluations of cellular uptake and localisation, using confocal microscopy, which will be discussed in Chapter 3.

2.2 Synthesis and Characterisation of mpdppz Complexes 33a and 33b

In the following sections, the synthesis and characterisation of $[Ru(L)_2mpdppz]$ will be described. Ligand L was either **phen** (complex **33a**) or **TAP** (complex **33b**).

2.2.1 Synthesis of $[Ru(L)_2mpdppz]^{2+}$

The synthesis of 3-methylpyrazino[2,3-*h*]dipyrido[3,2-*a*:2',3'-*c*]phenazine (**mpdppz**) is shown in Scheme 2.1 and Scheme 2.2. The quinoxaline derivative **34** was synthesized in the first step through a condensation reaction involving 4-nitrobenzene-1,2-diamine and methylglyoxal in ethanol.[135,136] Two isomers were formed in the reaction as a consequence of the two possible orientations of the methylglyoxal (Figure 2.4). Upon completion, the solvent was removed under reduced pressure, and the resulting residue was redissolved in CH_2Cl_2 and washed with H_2O. CH_2Cl_2 was removed under reduced pressure, and the product was isolated as white crystals by recrystallisation three times from *iso*-propanol in a yield of 42%. The ^1H NMR spectrum (400 MHz, $CDCl_3$) was in accordance with the reported spectrum for the desired product,[136,137] and it was confirmed by X-ray crystallography that the desired isomer was formed (Figure 2.4).

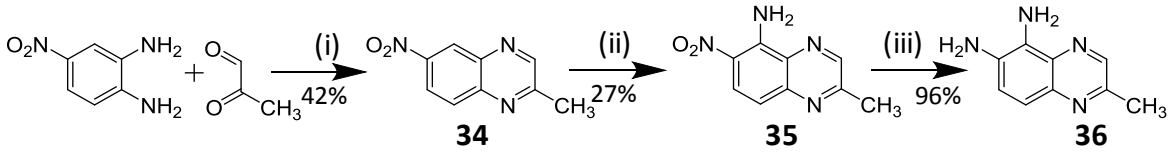

Scheme 2.1: *Synthetic pathway of diamine **13**. (i) EtOH, reflux, 2 h. (ii) H_2NOH, NaOMe in MeOH, rt, 16 h. (iii) N_2H_4, 10% Pd/C, EtOH, reflux, 2 h.*

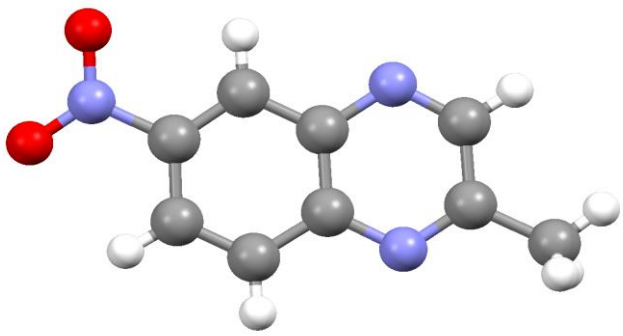

Figure 2.4: *An X-ray crystal structure for product **34** solved by Dr Salvador Blasco.*

In the second step, 2-methyl-5-amino-6-nitroquinoxaline, **35**, was formed by amination at position 5 of quinoxaline in a solution of methanol with the hydrochloride salt of hydroxylamine as amination agent and with NaOMe as a catalytic base. It was found important to restrict the amounts of base used as use of larger amounts of base, in accordance with the synthesis of the similar 5-amino-6-nitroquinoxaline compound,[6] gave poor or no yield.[138] This could be due to the slight acidity of the methyl group as a consequence of imine-enamine tautomerism, where one of the tautomers has the quinoxaline nitrogen atom next to the methyl group protonated. The acidity of the methyl group was confirmed by ^{1}H NMR spectroscopy, as, in a basic CD_3OD solution of the compound, the methyl signal was lost, which can be attributed to the substitution of the protons by deuterium (Figure 2.5). After the reaction, the solvent was removed under reduced pressure, and the resulting solid was redissolved in CH_2Cl_2 followed by washing with H_2O. The organic layer was separated and the solvent was removed under reduced pressure. The product was isolated as a yellow powder in a yield of 27% by automatic flash column chromatography with hexane:ethyl acetate as eluent. In step three in Scheme 2.1 the nitro group was reduced in ethanol using hydrazine as reducing agent and 10% palladium on carbon (Pd/C) as catalyst, forming 2-methyl-5,6-diaminoquinoxaline **36** in 96% yield.[135]

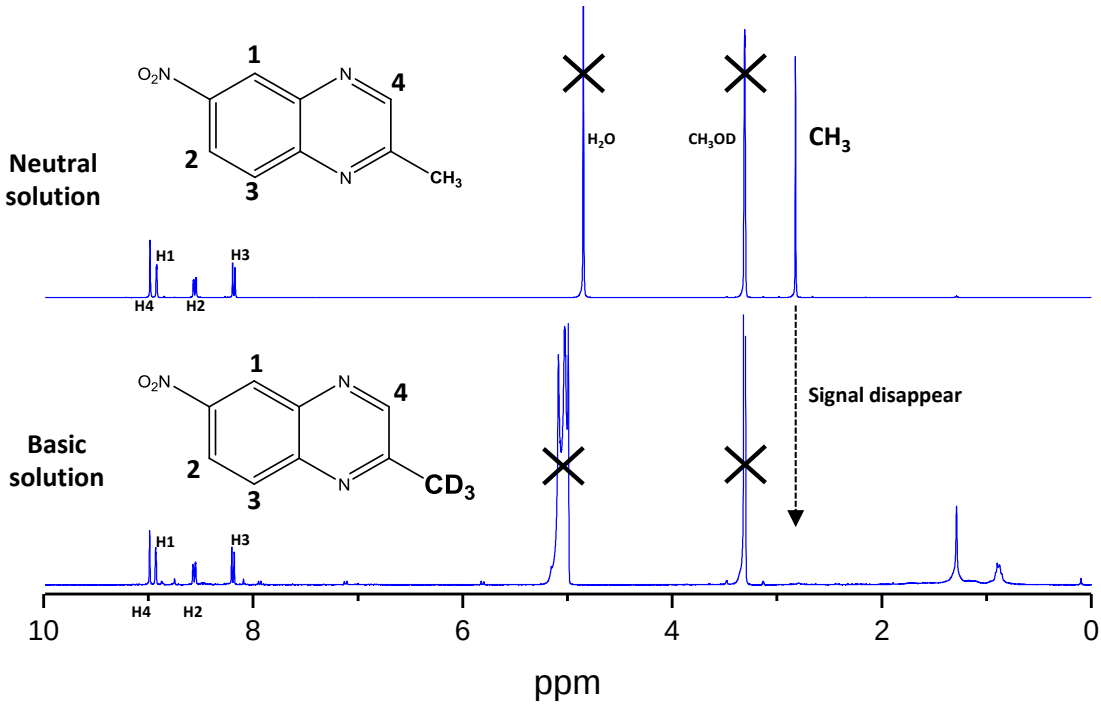

Figure 2.5: *^{1}H NMR (400 MHz, CD_3OD) spectra of 2-methyl-6-nitroquinoxaline (**34**) under neutral and basic conditions (CD_3ONa as base). The resonance of the methyl group disappears when under basic conditions as a consequence of substitution with deuterium, confirming that the methyl group is weakly acidic.*

1,10-Phenanthroline-5,6-dione (**phendione**) was synthesized using a standard procedure[139] by oxidizing 1,10-phenanthroline in a mixture of concentrated H_2SO_4 (95%) and concentrated aqueous or fuming HNO_3 (70% and 100%, respectively) upon heating with KBr as a catalyst (Scheme 2.2). At the end of the reaction, Br_2 gas was removed by flushing with N_2 gas and heating. The mixture was poured over ice, and excess acid was neutralized by adding 5 M aqueous NaOH dropwise until pH was between 5.0 and 7.0 (it was essential to avoid pH higher than 7.0 since **phendione** decomposes rapidly under basic conditions). The product was extracted into CH_2Cl_2, the solvent was removed under reduced pressure, and the resulting residue was recrystallised from ethanol, yielding the product as a yellow powder. The best result for this reaction was obtained when concentrated nitric acid was used rather than fuming nitric acid. The former resulted in a yield of 73% compared to a maximum yield of 33% when fuming nitric acid was used.

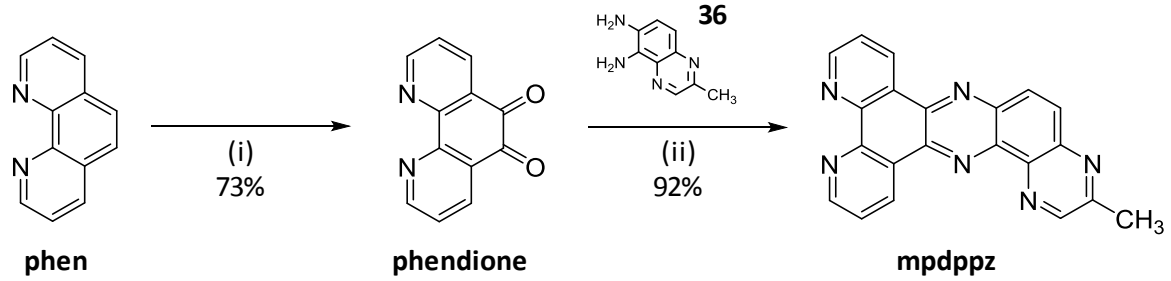

Scheme 2.2: *Synthetic pathway of ligand* ***mpdppz****. (i) H_2SO_4/HNO_3, KBr, reflux, 6 h; (ii) EtOH/H_2O, heating at high pressure, 16 h.*

The final step in the synthesis of **mpdppz** was the condensation of **phendione** and the diamine **36** (Scheme 2.2) in a mixture of ethanol and H_2O. The reaction was carried out in a sealed high-pressure tube at 140 °C for 12 hours, and after cooling to room temperature the product was isolated by filtration. The product **mpdppz** is highly insoluble in all solvents examined and was obtained as a white solid, following a wash with CH_2Cl_2 in a yield of 92%. ^{1}H NMR (400 MHz, $CDCl_3$) of the compound with trifluoracetic acid (TFA), is shown in Figure 2.6 (^{13}C NMR spectrum is shown in Figure A2.1). The ^{1}H NMR spectrum of the compound is similar to the spectrum of **pdppz**,[72] except the appearance of the methyl resonance at 3.27 ppm and nine aromatic signals with a singlet at 9.77 ppm for the aromatic proton next to the methyl group. Furthermore IR spectroscopy (Figure A2.2), and HRMS analysis were carried out, all of which confirmed the expected structure; the HRMS experiment gave a peak at 349.1202, corresponding to the $[M+H]^+$ ion.

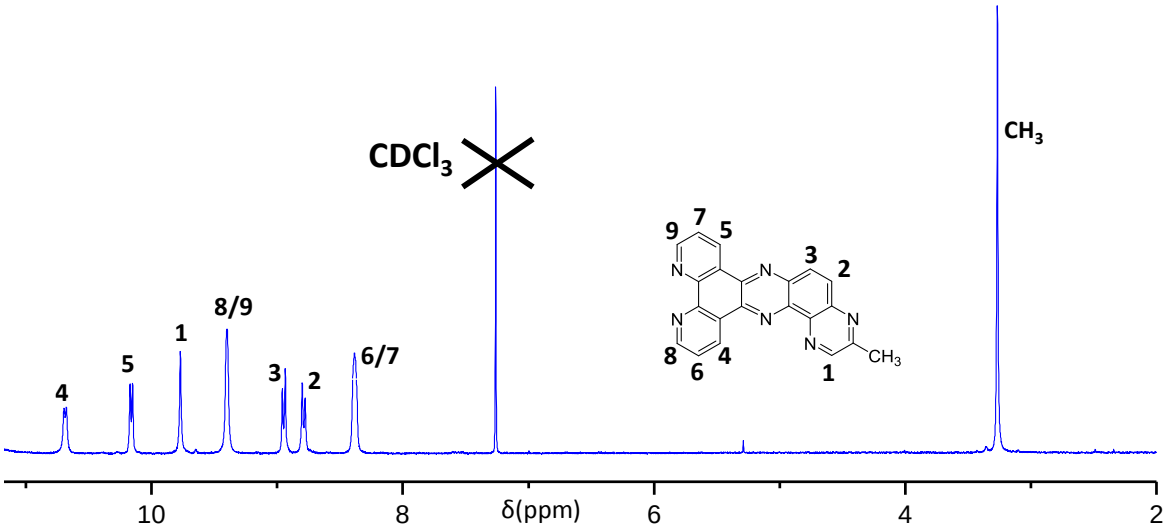

Figure 2.6: *^{1}H NMR (400 MHz, $CDCl_3$ with TFA) spectrum of protonated form of ligand* ***mpdppz****.*

As mentioned, one of the objectives of this project was to use the methyl group as a synthetic handle for the attachment to AuNPs as well as to introduce other groups and functionalities. With this in mind the next step was to convert the methyl group to a more reactive functional group, which would enable the attachment of a long aliphatic linker. Oxidation of the methyl group to a carboxylic acid was attempted in aqueous solution with $KMnO_4$ as oxidising agent using microwave irradiation at 140 °C with varied reaction time and temperatures (Scheme 2.3). Afterwards, the mixture was filtered to remove solid MnO_2, and the filtrate was acidified yielding the product as a yellow precipitate that was isolated by filtration. However, after several attempts with varied reaction conditions, it was only possible to obtain the desired product in a yield of 7%, and with low purity. The structure of the product has been confirmed by ^{1}H and ^{13}C NMR spectroscopy and with HRMS. The ^{13}C NMR spectrum shows one characteristic signal at 166.01 ppm, confirming the successful oxidation of the methyl group to a carboxylic acid group, and the HRMS shows a peak at 379.0958, corresponding to the mass of the $[M+H]^+$ ion. It was also confirmed that no starting material was left after end of reaction.

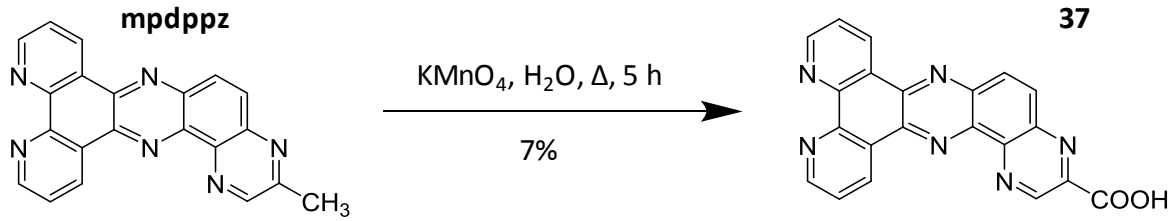

Scheme 2.3: *Synthesis of ligand* ***37*** *from* ***mpdppz****.*

Attempts to carry out this reaction with the oxidising agents $K_2Cr_2O_3$ or SeO_2 did not give any yield of **37**. Alternative routes for synthesis of **pdppz** with a carboxylic acid group involved the oxidation of the methyl group in an earlier step of the synthesis. The oxidation of the methyl group in **34** under condition similar to those described in Scheme 2.1 did not give any isolable product. The oxidation of the methyl group in complex **33a** after complex formation with **mpdppz** was also attempted, but this was unsuccessful. Based on these poor results it can be concluded that alternative reactions were more likely to occur rather than oxidation of the inert methyl group. For example, in the literature is reported that oxidation of quinoxaline with $KMnO_4$ under basic conditions will result in cleavage of the quinoxaline ring system and the formation of pyrazine-2,3-dicarboxylic acid.[140]

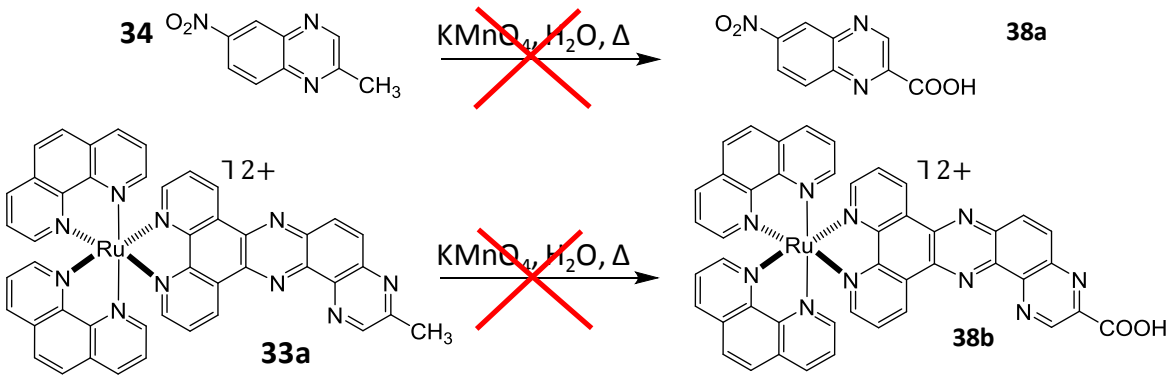

Scheme 2.4: *Attempts to oxidise the methyl group of quinoxaline derivative **34** and in complex **33a**.*

Alternatives to derivatise the methyl group were also tried. As mentioned in the description of the amination of **34**, the methyl group is acidic. Based on that it was expected that it would be possible to alkylate the methyl group by reaction with an alkylbromide after deprotonation of the methyl group with *n*-BuLi. Unfortunately, this attempt also failed, possibly due to delocalisation of the anion in the aromatic ring system after deprotonation, alkylation of one of the nitrogen atoms in the ligand, or because of very low solubility of **mpdppz**. Radical initiated bromination of the methyl group of **mpdppz** after formation of complex **33a** also failed. In this reaction, *N*-bromo succinimide (NBS) was used as bromination agent with azobisisobutyronitrile (AIBN) as radical initiator at heating with CH_2Cl_2, $CHCl_3$ or CCl_4 as solvent. Again, low solubility might be one explanation for the poor result.

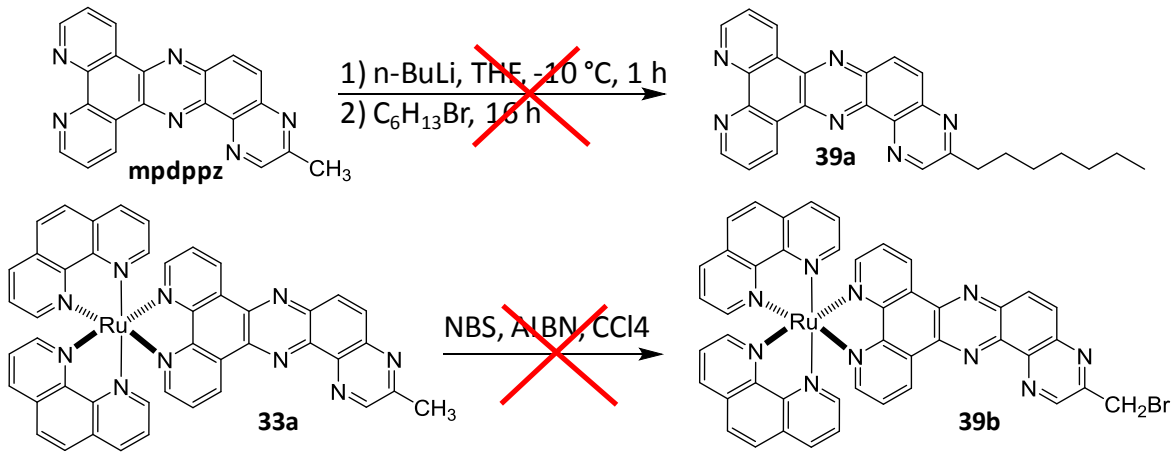

Scheme 2.5: *Attempts to alkylate methyl group in* ***mpdppz*** *and brominate methyl group in* ***33a****.*

After the unsuccessful attempts to convert the methyl group in **mpdppz** or its precursors to a more reactive group, the synthetic steps toward **33a** and **33b** was continued. The synthesis of 1,4,5,8-tetraazaphenanthrene (**TAP**) was achieved using an established procedure,[6,141] which initially involved condensation of glyoxal in H_2O with 4-nitrobenzene-1,2-diamine by refluxing in ethanol for four hours (Scheme 2.6). The mixture was cooled to room temperature, and the precipitate was isolated by filtration and washed with methanol, until the filtrate was colourless giving the product as a grey solid in a yield of 74%. Amination, using hydroxylamine in the presence of metallic sodium in methanol, gave a yield of 46%. Subsequent reduction of the nitro group using hydrazine in the presence of 10% Pd/C, gave the pure diamine as a red solid in 98% yield. Condensation of glyoxal in H_2O with the diamine was achieved by heating under reflux in ethanol for three hours. Removal of the solvent under reduced pressure, followed by recrystallisation from isopropanol, yielded the desired product as a red crystalline powder in 41% yield.

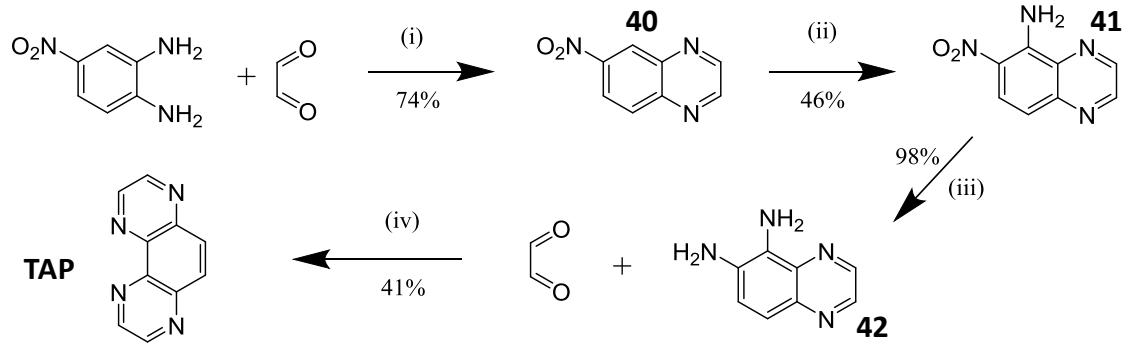

Scheme 2.6: *Synthetic pathway of* ***TAP****. (i) EtOH, reflux, 4 hours. (ii) Na, NH_2OH, MeOH, reflux, 1 hour. (iii) NH_2NH_2, 10% Pd/C, reflux, 2 hours. (iv) EtOH, reflux, 3 hours.*

The precursors for the formation of complexes **33a** and **33b** were synthesized from a standard procedure by initially reacting ruthenium(III) chloride with 1,5-cyclooctadiene (**cod**) in ethanol at reflux temperature for three days (Scheme 2.7).[142] A precipitate was isolated by centrifugation and washed with ethanol, giving dichloro(1,5-cyclo-octadiene)ruthenium(II) ([Ru(cod)Cl_2]) as a brown powder in a yield of 97%. Reactions of [Ru(cod)Cl_2] with two equivalents of **phen** or **TAP** were carried out under microwave irradiation at 140 °C in degassed DMF for 40 minutes yielding the **phen** (**44a**) and the **TAP** (**44b**) precursors in a yield of 76% and 85%, respectively (Scheme 2.7). The structures of the complexes were confirmed by ^{1}H NMR (400 MHz, DMSO-d_6).

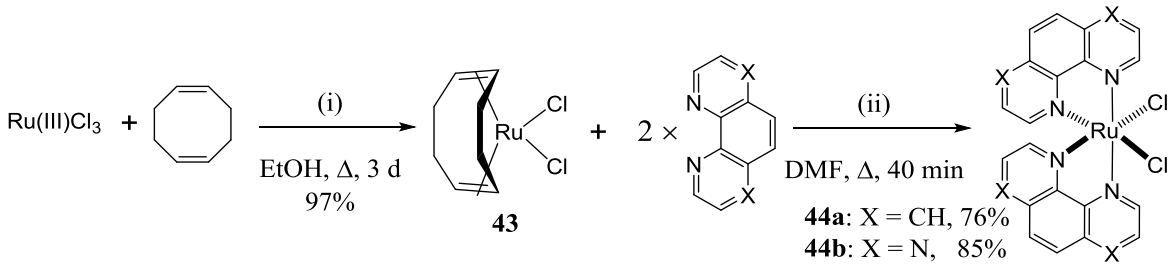

Scheme 2.7: *Synthetic pathway of precursors (**44a** and **44b**). (i) EtOH, reflux, 3 days. (ii) DMF, 140 °C, microwave irradiation, 40 min.*

The final step in the synthesis of complex **33a** and **33b** with **mpdppz** as ligand (Figure 2.7) were carried out under microwave irradiation at 140 °C in a mixture of ethanol and H_2O after degassing with N_2 to remove O_2. The products were purified by gradient column chromatography on alumina with a mixture of CH_3CN and H_2O as eluent. Both complexes were obtained in a reasonable yield of 74% and 59% for **33a** and **33b**, respectively. The structures of the complexes were confirmed by ^{1}H NMR (400 MHz, CD_3CN), ^{13}C NMR (100 MHz, CD_3CN) and IR spectroscopy and HRMS. The ^{1}H NMR spectrum of complex **33a** is shown in Figure 2.8 and is similar to the spectrum of **31a** (^{13}C and IR spectra can be found in Appendix 2), however, with a singlet at 2.89 ppm assigned to the methyl group and a singlet at 9.15 ppm assigned to the aromatic proton next to the methyl group. HRMS shows

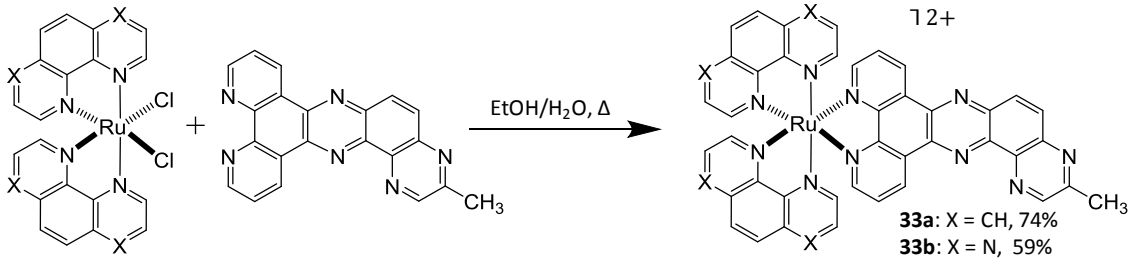

Figure 2.7: *Syntheses of ruthenium complexes **33a** and **33b**. H_2O/EtOH, 140 °C, microwave irradiation, 40 min and 10 min for **33a** and **33b**, respectively.*

a peak at 810.1567, corresponding to the mass of the molecular ion of **33a**·2Cl. The ^{1}H NMR spectrum of **33b** is shown in Figure 2.9. It is similar to the spectrum of **31b**, but with a singlet at 2.90 ppm, assigned to the methyl group, and a singlet at 9.16 ppm, assigned to the aromatic proton next to the methyl group. HRMS shows a peak for *m/z* at 407.0679, corresponding to the dication **33b**$^{2+}$. Purity of the compound was confirmed with elemental analysis.

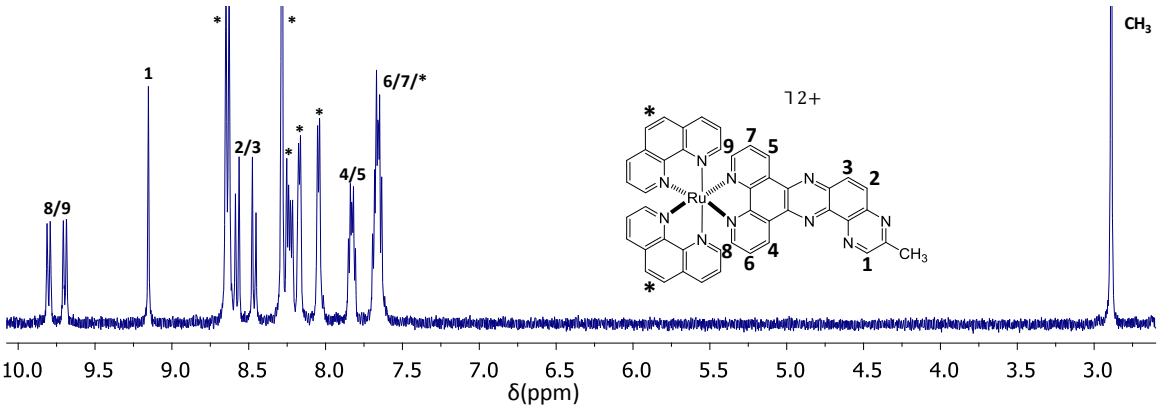

Figure 2.8: *^{1}H NMR (400 MHz, CD_3CN) spectrum of complex **33a**·2Cl. ^{13}C NMR spectrum of **33a**·2Cl can be found Figure A2.3.*

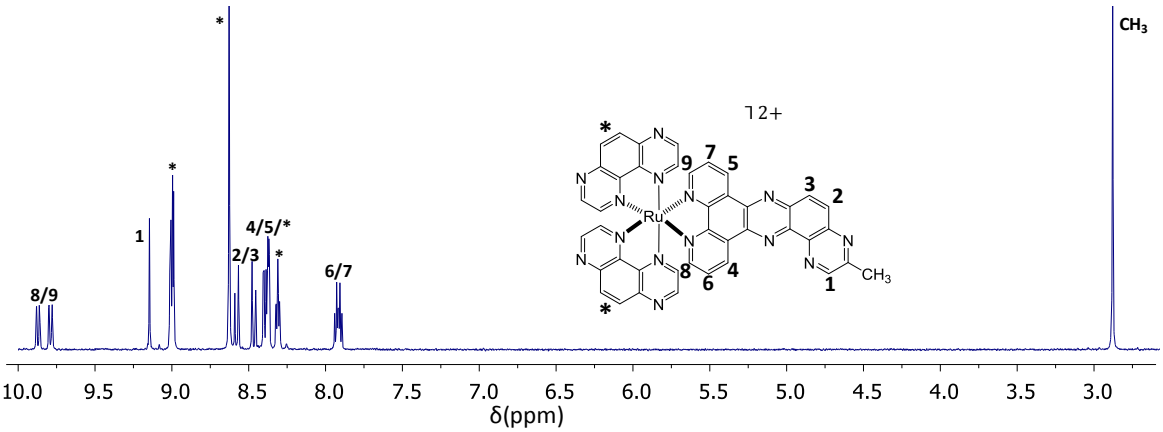

Figure 2.9: *^{1}H NMR (400 MHz, CD_3CN) spectrum of complex **33b**·2Cl. ^{13}C NMR spectrum of **33b**·2Cl can be found in Figure A2.4.*

In summary, the successful syntheses and characterisation have been carried out of Ru(II) polypyridyl complexes **33a** and **33b** which have the new ligand **mpdppz** in common. Attempts were made to convert the relatively inert methyl group in **mpdppz** to a more reactive group, unfortunately without success. Both of the new complexes were very soluble as their chloride salts in water, and their photophysical properties were investigated in 10 mM phosphate-buffered aqueous solution.

2.2.2 Photophysical Characterisation of $[Ru(L)_2mpdppz]^{2+}$

The photophysical properties of the complexes $[Ru(phen)_2mpdppz]Cl_2$ (**33a**) and $[Ru(TAP)_2mpdppz]Cl_2$ (**33b**) were studied in 10 mM sodium phosphate buffered aqueous solution at pH 7.4 and in CH_3CN using varied spectroscopic techniques. The absorption and emission spectra of the two complexes were very similar to those observed for $[Ru(L)_2dppz]^{2+}$ and $[Ru(L)_2pdppz]^{2+}$, Figure 2.10 and Figure 2.11.[6,143] The absorption spectrum of **33a** in phosphate buffered aqueous solution (pH 7.4) showed absorbance maxima at 223 nm, 262 nm, 310 nm, 365 nm, 385 nm and 440 nm (Table 2.1). The bands at 223 nm and 262 nm are characteristic of π-π* intra-ligand transitions of the ancillary **phen** ligands, while the intense band at 310 nm was attributed to π-π* transitions within the extended aromatic ligand **mpdppz**. Less intense bands at 365 nm and 385 nm were attributed to the n-π* transitions within the phenazine part of **mpdppz**. The broad band centered at 440 nm was characteristic of the metal to ligand charge transfer (MLCT) transitions from the Ru(II) center to the **dppz** like ligands.[6] Complex **33a** showed no emission in H_2O when excited at the absorption maximum corresponding to the MLCT band (440 nm) or at any

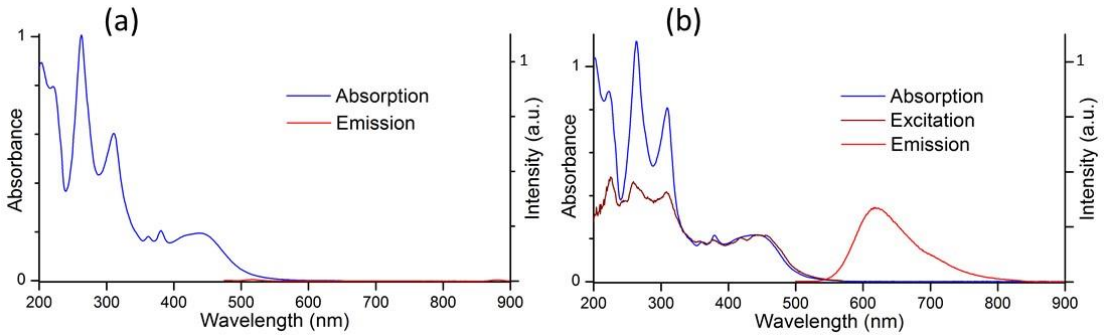

Figure 2.10: *Absorption, emission and excitation spectra of complex* ***33a***·*2Cl in (a) 10 mM sodium phosphate buffered aqueous solution, at pH 7.4, and (b) CH_3CN . λ_{exc} =440 nm and λ_{em} =620 nm.*

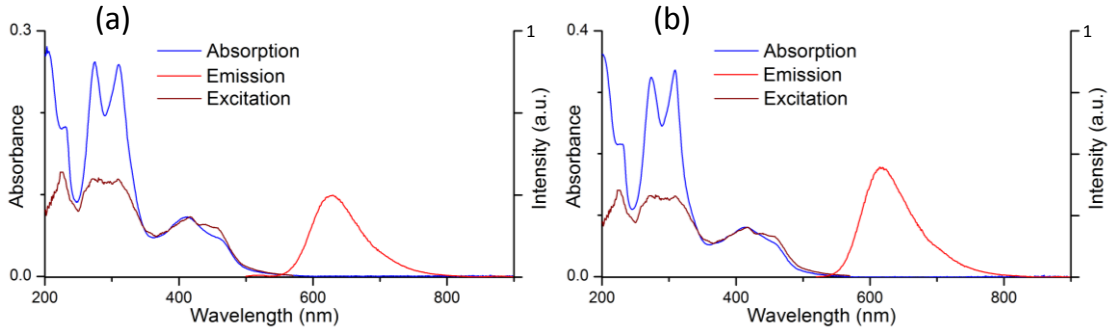

Figure 2.11: *Absorption, emission and excitation spectra of complex* ***33b***·*2Cl in (a) 10 mM sodium phosphate buffered aqueous solution, at pH 7.4, and (b) CH_3CN . λ_{exc} =415 nm and λ_{em} =630 nm.*

other wavelengths. These results were in accordance with previous studies of similar ruthenium complexes containing derivatives of **dppz** and **phen** as ligands, including **31a**, for which the excited state is expected to be quenched by interaction with H_2O, thus resulting in non-radiative decay.[73,78,144] On the other hand, the compound showed an emission band at 619 nm in CH_3CN, which confirms the theory that hydrogen bonds to non-coordinating nitrogen atoms at **mpdppz** were responsible for quenching of the excited state in H_2O.

Table 2.1: *Absorption properties for complexes **33a**·2Cl and **33b**·2Cl in 10 mM sodium phosphate buffered aqueous solution, at pH 7.4 and room temperature.*

λ_{max} [ε_λ (M^{-1} cm^{-1}) ± 10%]			
Complex	**$\pi - \pi^*$ phen or TAP**	**$\pi - \pi^*$ mpdppz**	**MLCT**
33a	262 nm [125000]	310 nm [750000]	440 nm [24100]
33b	275 nm [88000]	310 nm [87000]	412 nm [24000]

The spectrum of complex **33b** in H_2O showed an absorption band at 275 nm (Figure 2.11a) characteristic of π–π* intra-ligand transitions of the ancillary **TAP** ligands, an absorption band at 310 nm corresponding to π–π* transition within the ligand **mpdppz**; and an absorption band at 412 nm attributed to the typical MLCT transition for this kind of complexes where an electron transfer occurs from the metal centre to the **TAP** ligands.[80] In contrast to the properties of **phen** complex **33a**, an emission band was observed with a centre at 630 nm in H_2O (λ_{exc} = 415 nm). Similar absorption and emission properties were observed in CH_3CN as shown in Figure 2.11b.

To characterise further the photophysical properties of the complexes, the photoluminescence quantum yields (Φ_{em}) and the excited state lifetimes (τ_{em}) were determined in H_2O and in CH_3CN. These are shown in Table 2.2. Since **33a** is non-emissive in aqueous solution, attempts were not made to obtain the quantum yields and excited state lifetime in H_2O for this complex. The relative quantum yields were determined with the optically dilute method[145] with $[Ru(bpy)_3]$·2Cl as reference compound (Φ_{em} = 2.8% in H_2O).[146,147] Φ_{em} values of 1.8% and 2.4% were obtained in CH_3CN for **33a** and **33b**, respectively. These values were both significantly lower than values for the corresponding complexes with **pdppz** and **phen** (complex **31a**) or **TAP** (complex **31b**) as ligands. One explanation could be the higher degree of freedom of **mpdppz** compared to **pdppz**, because of the methyl group, which was allowed to rotate freely around the C-C single bond.

Excited state lifetime measurements were recorded using time correlated single photon counting (λ_{ex} = 458 nm, absorbance = 0.05). In all cases, the data were best-fitted to a single exponential decay function with randomly distributed residuals. τ_{em} values of 166 ns and 715 ns in aerated CH_3CN were obtained for **33a** and **33b**, respectively, which were similar to τ_{em} values for the related **phen** complex **31a** (170 ns) and **TAP** complex **31b** (557 ns). Complex **33b** exhibited a longer lifetime in CH_3CN than complex **33a**. Similarly, bubbling with N_2 for 30 minutes resulted in an increase in the excited state lifetimes due to the reduction of the excited state quenching caused by dissolved oxygen.[6]

Table 2.2: *Emission properties of complexes in CH_3CN and in 10 mM sodium phosphate buffered aqueous solutions at pH 7.4, room temperature.*

	Φ_{em} [a] Buffer	Φ_{em} [a] MeCN	τ_{em} (ns) [b] Buffer (air)	τ_{em} (ns) [b] Buffer (N_2)	τ_{em} (ns) [b] MeCN (air)	τ_{em} (ns) [b] MeCN (N_2)
33a	-	1.8%	-	-	166	324
33b	3.1%	2.4%	679	801	715	1070
31a[c]		7.3%	-	-	170	411
31b[c]		14.4%	655	813	557	914

[a] *Air-saturated aqueous solution of $[Ru(bpy)_3]^{2+}$ as reference (Φ_{em} = 2.8%).*[146] *Pooled SE ± 5%.* [b] *The luminescence decays are mono-exponential. Pulled SE ± 5%.* [c] *Cloonen et al.*[6]

Complexes **33a** and **33b** have shown photophysical properties similar to the structurally related complexes **31a** and **31b**. The emission quantum yields were lower, probably due to higher flexibility of the complex after introduction of the methyl group. Spectroscopic studies of the interactions of complexes **33a** and **33b** with double stranded DNA are presented in Section 2.3.

2.2.3 Crystal Structure and Structures in Water of $[Ru(L)_2mpdppz]^{2+}$ (33a and 33b)

Having synthesised and photophysically characterised the above complexes, investigations into their solid-state structures and their structures in solution were initiated using X-ray crystallography and theoretical calculations with density functional theory (DFT).

Crystal Structure of 33b

The **TAP** complex was successfully crystallised by Sandra Estalayo-Adrián, and a single crystal X-ray diffraction experiment was carried out by Dr Salvador Blasco. Attempts to crystallise the **phen** complex in order to obtain a solid-state structure were unsuccessful. The crystal structure of the **TAP** complex **33b**, is shown in Figure 2.12a. The diffraction data for

33b with two chlorine counterions were solved in the triclinic $P\bar{1}$ space group. The crystal used for crystallography was rather small, the reflections were very weak, and the data collection was difficult. Nonetheless the structure could be solved and refined to an R1(I>2σ(I))-value of 0.099. The solvent molecules were very disordered and could not be modelled properly. SQUEEZE was used to remove electron density from the disordered areas, and refinements were continued using the recalculated data. The unit cell contains four molecules of complex **33b** along with the corresponding chlorine counterions. The asymmetric unit contains two crystallographically different molecules of **33b**: one Λ-**33b** (Ru1) and one Δ-**33b** (Ru2) along with four chlorine atoms that balance the charge and, as mentioned, some very disordered solvent molecules. In both isomers the ruthenium core

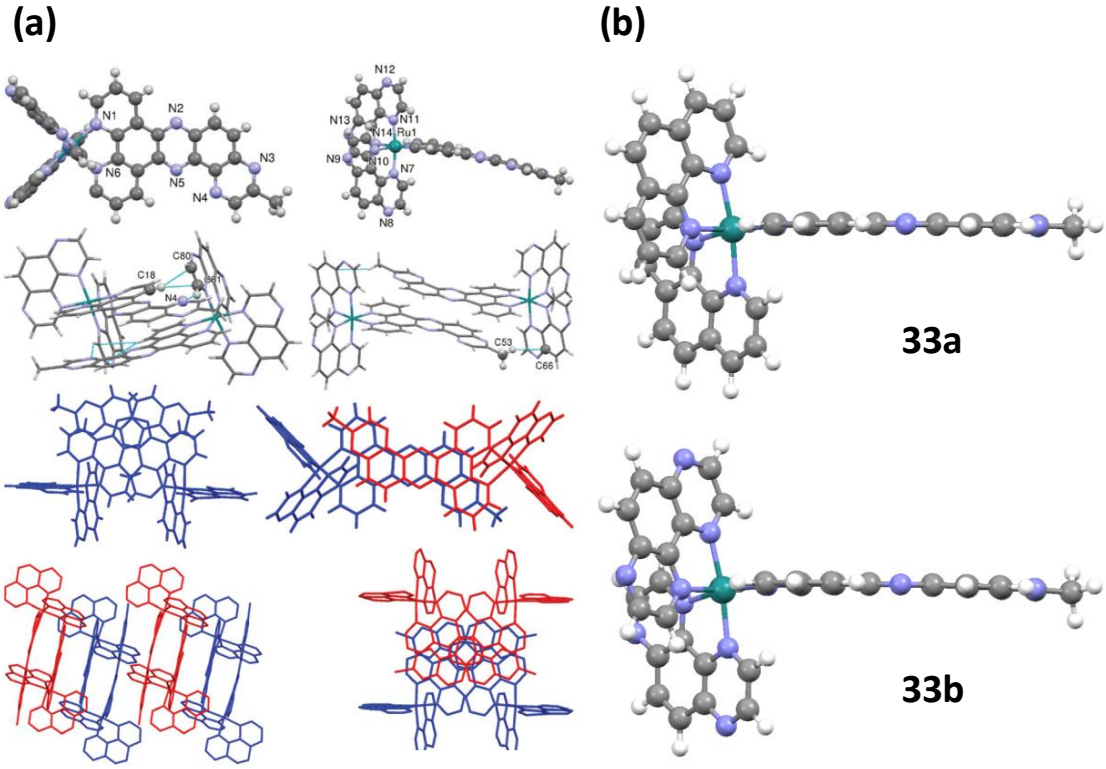

Figure 2.12: *(a) X-ray crystal structure for **33b**. (First row) crystal structure for complex **33b** with highlighting of the complex and the bending of the **mpdppz** moiety. Only one of the two units is shown. (Second row, left) Details of CH···π and CH···N interactions between neighbouring molecules. (Second row, right) Details of the CH_3···π interaction between neighbouring molecules. (Third row, left) Stacking mode between neighbouring molecules which form an angle of 87.6° (measured as the torsion angle of Ru atoms and centroids of the central pyrazine within either **mpdppz**). (Third row, right) Complexes are shown in red and blue. (Fourth row) Packing and chirality domains. For clarity, solvent molecules (H_2O) and counterions (Cl^-) are not shown in the crystal–structure. (b) DFT calculated equilibrium structures in water of **33a** and **33b** (M06/6-311G(d,p) and LANL2DZ, SMD).*

showed a fairly regular octahedral geometry with N–Ru bond distances ranging from 1.99 to 2.12 Å. The **mpdppz** moiety is non-planar. The bending angle between two planes can be quantified as such: (1) the mean plane defined by the ruthenium and the "phenanthroline" part of the **mpdppz** moiety and (2) the mean plane defined by the "methyldiazine" part of the **mpdppz**. This distortion was 14.13° for Ru1 and 14.62° for Ru2. The **mpdppz** moieties associate parallel to the a-axis forming strands of alternate couples of isomers with the relative conformation difference depending on whether they are the same enantiomer or two different ones. This can be explained in terms of the different interaction modes between the ΔΛ and ΔΔ/ΛΛ isomers and might explain the bending of the **mpdppz** moiety.

Geometry Optimised Structures of $[Ru(L)_2mpdppz]^{2+}$ in Water

The equilibrium structures in aqueous solution of the two complexes **33a** and **33b** were calculated using Density Functional Theory (DFT) with the software package Gaussian 09.[148] The M06 functional was used together with the Pople style basis set 6-311G(d,p) for all atoms except ruthenium, for which the basis set LANL2DZ was used. Solvation Model based on Density (SMD) was used to include the effects of water in the calculations. The geometry optimisation was done of the crystal structure of $[Ru(TAP)_2mpdppz]^{2+}$ and, to obtain the structure of $[Ru(phen)_2mpdppz]^{2+}$, optimisation was done of the same structure with the non-coordinating nitrogen atoms in **TAP** substituted with CH groups. It was ensured that all second order derivatives of the energy with respect to the atomic coordinates were positive, which is a criterion for an energy minimised structure.

The DFT minimum energy structure of $[Ru(TAP)_2mpdppz]^{2+}$ was similar to the crystal structure, however, the **mpdppz** ring system was much more planar (Figure 2.12). The non-planarity of the solid-state structure may be explained by interactions with neighbouring complexes, interactions that are not present in solution. The minimum energy structure of $[Ru(phen)_2mpdppz]^{2+}$ was similar to that of the corresponding **TAP** complex, both with a planar **mpdppz** ring system.

2.3 Titrations of *rac*-$[Ru(L)_2mpdppz]^{2+}$ (33a and 33b) with st-DNA

To explore the potential biological activity at the genome level, the binding of racemic mixtures of the complexes to DNA was investigated. Spectroscopic DNA titrations were carried out in 10 mM phosphate buffered solution at pH 7.4, and either in the presence or absence of 160 mM NaCl. A solution of st-DNA was added to the solution of the complexes in a 1 cm emission quartz cuvette, and the absorption and emission were recorded after each

addition. Titrations were done in triplicates for each set of conditions to ensure reproducibility. The increase in the concentration of st-DNA resulted in a significant change in both the absorption and the emission spectrum as shown in Figure 2.13. The general behaviour for the complexes was similar to that previously reported for $[Ru(phen)_2pdppz]^{2+}$ (**31a**) and $[Ru(TAP)_2pdppz]^{2+}$ (**31b**)[6] as well as many other Ru(II) polypyridyl complexes with **dppz**-like ligands.[80] The general trend was an overall decrease in the MLCT absorption band with increasing concentrations of DNA. At low ionic strength (no NaCl), the decrease in the absorbance of the MLCT band at 440 nm for complex **33a**, which contained **phen** as ancillary ligand, was 17%, and the decrease in the π–π* band for the extended aromatic moiety at 310 nm was 44%. Similarly for the **TAP** complex **33b** the decrease in the MLCT band at 412 nm was 22%, and the decrease in the π–π* band for the extended aromatic moiety at 310 nm was 34% (low ionic strength). This hypochromic behaviour indicated intercalation where, particularly, the large decrease in the absorbance at 310 nm can be explained by a strong interaction between the chromophore of the extended aromatic moiety and the chromophores of the base pairs in the form of π–π stacking.

A fundamental difference was observed between the change in the emission spectra for complexes that had **phen** and **TAP** as ligands. The **phen** complex **33a** exhibited the well-known "light switch effect", mentioned in Chapter 1, where the emission was fully quenched in aqueous solution, but the complex became highly emissive upon binding to DNA.[6] This effect was explained by the change in the environment due to the intercalation of the extended aromatic moiety, which prevented solvent molecules from interacting with N-atoms of the phenazine moieties (which will quench the emission). The emission showed biphasic behaviour in solutions containing only 10 mM phosphate buffer. In Figure 2.13 (inset) can be seen that in the first phase a strong emission enhancement was observed, while in the second phase the emission intensity began to decrease slowly. A decrease was not observed at high ionic strength (160 mM NaCl). This difference between high and low ionic strength was explained by the fact that the saturation of DNA with bound complex in the beginning of the titration at high ionic strength was smaller than at low ionic strength, as will be explained later. A similar behaviour has been observed for **31a**.[6]

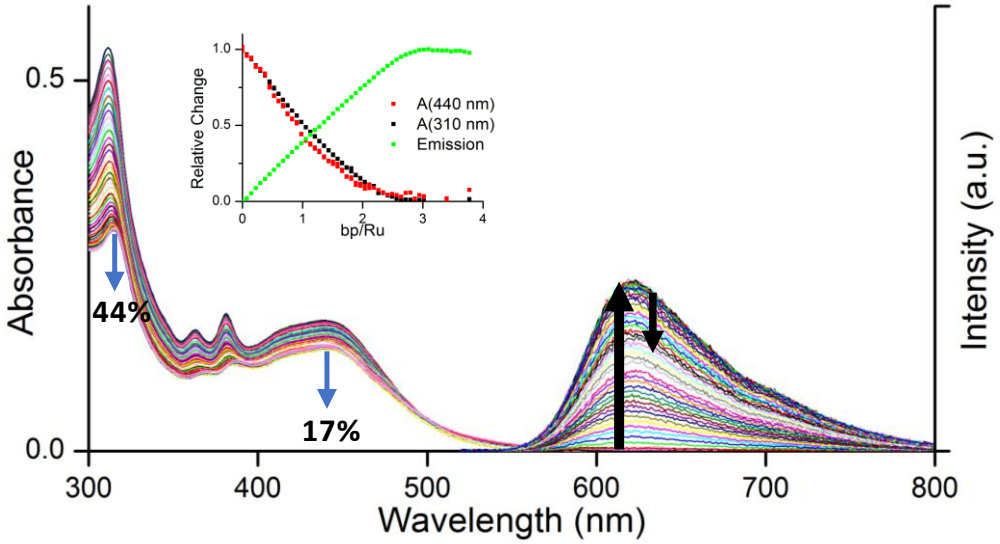

***Figure 2.13**: The changes in the UV/Vis absorption and emission spectra of **33a**·2Cl with increasing concentration of st-DNA in 10 mM aqueous sodium phosphate buffer at pH 7.4. Insets: plots of relative change in molar absorbance and emission with increasing DNA base pairs to ruthenium complex (bp/Ru) ratio.*

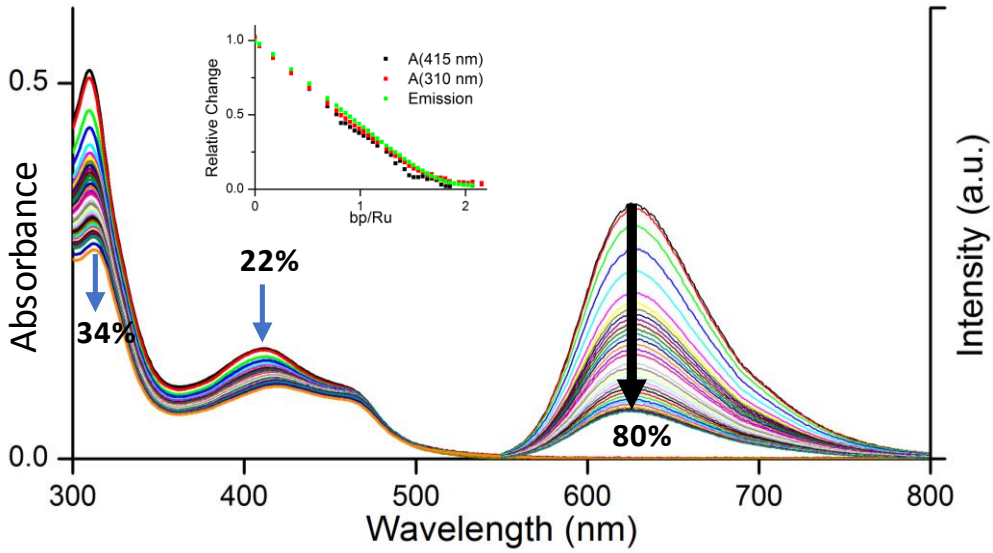

***Figure 2.14:** The changes in the UV/Vis absorption and emission spectra of **33b**·2Cl with increasing concentration of st-DNA in 10 mM aqueous sodium phosphate buffer at pH 7.4. Insets: plots of relative change in molar absorbance and emission with increasing DNA base pairs to ruthenium complex (bp/Ru) ratio.*

In contrast to the **phen** complex, the **TAP** complex at low ionic strength exhibited 80% quenching of the emission upon binding to DNA. This is a common characteristic of many $Ru(TAP)_2$ complexes since the excited state, instead of undergoing radiative decay, can photo-oxidize guanine residues in DNA resulting in an overall quenching of the emission.[52,80]

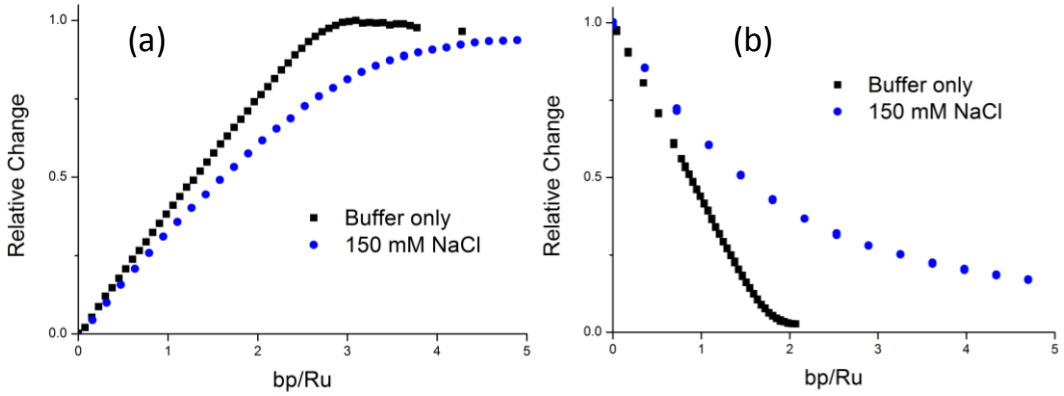

Figure 2.15: *Plots showing the changes in the emission spectra of (a)* ***33a****·2Cl and (b)* ***33b****·2Cl with increasing concentration of st-DNA at low and high ionic strength corresponding to pure buffer (10 mM sodium phosphate) and buffer with 160 mM NaCl, respectively.*

2.4 DNA Binding Interactions of $[Ru(L)_2mpdppz]^{2+}$ (33a and 33b)

2.4.1 Calculation of Binding Parameters from Spectroscopic Titrations with st-DNA

From the spectrophotometric data presented in Section 2.3, the affinities of the complexes for DNA have been quantified by calculating values for the site binding constant (*k*) and for the binding site size (*n*). This includes use of the Scatchard model, using equation (1.46), and the global fitting program ReactLab EQUILIBRIA®. The program has been used, also, to calculate the non-cooperative McGhee-von Hippel (MGVH) binding parameters. It must be kept in mind that the solution of the complex was a racemic mixture of the Δ- and Λ-enantiomers, and that the complex was bound to a heteropolymer of DNA. It was expected that a very complex binding model was needed to exactly describe the binding event. In cases where both enantiomers bind in a similar way with similar binding constants, and all binding sites on DNA have similar affinity for DNA, it would be expected that the Scatchard or the MGVH model would give a precise description of the binding event. However, it has been shown for many Ru(II) polypyridyl complexes with **dppz**-like ligands that there is a large variation for the binding constants of the two enantiomers and a strong site specificity in the binding to DNA, which means that the calculated results have to be treated with some caution. However, in all cases both models have a relatively good fit to the spectroscopic changes, which indicated that the models at least explain the data well.

Calculation of Binding Parameters from Changes in Absorbance and Emission

The parameters were calculated using the changes in the absorbance of the MLCT bands (440 nm and 412 nm for **33a** and **33b**, respectively) as well as the changes of the integrated emissions. Both the absorptions, corresponding to the MLCT bands, and the integrated emissions indicated a very strong interaction between the complexes and DNA at low ionic

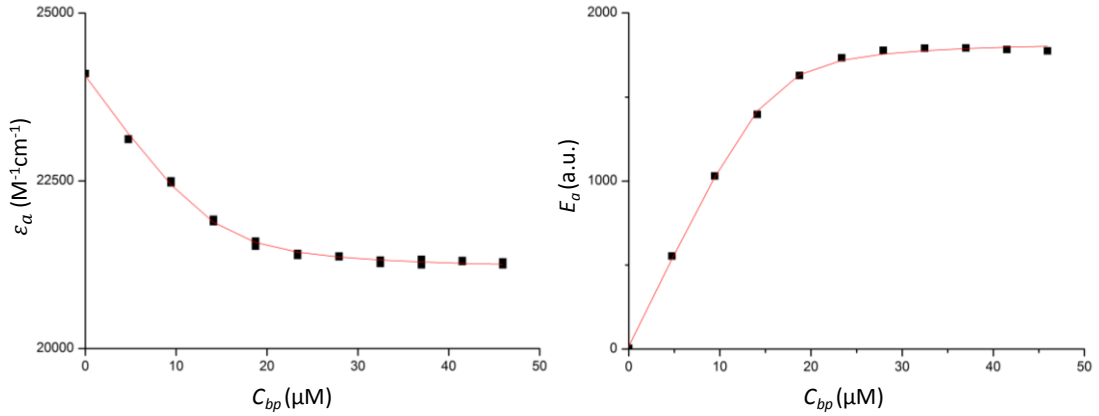

Figure 2.16: *Fits of the Scatchard binding parameters for complex* ***33a****·2Cl to absorption and emission titrations data using equation (1.46) at high ionic strength (160 mM NaCl).*

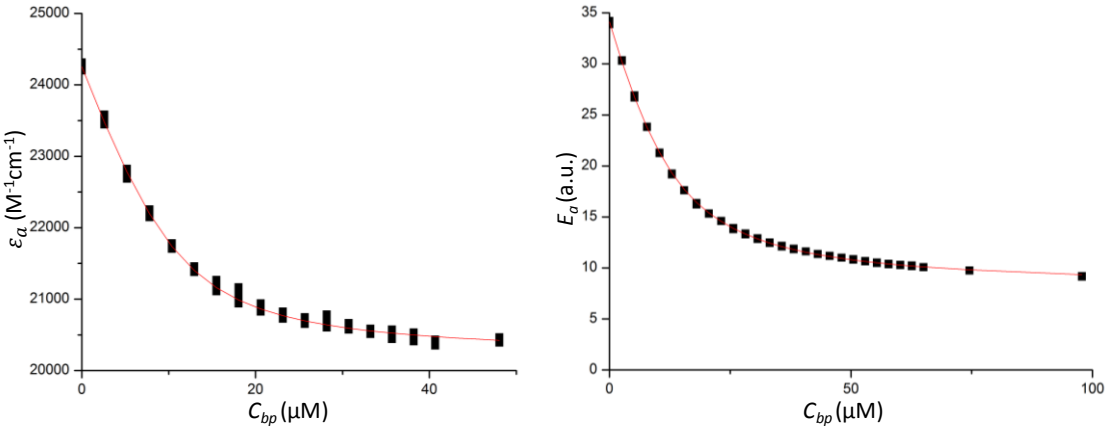

Figure 2.17: *Fit of the Scatchard binding parameters for complex* ***33b****·2Cl to absorption and emission titration data at high ionic strength (160 mM NaCl).*

strength (10 mM sodium phosphate) with binding constants of 27×10^6 M^{-1} and 42×10^6 M^{-1} for **33a** and **33b**, respectively when calculated from the emission data (Table 2.3). The data showed that values of *n* for both complexes were about two base pairs (bp). It should be noted that fitting parameters obtained for the absorbance and emission data were empirical, and the interpretations were necessarily approximate. It was assumed that the binding modes of both enantiomers were similar, that the affinities of the 16 discrete two-base-pair intercalation pockets were equal,[3] and that binding occurs only at one of the grooves. In the crystal structures reported for the binding of $[Ru(phen)_2dppz]^{2+}$ and $[Ru(TAP)_2dppz]^{2+}$ with DNA duplexes, the complex intercalates via the minor groove,[149,150] although some solution experiments indicate that entry from the major groove is possible.[151] Crystal structures have

[3] Pockets correspond to the following order of two bases sequences for one of the two complementary strand: AA, TT, CC, GG, AT, TA, CG, GC, AC, CA, AG, GA, TC, CT, TG, GC , in the order from 5' to the 3' end.

also shown that semi-intercalation of the ancillary ligand of the Λ-enantiomer was possible in the solid.[150] However, in solution, alternative binding modes were likely to be much weaker than intercalation. The work of Lincoln and co-workers has shown that the DNA binding of the enantiomers of $[Ru(phen)_2dppz]^{2+}$ (**9a**) and $[Ru(bpy)_2dppz]^{2+}$ (**9**) is complex.[45] The complexes have also shown some preference for binding to particular sequences and the enantiomers show contrasting behaviour.[152] For $[Ru(phen)_2dppz]^{2+}$, both cooperative and non-cooperative interactions have been demonstrated. Similar effects may be expected here and could be the reason for the relatively low site size recorded for the present complexes, for **33b** smaller than two.

Table 2.3: *Scatchard site binding constants (k) and site size (n) for the binding of* ***33a***·*2Cl and* ***33b***·*2Cl to st-DNA with varied ionic strength at 25 °C, calculated from emission data. The reported values and errors are the mean and standard error for all replicates. Parameters calculated from absorption data can be found in Table A2.1.*

	k **(x 10^6 M^{-1})**		***n*** **(#bp)**	
	33a	**33b**	**33a**	**33b**
Buffer only[a]	27 ± 4	42 ± 9	2.5 ± 0.1	1.8 ± 0.1
160 mM NaCl[b]	2.6 ± 0.2	0.33 ± 0.02	2.7 ± 0.1	1.6 ± 0.1

[a] 10 mM sodium phosphate buffer, pH 7.4. [b] Buffer and 160 mM NaCl.

Binding constants for the two complexes are still large in 160 mM NaCl, but they decrease by more than an order of magnitude to *ca.* 10^6 M^{-1} (Table 2.3) as a result of decreased electrostatic attraction between the positively charged complexes and the negatively charged DNA. There was no significant change in *n*, which indicated a similar binding mode under both conditions, however with a significantly weaker binding at increased ionic strength. The emission data yielded *k* for **33a** and **33b** of 2.6×10^6 M^{-1} and 0.33×10^6 M^{-1}, respectively. A concentration of 160 mM NaCl corresponded better to the ionic strength under physiological conditions, and these binding constants were a better representation of the affinity for DNA inside cells.

Global Analysis for Calculation of Binding Parameters

From the clear non-linear relation between the concentration of bound complex and the molar signal, it could not be concluded with confidence that the calculated binding parameters were accurate for **phen** complex **33a**. As described in Section 1.4.5, this problem can be handled using the program ReactLab EQUILIBRIA.

Scatchard Binding Parameters

A linear relation between emission and complex bound to DNA is only observed at high ionic strength (160 mM NaCl) as described in Section 2.3. At low ionic strength, a much more complex behaviour appears. In 10 mM sodium phosphate buffer, an initially linear increase in emission was observed followed by a steady decrease at a further increase of the DNA concentration. In pure water, an initial accelerating increase in the emission was observed followed by a steady decrease in the emission after a maximum had been reached.

Instead of using equation (1.46) to calculate the binding parameters, as was done in the last section,[54] ReactLab EQUILIBRIA was used. The observations in pure water indicate the presence of at least three different molar emissions of the complex when it is bound to DNA. The emission at high and low saturation is weak, and the strongest emission is present at intermediate saturation. To avoid over-parametrisation only one binding constant has been calculated, presuming no cooperativity, in which case all macroscopic binding constants are given from equation (1.12). This corresponds to using the Scatchard binding models to describe the binding strength; however, different molar signals for bound complex are expected for different degree of saturation. Table 2.4 shows the values of *k* and *n* obtained using ReactLab at different ionic strength, and Figure 2.18 shows the molar emission spectra ("emission quantum yield") for the ligand bound to DNA at different saturation.

Table 2.4: *Scatchard site binding constants (k) and site size (n) calculated from emission spectra using ReactLab EQUILIBRIA for the binding of* ***33a****·2Cl and* ***33b****·2Cl to st-DNA with varied ionic strength at 25 °C. The reported values are mean values, and errors are the mean standard errors for all replicates. Parameters calculated from absorption data can be found in Table 2.2.*

	k **(x 10^6 M^{-1})**		***n*** **(#bp)**	
	33a[d]	**33b[e]**	**33a[d]**	**33b[e]**
No buffer[a]	4.3 ± 0.1 ^{3eq}	n.d.	1.8 ± 0.1 ^{3eq}	n.d.
Buffer only[b]	25 ± 2 ^{2eq}	47 ± 13 ^{2eq}	2.9 ± 0.1 ^{2eq}	2.2 ± 0.1 ^{2eq}
160 mM NaCl[c]	1.4 ± 0.1 ^{2eq}	0.36 ± 0.04 ^{1eq}	3.1 ± 0.1 ^{2eq}	1.9 ± 0.1 ^{1eq}

[a] Pure deionised water; [b] 10 mM sodium phosphate buffer, pH 7.4; [c] buffer and 160 mM NaCl; ^{1eq}, ^{2eq} and ^{3eq} refer to the one, two or three equilibria, respectively, which have been used to fit the data. n.d.: not determined.

The results obtained in pure buffer and at high ionic strength (Table 2.4), differ slightly from the results obtained in the previous section (Table 2.3). It is surprising that the largest difference in the binding constants appears at high ionic strength, since this condition seemed

to give the most harmonic change in the spectrum (1.4×10^6 M^{-1} and 2.6×10^6 M^{-1} for use of integrated emission and global fitting, respectively). Evaluation of the molar signal of the bound complex at high and at low saturation reveals that the signals were very similar under both conditions, as shown Figure 2.18. This result was reproducible. The steady increase in the molar emission seen at high ionic strength was explained by the fact that the maximum degree of saturation was lower at high ionic strength for the titrations.

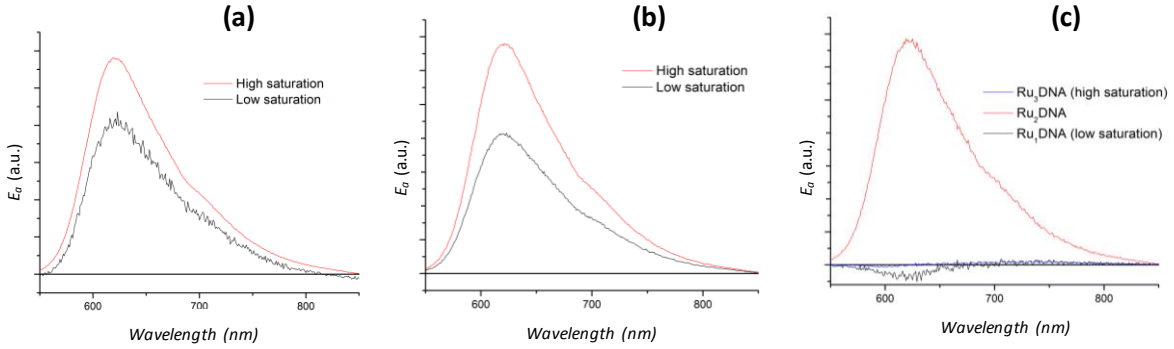

Figure 2.18: *Molar emission (E_a) of complex **33a**·2Cl bound to DNA at different degrees of saturation and calculated using ReactLab EQUILIBRIA. (a) and (b) show molar emission in 10 mM sodium phosphate buffer with or without 160 mM NaCl, fitted with two equilibria. (c) Molar emission in pure water, fitted with three equilibria.*

The difference in the emission of bound complex at different saturation in pure water is remarkable. The emission at both low and high saturation seems to be totally quenched (Figure 2.18). Besides the fact that the binding site size and binding constant are smaller than at higher ionic strength, it appears that there are differences in the binding mode of the complex. Usually, it would be expected that the binding constant increases at decreasing

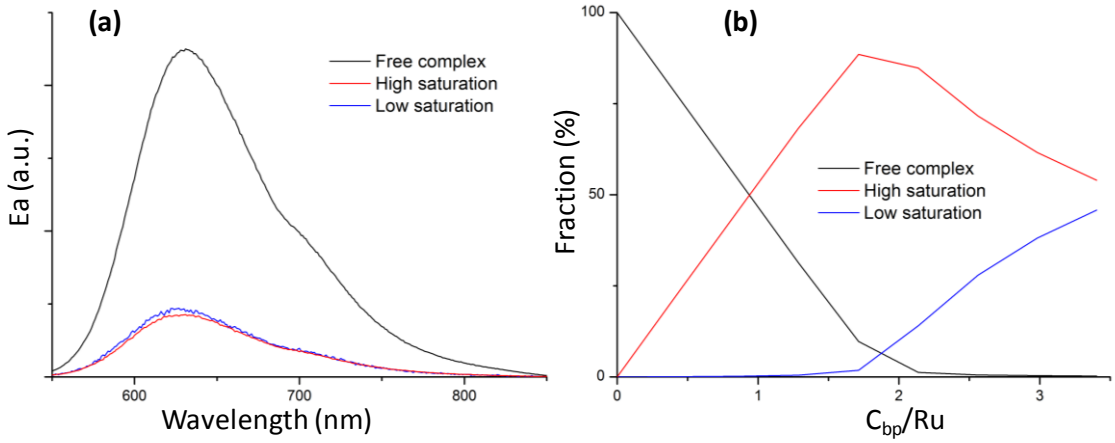

Figure 2.19: *(a) Molar emission (E_a) of complex **33b**·2Cl free in solution and bound to DNA at different degrees of saturation calculated using ReactLab EQUILIBRIA. (b) Species distribution of free and bound complex; 10 mM sodium phosphate buffer, pH 7.4.*

ionic strength, since the electrostatic attraction to DNA will increase.[18] Obviously, some reservations must be taken, since this is a racemic mixture of the complex, and a non-cooperative model is used to describe this relatively complex binding behaviour.

There is good agreement between the values of the binding parameters calculated from the relative change in the integrated emission (Table 2.3) and from a fit with ReactLab EQUILIBRIA to the change in the whole spectrum (Table 2.4) for complex **33b**. It is in accordance with similar molar signals of bound complex at different saturations. The molar signal seems to be slightly higher at low saturations. This might be explained by the fact that **33b** has a higher affinity for the intercalation pockets with AT base pairs, a binding mode that do not quench the emission. It has been demonstrated that **9b** and **31b** experience an increase in the emission upon binding to poly(dA)poly(dT).[6,80] At low saturation, the complex will preferentially bind next to AT base pairs rather than next to GC base pairs (this will be discussed further in Chapter 5 in connection with the binding of **TAP** complex **9b** to DNA). It was not possible to fit more than one equilibrium at high ionic strength. This limitation is expected to be a consequence of the relatively small binding constant, which makes it difficult to fit the molar spectrum for bound complex at high saturation.

MGVH Binding Parameters

It has also been possible to fit the data to the non-cooperative MGVH model in the way described in Chapter 1. The protocols are presented in Chapter 7. The methods to fit the cooperative MGVH model involving different spectroscopic signals were used to fit the titrations of complex **33a** in pure H_2O because of the complex triphasic changes observed in this solvent. However, in the calculations the cooperativity constant *y* was fixed as one, which corresponds to a fit in the non-cooperative MGVH model with different molar spectra for different binding modes (B_{isol}, B_{sc} and B_{dc}, *c.f.* Section 1.4.5).

The binding site sizes were, in all cases, smaller than the corresponding Scatchard site sizes (Table 2.5 and Table 2.4). This was expected because the Scatchard model assumes that all bound complexes are closely packed to the DNA lattice at saturation, while the MGVH model assumes that certain base pairs are non-occupied as the model does not allow binding of a complex in all sites (Figure 1.12). In other words, the Scatchard model counts certain base pairs as part of occupied binding sites, which are counted as unoccupied in the MGVH model. The MGVH binding constants (k_{MGVH}) were in some cases larger than the Scatchard binding constants ($k_{Scatchard}$). This was more surprising since, for k_{MGVH}, the concentration of free sites in the denominator of the defined binding constant are given as

unoccupied base pairs with the potential for acting as the start of the binding of a complex [equation (1.56)]. This will always be larger than the concentration of free sites defined in the Scatchard model; *e.g.* at zero saturation of DNA with bound complex, the concentration of unoccupied base pairs are C_{bp} and the relation between the two binding constants will be:

$$k_{Scatchard} = \frac{[B]}{[L]C_{bp}/n} = n \cdot k_{MGVH} \qquad (2.1)$$

In short terms, $k_{scatchard}$ would be *n* times the value of k_{MGVH}.

An explanation why the site binding constants were larger in some cases might be that the molar signals were fitted and that the Scatchard, the non-cooperative MGVH or both models, were imperfect, since they both are based on some very simplified assumptions of the nature of the binding. Based on the unusually small binding site size for **33b** obtained at high ionic strength using the MGVH model it is probable that the Scatchard model was better suited to describe the data for this compound.

Table 2.5: *MGVH (non-cooperative) site binding constants (k) and site size (n) calculated from emission spectra with ReactLab EQUILIBRIA for the binding of **33a** and **33b** to st-DNA with varied ionic strength at 25 °C. The reported values and errors are the mean and standard error for all replicates.*

	***k* (x 10^6 M^{-1})**		***n* (#bp)**	
	33a	**33b**	**33a**	**33b**
No buffer[a]	14	-	1.6	-
Buffer only[b]	20 ± 3	57 ± 2	2.4 ± 0.1	2.1 ± 0.7
160 mM NaCl[c]	3.4 ± 1.3	0.20 ± 0.01	2.4 ± 0.2	1.5 ± 0.1

[a] *Pure deionised water;* [b] *10 mM sodium phosphate buffer, pH 7.4;* [c] *Buffer and 160 mM NaCl.*

Binding parameters have been calculated from spectroscopic titrations with st-DNA for **mpdppz** complex **33a** ($[Ru(phen)_2mpdppz]^{2+}$) and **33b** ($[Ru(TAP)_2mpdppz]^{2+}$). It was found that both complexes bind strongly to DNA with binding constants comparable with other Ru(II) polypyridyl complexes with **dppz**-like ligands.[6,80] The *"light-switch" effect* was observed for **phen** complex **33a** as expected, with an emission enhancement upon binding to st-DNA. The opposite behaviour was observed for **TAP** complex **33b**, for which a quenching in the emission was observed upon binding to DNA, which was expected to be due to photo-oxidation of guanine in DNA.[52] The binding sites were in both cases close to 2, which were usual in case of intercalation, the expected binding mode according to what

has been found for similar complexes in the past.[6] The binding mode and binding strength will be evaluated further in the following sections with different techniques, including DNA denaturation measurements, circular and linear dichroism, and viscosity measurements.

2.4.2 Thermal Denaturation Studies

The binding of a compound to DNA can be deduced by an increase in the melting temperature (T_m) of the double stranded structure (the temperature at which 50% of the duplex has dissociated to the single stranded form). For this reason, thermal denaturation studies are useful to evaluate the ability of a compound to bind to DNA. Thermal denaturation curves of st-DNA (75 μM bp) in the presence of complexes **33a** and **33b** in 10 mM phosphate buffer and at bp/Ru ratios of 25, 10 and 5 are shown in Figure 2.20. The T_m was determined as the temperature corresponding to the steepest increase in the absorption at 260 nm; in other words, the temperature related to the maximum of the first derivative of the absorption curve. The measurements were done in triplicate to ensure reproducibility. In the absence of Ru(II) complexes, st-DNA exhibited a T_m of 69.8 °C. At bp/Ru of 25 and 10, there was a small increase in the T_m for the four complexes, as shown in Table 2.6. At bp/Ru ratio of 5, complexes **33a** and **33b** displayed an increase in T_m for st-DNA of *ca.* 6 °C in both cases, indicating stabilisation of the DNA duplex by DNA–Ru complex interactions. These values are smaller than those observed for the complex $[Ru(phen)_2dppz]^{2+}$ (ΔT_m = 9.1 °C) with calf thymus DNA (ct-DNA) at the same bp/Ru ratio, but similar to ΔT_m values determined for other Ru(II) complexes.

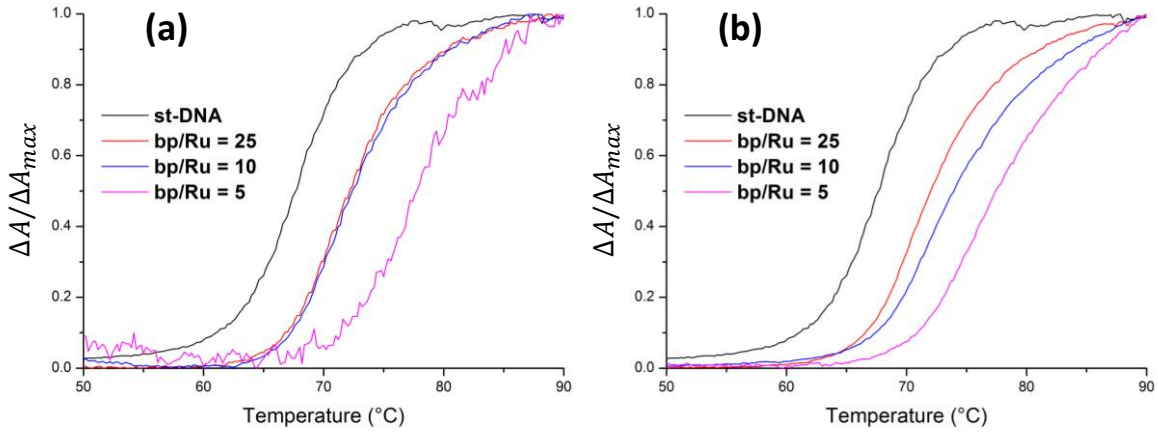

Figure 2.20: *Thermal denaturation curves of st-DNA (75 μM bp) in 10 mM aqueous sodium phosphate buffered solution at pH 7.4, in the absence and presence of* ***33a****·2Cl (a) and* ***33b****·2Cl (b) at different bp/Ru ratios.*

Table 2.6: *Melting temperature values for thermal denaturation of st-DNA (75 μM bp) in 10 mM aqueous sodium phosphate buffered solution at pH 7.4, in the absence and presence of* ***33a*** *and* ***33b****.*

ΔT_m (°C)	*bp/Ru* = 25	*bp/Ru* = 10	*bp/Ru* = 5
33a·2Cl	0.7 ± 0.1	1.2 ± 0.8	6.6 ± 1.3
33b·2Cl	0.3 ± 0.4	2.1 ± 0.1	6.3 ± 0.4

2.4.3 Circular Dichroism

Circular dichroism (CD) is a useful spectroscopic technique in the study of binding of ligands to DNA with respect to studies of the binding modes as well as studies of the conformational changes of DNA.[153,154] A CD signal for a sample is defined as the observed absorption difference between left- and right-circularly polarised light for the sample:

$$\Delta A = A_L - A_R \qquad (2.2)$$

Where ΔA is the difference in absorbance, and A_L and A_R are the absorbance of left- and right circularly polarised light, respectively. CD signals are reported in units of absorbance or ellipticity (θ), which are related by the equation:

$$\theta = \Delta A \times 32.98° \qquad (2.3)$$

Chiral molecules show intrinsic CD spectra, and the bands in these spectra occur at wavelengths corresponding to electronic transitions within the molecule. DNA is an optically active molecule as a result of the chiral sugar-phosphate backbone and its helicity. The B-DNA form exhibits a typical CD spectrum characterised by a positive band around 280 nm and a negative band around 245 nm. In addition, chiral and achiral molecules bound to DNA can possess induced CD (ICD) signals. Strong ICD signals indicate groove binding, since this will place the ligand molecule close to the chiral sugar backbone. On the other hand, intercalation will place the ligand molecules between the achiral base pairs. ICD signals are known to be an order of magnitude stronger for groove binders than for intercalators.[153]

In order to evaluate the ability of complexes **33a** and **33b** to bind to DNA, CD titrations were carried out, in triplicate to ensure reproducibility. The concentration of st-DNA was kept constant (75 μM bp), and the CD spectra were measured for different concentrations of complex corresponding to different bp/Ru ratios (Figure 2.21). In these experiments, the lowest concentration of complex used (3 μM) was much larger than the dissociation constant (*ca*. 0.05 μM), and all bp/Ru ratios used were larger than, or equal to, the largest binding site size for the complex (2.5 bp). In this range, almost all complexes in the solution were bound to DNA.

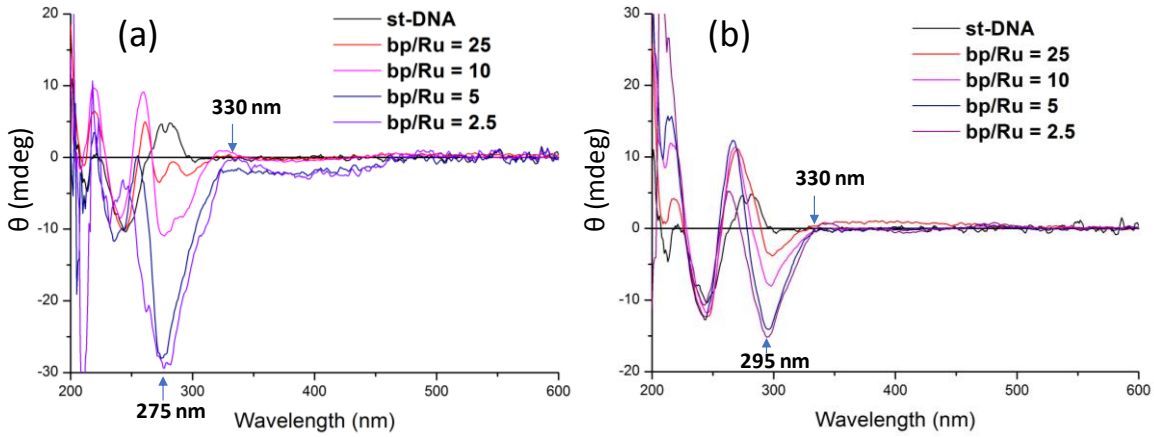

Figure 2.21: *Circular dichroism (CD) spectra of st-DNA (75 μM bp) in 10 mM sodium phosphate buffered aqueous solution at pH 7.4, in the absence and presence of* ***33a***·*2Cl (a) and* ***33b***·*2Cl (b).*

Racemic mixtures of each complex were used in the titrations, and therefore they showed no optical activity. However, the CD spectra of st-DNA, Figure 2.21, showed significant changes in the presence of complexes **33a** and **33b** at wavelengths up to 330 nm. This confirmed binding of the complexes to DNA. st-DNA does not absorb at wavelengths larger than 310 nm and changes here can be assigned to ICD signals of the complexes or differences in the spectroscopic changes of the Δ and Λ enantiomers on binding to DNA. An alternative explanation could also be that one enantiomer binds more strongly to DNA than the other, resulting in less free complex in solution for the strongest binding enantiomer. The hypochromic effect for this stronger binding enantiomer would be strongest which would contribute to the overall CD activity. However, as mentioned at the beginning of the section, the concentration of free complex in solution was so small that this can be ignored. At short wavelengths, the evolution of a strong negative band was observed with a maximum at *ca.* 275 nm for complex **33a**, and *ca.* 295 nm for complex **33b**. These bands could be attributed to π–π* intra-ligand transitions of the auxiliary **phen** and **TAP** ligands, respectively, and the strong signal indicated that the **phen** and **TAP** complexes were positioned in the grooves. This is the expected placement of the auxiliary ligands when **mpdppz** was intercalating. After the studies of the interactions of the complexes using CD spectroscopy, the orientations of the bound complexes were investigated further, by linear dichroism spectroscopy.

2.4.4 Linear Dichroism

Linear dichroism (LD) is a technique that measures the differences in the absorbance of plane polarised light in two perpendicular planes (Figure 2.22).[154] The absorbance of a chromophore in a molecule will depend on the orientation of its transition moment relative

to the orientation of the electric component of plane polarised light. The strongest absorbance will be present when these components are parallel, while the chromophore will have no absorption when they are perpendicular to each other. In flow LD, linear molecules such as DNA are aligned parallel to an axis, and the absorbance of plane polarised light is measured with its electric component parallel ($A_{\parallel}$) as well as perpendicular ($A_{\perp}$) to the axis. The LD signal is defined as the absorbance difference between the two signals:

$$LD = A_{\parallel} - A_{\perp} \tag{2.4}$$

It is often more informative to know the relative absorbance difference, which is called the reduced LD signal:

$$LD^r = \frac{A_{\parallel} - A_{\perp}}{A} = \frac{A_{\parallel} - A_{\perp}}{A_{\parallel} + A_{\perp}} \tag{2.5}$$

B-DNA itself shows a strong negative signal at 260 nm due to the absorbance of the DNA bases which are always perpendicular to the helical axes, as well as to their transition moments. LD is ideally suited to investigate the orientation of the chromophore of species bound to DNA, since the sign of the LD signal can tell if the electrical component of the plane polarised light is primarily parallel ($A_{\parallel} > A_{\perp}$, positive signal) or perpendicular ($A_{\parallel} < A_{\perp}$, negative signal) to the DNA helix. Positive or negative signals will indicate groove binding or intercalation of the chromophore, respectively. Weak LD signals indicate many possible orientations of the chromophore, which is typical of electrostatic association to DNA.

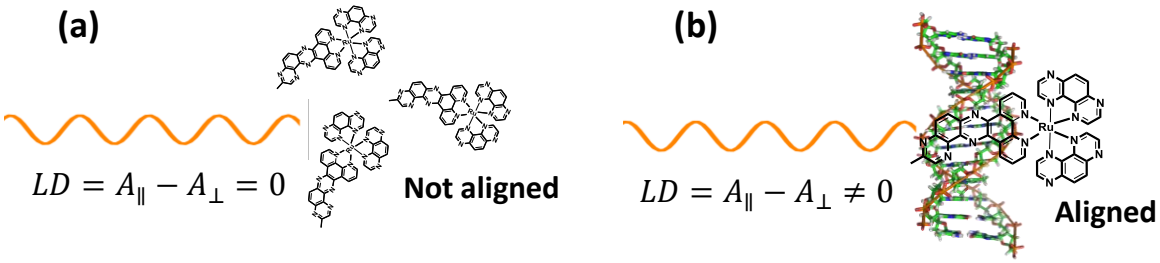

Figure 2.22: *Schematic representation of a flow LD experiment. (a) Complexes in solution. The complexes are not aligned. (b) A complex that has become aligned by the binding to a DNA helix that is orientated in a flow.*

The LD studies were carried out in a manner similar to the CD titrations, by keeping the concentration of st-DNA constant (200 μM bp) while varying the concentration of complexes **33a** and **33b** (Figure 2.23). As for CD it could be presumed that almost all of the complex in solution was bound to DNA. The st-DNA alone has the typical negative LD signal at *ca*. 260 nm. At increasing concentration of complex a large change was observed in the LD spectrum, also at wavelengths larger than 310 nm. Since this range was outside

the range for the absorbance of DNA, these changes were assigned to absorption of the complexes. For both **33a** and **33b**, the LD signal at *ca*. 310 nm was negative, corresponding to the intra-ligand transition in **mpdppz**. This result tells that **mpdppz** is perpendicular to the DNA helix ($A_{\perp} > A_{\parallel}$) and confirms that the complexes bind to DNA through intercalation by this part of the molecule. Strong LD signals were also observed in the MLCT region of the spectra above 400 nm. For **33a**, a positive LD signal was observed at *ca*. 400 nm and a negative signal at *ca*. 500 nm. The negative signal at 500 nm corresponds to the region where the MLCT transition from the Ru(II) centre to **mpdppz** absorb, which would be perpendicular to DNA in case of intercalation. On the other hand, the positive signal at *ca*. 400 nm could be due to an MLCT signal from the metal centre to **phen**, which would be more parallel with the DNA duplex in case of intercalation, since it will be placed in the groove. Overlap with this positive band may also explain why the negative band had a minimum at *ca*. 500 nm, which was more redshifted than the maximum for the MLCT band in the absorption spectrum at 440 nm. The presence of a positive band at *ca*. 475 nm for complex **33b** can also be explained by the known MLCT transition of Ru(II) to the ancillary **TAP** ligands for similar complexes.[80] The reason why the maximum for the signal was at 475 nm and not at 412 nm, as was the maximum for the MLCT band in the absorption spectrum, can be explained by overlap with the negative band for the π-π* intra-ligand transition of **dppz** at 310 nm. The obtained spectra were similar to those obtained for the structurally similar complexes **31a** and **31b** by Elmes *et al*.[6]

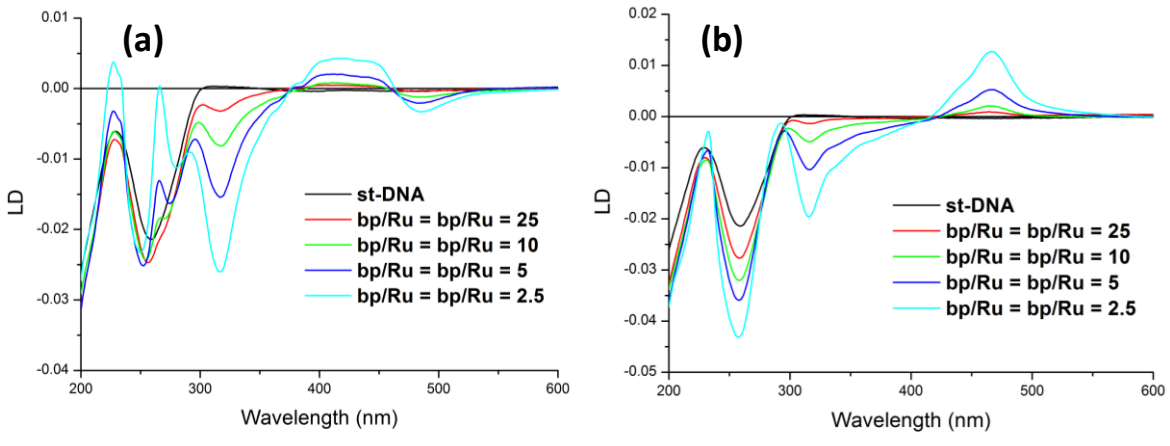

Figure 2.23: *Linear dichroism (LD) spectra of st-DNA (200 μM bp) in 10 mM sodium phosphate buffered aqueous solution at pH 7.4, in the absence and presence of* ***33a***·*2Cl (a) and* ***33b***·*2Cl (b) at different bp/Ru ratios.*

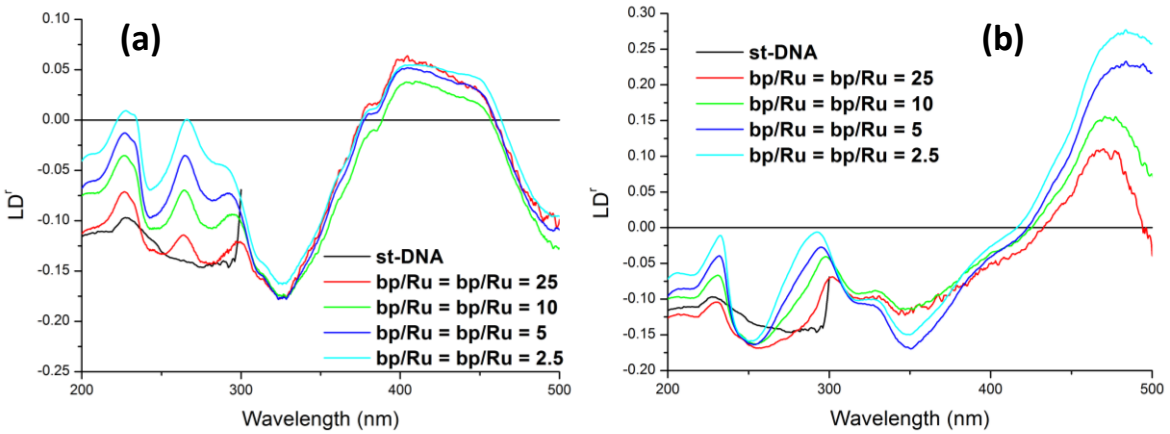

Figure 2.24: *Reduced linear dichroism (LD^r) spectra of st-DNA (200 μM bp) in 10 mM sodium phosphate buffered aqueous solution at pH 7.4, in the absence and presence of (a)* ***33a***·*2Cl and (b)* ***33b***·*2Cl at different bp/Ru ratios. LD^r signals from 500 nm are not included due to low absorption.*

2.4.5 Viscosity Measurements

All experiments have so far supported that both complexes under investigation bind to DNA through intercalation, which is also the expected binding mode according to literature precedence. To confirm further this binding mode, the viscosity (η) of a solution of st-DNA at increasing concentration of the complexes and using a capillary u-tube viscometer was measured in collaboration with Dr Salvador Blasco. DNA was sonicated before the experiment to "cut" it into sequences of approximately 200 bps. DNA sequences up to this length can be considered as rigid rods. An intercalator will elongate the DNA when it inserts between the base pairs. The viscosity increases with increasing length of DNA, thus making a large increase in the viscosity at increasing concentration of bound complex ([B]) a strong indication of intercalation. A linear relation between $(\eta/\eta_0)^{1/3}$ (η_0 = viscosity without complex) and the degree of saturation of DNA (r = [B]/[bp]) is usually considered to be a strong proof of intercalation.[155] As shown in Figure 2.25, both complexes displayed linear behaviour with a strong increase of the viscosity accompanied by an increasing saturation of DNA with bound complex, and with a slope similar to what has been observed for the known intercalator ethidium bromide in the past (0.91).[156] The linearity slopes are very similar for **33a** (0.80) and **33b** (0.79), indicating that the two complexes result in similar elongations of DNA and affect the structure of the duplex in a similar manner upon intercalation.

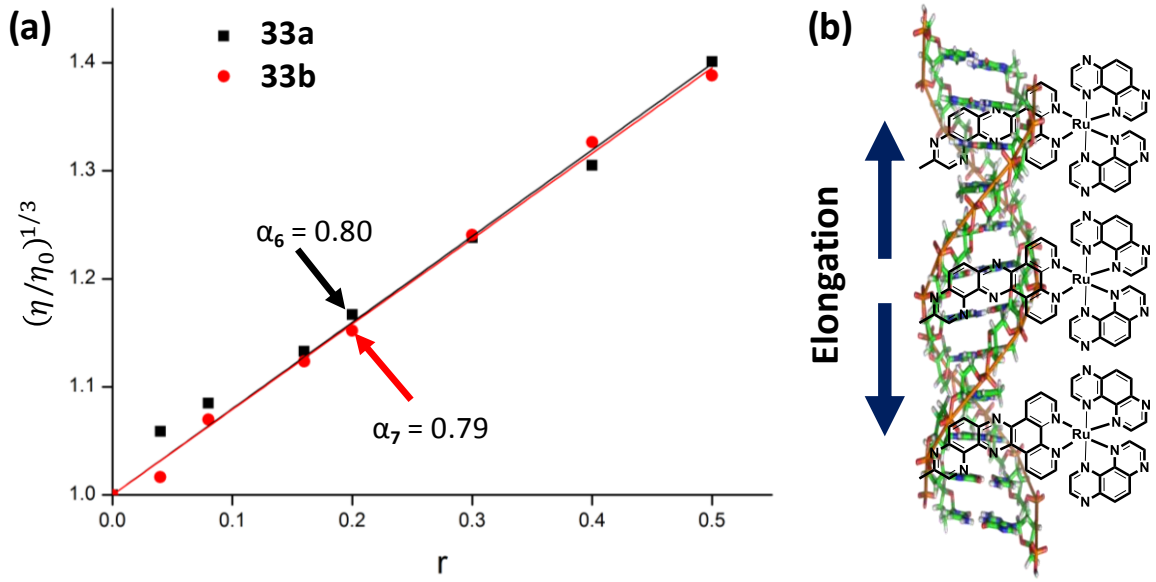

Figure 2.25: *(a) The change in the third root of the relative viscosity at increasing saturation of st-DNA (0.6 mM bp) with complex **33a**·2Cl and **33b**·2Cl in 10 mM sodium phosphate buffered aqueous solution, pH 7.4, 25 °C. (b) Representation of elongation of DNA upon intercalation.*

2.4.6 Conclusion and Future Perspectives

Herein, the syntheses and characterisation of two new Ru(II) polypyridyl complexes, based on the new ligand **mpdppz**, with potential as phototherapeutic or imaging agents have been detailed. Both complexes showed a relatively strong emission in CH_3CN with luminescence quantum yields at 1.8% and 2.4% for the complex with **phen** (**33a**) and **TAP** (**33b**) as ancillary ligands, respectively. Complex **33b** was emissive in water while **33a** was non-emissive.[6] A crystal structure of **33b** was obtained by X-ray crystallography. In contrast to the structure calculated with DFT geometry optimisation, the solid state structure showed a bending of the **mpdppz** moiety. This was explained by packing interactions between neighbouring complexes.

The DNA binding interactions of the Ru(II) polypyridyl complexes **33a** and **33b**, with the extended **dppz**-like ligand **mpdppz** were evaluated. It was confirmed that the complexes show a similar modulation of the photophysical properties in solution as previously reported for **dppz** and **pdppz** complexes. The **phen** complex **33a** showed the well-known light switch effect. In aqueous media, it was non-emissive, however, upon binding to DNA it became emissive, which makes the complex a potential candidate as a luminescent stain for imaging of DNA. **TAP** complex **33b**, on the other hand, showed the inverse light switch effect with a quenching of the emission upon binding to DNA. As described in Chapter 1, this behaviour for similar **TAP** complexes was assigned to photo-induced oxidation of guanine, an expected

mechanism of action for the photo-cleavage of DNA by this type of complex after light activation, and accompanied by the induction of apoptosis in cancer cells (*c.f.* Section 4.2).

The methods introduced in Chapter 1 for the study of multivalent binding were used to calculate the Scatchard and the non-cooperative MGVH binding parameters for the two complexes under investigation. Global fitting with ReactLab EQUILIBRIA gave high values of the binding constants. The Scatchard binding constants were 25×10^6 M^{-1} and 47×10^6 M^{-1} when measured in 10 mM sodium phosphate buffer for complex **33a** and **33b**, respectively. These binding constants were higher than the values reported in the past for the corresponding **phen** complex **31a** (12×10^6 M^{-1}) and **TAP** complex **31b** (5.4×10^6 M^{-1}) using a similar method. The binding constants when measured in 160 mM NaCl were more than an order of magnitude lower, indicating that there is a significant electrostatic contribution to the binding energy. A strong binding to DNA was confirmed with DNA melting experiments. With a Ru/bp ratio of 5, an increase of the denaturation point of *ca*. 6.5 °C was found for both **33a** and **33b**.

The Scatchard binding site size was found to be larger than two base pairs at both low and high ionic strength. This is typical of an intercalator. The indication that intercalation was actually the binding mode was confirmed further using CD and LD spectroscopy. These experiments yielded spectroscopic features characteristic of intercalation. The strongest confirmation of intercalation was obtained through viscosity measurements that showed a high increase in the viscosity of a solution of DNA at increasing concentration of bound complex.

The strong binding to DNA of the two Ru(II) polypyridyl complexes and the concomitant photophysical modulation show great potential for use of these or similar complexes as DNA imaging probes or sensors. In the next section, the complexes will be evaluated in cellular studies, including evaluation of whether the compounds enter the nuclei of cells, which is the primary target for a DNA binding agent at the cellular level. The new methods for fitting binding constants have much broader applicability than demonstrated in this chapter; in Chapter 5 they will be used to treat other systems and to calculate cooperativity constants.

With the scope of preparing functionalised gold nanoparticles (AuNPs) with some of the same functionalities as those observed for **dppz** complexes, oxidation of the methyl group in **mpdppz** to a carboxylic acid was carried out using permanganate as oxidising agent. The intention was to explore the possible use of this part of the molecule as a handle

for the attachment to AuNPs as well as to other interesting molecular systems. However, a yield of only 7% was achieved. Several other attempts were tried including use of other oxidising agents and alternative synthetic strategies or routes for attachment of an aliphatic chain. All attempts failed and it was expected that the use of **mpdppz** was not a good starting point for the functionalisation of AuNPs. In Chapter 6, functionalisation will be described using alternative bipyridine derivatives as linker for attachment to the surface of AuNPs.

In summary, new Ru(II) polypyridyl complexes with an apparently higher binding constant for DNA than structurally similar complexes have been synthesised and characterised with different spectroscopic techniques. The interactions with DNA have been studied with absorption, emission, CD and LD spectroscopy. A large increase in the DNA denaturation point indicated a strong stabilisation of the DNA duplex upon binding of the complexes. It was confirmed with viscosity measurements that complexes bind to DNA through intercalation. New methods to calculate binding parameters from spectroscopic titrations more accurately than with current practice have been introduced, including the use of the global fitting. In Chapter 4, cellular studies will be carried out in order to evaluate the cellular uptake and the possible application of the compounds in PDT treatment of cancer and in cellular imaging. Chapter 6 shows alternative ways to functionalise gold nanoparticles with Ru(II) polypyridyl complexes, ways that do not involve **mpdppz** as bridging ligand.

Chapter 3

Synthesis and Characterisation of phendione Derived Compounds

3.1 Introduction

In addition to being an important precursor for the synthesis of many **dppz**-like ligands, **phendione** itself has a high toxicity in several cancer cell lines, with IC_{50} values in the sub micromolar range (*e.g.* 0.4 μM for CHANG cancer cells),[157] and similar toxicities have been observed for many metal complexes with **phendione** as ligands.[157,158] Like the **pdppz** complex **31b**, some **phendione** metal complexes, including the ruthenium complex **45a**, are able to photo-cleave DNA upon light activation, making PDT a potential application for this class of compounds.[159] In this chapter the synthesis and photophysical characterisation of **phendione** based compounds are described. In next chapter biological evaluation of the **phendione** compounds will be carried out together with evaluation of **mpdppz** complexes **33a** and **33b**.

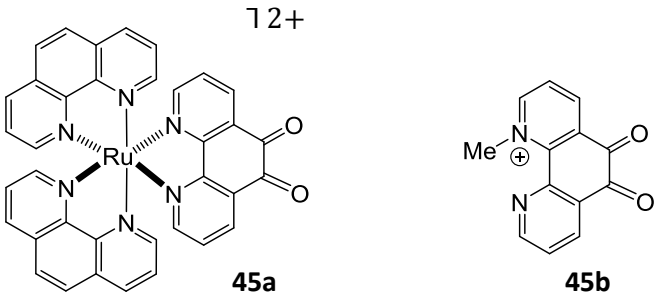

***Figure 3.1: phendione** based compounds, which have been evaluated for biological applications.*

3.2 Synthesis and Characterisation of phendione Based Compounds

In the following section, the syntheses and characterisation will be described for complex [Ru(phen)$_2$phendione] (**45a**) and for the methyl alkylated **phendione** (**45b**).

3.2.1 Synthesis of [Ru(phen)$_2$phendione]$^{2+}$ (45a)

The **phendione** complex was synthesised in a similar manner as reported in the literature (Scheme 2.10).[44,164,165] [Ru(phen)$_2$Cl$_2$] (**44a**) and **phendione** were suspended in a mixture of ethanol and H_2O and heated under microwave irradiation. Subsequently, the complex was precipitated as the PF_6-salt. The precipitate was isolated by centrifugation and purified by recrystallisation by dissolving the compounds in CH_3CN followed by slow addition of diethyl ether. The solid was isolated by centrifugation, and the complex was converted to the chloride form by ion exchange with Cl-resin in methanol. The structure of the complex was confirmed with NMR spectroscopy and HRMS. HRMS of **phen** complex **45a** both showed a peak corresponding to the molecular ion, and to the molecular ion plus water (Figure 3.2). This indicated the presence of a hydrated form of the molecule.

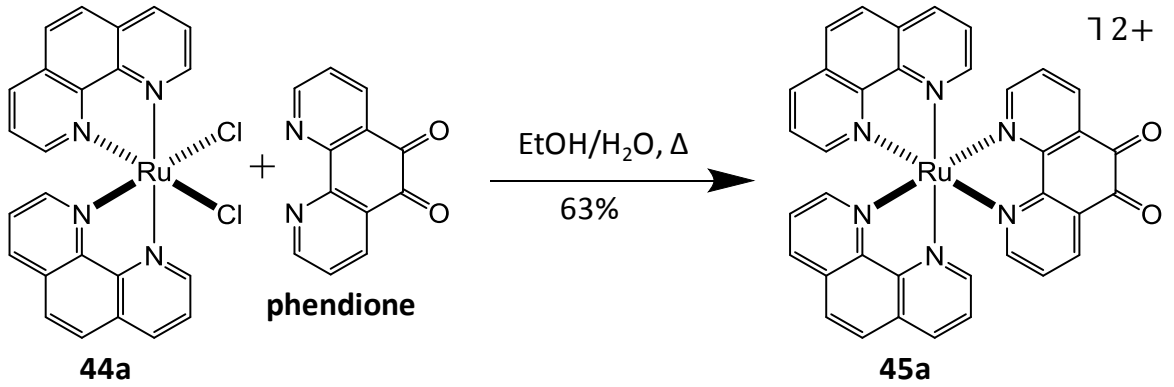

Scheme 3.1: *Syntheses of Ru(II) polypyridyl complex* ***45a*** *with* ***phendione*** *and* ***phen*** *as ligands. H_2O/EtOH, 140 °C, microwave irradiation, 30 min.*

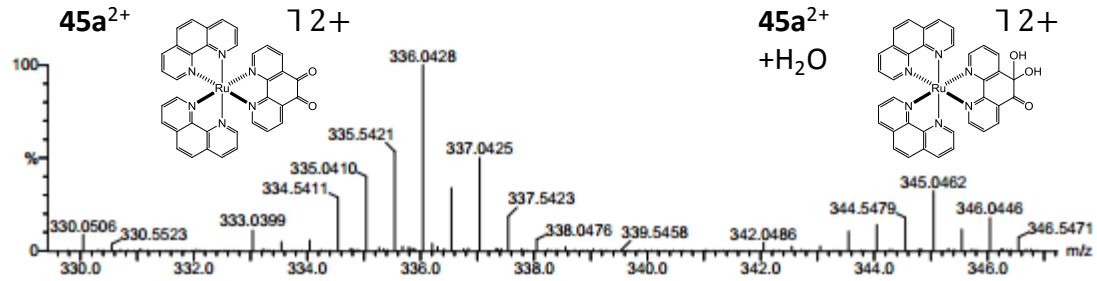

Figure 3.2: *HRMS (ESI) spectrum of compound* ***45a*** *in CH_3CN.*

This may also explain why very complex ^{1}H NMR spectra (400 MHz) were obtained for **45a**, as shown in Figure 3.3. The spectrum in standard grade CD_3CN (non-dry) indicated the presence of several species according to the values of the integrals of the peaks that did not fit the target molecule. Purity was confirmed by elemenetal analysis, and thus the observation of additional NMR peaks could be assigned to the presence of hydrated forms of the complex, as observed with HRMS. This was confirmed further by large changes observed in the NMR spectra when the amount of water was increased, in accordance with a change in the equilibrium between the hydrated and non-hydrated forms of the complex. The ^{1}H NMR spectrum for the complex in D_2O was very noisy, and had broad peaks indicating medium-fast exchange between the hydrated and non-hydrated forms.

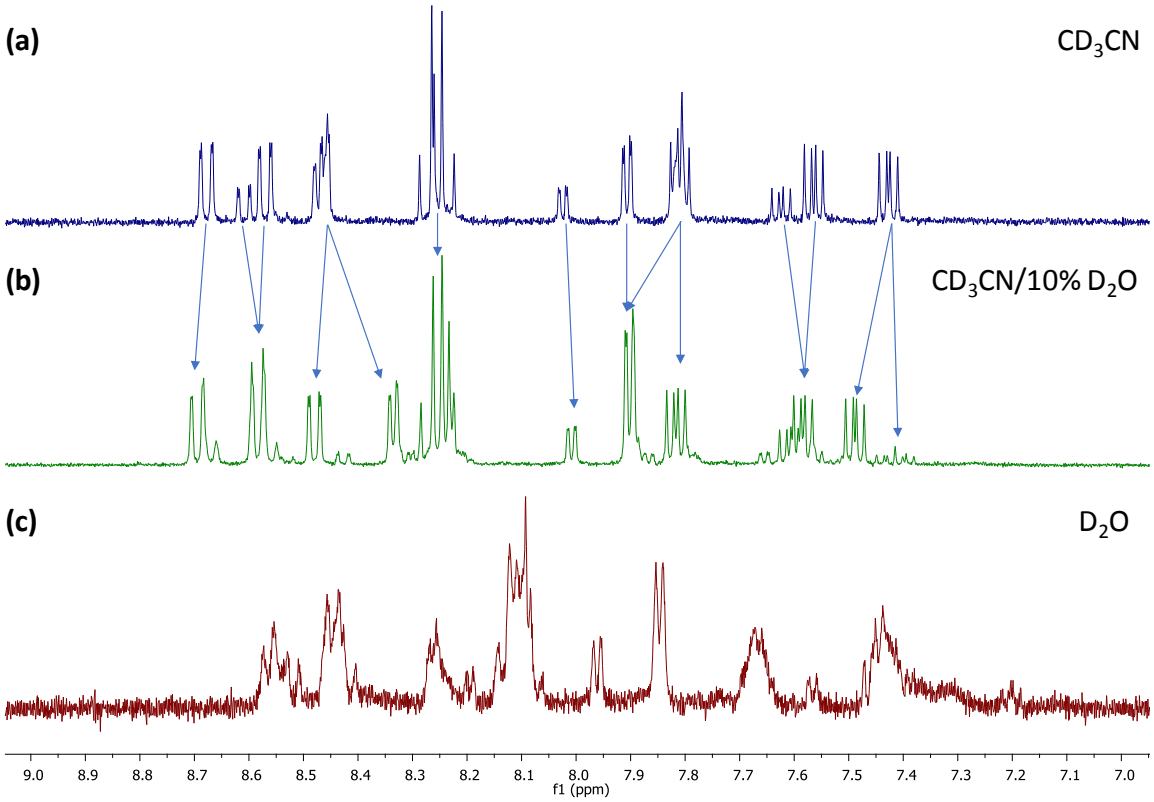

Figure 3.3: *^{1}H NMR (400 MHz) spectrum of complex **45a**·2Cl in different solvents: (a) CD_3CN, (b) CD_3CN with ca. 10% D_2O and (c) D_2O.*

3.2.2 Synthesis of *N*-methyl-1,8-phen-5,6-dionium iodide (45b)

N-Methylated **phendione** (**45b**)[166] was synthesised using a procedure similar to that reported for methylated 1,10-phenanthroline.[167] Methyl iodide was added to a suspension of **phendione** in CH_3CN. The mixture was heated to 80 °C in a sealed microwave vessel. The mixture was stirred for 24 hours in the dark. A very dark precipitate was isolated by centrifugation and washed with CH_3CN and acetone, giving the product as a dark red solid in a yield of 72%. The structure of the compound was confirmed with NMR spectroscopy and HRMS. The ^{1}H NMR (400 MHz, DMSO-d_6) spectra exhibited more peaks than would be expected, with some very broad peaks in the aromatic region (Figure 3.4). Six signals corresponding to methyl were present, indicating the presence of a number of species in solution. Purity was confirmed by elemental analysis, and thus the observation of additional NMR peaks could be assigned to the presence of hydrated forms or dimerised form of the compound. It has been reported in the past that the compound can be hydrated.[168] HRMS confirms that similar behaviour was present in methanol as the observations obtained for **45a** (Figure 3.2), where methanol binds to the carbonyl carbons (Figure 3.5).

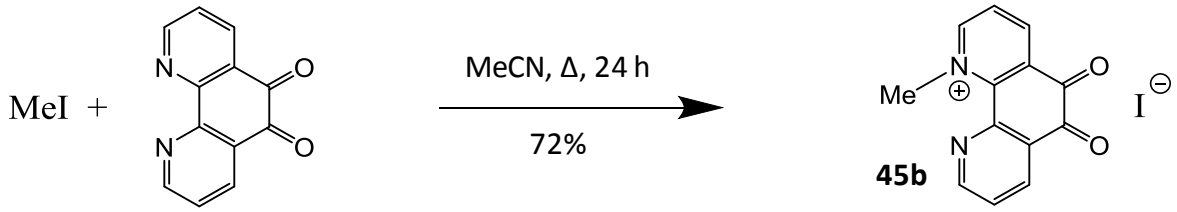

Scheme 3.2: *Synthesis of N-methyl-1,10-phenanthroline-5,6-dionium iodide (**45b**·I) from **phendione** and methyl iodide.*

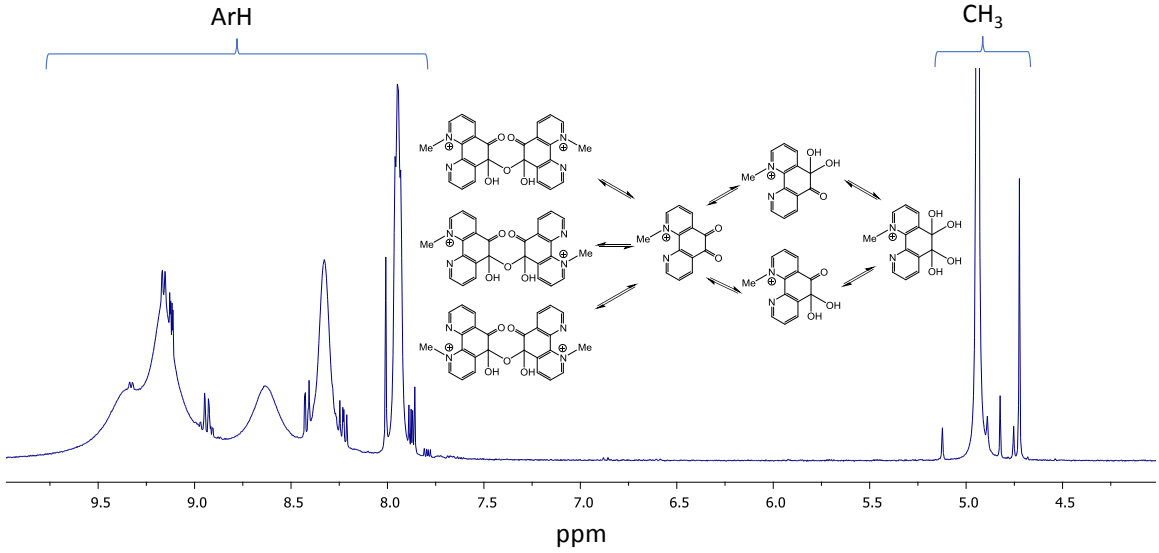

Figure 3.4: *^{1}H NMR (400 MHz, DMSO-d_6, non-anhydrous) spectrum of compound **45b**·I with its hydrated and dimeric forms.*

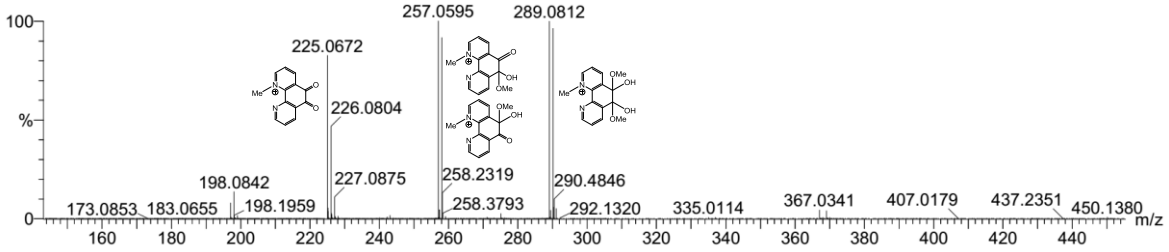

Figure 3.5: *HRMS (ESI) spectrum of compound **45b** in MeOH.*

Several attempts have been made to synthesise other alkylated versions of **phendione**. These trials, which all failed, are shown in Scheme 3.3. The compounds were expected to have a variety of properties that would make them suitable for treatment of cancer; *e.g.*, it was expected that the attachment of a long aliphatic chain (Scheme 3.3a) would improve the cellular uptake by increasing the affinity of the **phendione** for the hydrophobic cell-membrane. It was also likely that a diquaternerised compound (Scheme 3.3b) would be readily taken up by cells because of the dicationic nature of the compound that makes it suitable to be taken up by cells as a consequence of the negative membrane potential of

cells.[133] The purpose of connecting two phendiones (Scheme 3.3c) was to decrease the stability of the compounds at physiological pH by enabling **phendione** to react with itself. **phendione** is unstable under basic conditions, and the intention was to further decrease the stability to make the compound unstable under neutral conditions. Cancer tumours are acidic and expected to act as a stabilising environment, making the compound more toxic in the tumour than in the rest of the body, where it will quickly decompose.

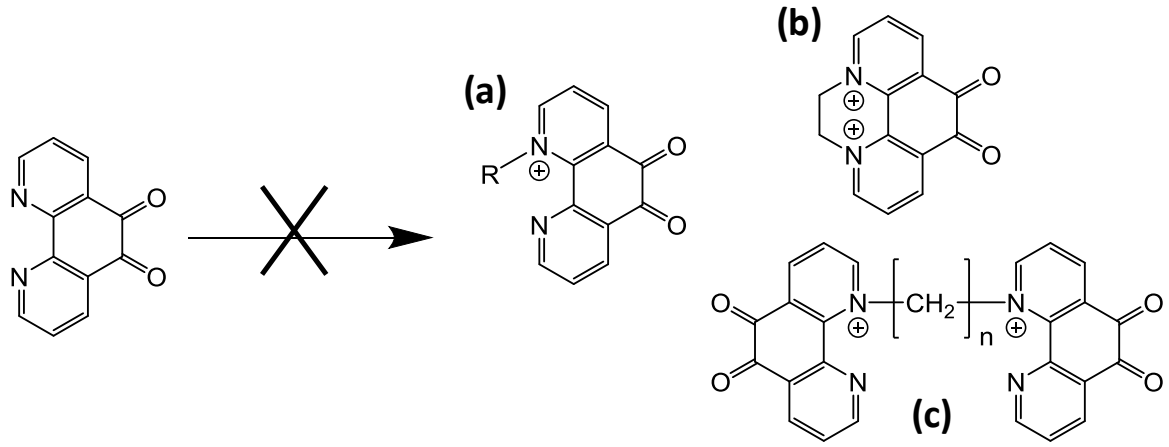

Scheme 3.3: *Attempts to alkylate* ***phendione*** *with different alkylation agents: (a)* $Br(CH_2)_{16}H$, $Br(CH_2)_{10}COOCH_3$ *or* ICH_2COOH. *(b)* $BrCH_2CH_2Br$ *or* ICH_2CH_2I. *(c)* $Br(CH_2)_nBr$ *(n = 2, 4, 6, 10 or 12). A variety of reaction conditions have been used including those used for the synthesis of* ***45b****.*

In the unsuccessful syntheses alkyl bromides or iodides have been used under a variety of reaction conditions, including different solvents, temperatures, and reaction times. Apparently, the reaction conditions for the synthesis of **45b** were an exception under which **phendione** can be *N*-alkylated. It is likely that part of the explanation for the common low success rate was due to the high instability of *N*-alkylated phendiones. The **phendione** group contains four electronegative atoms including two oxygen atoms making the compound very electron deficient.[164,169] Quaternerisation of one or both nitrogen atoms will make the compound even more electron deficient, by introducing a positive charge on the molecule.[170] This may destabilise the molecule by weakening the bonds, and activating the molecule to a variety of redox reactions.

3.2.3 Photophysical Characterisation of phendione Based Compounds

The photophysical properties of the complex $[Ru(phen)_2phendione]Cl_2$ (**45a**) were studied in H_2O. The absorption and emission spectra of the complex were very similar to spectra obtained for the complex in the literature under similar conditions. The absorption spectrum

for **45a** had some similarity with **phen** complex **33a**, with an absorption band with maximum at 40 nm. Bands at 222 nm and 262 nm were characteristic of π-π* intra-ligand transitions of the ancillary **phen** ligands. A shoulder at *ca*. 300 nm might correspond to π-π* intra ligand transition for **phendione**. Complex **45a** was emissive with an emission maximum at *ca*. 620 nm, like complex **33a** (λ_{exc} = 440 nm).

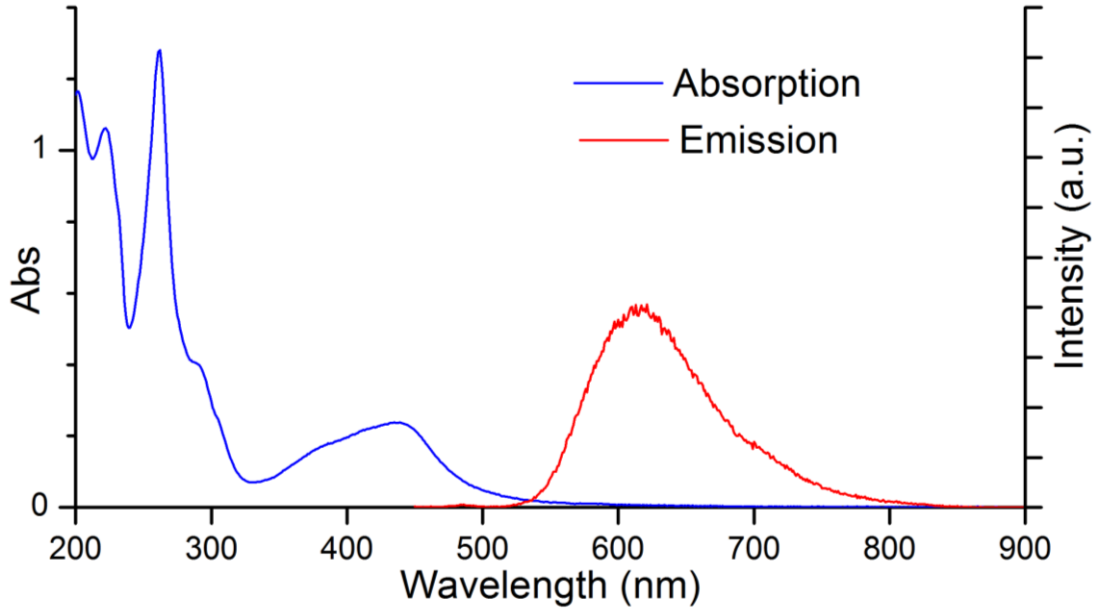

Figure 3.6: *Absorption and emission spectra of complex* ***45a****·2Cl in water. Excitation wavelength for the emission spectra was 440 nm.*

The absorption spectrum of the methylated **phendione** was very different from the spectrum for **phendione** itself. The unmodified **phendione** had a very strong absorption profile in the UV region, with intense absorption bands at 254 and 294 nm, and with weak absorption in the visible region. Both bands may correspond to π-π* transition in **phendione** in accordance with similar absorption maxima for corresponding transitions in many Ru(II) polypyridyl complexes.[9,44,171] Compound **45b** was a dark powder in the solid state, but when dissolved in water the compound became colourless with no absorption observed in the visible region. This might be a result of the formation of the hydrated form in solution, which will remove the planarity of the fused ring system and disrupt the conjugation of the π-electrons. Because of the lack of absorption in the visible region the compound has not been evaluated with respect to photochemotherapy or studied with confocal microscopy, as done for complex **45a**. Compound **45b** and **phendione** did not show any emission upon excitation at any of the mentioned absorption maxima.

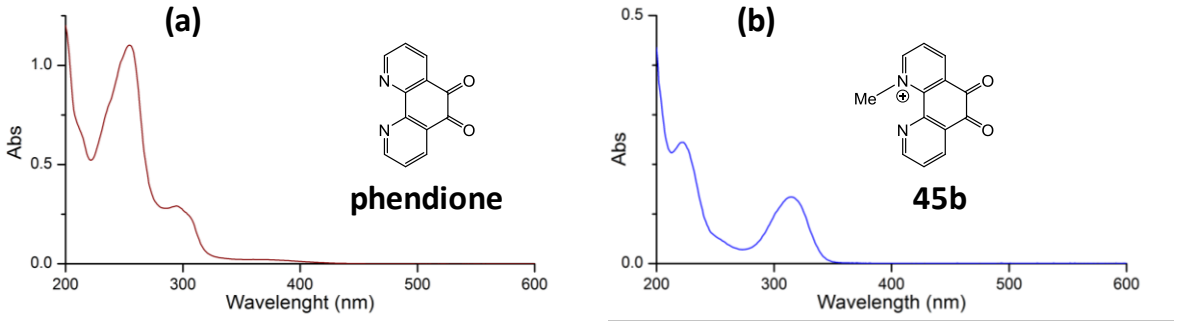

Figure 3.7: *Absorption spectra of* ***phendione*** *(a) and* ***45b***·*I (b) in water.*

3.2.4 Geometry Optimised Structures of phendione Based Compounds in Water

The equilibrium structures of the synthesised **phendione** compounds in water are shown in Figure 3.8. The geometry optimised structures have been calculated with the same computational methods described in Section 2.2.3. Without modification, **phendione** forms a planar ring system in the two ruthenium complexes, as also seen for **phendione**, as a free ligand. However, this regularity disappeared in compound **45b**, for which a non-planar ring system was observed. This indicated that the ring system was destabilised with less conjugation after *N*-alkylation, which may explain the difficulties in the synthesis of this type of molecules.

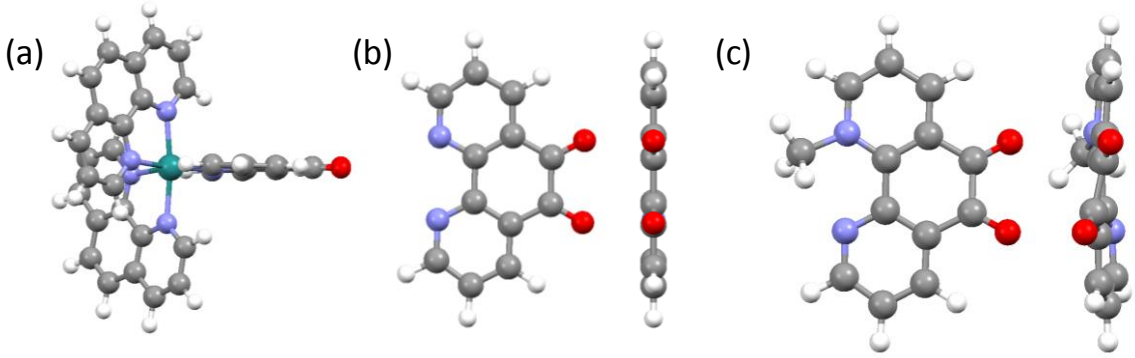

Figure 3.8: *Equilibrium structures in water of (a)* ***45a****, (b)* ***phendione*** *and (c)* ***45b****, calculated with DFT (M06/6-311G(d,p) and LANL2DZ, SMD).*

3.3 Conclusion and Future Perspectives

Herein, the syntheses and characterisation of compounds derived from **phendione**, with potential as phototherapeutic agents have been detailed. In the next chapter the biological properties of the compounds will be evaluated.

Chapter 4

Ru(II) Complexes and Tröger's Bases for Cellular Imaging and as Anti-Cancer Agents

4.1 Introduction

In Chapter 2, the affinity of complexes **33a** and **33b** for DNA was investigated, as well as how the photophysical properties of these complexes were modulated upon DNA binding. In this chapter, an investigation into the biological activity of these compounds will be conducted, with particular focus on applications as anti-cancer agents and in cellular imaging. Confocal microscopy has been used to probe the cellular uptake and the localisation of the compounds within cells to elucidate the potential of applying these compounds in the imaging of live-cells. Furthermore, toxicity studies with HeLa cervical cancer cells have been carried out to investigate the photo-toxicity of the compounds with the purpose of evaluating their potential to be used in photochemotherapy. Singlet oxygen photosensitisation studies have been carried out by Sandra Estalayo-Adrián to evaluate whether the ability of these complexes to generate singlet oxygen is correlated with the observed photo-toxicities.

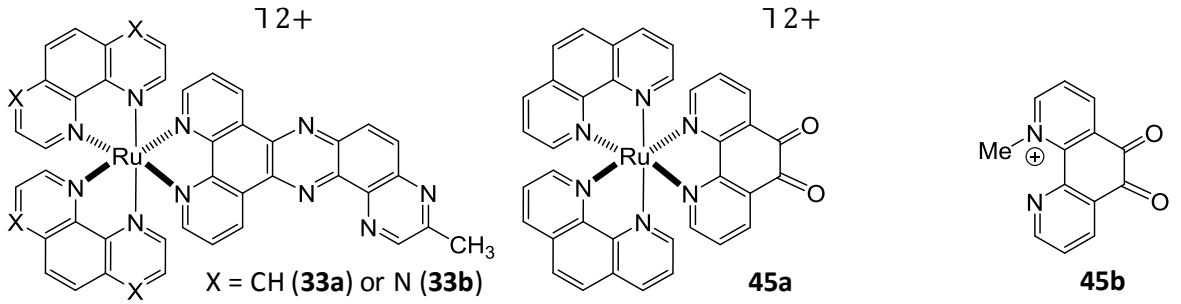

Figure 4.1: *Polypyridyl compounds, which have been evaluated for various biological applications.*

Similar studies were carried out for the **phendione** compounds **45a** and **45b**. In addition to being an important precursor for the synthesis of many **dppz**-like ligands, **phendione** itself has a high toxicity in several cancer cell lines, with IC_{50} values in the sub micromolar range (*e.g.* 0.4 μM for CHANG cancer cells),[157] and similar toxicities have been observed for many metal complexes with **phendione** as ligands.[157,158] Like the **pdppz** complex **31b**, some **phendione** metal complexes, including the ruthenium complex **45a**, are able to photo-cleave DNA upon light activation, making PDT a potential application for this class of compounds.[159]

Lately, the biological activity of a series of new naphthalimide-based Tröger's bases, synthesised by Dr Sankarasekaran Shanmugaraju and Mr Tobi Arisa from the Gunnlaugsson group, has been evaluated. Confocal luminescence microscopy was undertaken to obtain

insight into their cellular uptake and localisation in cells, and their potential application as cellular imaging agents. The cytotoxicity towards cancer cells was also determined to evaluate the use of these compounds as anti-cancer agents. The photo-toxicity of Ru(II) compounds containing naphthalimide-based Tröger's bases and curcumin ligands have been measured in order to evaluate the use in photochemotherapy. Curcumin is known to have increased toxicity upon light activation,[160-162] and similar properties have been demonstrated for many naphthalimides[163] and ruthenium complexes[6].

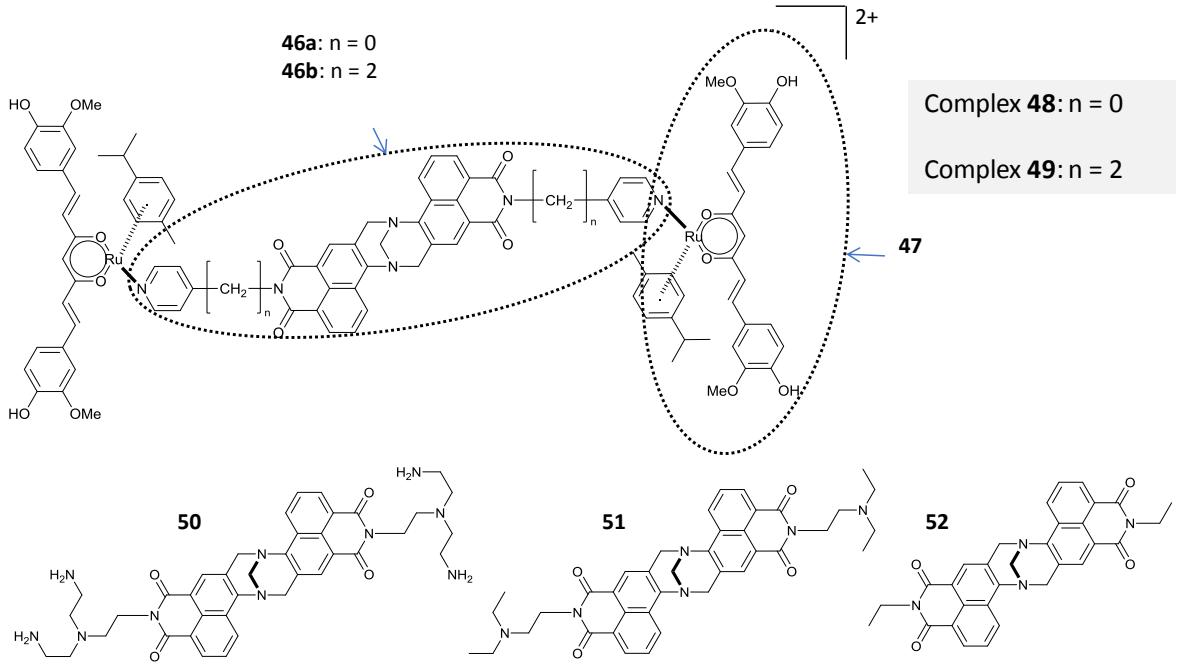

Figure 4.2: *Naphthalimide based Tröger's bases, which have been evaluated for various biological applications.*

4.2 Biological Studies of $[Ru(L)_2mpdppz]^{2+}$

4.2.1 Cellular Uptake and Localisation Studies of $[Ru(L)_2mpdppz]^{2+}$ (33a and 33b)

The uptake of the two luminescent **mpdppz** complexes **33a** and **33b** into HeLa cells was investigated using confocal laser microscopy (Figure 4.3). The results demonstrate that both complexes were taken up by the cells at 100 μM concentration within 24 hours of incubation. The complexes appear within the cytoplasm of the cells, with red emission observed outside the nucleus, where it formed discrete "packets" of luminescence in the cytoplasm. These observations agree with previous results observed for complexes **31a** and **31b**. For both compounds the emission inside the cells was relatively weak compared to the emission of the nuclear stain Hoechst 33342. High laser strength at the excitation wavelength was

necessary to visualise the localisation of the complexes. This may be explained by low uptake of the complexes because of low lipophilicity. Their positive charge may impede passive diffusion through the cell membrane.[3] Some toxicity against the cells was observed during the confocal microscopy imaging, as observed for most Ru(II) polypyridyl complexes when taken up by cells.[81] A "half-moon" sharped structure of the nuclei was seen for two complexes. This is indicative of mitochondrial stress as explained for similar observation for **31a** and **31b**, and it was likely that the toxicity arose due to localisation of the complexes in the mitochondria.

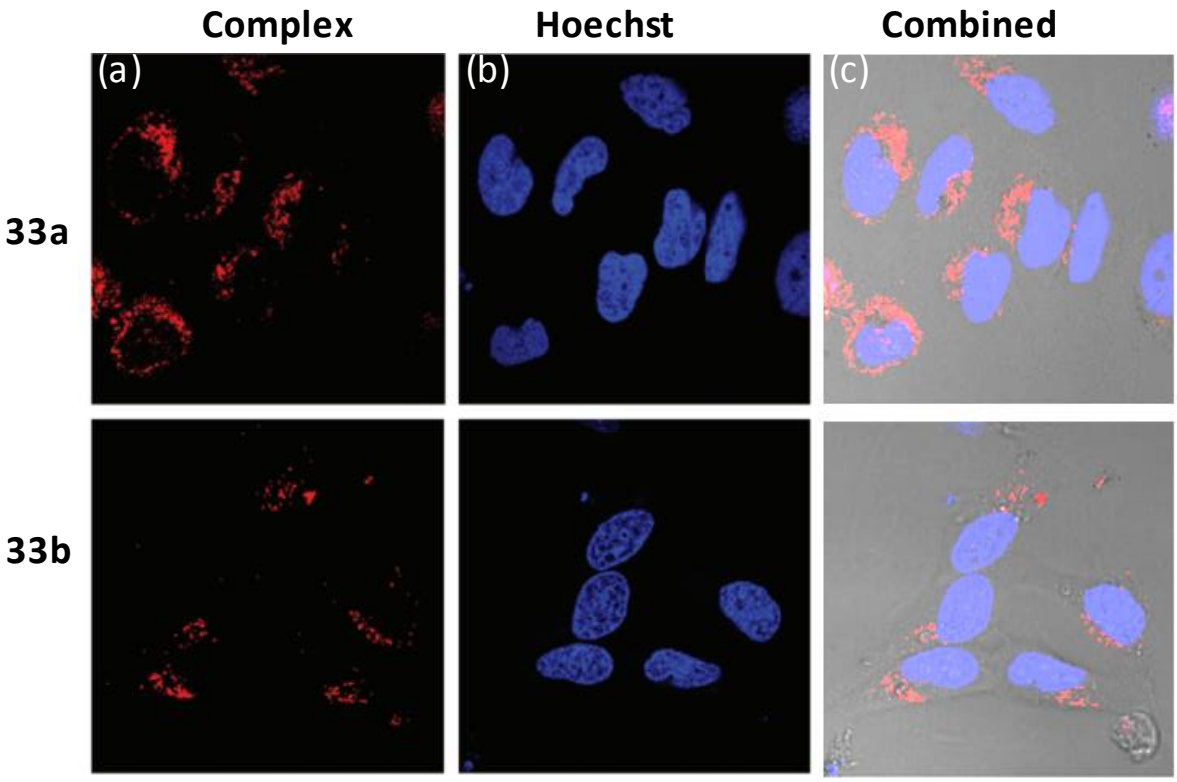

Figure 4.3: *Confocal images of HeLa cells after 24 hours incubation with 100 μM of* ***33a*** *(top) and* ***33b*** *(bottom). (a) Red emission (580-680 nm) from the complexes. (b) Blue emission from nuclear stain Hoechst 33342. (c) Red and blue emission combined with bright field.* λ_{exc} *= 450 nm.*

An alternative explanation for the weak emission may be due to the low photoluminescence quantum yield. In particular for complex **33a**, which contains **phen** as ancillary ligands, this is a likely explanation since the complex was non-emissive in water, and emission relies on binding to non-protic structures inside the cells, such as DNA or endoplasmatic reticulum.[172] By contrast, complex **33b**, which contains **TAP** as ancillary ligands, was emissive in water, but binding to structures inside the cells may quench the

excited state, as is the case upon DNA binding.[80] Localisation inside the nucleus may be difficult to observe, since DNA quenches the emission of the **TAP** complex as shown in the previous chapter. As mentioned in the introduction to Chapter 2, complexes **31a** and **31b** show a high degree of localisation in the mitochondria.[6] Based on the structural similarities between the two classes of complexes, and the similar observations in confocal microscopy, it was expected that **33a** and **33b** had a similar localisation in the cells.

4.2.2 Cellular Photo-toxicity Studies of $[Ru(L)_2mpdppz]^{2+}$

The complexes were assessed for cytotoxicity against HeLa cells under both dark and visible light conditions, using an Alamar Blue cytotoxicity assay. Such assays rely on the non-fluorescent resazurin dye, which is reduced to the pink coloured and highly red fluorescent resorufin dye; a process that can be directly related to cell viability.[173] The light source was an HgXe arc lamp filtered from UV light using an aqueous solution of $NaNO_3$ (Figure 4.4). Cells were seeded into 96-well plates using 25×10^3 cells per well and treated with compounds for 24 hours at 37 °C. Subsequently, the cells were either irradiated with 18 J cm^{-2} of light for one hour or maintained in the dark. After a further 24 hours of incubation, each well was treated with 20 µL of Alamar Blue and incubated for four hours. Emission intensity was recorded at 590 nm with excitation at 544 nm. The chemotherapeutic drug paclitaxel (Taxol®) and the previously studied **phen** complex **31a** were used as references. Three replicates have been done to show reproducibility.

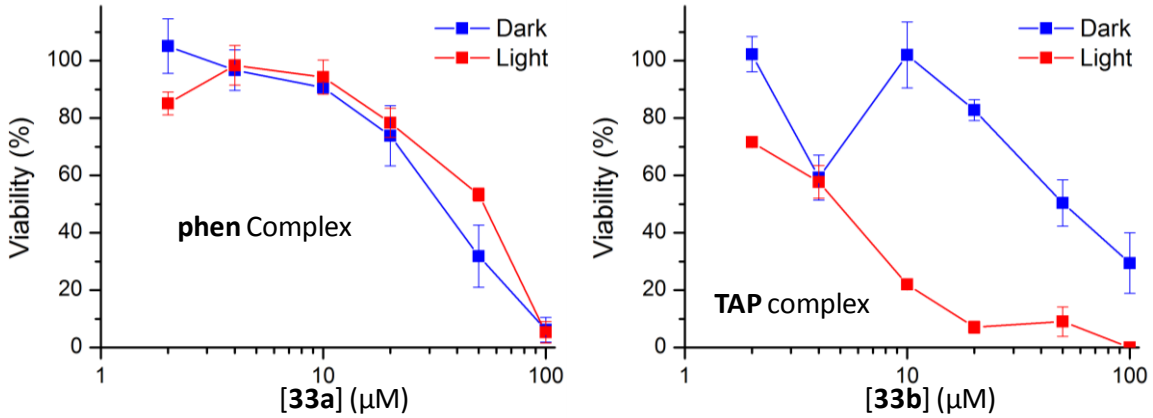

Figure 4.4: *Viability profiles of **33a** and **33b** in HeLa cells with or without light activation. All points have shown reproducibility with three replicates.*

The studies demonstrated that the **phen** complex **33a** did not show light-dependent cytotoxicity, yielding IC_{50} values at *ca*. 40 µM under both dark and light conditions, as can be seen in Figure 4.4 and Table 4.1. These IC_{50} values were, however, significantly lower than those observed previously for **phen** complex **31a**. These results suggest that the modifications to the **pdppz** ligand have increased the overall cytotoxicity of the complexes. An increased toxicity has been confirmed by comparison of the viability of cells at 100 µM of the compounds. After 48 hours incubation time in the dark, the cell viabilities were 35% for **31a** and only 6% for **33a**. One explanation could be that the methyl group increases the lipophilicity, which will increase the cellular uptake. The apparently larger binding constant for **33a** could also explain the increase in the toxicity, even though no nuclear localisation was observed. A non-significant amount of complex may not be observed in the nuclei, but can still cause harm to the cells. As was shown previously for **31a**, the compound might be taken up by the mitochondria allowing it to bind to the mitochondrial DNA.

Table 4.1: *Effects of Ru(II) complexes **33a** and **33b** on cell viability of HeLa cervical cancer cells with or without light activation. IC_{50} values for the chemotherapeutic drug Taxol® are included as references. Results are presented as the mean ± SEM.*

Complex	$IC_{50,Dark}$ (µM)	$IC_{50,Light}$ (µM)	PI[a]
33a	37 ± 6	48 ± 8	0.8
33b	60 ± 15	4.8 ± 0.5	13
Taxol®	0.0028 ± 0.0005	0.0026 ± 0.0006	1.1

[a] Photo-index = $IC_{50,Dark}/IC_{50,Light}$.

On the other hand, photo-activation of **TAP** complex **33b** resulted in a more than 10-fold increase in the toxicity compared to the one observed for complex **31b**. The IC_{50} values for **33b** in the dark was determined to be 60 µM, decreasing to 5 µM after photo-activation. These IC_{50} values were slightly lower than the corresponding values reported for $[Ru(TAP)_2pdppz]^{2+}$ (**31b**) and significantly lower than the values reported for $[Ru(TAP)_2dppz]^{2+}$ (**9b**).[6] This enhancement in the cytotoxicity may be explained by a higher lipophilicity and cellular uptake of the compound, or stronger binding to nuclear or mitochondrial DNA, as also described for **33a**.

For complex **33b** the observed viability in the dark at 4 µM was 42% lower than the viability at 10 µM, which was unexpected since the viability usually decreases with

increasing concentration of complex.[4] There could be several reasons for this. The intracellular processes are very complex, and it cannot be ruled out that, in some cases, an increase in the concentration of a harmful agent will result in improved survival rate. As mentioned in the start of this section, Alamar Blue does not measure the number of cells that survive, but the rate at which the cells will reduce resazurin to the fluorescent resorufin. Thus, an apparent higher "viability" may not always represent a larger number of living cells under certain conditions. The same unexpected behaviour was not observed in the case of light activation.

4.2.3 Singlet Oxygen Sensitisation Ability of $[Ru(L)_2mpdppz]^{2+}$

It has been demonstrated that **TAP** complex **31b** acts as a photosensitiser (S). After excitation of **31b** in the MLCT band (HgXe arc lamp filtered from UV light), an energy transfer (ET) occurs to dioxygen, [6] converting the triplet ground state to a singlet state:

$$S + h\nu \rightarrow S^* + {}^3O_2 \rightarrow {}^1S + {}^1O_2 \qquad (4.1)$$

Singlet oxygen is a reactive oxygen species (ROS) and is known to be responsible for the photoinduced toxicity of many PDT agents including Photofrin.[174] A probable formation of singlet oxygen was used to explain the high increase in the toxicity of **31b** in the presence of light, as described in the introduction to this chapter.[175] Sandra Estalayo-Adrián has quantified the singlet oxygen quantum yield (Φ_Δ) of the two complexes in collaboration with Prof. Guillermo Orellana in Complutense University of Madrid. The measurements were performed on an Edinburgh Instrument (UK) LP-900 Laser Kinetic Spectrometer System Equipped, with a Nd:YAG laser for excitation at 532 nm and a Hamamatsu H10330 NIR-PMT module for the singlet oxygen emission monitoring at 1260 nm. The quantity Φ_Δ is the fraction of all photons absorbed at a certain wavelength that results in the formation of singlet oxygen. The experiment was carried out in the following way: the complex under investigation was excited at 532 nm in D_2O saturated with dioxygen ($p(O_2) = 1$ bar) and the emission was measured at 1260 nm, corresponding to decay from the singlet state to the triplet ground state of O_2 (Figure A4.1).

The intensity (or signal) of the emission in the presence of the complex was compared with the corresponding value for $[Ru(phen)_3]\cdot 2Cl$ measured under the same conditions and

[4] The result was reproducible and significant at a 0.05 significance level. The pulled standard error (SE) for all data points was 5%, which corresponds to a least significant difference ($LSD = 2 \times \sqrt{2 \cdot SE}$) on a 0.05 significance level (α) at 15%. (D. R. Cox and C. A. Donnelly, *Principles of applied statistics*, Cambridge University Press, 2011).

at the same time point after excitation. From this it was possible to calculate the singlet oxygen quantum yield in D_2O at O_2 saturation ($\Phi^{complex}_{\Delta,D_2O,O_2}$), using the formula:

$$\Phi^{complex}_{\Delta,D_2O,O_2} = \Phi^{ref}_{\Delta,D_2O,O_2} \frac{I_{complex}/A_{complex}}{I_{ref}/A_{ref}} \quad (4.2)$$

$\Phi^{ref}_{\Delta,D_2O,O_2}$ is the quantum yield for $[Ru(phen)_3]^{2+}$, 39% according to the literature.[175] $I_{complex}$ and I_{ref} are the emission intensities at 1260 nm (arbitrary units) for a solution of the complex under investigation and of the reference complex $[Ru(phen)_3]^{2+}$ (**8a**), respectively. $A_{complex}$ and A_{ref} are the absorbance at the excitation wavelength for the solutions with the studied complex and the reference, respectively.

The singlet oxygen quantum yield was quantified further under ambient conditions in normal H_2O and with a level of oxygen corresponding to atmospheric air saturation ($p(O_2)$ *ca*. 0.2 bar). Further quantification was performed by measuring the lifetime of the excited state of the complex under different conditions, including in D_2O saturated with oxygen, as just described ($\tau^{complex}_{D_2O,O_2}$), and with all oxygen removed by flushing the solution with argon for 30 minutes ($\tau^{complex}_{D_2O,Ar}$). In H_2O, the lifetime was determined under ambient conditions ($\tau^{complex}_{H_2O,air}$) as well as in an oxygen free solution, degassed by flushing with argon ($\tau^{complex}_{H_2O,Ar}$). The value obtained for the quantum yield in D_2O under oxygen saturated conditions can be converted to the corresponding value in H_2O under ambient conditions, using the formula:

$$\Phi^{complex}_{\Delta,H_2O,air} = \Phi^{complex}_{\Delta,D_2O,O_2} \frac{1-\left(\tau^{complex}_{H_2O,air}/\tau^{complex}_{H_2O,Ar}\right)}{1-\left(\tau^{complex}_{D_2O,O_2}/\tau^{complex}_{D_2O,Ar}\right)} \quad (4.3)$$

The results obtained from the singlet oxygen measurements were in accordance with the assertion that the observed photo-toxicity is a result of singlet oxygen formation. The **phen** complex **33a** did not show any indication of singlet oxygen formation. This result was expected since the excited state of this compound is quenched extremely rapidly by water and complex **33a** did not show increased toxicity upon exposure to light. On the other hand, the **TAP** complex **33b** has increased toxicity upon exposure to light, and it is likely that this is a result of the formation of singlet oxygen. The complex did show a large singlet oxygen quantum yield of 58% in D_2O saturated with O_2 and 17% at ambient conditions. However, Dr Robert Elmes demonstrated for **31b** that photo-cleavage of DNA was independent of the formation of singlet oxygen, which implies that there are other possible mechanisms by which the structurally similar complex **33b** could induce damage to cells.[6,176] However, there was no evidence that it was DNA damage that resulted in cell death in the presence of **31b** and **33b** upon light activation. Further studies must be conducted to provide insight into

whether singlet oxygen formation of both complexes is involved in the mechanism of action that kills the cancer cells, such as by studying the possibility of photo-activated damage to other types of biomolecular structures, *e.g.* proteins and RNA.[177]

In summary both complexes **33a** and **33b** show cellular uptake in HeLa cervical cancer cells, with weak emission inside the cells. Complex **33b** showed a high increase in the toxicity upon photo-activation with a *PI* value at 13. It was confirmed that the complex formed singlet oxygen upon photo-activation, which may be involved in the observed increase in toxicity.

4.3 Biological Studies of phendione Compounds

4.3.1 Cellular Uptake and Localisation Studies of $[Ru(phen)_2phendione]^{2+}$ (45a)

The uptake of the complex **45a** into HeLa cells was investigated using confocal laser microscopy with the same procedure as used for complexes **33a** and **33b**, which is described in Section 4.2.1. The studies indicated that there was a very low uptake of the complex (Figure 4.5); complex **45a** did show some emission inside the cells at high laser strength when the cells had been treated with 100 μM of the complex for 24 hours.[81] Lower uptake of the complex compared to complexes **33a** and **33b** was expected due to the higher polarity of the compound conferred by the ketone groups, which lowers the lipophilicity.

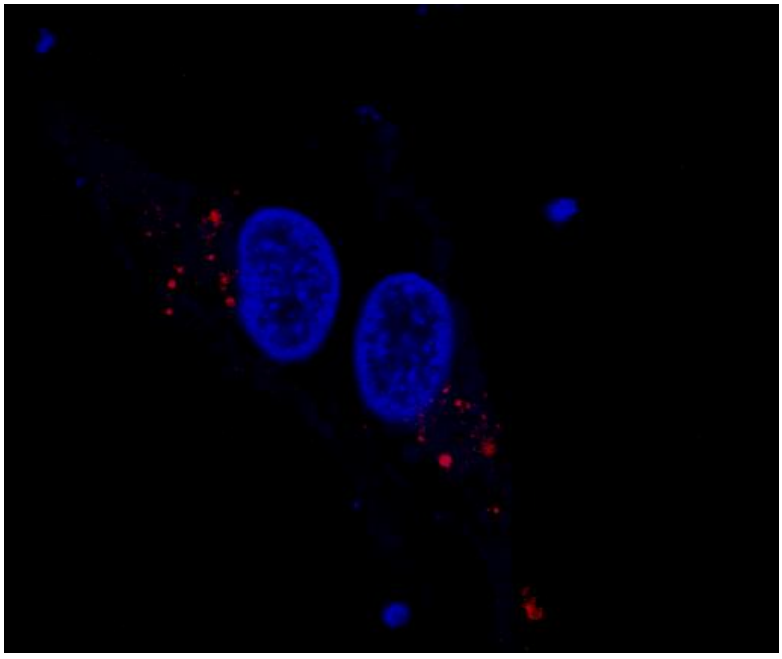

45a

Figure 4.5: *Confocal images of HeLa cells after 24 hours incubation time with 100 μM of* ***phendione*** *complex* ***45a****. Nuclei were stained blue with Hoechst 33342. Red emission (580-680 nm) from the complexes.* λ_{exc} *= 450 nm.*

4.3.2 Cellular Toxicity Studies of phendione Compounds

The toxicity was evaluated using an Alamar Blue toxicity assay under the same conditions and with the same procedures as used for complexes **33a** and **33b**, which is described in Section 4.2.2. Both modifications of **phendione** resulted in a large decrease in toxicity, and no increase in toxicity of the luminescent complex **45a** was observed upon exposure to light. The IC_{50} value for unmodified **phendione** with HeLa cells was only 0.6 μM in the dark (Figure 4.7), which is comparable to the 0.4-4 μM range reported for other cancer cell lines (HK-2, A-498, CHANG, Hep-G2, HCT116, HepG2 and MCF-7).[157,159] Both modifications resulted in an approximately 50-fold increase in the IC_{50} value in the dark (28 and 31 μM for **45a** and **45b**, respectively), which were more similar to what has been observed for the Ru(II) **phendione** complex **45c**, which has an IC_{50} value at 57 μM for HeLa cells.[7,178] The low toxicity of both compounds compared to the unmodified **phendione** may be due to changed reactivity of the compounds, or it may be a result of lower cellular uptake of the compounds because of the introduction of positive charges, which will complicates the penetration of the cell membranes because of lower lipophilicity. The toxicities of **phendione** complex **45a** was also investigated upon light-activation, as done for **33a** and **33b**, however, no decrease in the IC_{50} values was observed.

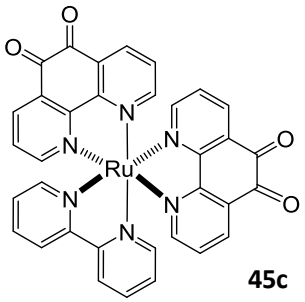

Figure 4.6: *Litterature example of a Ru(II) polypyridyl complex with* ***phendione*** *as a ligand.*

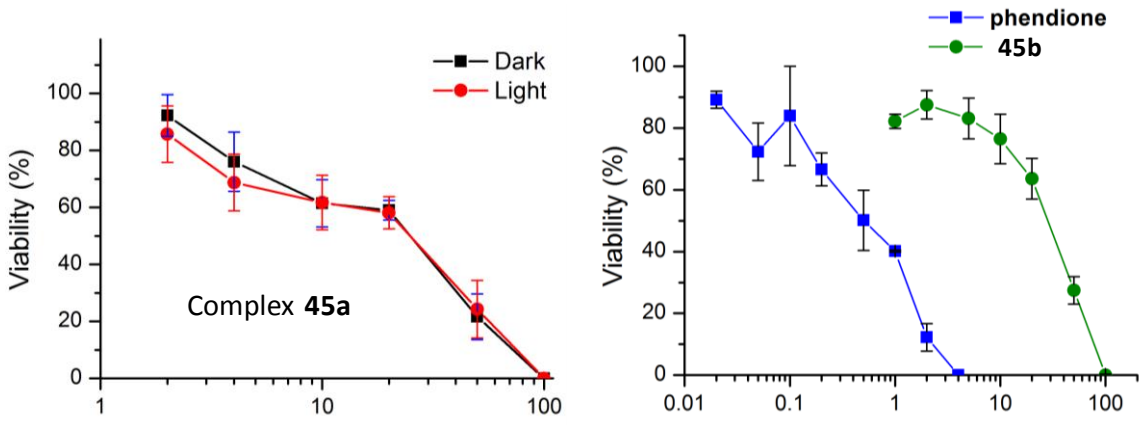

Figure 4.7: *Viability profiles for* ***phendione*** *compounds on HeLa cells with or without visible light activation.*

Table 4.2: *Effects of* ***phendione*** *derived compounds* ***45a*** *and* ***45b*** *on cell viability of HeLa cervical cancer cells with or without light activation.* IC_{50} *values for the chemotherapeutic drug Taxol® are included as references. Results are presented as the mean ± SEM.*

Complex	$IC_{50,Dark}$ (µM)	$IC_{50,Light}$ (µM)	PI[a]
45a	28 ± 4	26 ± 9	1
phendione	0.6 ± 0.2	0.6 ± 0.2	1
45b	31 ± 5	n.d.	n.d.
Taxol®	0.0028 ± 0.0005	0.0026 ± 0.0006	1.1

n.d.: not determined.

Considering that almost all previous studies show similar IC_{50} values for **phendione** and its metal complexes, it was surprising that a ruthenium complexes with **phendione** as a ligand had a very low toxicity (**45a**). However, the most IC_{50} values reported previously for **phendione** complexes have been for complexes with metal centres, for which **phendione** is expected to be a much more labile ligand than it will be in a Ru(II) complex.[179] Comparison between the toxicity of the complexes and **phendione** itself indicates very strongly that the toxicities reported in the literature represent primarily the toxicity of the dissociated **phendione** ligand, rather than that of the complexes. Figure 4.8 shows that for all literature values, the toxicity for a complex with *N* numbers of **phendione** ligands is approximately *N* times the value for **phendione** alone (Figure 4.8). Relative toxicity compares the toxicity of a **phendione** complex with the toxicity of **phendione** alone for a specific cell line and is here defined as IC_{50}(**phendione**)/IC_{50}(complex). The proportionality constant (α) is very close to one (0.99) for the best fit to the relative toxicity of the complexes as a function of number of **phendione** ligands in the complexes.

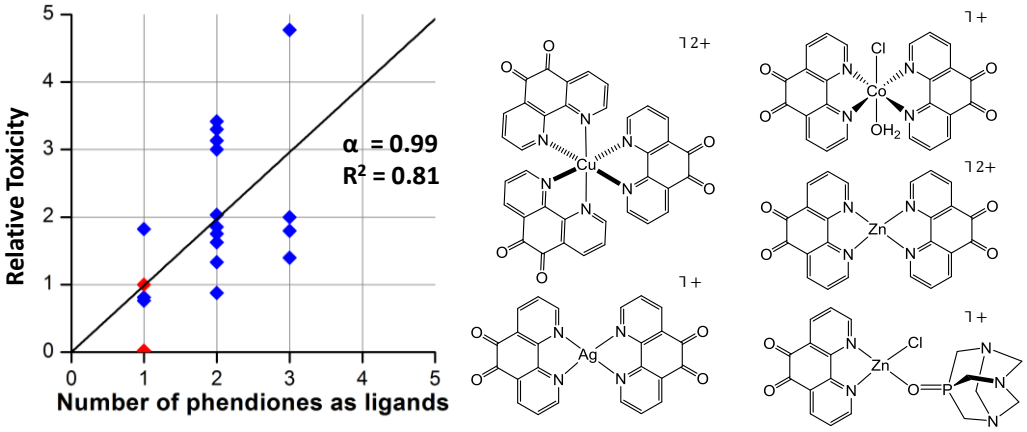

Figure 4.8: *Correlation between all published toxicity values of* ***phendione*** *complexes, without Ru(II) centre, and number of* ***phendione*** *ligands that are present in the compounds (blue points).*[157,159] *The trend line shows the best fit of the proportionality between the two variables. The red points correspond to the toxicity of the two Ru(II) complex* ***45a*** *and of* ***phendione*** *alone.*

It has been demonstrated that Ru(II) **phendione** complex **45a** and N-methylated **phendione** compound **45b** show low toxicity compared to **phendione** alone. The low toxicity may be explained by decreased cellular uptake after the modifications, which was demonstrated for complex **45a** with confocal microscopy. The high toxicity of many **phendione** complexes in the literature has been explained by the lack of stability of the complexes, which will release the very toxic **phendione** ligand after being dissolved in aqueous media. There was no increase in the toxicity of **phendione** complex **45b** upon light-activation.

4.4 Cellular Studies of Ru(II) Complexes with Curcumin and Naphthalimide-Based Tröger's Bases as Ligands

Curcumin is a natural product that can be found in the plant turmeric. Some studies have shown that curcumin is photo-toxic through the formation of reactive oxygen species, which has made it a candidate as a phototherapeutic agent.[162] As described in Chapter 1 and demonstrated in Section 4.2.2, some ruthenium complexes[6,54] and naphthalimides[163] have also shown potential as photochemotherapeutic agents. Two new bimetallic ruthenium complexes have been synthesised by Dr Shanmugaraju (complex **48** and **49**), both of which have curcumin and naphthalimide-based Tröger's bases as ligands (ligand **46a** and **46b**). These were examined in the same manner as described above for possible use in photochemotherapy, and also to see whether the toxicity of the two complexes can be considered as additive, synergistic or antagonistic when compared with the toxicity of the individual parts. A synergetic effect is defined as a case where several active components come together and result in an effect that is larger than the sum of the effects of the individual components (additive effect).[180] An antagonistic effect corresponds to the opposite case where the effect will be smaller than the sum of the effects of individual components. The change in toxicity of the **phendione** derived compounds studied in the last section were examples of an antagonistic effect since the toxicity decreased.

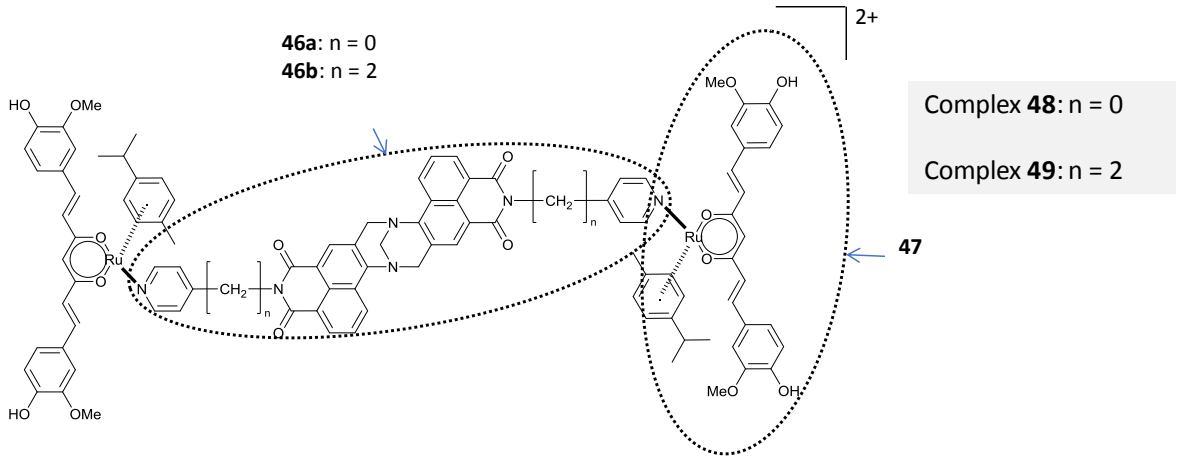

Figure 4.9: *Bimetallic Ru(II) complexes with naphthalimide based Tröger's bases as bridging ligands together with curcumin.*

4.4.1 Cellular Uptake and Localisation Studies

The uptake and emissive properties in HeLa cells of the four naphthalimide-based Tröger's bases in the dark were investigated using confocal laser microscopy with the same procedure used for complexes **33a** and **33b**, which is described in Section 4.2.1. The cells were followed for one hour just after addition of the compound. The experiment demonstrated a fast uptake of **46b** and the corresponding ruthenium complex **49**, likely by passive diffusion through the cellular membrane because of the low polarity of these compounds. However, **46a** and the corresponding ruthenium complex **48** showed little or no uptake. As will be described in Section 4.6, the differences in cellular uptake may be explained by differences in lipophilicity. Compound **46b** has two extra ethylene groups compared to **46a**, which may increase the affinity for the aliphatic lipid membrane and improve the cellular uptake.[81] The compounds appeared to be distributed evenly within the cytoplasm of the cells, with green fluorescent emission observed outside the nuclei. The results were comparable to those observed for similar naphthalimide-based Tröger's bases.[181] Active transport mechanisms could be involved, which would need alternative explanations for the difference in cellular uptake. However, the even distribution of the compound in the cytoplasm speaks against this explanation, since endocytosis would be expected to be trapped in vesicles inside the cells.[182] Transport through membrane channel proteins was unlikely because of the large size of the molecular systems.[81]

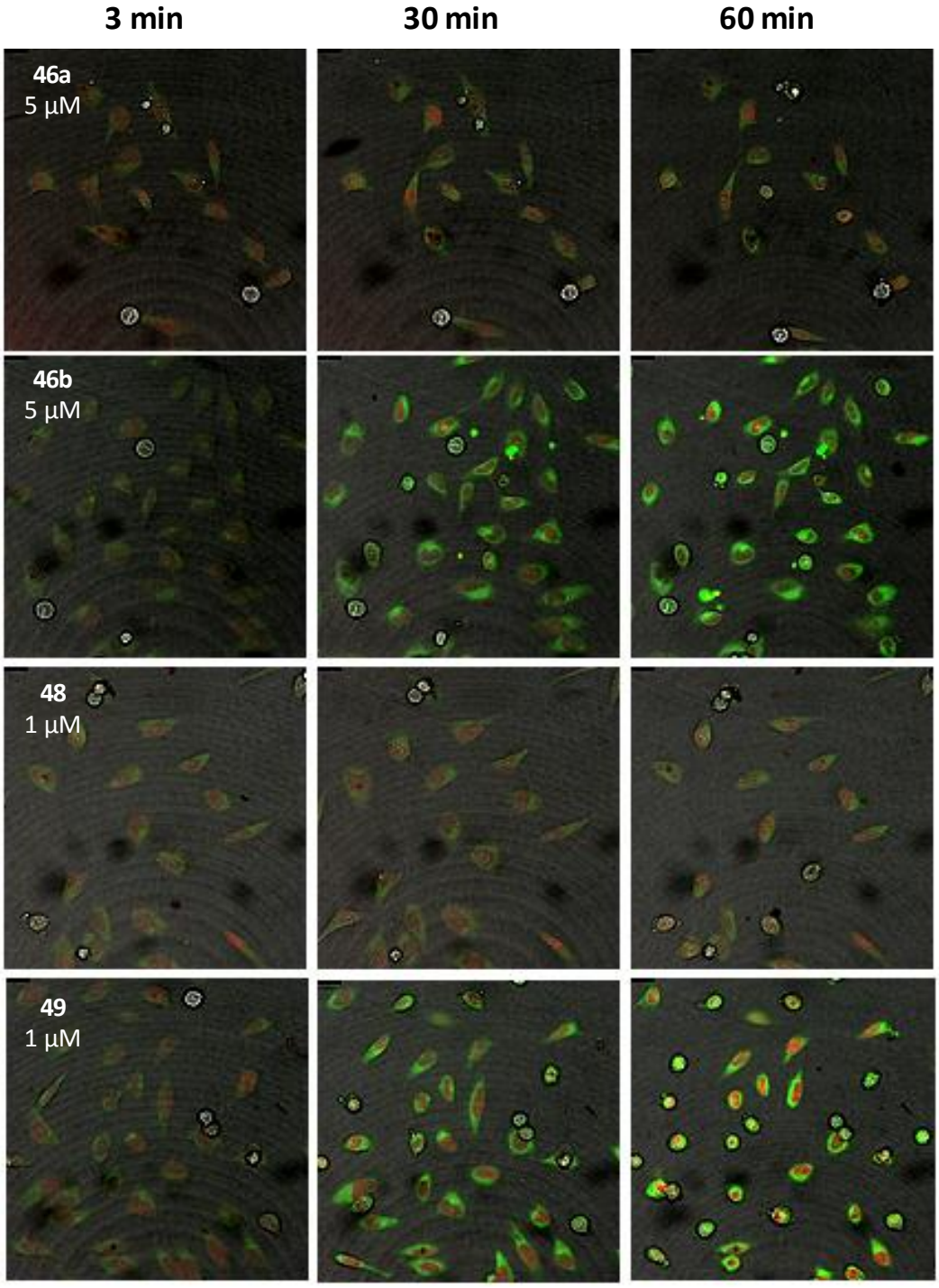

Figure 4.10: *Compound* ***46b*** *and the corresponding ruthenium complex* ***49*** *were taken up fast by HeLa cells and localised in the cytoplasm. Compound* ***46a*** *and the corresponding ruthenium complex* ***48*** *showed low or no uptake by the cells. Nuclei were stained red with DRAQ5.*

4.4.2 Cellular Toxicity Studies

The toxicity was evaluated using an Alamar Blue toxicity assay under the same conditions and using the same procedures as for complex **33a** and **33b**, which are described in Section 4.2.2. However, the IC_{50} value will, in the following, be reported in µg/mL in contrast to µM as done for the Ru(II) polypyridyl complexes. This change of unit has been done to have a meaningful discussion of the relative toxicity of the different compounds, especially when the presence of synergetic effects has to be evaluated. This will help to avoid misleading conclusions of the relative toxicity of the compounds, such as those obtained for **phendione** complexes in the past (Section 4.3.2).[157]

All compounds, except **46a**, showed high dark toxicity with no significant increase in toxicity upon exposure to light. The ruthenium complex **48** had the highest toxicity with an IC_{50} value of 3.7 µg/mL (2.0 µM), which is similar to what was observed for cisplatin (3.9 µg/mL or 13 µM).[183] The other ruthenium complexes **49** and **47** and Tröger's base **46b**, also showed relative high toxicities with IC_{50} values at 9.2 µg/mL (4.9 µM), 10 µg/mL (15 µM) and 17 µg/mL (26 µM), respectively. The IC_{50} value of reference compound **47** was similar to values reported for other cancer cell lines (9-41 µg/mL).[184] By far the lowest toxicity was observed for Tröger's base **46a** with an IC_{50} value that exceeded 61 µg/mL (100 µM). There was some indication of increased toxicity upon exposure to light for Tröger's base **46b** and the corresponding complex **49**. There were some synergetic effects for the combinations of the naphthalimide-based Tröger's bases with complex **47**. The reported IC_{50} value for complexes **48** and **49** were, in both cases, lower than the value for any of its components. Compound **46a** (IC_{50} > 61 µg/mL) and **47** (IC_{50} = 10 µg/mL), especially, showed an increase in the toxicity when they were combined to give complex **48** with a large decrease in the IC_{50} value (3.7 µg/mL).

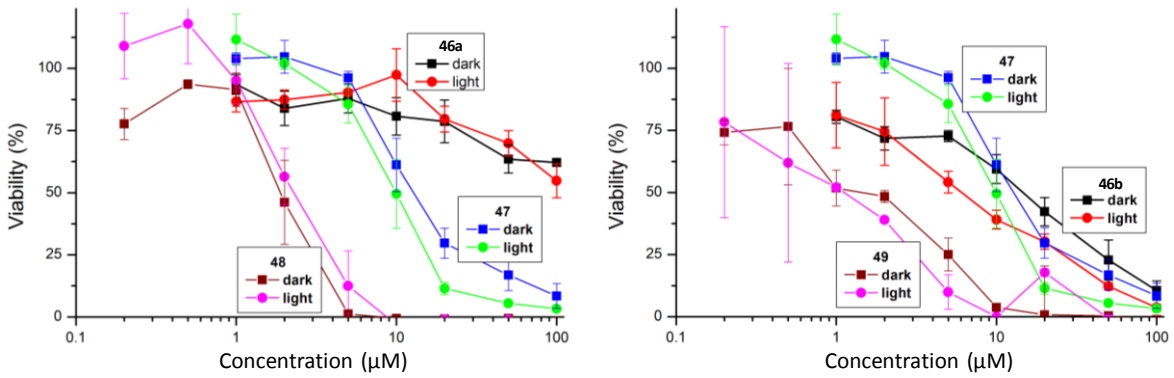

Figure 4.11: *Viability profiles of tested compounds in HeLa cells with or without light activation.*

Table 4.3: *Effects of tested compounds on HeLa cervical cancer cells with or without light activation. Literature value for the chemotherapeutic drug cisplatin is included as a reference. Results are presented as the mean ± SEM.*

Compounds	$IC_{50,Dark}$ (µg/mL)	$IC_{50,Light}$ (µg/mL)	PI^a
46a	> 61	> 61	-
46b	17 ± 3	8 ± 4	2.1
47	10 ± 2	6 ± 1	1.7
48	3.7 ± 0.5	4.4 ± 0.5	0.8
49	9.2 ± 0.7	5 ± 1	1.8
Cisplatin[183]	3.9	-	-

[a] *Photo-index* = $IC_{50,Dark}/IC_{50,Light}$.

4.4.3 Computational Studies of the Structures of 46a and 46b

Computational studies have been carried out for the two Tröger's base ligands **46a** and **46b** to gain insight into their structures in aqueous medium. All quantum mechanical calculations were done with density functional theory (DFT) using the Gaussian Software package.[148] The functional M06 has been used with the basis set 6-311G**. Geometry optimised structures of the compounds were calculated from crystal structures of the R,R-enantiomers of both Tröger's bases. The quantum mechanical calculations in solvent were carried out with solvation model based on density (SMD).[185] Calculation of partition coefficients will be discussed in Section 4.6 to evaluate the hypothesis that the cellular uptake occurs through passive diffusion through the cell membrane.

There was some inconsistency between the crystal structures of the two Tröger's bases and the calculated structures in water (Figure 4.12). Calculated structure of **46a** showed a C_2-symmetry axis in water with equivalent values of the two dihedral angels between pyridine and naphthalimide in contrast to the crystal structure. The value of 73.8° was close to the average of the dihedral angels in the crystal structure, which were 57.0° and 81.8°, respectively. Both the crystal structure and the calculated solution state structure of **46b** showed C_2-symmetry of the molecule. However, in contrast to the crystal structure, the solution state structure had the naphthalimide and pyridine ring systems almost parallel to each other. The dihedral angles between pyridine and the neighbouring ethylene group were 79.7° for the solution state structure compared to 53.4° for the crystal structure. The different structures obtained in solution and in the solid state may be due to the fact that no packing forces are present in solution.

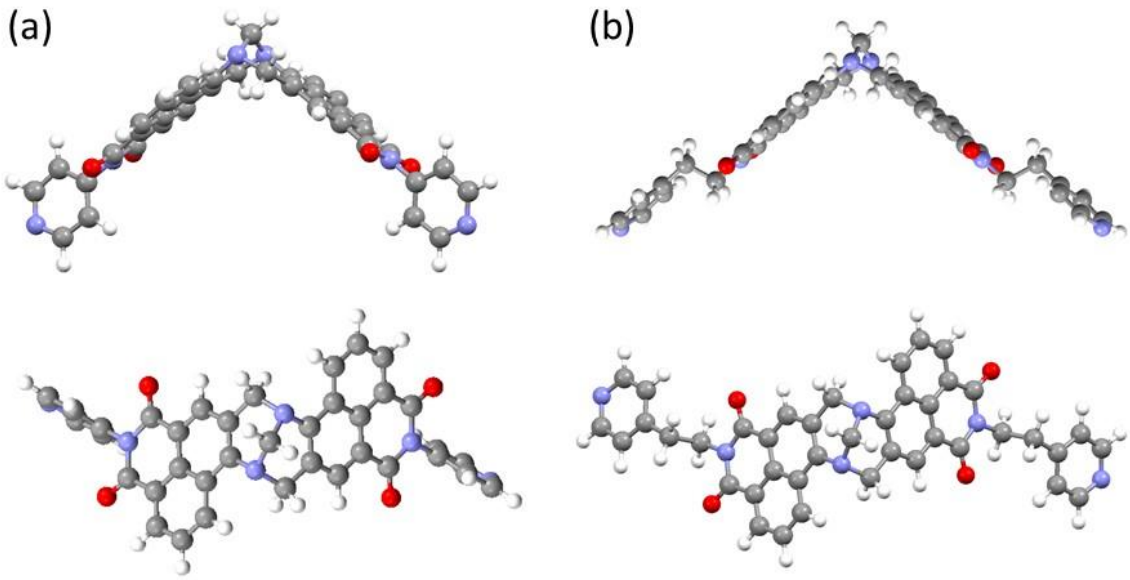

Figure 4.12: *Compound* ***46a*** *(a) and* ***46b*** *(b) optimised in water with M06/6-311G** and SMD.*

In summary the two naphthalimide based Tröger's bases **46a** and **46b**, Ru(II) curcumin complex **47** and the bimetallic Ru(II) complexes, which had **46a** or **46b** as bridging ligands together with curcumin, have been evaluated for use in cellular imaging. Compound **46b** and **49** showed strong emission confirming efficient uptake in cells and potential for use in cellular imaging. No significant uptake was observed for compound **46a** and **48**. It was expected that the uptake occurred by passive diffusion through the cell membrane. Apart from **46a**, all compounds showed relatively high toxicity in the dark. The highest toxicity was observed for complex **48**, which had an IC_{50} value at 3.7 μg/mL (2.0 μM), which was much lower than the IC_{50} value for any of the compounds of which it was composed (17 and 10 μg/mL for **46b** and **47**, respectively), and one of the lowest IC_{50} values observed for naphthalimide based Tröger's bases until now.[186] No significant increase in the toxicity of the tested compound upon light-activation was observed.

4.5 Cellular Studies of Naphthalimide-based Tröger's Bases with Terminal Tertiary Amino Groups

One challenge in the design of drugs is to achieve cellular uptake of the compounds since the activity often takes place inside the cells. For luminescent molecular species, like naphthalimides, a good cellular uptake will enable also the use of the compounds in cellular imaging. Small molecules, which have a low polarity, can often be taken up by the cells by passive diffusion through the lipid cell membrane. Lower polarity and higher lipophilicity will often result in larger cellular uptake. While low polarity and no charge on a molecule

will increase the rate of diffusion through the cell membrane, a positive charge makes it energetically favourable for a molecule to enter the cells because of the negative membrane potential (Appendix 1). Also, a positive charge will increase the solubility of the molecule in aqueous media, which is an essential property for use in biological systems.

Aliphatic tertiary amines fulfil well the criteria mentioned above. They are relatively lipophilic in their neutral form, which enables passive diffusion through the cell membrane. On the other hand, they will, primarily, be protonated and positively charged at neutral pH, which makes it thermodynamically favourable for the compounds to enter the cells and to increase their solubility. As mentioned in Chapter 1, Section 1.6, it has been demonstrated by the Gunnlaugsson group that **28** and two other tertiary amines showed efficient uptake in cancer cells and high cytotoxicity.[109] Inspired by these observations compounds **50**, **51** and **52** were synthesised by Shanmugaraju and Tobi Arisa, and the compounds have been studied for cellular uptake, imaging and toxicity. Compound **51** contains two tertiary amines with ethyl groups attached instead of the methyl groups in **43**. The substitution of methyl with ethyl is expected to increase the lipophilicity of the compound, which may result in improved cellular uptake. Compound **50** has, in addition, four primary amino groups. Protonation of the amines will increase the solubility of the compound, and the positive charge will make it thermodynamically more favourable for the compound to enter the cells. However,

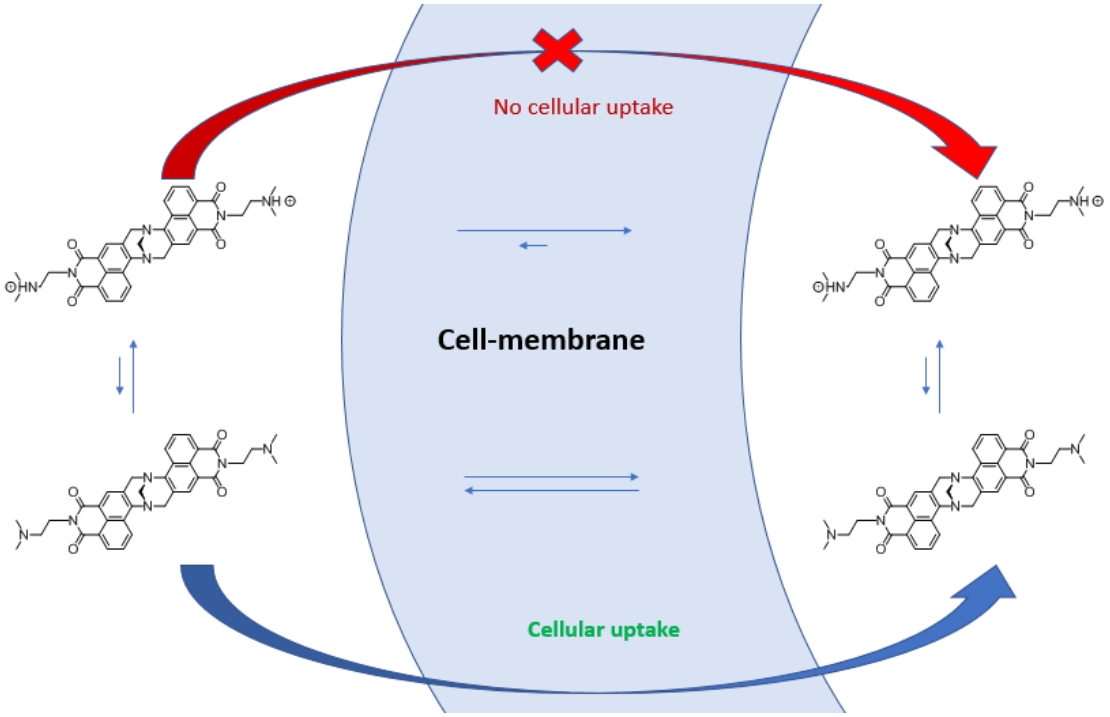

Figure 4.13: *Schematic presentation of how cellular uptake is expected to occur for* ***28****.*

protonation will reduce the lipophilicity of the compound, as well, and complicate the cellular uptake. Compound **52** has no amino groups attached to the Tröger's base moiety, which will make the compound more lipophilic due to the lack of the presence of electronegative atoms. However, the solubility of the compound is expected to be very low, which is an undesirable property in a biological setting, and the lack of a positive charge will make it thermodynamically less favourable to be taken up by cells.

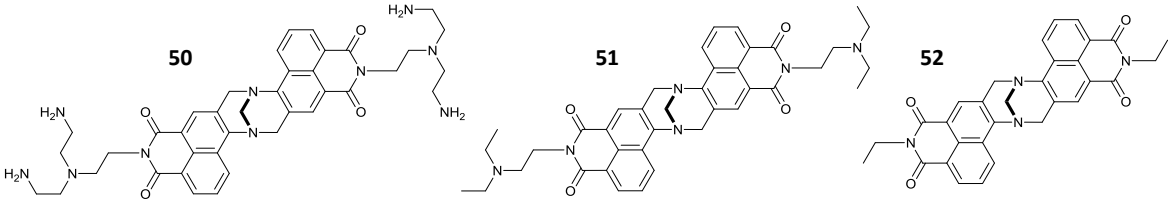

Figure 4.14: *Naphthalimide based Tröger's bases.*

4.5.1 Cellular Uptake and Localisation Studies

The uptake and emissive properties in HeLa cells of the naphthalimide-based Tröger's bases **51** and **52** in the dark were investigated using live confocal microscopy (Figure 4.15). Compound **50** was also evaluated, but as expected it showed no emission since the compound was non-emissive in aqueous as well as in organic solvents (Figure A4.2). The cells were treated with the compounds for 24 hours at 37 °C at a concentration of 1 μM.

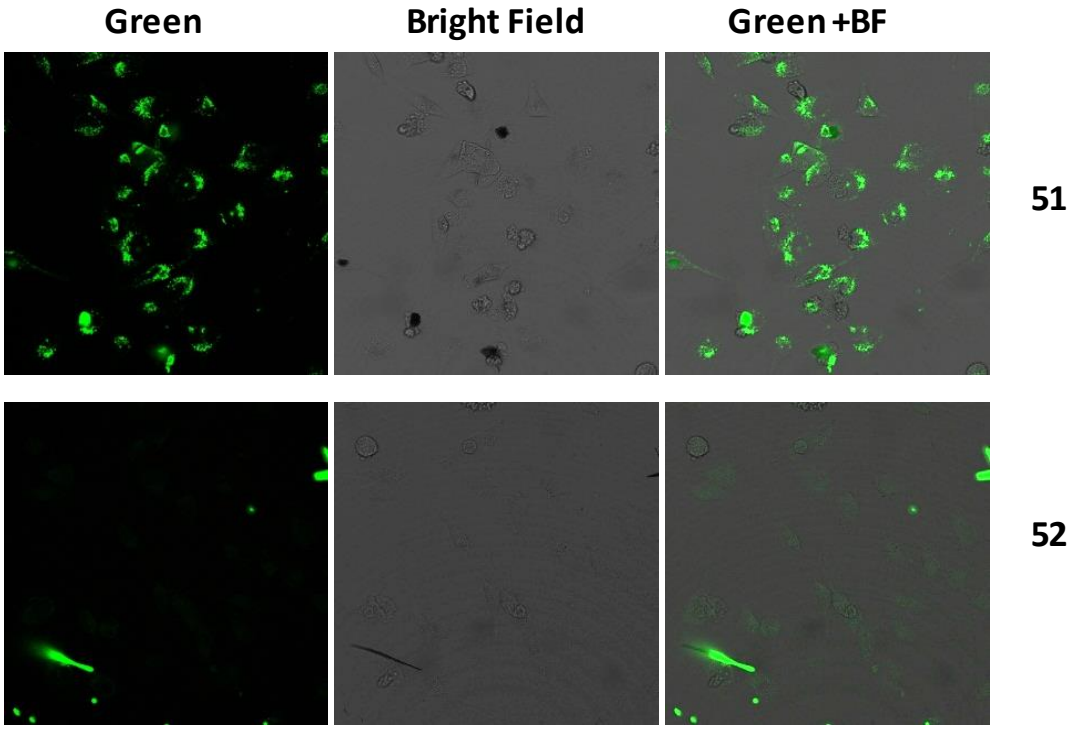

Figure 4.15: *Tröger's base **51** was successfully taken up by HeLa cells and localised in the cytoplasm while **52** showed low or no uptake. 1 μM of the compounds have been used in all cases.*

Compound **51** was the only compound that showed any significant emission inside the cells. An increase in the concentration of **52** to 5 μM did not result in any significant uptake (Figure A4.2). The better uptake of compound **51** compared to the uptake of **52** was expected to be a result of a higher solubility of **51**. Compound **51** seemed to induce some cell death, while **50** and **52** did not show any significant influence on the cell viability at concentrations in the range 1-5 μM.

4.5.2 Cellular Toxicity Studies

The complexes were assessed for cytotoxicity against HeLa cells with the same protocol as described in Section 0, except that light toxicity was not evaluated. Compound **51** showed a very high toxicity with an IC_{50} value of 2.4 μM (1.7 μg/mL), less than what is seen for cisplatin (13 μM or 3.9 μg/mL)[183] and one of the lowest values reported for Tröger's bases.[186] The compounds **50** and **52** showed low toxicities with IC_{50} values of 24 μM (18 μg/mL) and 75 μM (52 μg/mL), respectively. The low toxicities of these two compounds can be explained by the low uptake reported in the previous section.

Table 4.4: *Effects of tested compounds on HeLa cervical cancer cells. Literature value for the chemotherapeutic drug cisplatin is included as a reference. Results are presented as the mean ± SEM.*

Compounds	IC_{50} (μM)
50	24 ± 7
51	2.4 ± 0.6
52	75 ± 3
Cisplatin[183]	13

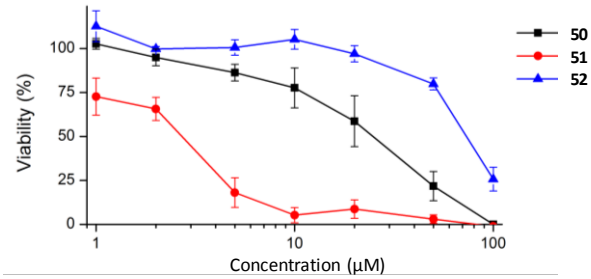

4.5.3 Computational Studies of the Structures of 50, 51 and 52

Computational studies have been carried out for the three Tröger's bases **50**, **51** and **52** to get insight into their structures in aqueous medium. The same quantum mechanical methods were applied as used for the description of compounds **46a** and **46b** in section 4.4.3. Geometrically optimised structures of the compounds were found for the *R,R*-enantiomers of all Tröger's bases, and the structures can be seen in Figure 4.16. All three compounds show C_2-symmetry for the central Tröger's base and the naphthalimide moiety. For **50**, a hydrogen bond is present in each end of the molecule, with the primary amines acting as hydrogen donors and the naphthalimide oxygen atoms as acceptors.

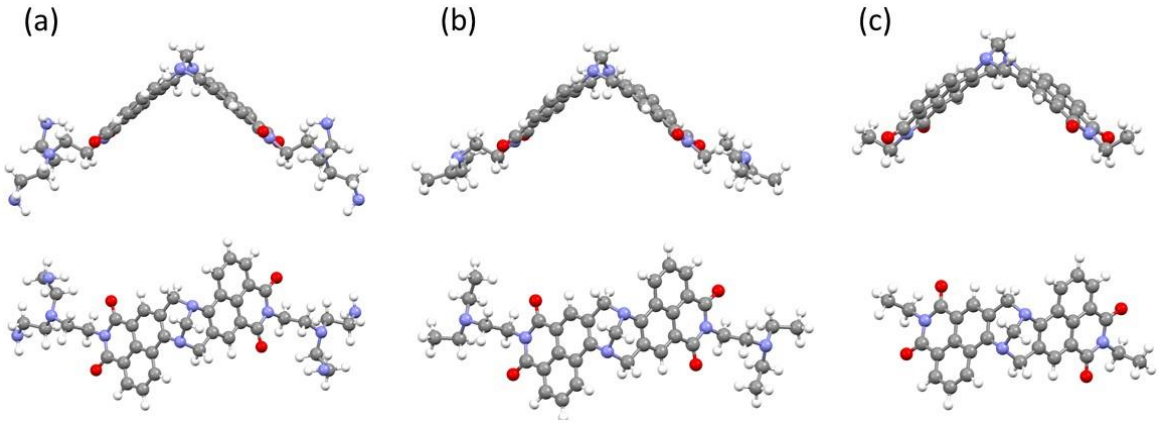

Figure 4.16: *Compound* ***50*** *(a),* ***51*** *(b) and* ***52*** *(c) geometry optimised in water with M06/6-311G** and SMD.*

4.6 Calculation of Partition Coefficients to Get Insight Into Cellular Uptake and Explain Differences in Toxicity

A likely explanation for the differences in the ease with which the different compounds are taken up by cells are differences in their lipophilicity. There is, in general, a positive correlation between lipophilicity and cellular uptake.[187] Especially in cases where cellular uptake occurs by passive diffusion, a high affinity for the lipid cell membrane will be essential. Lipophilicity is often quantified using the partition coefficient for the distribution of a solute between octanol and water:

$$P_{oct/water} = \frac{[solute]_{octanol}}{[solute]_{water}}$$

From DFT calculations of the free energy of the compound in water and octanol a value of *P* can be obtained:[185]

$$\Delta G_{oct/water} = G_{oct} - G_{water}$$

$$P_{oct/water} = \mathrm{e}^{-\left(\frac{\Delta G_{oct/water}}{RT}\right)}$$

The significance of the calculated value differs from experimental values by representing the "actual" partition coefficient for the non-protonated compounds without the presence of counterions such as chloride and iodide. The expected errors in the *logP* values have been quantified by comparing the experimentally obtained values for a series of 10 flavonoids reported in a paper by Rothwell *et al.*[188] with values obtained herein using the computational methods presented here.[188] The errors in the $logP_{oct/water}$ values were large with a mean unsigned error (*MUE*) of 3.2 and a maximum unsigned error (*Max UE*) of 5.6. However, the

errors in the relative differences between the *logP* values for different flavonoids ($\Delta logP_{oct/water}$) are much smaller with a *MUE* of only 1.1 and a *Max UE* of 2.5.

The logarithmic values of the partition coefficients for the different compounds studied in this chapter for the distribution between octanol and water ($logP_{oct/water}$) and between

Table 4.5: *Logarithmic values of the partition coefficients for the distribution of the compounds between octanol ($logP_{oct/water}$) or heptane ($logP_{hep/water}$) and water. The values are calculated with DFT (M06/6-311G**+LANL2DZ) and SMD as solvation model at 25 °C. The IC_{50}-values for the compounds in the dark are included in the table.*

Compounds	$logP_{oct/water}$	$logP_{hep/water}$	$IC_{50,Dark}$ (µM)
33a	1.1	-31.1	37
33b	-8.1	-48.2	60
45a	0.5	- [a]	28
phendione	-2.0	-3.6	0.6
45b	-2.0	-17.6	31
46a	0.1	-3.3	> 100
46b	1.8	-1.1	26 ± 3
50	-0.7	-10.0	24 ± 7
51	2.7	0.7	2.4 ± 0.6
52	2.4	1.1	75 ± 3

[a] *Convergence problems in the calculations.*

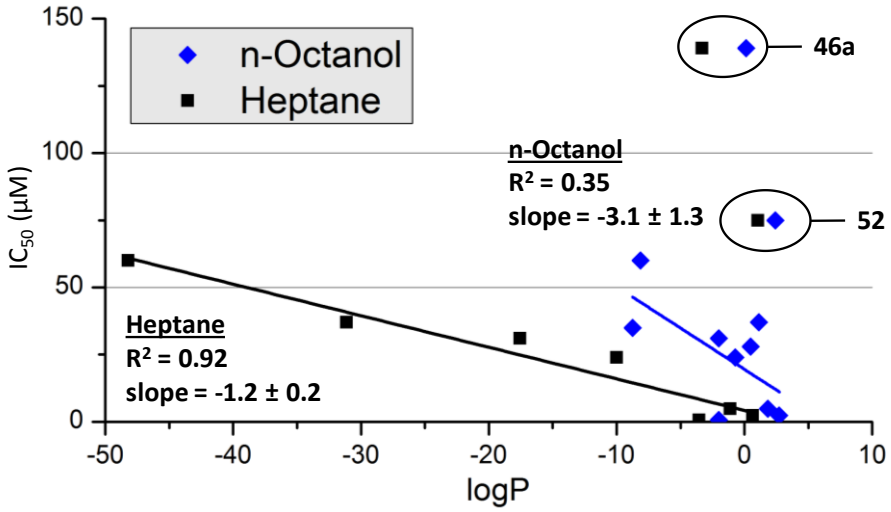

Figure 4.17: *Correlation between IC_{50} values with HeLa cells (no light) for compounds studied in this chapter and the logarithmic values of the calculated partition coefficients for the distribution between water and either n-octanol or heptane. Trend line is not fitted to the two outliers corresponding to compound* ***46a*** *and* ***52****. The IC_{50} value for* ***46a*** *exceed the used concentration range in the experiment and is estimated by extrapolation with a logistic function fitted to the viability plot.*

heptane and water ($logP_{hep/water}$) as well as the IC_{50} values of all compounds in the dark are given in Table 4.5. $logP_{hep/water}$ was expected to be a better measure for how easily the compounds will penetrate the cell membrane, since the interior of the cell membrane is aliphatic like heptane. There was, in general, a negative correlation between the IC_{50} values and *logP*. The correlation between IC_{50} and $logP_{hep/water}$ was very pronounced with an R^2 value at 0.92 (excluding two outliers).

4.7 Conclusion and Future Perspectives

In this chapter, 13 compounds were studied with the intention of evaluating their therapeutic and diagnostic potential, including their use in photochemotherapy and cellular imaging. The Ru(II) polypyridyl complexes **33a** and **33b**, which have **mpdppz** as a ligand, were internalised by HeLa cervical cancer cells; however, no indication of nuclear localisation was observed. The **phen** complex **33a** shows very similar IC_{50} values in the dark and in the light. On the other hand, the IC_{50} value of the **TAP** complex **33b** decreases by an order of magnitude upon irradiation of treated cells with visible light, from 60 μM to 4.8 μM. A mechanism for the increase in toxicity for complex **33b** after exposure to light might involve singlet oxygen photosensitisation. A singlet oxygen quantum yield of 17% under ambient conditions was observed for complex **33b**. The quantum yield for **33a** was too low to be measured, which was expected since no increase in toxicity was seen for this complex in the presence of light. The IC_{50} values for **33a** and **33b** were smaller than the reported values for **31a** and **31b**, respectively. One explanation that the methyl group leads to increased toxicity is that methyl group makes the complex more lipophilic, facilitating cellular uptake. Another explanation may be that the intracellular localisation are changed. For example, the DNA binding studies described in Chapter 2 indicated that the binding to DNA was increased after the modification for both complexes, which could have an effect on how it affects DNA in the cells, including mitochondrial DNA.

The complex with **phendione** as the ligand rather than **mpdppz** was also tested with the intention to evaluate the potential use in PDT. The **phen** complex showed no increase in toxicity upon exposure to visible light. Furthermore, the complexes had a much lower toxicity in the dark than **phendione** alone. A large decrease in the toxicity of **phendione** was also observed when one of the nitrogen atoms was methylated. It is expected that the decrease in toxicity is a result of decreased cellular uptake because of difficulties for the charged compounds to diffuse through the cellular lipid membrane. Computational studies

for all studied compounds in this chapter showed a negative correlation between the IC_{50} values and the lipophilicity.

Based on the positive correlation between high lipophilicity and good cellular uptake, future work will focus on increasing the lipophilicity of the compounds. One strategy is to attach a long aliphatic linker to the **dppz** ligand. Similar reported modifications of Ru(II) polypyridyl complexes has been shown to induce increased uptake[189,190] including those of Sandra Estalayo-Adrián from our group.[191] It was observed in the previous chapter that complexes **33a** and **33b** have a very high affinity for DNA. However, as shown in this chapter, no nuclear localisation is observed for any of the complexes. To fully take advantage of the benefits gained through strong interactions with DNA, future work will focus on achieving nuclear localisation through minor modification of the molecular structure of these complexes. For complex **33a** nuclear localisation would enable the use of the compound in cellular imaging of the nucleus since the emission is switched on upon binding to DNA. Complex **33b** is expected to have a high increase in the light induced toxicity since many structurally similar compounds are able to photo-cleave DNA.[6] One strategy is to attach a nuclear localisation sequence (NLS), a small peptide that can direct the localisation of a compound to the nucleus.[192] Other molecular systems that may have suitable properties are functionalised gold nanoparticles with modifications of complexes **33a** and **33b** as surfactants. Such attempts have already been made, as described in Chapter 2. The functionalisation of gold nanoparticles with other types of ruthenium polypyridyl complexes will be described in Chapter 6.

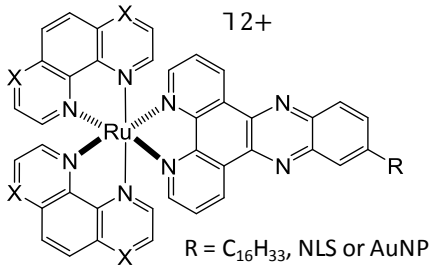

Figure 4.18: *Designed Ru(II) polypyridyl complexes with expected improvement in the biological properties.*

In this chapter, several naphthalimide-derived Tröger's bases were studied with the intention to evaluate their therapeutic and diagnostic potential, including the use in treatment of cancer and cellular imaging. Bimetallic ruthenium complexes containing **46a** or **46b** as bridging ligands were evaluated for treatment of cancer including the potential for use in PDT. Both ligands showed a relatively low toxicity; however, complex **48** had a high impact on the viability of HeLa cells with an IC_{50} value of only 2.0 μM. Only a small and non-significant increase in the toxicity was observed upon light activation for some of the compounds making it unlikely that the compounds have potential for use in photochemotherapy.

Compound **51**, which has two tertiary amine groups, showed good uptake in HeLa cells and an IC_{50} value of only 2.4 μM. This was in accordance with similar results observed for other compounds containing tertiary amines, and it is expected that an explanation may be high lipophilicity. Compound **50** showed poor cellular uptake and had a high IC_{50} value at 24 μM, which was expected since the compound contains four primary amine groups, which decreased the lipophilicity. A low uptake and toxicity was observed, also, for **52** with an IC_{50} value of 75 μM. This compound has no tertiary or primary amine groups, and computational studies showed that the lipophilicity of the compound was approximately equal to the lipophilicity of **51**. However, the low uptake and toxicity may be explained by poor solubility of the compound in water because of its aliphatic nature.

As far as the ruthenium-curcumin complex (**47**) is concerned, this complex showed a small but non-significant increase in the toxicity in the presence of light compared to the toxicity in the dark. Ruthenium complex **9b**, discussed in Chapter 1 and 5, has shown a large increase in toxicity at exposure to light,[6] making the bimetallic complex **53**, a more promising photochemotherapeutic agent than curcumin complexes **48** and **49**.

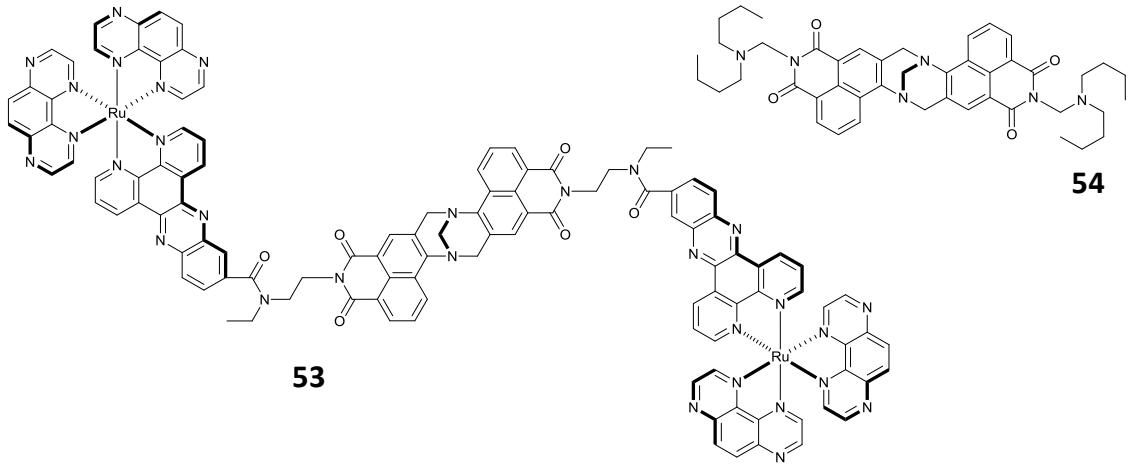

Figure 4.19: *Designed Tröger's bases with expected improvement in the biological properties.*

It was presumed that the high cellular uptake and toxicity of compound **51**, compared to other naphthalimide-based Tröger's bases such as **50**, was a result of higher lipophilicity. Further work will evaluate the relationship between the length of the alkyl groups attached to the nitrogen atom in the tertiary amine and the cellular uptake. It is expected that longer linkers will increase the cellular uptake and decrease the IC_{50} value provided that the compound is soluble in water. An example target molecule with *n*-butyl groups (**54**) is shown.

Chapter 5

Selective and Cooperative Binding of Ru(II) Polypyridyl Complexes to DNA

5.1 Introduction

Site selectivity is important in drug design, diagnostics and sensing where certain nucleic acid sequences or other types of potential binding sites might be important targets. For example, considerable effort has been invested in targeting base sequences characteristic of certain viruses[193,194] and numerous studies have been carried out to develop ligands capable of targeting quadruplex DNA, an important target in many cancer therapies.[195-197] The study of site selective binding can also reveal important insight into how binding occurs at the site level, which will be a focus of this chapter. Cooperativity is essential for regulation of many biological systems, such as binding of oxygen to haemoglobin, which keep a stable oxygen level in the blood.[198,199] Knowledge of cooperativity can, also, give insight into the binding event such as direct interactions between ligands[33] and allosteric effects with conformational changes of DNA.[32] The specificity and cooperativity in binding of the of the two enantiomers of the complex $[Ru(TAP)_2dppz]^{2+}$ (**9b**) to DNA will be evaluated in this chapter as well as differences in their modes of binding to DNA and to oligomeric and polymeric sequences. Complex **9b** has been synthesised and the two enantiomers have been separated to investigate the site selectivity and cooperative binding of enantiopure samples.

As described in Chapter 1 the excited state of **9b** is quenched upon binding to poly(dG)poly(dC) in contrast to its binding to poly(dA)poly(dT) which enhances the emission. This is explained by photo-oxidation of guanine, which has a high oxidation potential (Figure 5.1).[52] One electron is transferred from guanine to **9b** after excitation because of a higher oxidation potential of the excited state followed by a back electron transfer. However, Gunnlaugsson, Kelly and co-workers have demonstrated recently for a guanine containing self-complementary decameric DNA sequence that the degree of oxidation was enhanced for binding of Λ-**9b** by substitution of guanine with inosine at position 9 (Figure 5.1).[200] This is surprising since inosine has a lower oxidation potential than guanine, and because photo-oxidation is expected to be less efficient. Crystal structures of the complex bound to the studied sequences indicated that a weaker binding next to guanine might explain the less efficient photo-oxidation. Inosine is structurally similar to guanine; however, it differs by lacking an amine group, which, as seen in the crystal structure, creates a steric clash in the minor groove between guanine and the intercalating complex. A crystal structure in which the GC-base pair is replaced by an AT-base pair showed a similar structural feature of the minor groove and of the binding mode. The three sequences with guanine, inosine and adenine at position 9 will be referred to as **G9**, **I9** and **A9**, respectively.

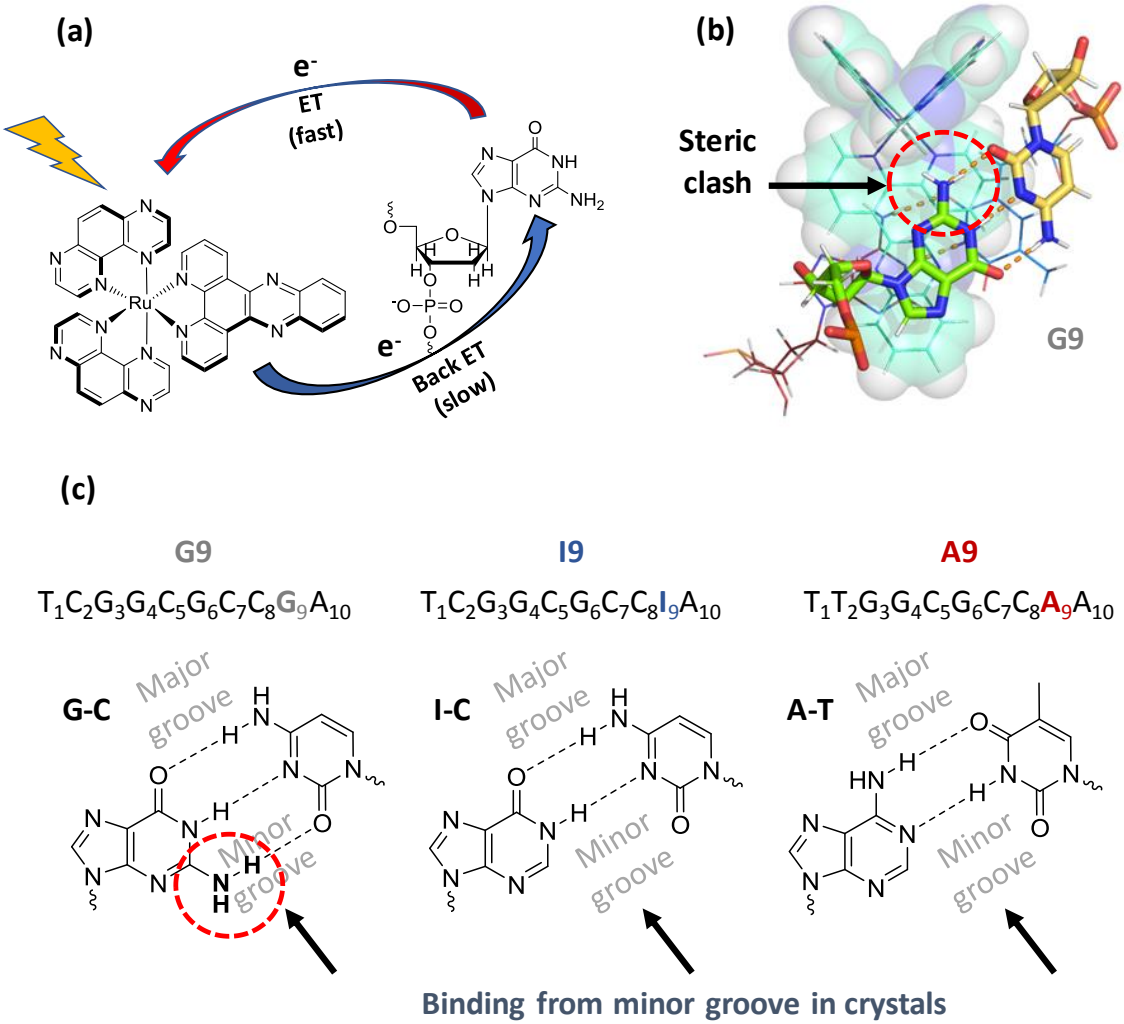

Figure 5.1: *(a) Illustration of electron transfer from guanine to Λ-**9b** after excitation followed by back electron transfer. (b) X-ray crystal structure of Λ-**9b** bound next to guanine in sequence **G9**. (c) **G9** and the two other self-complementary DNA sequences studied in the project with illustration of the base pair at position 9 of the synthetic decamers.*[200]

One objective in this chapter was to confirm that the binding strength of the complex to **I9** in aqueous media was stronger than the binding to **G9** as a consequence of the presence of the primary amine in the minor groove of **G9** at position 9. Presuming the binding occurs at this position it was expected that the affinity of the complex for **A9** was of a similar magnitude as the affinity for **I9**, since they both lack a primary amine in the minor groove in this position. A similar binding constant for **A9** and **I9** would confirm that the binding was from the minor groove in **I9** at this central step. Determination of the electrostatic and non-electrostatic contributions to the binding energy will allow further evaluation of the structural features of the binding mode and contribute to the comparison of the binding to the three sequences. The binding of Λ-**9b** to **G9** and **I9** was also studied using NMR spectroscopy.

The delta enantiomer of **9b** is expected to show little sequence specificity when binding to DNA, in contrast to the lambda enantiomer.[200] This hypothesis was tested using titrations of solutions of Δ-**9b** with poly(dG)poly(dC) and poly(dA)poly(dT). The cooperativity of the binding of Δ-**9b** to natural st-DNA was also evaluated. As far as the DNA titration experiments are concerned, several of the models described in Chapter 1 have been used to quantify binding strength, binding site size, and cooperativity. This was done with the intention of better understanding the cooperative behaviour of binding of this important compound to natural DNA and to demonstrate the applicability of the models.

5.2 Synthesis, Enantiomer Separation and Characterisation of 9b

5.2.1 Synthesis of Complex 9b

The complex $[Ru(TAP)_2dppz]^{2+}$ (**9b**) was synthesised using a standard procedure analogous to the synthesised $[Ru(L)_2mpdppz]^{2+}$, described in Chapter 2 (Figure 5.2).[80] 1,2-Phenyldiamine and 1,10-phenanthroline-5,6-dione were suspended in ethanol and heated with acetic acid. The product was isolated by centrifugation and washed with ethanol yielding the product as a grey-white solid.

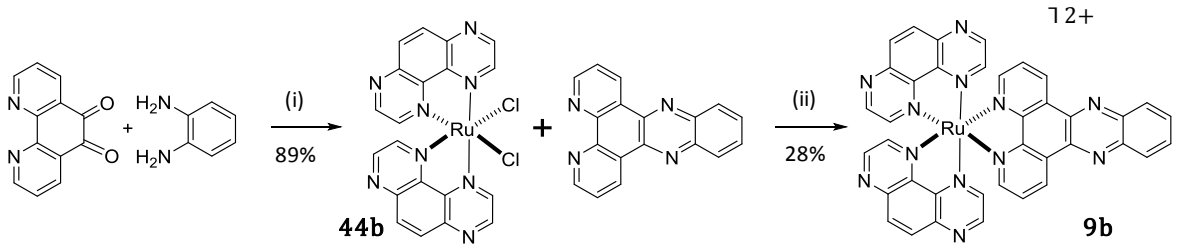

Figure 5.2: *Synthesises of ruthenium complex $[Ru(TAP)_2dppz]\cdot 2Cl$ (**9b**); (i) AcOH, EtOH, Δ, 4 h; (ii) EtOH/H_2O, Δ, 40 min.*

Complex **9b** was synthesised from $[Ru(TAP)_2Cl_2]$ (**44b**) by heating **44b** and **dppz** in a mixture of ethanol and water in a microwave. The solution was observed to change colour from dark purple to orange. Purification was achieved through alumina gradient column chromatography with a mixture of acetonitrile and water as eluent. The complex was purified further by solubilising in water followed by precipitation as the PF_6-salt by adding NH_4PF_6. The chloride form was regenerated from Amberlite and dried *in vacuo* to yield a red-brown solid. The complex was fully characterised by NMR, UV-Vis absorption and emission spectroscopy and it was confirmed that the successfully synthesis of the complex was obtained by comparing with literature values.[80] Chiral resolution was then carried out as explained in the following section.

5.2.2 Chiral Resolution of Δ- and Λ-9b

The separation of the two stereo isomers of the complex $[Ru(TAP)_2dppz]^{2+}$ was carried out by a procedure developed by a member of our group, Dr Fergus Poynton,[52,74] which is a modification of the procedure reported by Fletcher *et al.*[111,201,202] (Chapter 7). This involved the adsorption of a racemic mixture of the cationic complex onto a chiral anionic stationary phase and elution of the complex with an aqueous solution of a chiral sodium salt (Figure 5.3). Separation of the two enantiomers was achieved because of the different interactions between the two enantiomers and the chiral stationary phase and the chiral anion of the mobile phase. This resulted in an increased rate of travel through the column for one of the enantiomers, which led to the gradual separation of the enantiomers into two separate bands. In the present study, CM Sephadex C-25 was utilised as the chiral anionic stationary phase (the chirality of which arises from the five chiral centres of each of the Sephadex sugar units), whilst an aqueous solution of the chiral sodium salt (−)-*O*,*O*′-dibenzoyl-*L*-tartrate (0.1 M) was used as the mobile phase (pH 7).

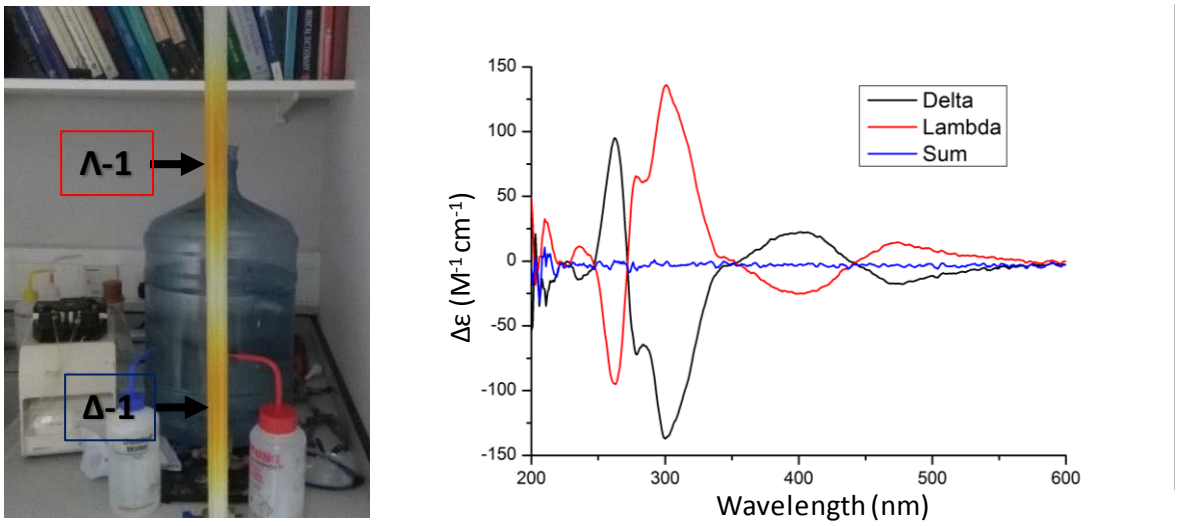

Figure 5.3: *(a) Column for chiral separation of Δ- and Λ-**9b**. (b) CD spectra of ca. 10 μM Δ- and Λ-**9b** in 50 mM potassium phosphate buffered aqueous solution (pH 7.0).*

The circular dichroism (CD) spectrum of each fraction was obtained to identify the enantiomer and to ensure adequate resolution of the complex. Large excess of solid NH_4PF_6 was added to the fractions (> 250 mg salt/10 mL H_2O) resulting in formation of the PF_6-salt, which was isolated by centrifugation and washed with water. The chloride salt of the complex was formed by swirling a solution of the complex in methanol in the presence of Amberlite. The successful and adequate resolution of each enantiomer by CD spectroscopy is described below.

5.3 Circular Dichroism Spectroscopy of Λ- and Δ-9b

The CD spectra for the two enantiomers of **9b** after successful chiral resolution is shown in Figure 5.3b. Comparison of the $\Delta\varepsilon$ values of each band in the CD spectrum of Λ- and Δ-**9b** showed that these were of equal magnitude but with opposite sign for the two enantiomers. The absolute configuration of the enantiomers was also determined by comparison of the CD spectra with those obtained by Dr Poynton from the Gunnlaugsson group.[150]

The strong CD bands in the UV-region of Λ- and Δ-**9b** correspond to the intra ligand π-π* transitions of the polypyridyl ligands, while the CD bands of moderate intensity in the visible region corresponded to MLCT transitions. These bands arose due to the chiral arrangement of ligands around the ruthenium centre.[203] Two pairs of bisignate bands (bands with opposite sign) were observed for each enantiomer at 262 and 301 nm, as well as at 397 and 476 nm. The band at 301 nm was found to be distorted due to overlap with another strong band with a maximum at 279 nm. Bisignate bands have often been observed in the CD spectra of a number of other chiral Ru(II) polypyridyl complexes,[44,205,206] and are usually due to coupling of the non-parallel electronic transition moments between different chromophores through-space by Coulombic interactions, which is termed exciton coupling.[207-209] The magnitude of exciton coupling depends on the distance and angle between the two transition moment and the strong bisignate bands in the UV region can be assigned to the perpendicular orientation between the two **phen** ligands.

5.4 Studies of Specific Binding of Λ-9b to DNA

The titrations of Λ-**9b** with the oligomer **G9**, **I9** and **A9** were carried out by addition of small aliquots of a solution of the oligomeric sequences to dilute solutions of the complex until a plateau in the absorbance and emission of the complex was reached. All oligomers were purchased from Atdbio®. The titrations were done using solutions of potassium phosphate buffer (50 mM, pH 7.0) at three different concentrations of KCl: 0 mM, 100 mM and 500 mM. The changes in the MLCT absorption band at 412 nm were monitored over the course of each titration. All titrations were repeated to ensure reproducibility.

5.4.1 Spectroscopic Changes in Spectra of Λ-9b upon Binding to DNA Oligomers

At increasing concentration of DNA, a decrease in the absorbance and emission of the complex was observed (Figure 5.4). This was consistent with similar studies previously

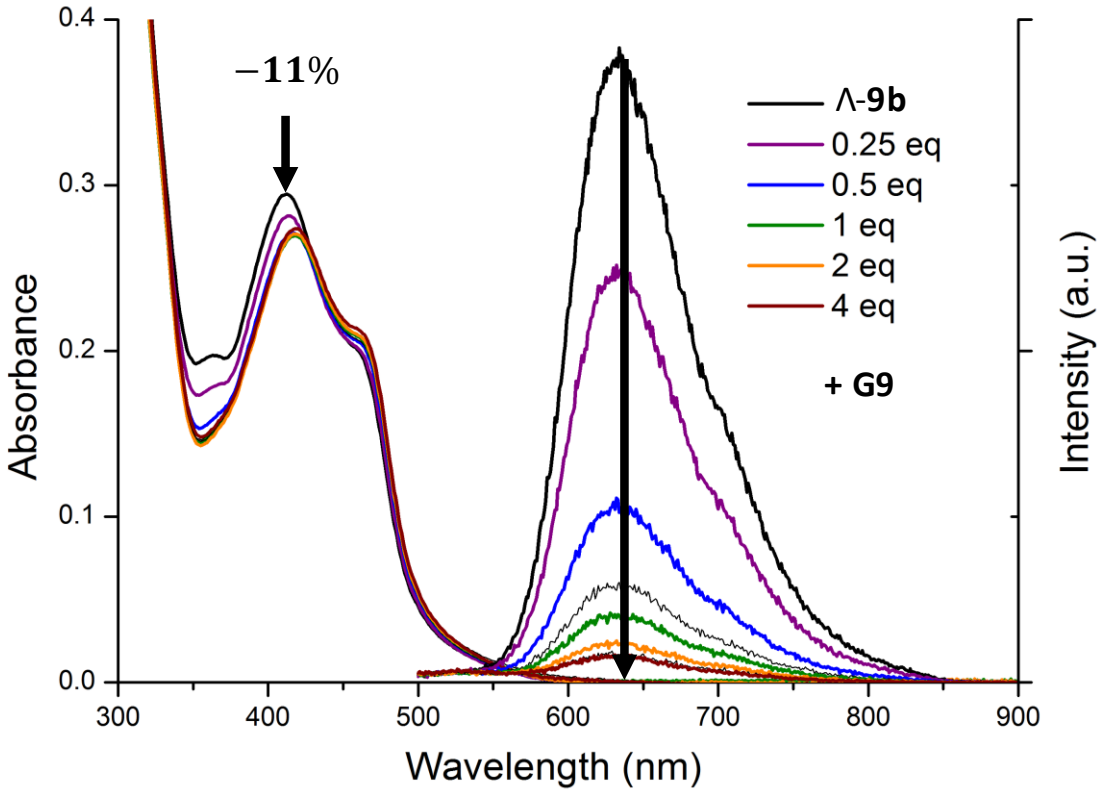

Figure 5.4: *Changes in absorption and emission spectra of Λ-**9b** (ca. 10 μM) upon titration with **G9**; changes in spectra of Λ-**9b** upon titration with **I9** and **A9** can be found in Figure A5.1; 50 mM potassium phosphate aqueous buffer at pH 7.0 and 25 °C.*

reported for **9b** with GC rich sequences of DNA, and a similar trend was seen for the titration of $[Ru(TAP)_2mpdppz]^{2+}$ (**33b**) with st-DNA (Chapter 2). As described previously, the excited state is quenched by photo-oxidation of guanine, and the hypochromic change of the absorption spectrum was a result of intercalation between the base pairs where the chromophores of the complex are near the DNA bases. The same trend was observed at all three ionic strengths (buffer only, 100 mM KCl and 500 mM KCl), however, the molar signal of the absorbance (412 nm) and the emission (integrated) reached a plateau at higher concentration of DNA duplex to ruthenium complex ratio ([duplex]/[Ru]) for increasing concentration of potassium chloride. Binding constant, binding site size, and the molar signal of bound complex were calculated from the modified Bard equation described in Chapter 1 and from ReactLab EQUILIBRIA.

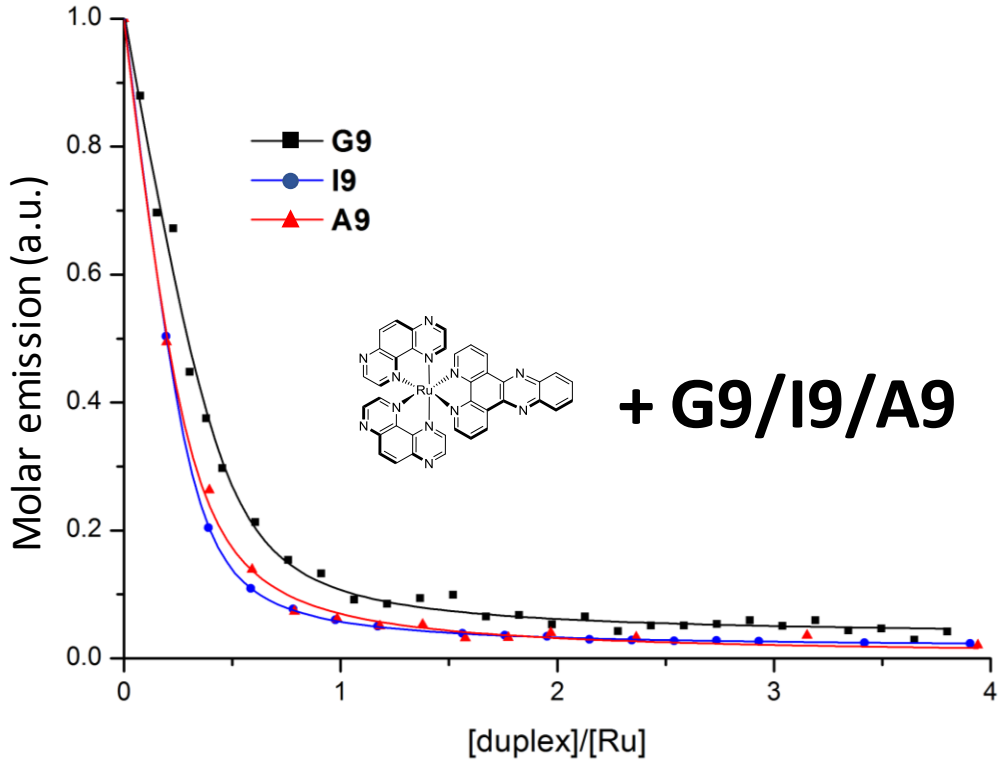

Figure 5.5: *Changes in molar emission of Λ-**9b** upon titration with **G9**, **I9** and **A9**. 50 mM potassium phosphate aqueous buffer at pH 7.0 and 25 °C.*

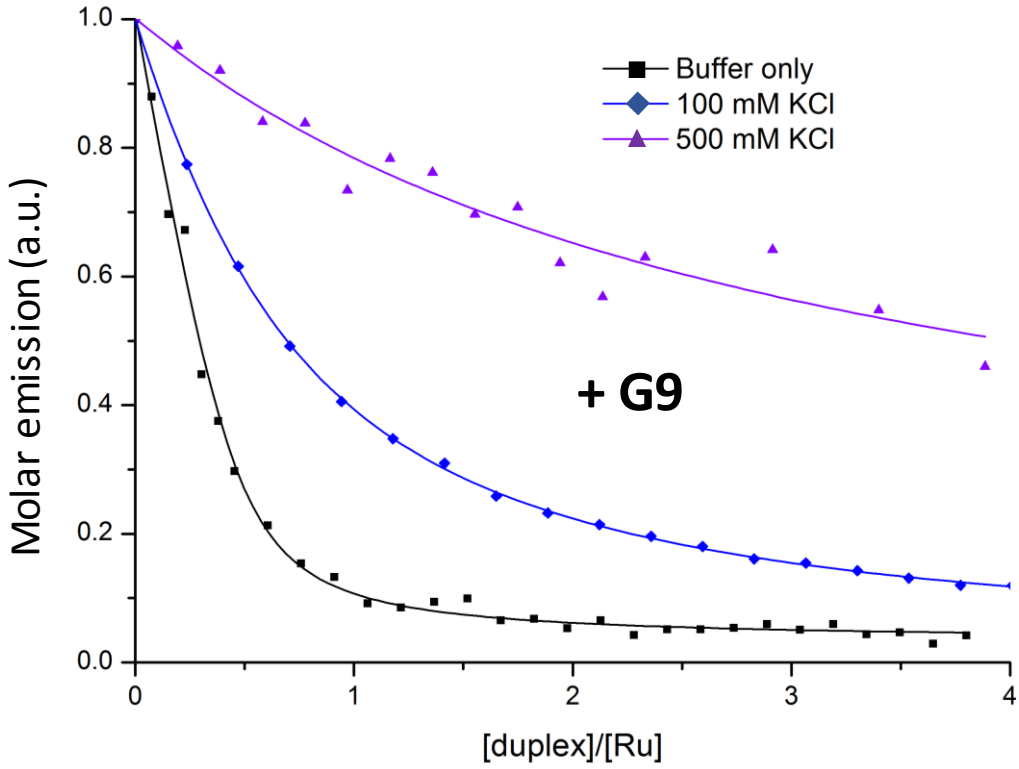

Figure 5.6: *Changes in molar emissions upon titration with **G9** at varied ionic strengths. 50 mM potassium phosphate aqueous buffer at pH 7.0 and 25 °C.*

In buffered solution, 11%, 13% and 14% decrease in the extinction coefficient at 412 nm were observed at binding to DNA for **G9**, **I9** and **A9**, respectively. The emission was fully quenched when the complex was fully bound to any of the three oligomeric sequences, which was also observed for the binding of $[Ru(TAP)_2dppz]^{2+}$ to poly(dG)poly(dC).[80] It was striking that the relative change in the molar emission was very similar for **I9** and **A9** at all three ionic strengths, while the molar signal in **G9** reached a minimum at a higher [duplex]/[Ru] ratio. This imply that Λ-**9b**, as expected, binds more strongly to **I9** and **A9** than to **G9** in accordance with the structural similarity of the expected binding site.

5.4.2 Calculations of Binding Parameters

Scatchard Binding Parameters

The modified Bard method introduced in Chapter 1 was used to calculate the Scatchard binding parameters assuming that no cooperativity is involved in the binding. Parameters calculated from absorption and emission data are of a similar size, however, the values calculated from the variations in the emission are more precise and will be used in the following discussion (Table 5.1). As expected from the crystal structure and the photo-physical behaviour, the binding constant of **I9** is closer to the binding constant of **A9** than to that of **G9** at all ionic strengths. At low ionic strength (50 mM phosphate buffer), the binding constants are 5.3×10^5 M^{-1}, 13×10^5 M^{-1} and 11×10^5 M^{-1} for **G9**, **I9** and **A9**, respectively. The binding site sizes were 4.6 bp, 3.2 bp and 3.5 bp for **G9**, **I9** and **A9**, respectively, which corresponded to the binding of two (**G9**) or three (**I9** and **A9**) complexes to the decameric duplexes (maximum number of complexes bound per duplex were given as the number of base pairs in the decamer divided by *n*).

Table 5.1: *Binding parameters calculated from emission data for the binding of Λ-**9b** to oligomeric sequences of DNA in 50 mM potassium phosphate buffer at pH 7.0 and 25 °C. The reported values and errors of the binding constant and binding site size are the mean and standard error for all replicates.*

	G9	I9	A9
k (x 10^5 M^{-1})	5.3 ± 1.0	13 ± 0.9	11 ± 2
n (bp)	4.6 ± 0.1	3.2 ± 0.1	3.5 ± 0.4
ΔG_{tot} (kJ mol^{-1})	-32.7	-34.8	-34.4
ΔG_{el} (kJ mol^{-1})	-14.6	-9.6	-9.1
ΔG_{ne} (kJ mol^{-1})	-18.1	-25.2	-25.3

As expected, the affinity of the complexes for DNA decreases with increasing ionic strength because of decreasing electrostatic attraction between the positively charged complex and the negatively charged phosphate backbone of the DNA. With increasing ionic strength the binding sites also seemed to be larger with an increase in *n* to *ca.* 10 bp for **G9** (one complex per duplex) and *ca*. 5 bp for **I9** and **A9** (two complexes per duplex) at 500 mM KCl. Apparently, the decreased electrostatic binding to the complexes decreased the "capacity" for the number of complexes that can bind to the duplexes.

Table 5.2: *Site binding constants calculated from emission data for the binding of Λ-**9b** to oligomeric sequences of DNA in 50 mM potassium phosphate buffer at pH 7.0 and 25 °C with varied concentration of KCl. The reported values and errors are the mean and standard error for all replicates. Binding constants calculated from absorption data can be found in Table A5.1.*

k (x 10^5 M^{-1})	G9	I9	A9
0 mM KCl	5.3 ± 1.0	13 ± 0.9	11 ± 2
100 mM KCl	1.6 ± 0.3	2.8 ± 0.4	5.1 ± 0.9
500 mM KCl	0.3	0.8 ± 0.1	1.3 ± 0.3

Table 5.3: *Binding site size calculated from emission data for the binding of Λ-**9b** to oligomeric sequences of DNA in 50 mM potassium phosphate buffer at pH 7.0 and 25 °C with varied concentration of KCl. The reported values and errors are the mean and standard error for all replicates. Site sizes calculated from absorption data can be found in Table A5.2.*

n (bp)	G9	I9	A9
0 mM KCl	4.6 ± 0.1	3.2 ± 0.1	3.5 ± 0.4
100 mM KCl	4.9 ± 0.7	3.3 ± 0.3	5.2 ± 0.5
500 mM KCl	10	4.8 ± 0.6	6.9 ± 0.1

Electrostatic and Non-Electrostatic Contribution to Binding

To further investigate the effect of ionic strength on binding, the recovery of the emission was monitored when KCl was added gradually to a solution containing Λ-**9b** almost fully bound to the appropriate decamer, the condition corresponding to the final terms of the spectroscopic titrations. The concentration of bound complex was calculated for increasing concentrations of KCl. Ideally, it should have been possible to calculate the concentration for the known values of E_L and E_B when E_a was measured. Unfortunately, the emission of the complex is partly quenched at the presence of KCl in the solution, most likely because

of photo-oxidation of the chloride ions.[210] To correct for this problem a solution of free complex was titrated with KCl. The molar emission was measured in pure buffer (50 mM potassium phosphate) followed by addition of a concentrated stock solution of KCl (3.95 M). After each addition, the molar emission was monitored to calculate the value of $f_{[KCl]}$ that represents the relative value of the molar emission at varied concentration of KCl (E_L([KCl])) compared to the molar emission with no KCl present (E_L). To calculate the concentration of bound complex, it is necessary to recalculate E_L and E_B, also, to account for the dependence on the concentration of KCl. Presuming the relative effect on the molar emission is independent of the presence of DNA, E_L and E_B will have to be multiplied by $f_{[KCl]}$ to get the actual value. The expression to calculate [B] becomes:

$$[B] = \frac{E_a - f_{[KCl]} \times E_L}{f_{[KCl]} \times E_B - f_{[KCl]} \times E_L} C_L = \frac{E_a / f_{[KCl]} - E_L}{E_B - E_L} C_L \quad (5.1)$$

$$f_{[KCl]} = \frac{E_L([KCl])}{E_L} \quad (5.2)$$

From the calculated values of [B], the known values of C_{bp}, and the binding site size n, the site binding constant can be calculated after each addition of KCl:

$$k = \frac{[B]}{[L]\left(\frac{C_{bp}}{n} - [B]\right)} \quad (5.3)$$

According to poly electrolyte theory[211] there is a linear relation between the logarithmic value of the binding constant for a positively charged compound to the negatively charged DNA duplex and the logarithmic value of the concentration of potassium ions:

$$\log(k) = \alpha \times \log[K^+] + \beta \quad (5.4)$$

The slope for a plot with log(k) as a function of log[K^+] will depend on the relative contribution of electrostatic and non-electrostatic interactions in the binding of the complex to DNA. When the slope α is known the electrostatic contribution to the binding energy (ΔG_{el}) can be estimated from a relatively simple expression:

$$\Delta G_{el} = -\alpha \cdot RTln[K^+] \quad (5.5)$$

When the total binding energy (ΔG_{tot}) is known, the non-electrostatic contribution (ΔG_{ne}) can be calculated:

$$\Delta G_{ne} = \Delta G_{tot} - \Delta G_{el} \quad (5.6)$$

$$\Delta G_{tot} = -RTln(k) \quad (5.7)$$

The double logarithmic plot of the variation of the site binding constants at increasing concentration of potassium ions is shown in Figure 5.7 . Again, a very similar trend is seen for **I9** and **A9**, while **G9** shows a distinct behaviour with a much more dramatic decrease in

the binding constant for increasing concentration of KCl. In Table 5.1 the calculated values are shown for the electrostatic and non-electrostatic contributions to the binding energy in pure buffer (50 mM potassium ions). The derived values for ΔG_{ne} were -18.1 kJ mol^{-1}, -25.2 kJ mol^{-1} and -25.3 kJ mol^{-1} for binding to **G9**, **I9** and **A9**, respectively. The values were, as expected, relatively unaffected by variations in the ionic strength. The higher non-electrostatic contribution to the binding energy of **I9** and **A9** is consistent with a larger hydrophobic interaction, possibly due to more overlap between the **dppz** and the base-pairs of the intercalation pocket.

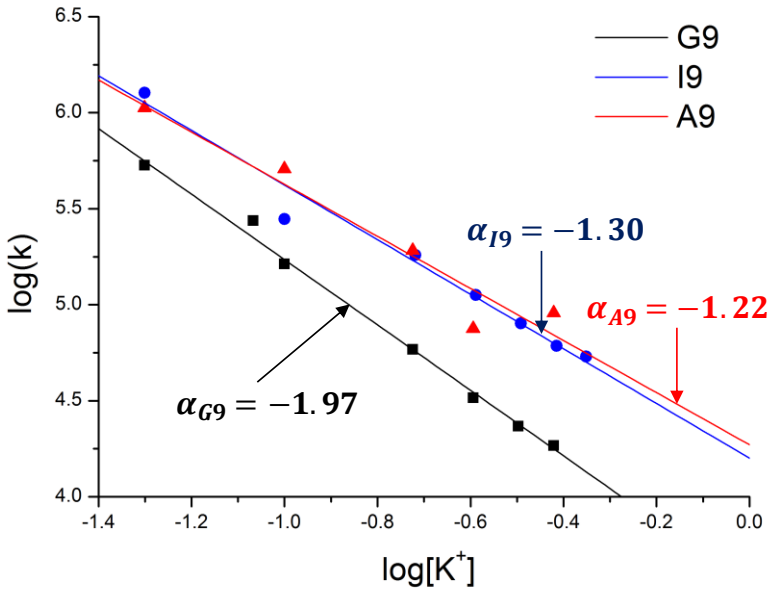

Figure 5.7: *Double logarithmic plots with site binding constants (k, M^{-1}) for affinity of Λ-**9b** for duplexes and concentration of potassium ions ([K^+], M) as dependent and independent variables, respectively. Linear fits to determine electrostatic (ΔG_{el}) and non-electrostatic (ΔG_{ne}) contributions to the free energy (ΔG_{tot}). 50 mM phosphate buffered aqueous buffer at pH 7.0 and 25 °C.*

A larger electrostatic contribution to the binding to **G9**, indicated that the relative differences between the site binding constant for **G9** on one side versus **I9** and **A9** on the other become larger at increasing ionic strength (Table 5.2). Especially for **A9** that had a site binding constant at low ionic strength twice as large as the binding constant for **G9**. With 500 mM KCl added this was four times larger. The higher electrostatic contribution to binding to **G9** may be a consequence of the lower degree of intercalation making the positively charged Ru(II) centre closer to the negative phosphate backbone resulting in stronger electrostatic attraction. The stronger non-electrostatic contribution can be explained by better overlap between **dppz** and the base pairs because of the deeper intercalation.

Calculation of Step-wise Binding Constant and the Interactions Parameter

The step-wise binding constants have been calculated from the titration data using ReactLab EQUILIBRIA to find the proper step-wise binding constants. Attempts were made to fit the titration data to different binding models to find the maximum number of complexes that will bind to the different oligomers. For the titrations at low ionic strength a maximum of two complexes can bind to **G9** (n = 5 bp), while a maximum of three complexes can bind to both **I9** and **A9** (n = 3.3 bp). The different species have been named RuD, Ru_2D and Ru_3D depending on if the number of Ru(II) polypyridyl complexes, which is bound to a DNA duplex, are one, two or three, respectively. The species distribution and calculated molar emission spectra can be found in Figure 5.8 and Figure 5.9.

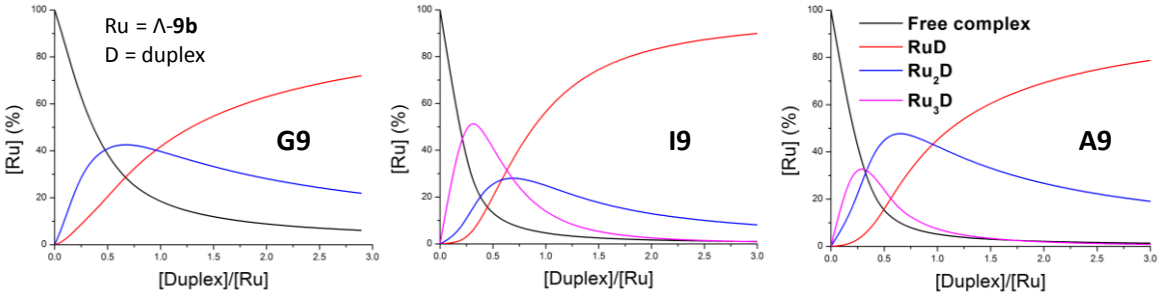

***Figure 5.8**: Change in species distribution for Λ-**9b** in the presence of **G9**, **I9** and **A9** in 50 mM aqueous phosphate buffer at pH 7.0 obtained with ReactLab EQUILIBRIA.*

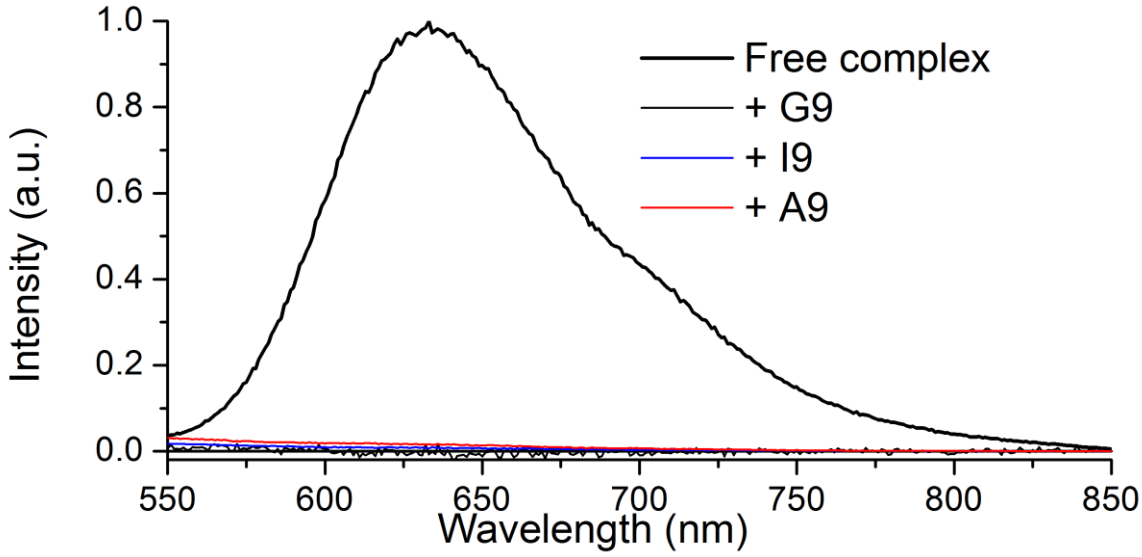

***Figure 5.9:** Molar emission spectra of Λ-**9b** as free complex in solution and at binding to each of the three oligomers; 50 mM aqueous potassium phosphate buffer at pH 7.0; obtained with ReactLab EQUILIBRIA.*

***Table 5.4**: Site binding parameters for Λ-[Ru(TAP)$_2$dppz]$^{2+}$ bound to decamers **G9**, **I9** and **A9** in 50 mM potassium phosphate buffered solution. The parameters are calculated from emission data with ReactLab EQUILIBRIA with freely parametrised binding constants.*

	G9	I9	A9
k (10^5 M^{-1})[a]	4.2 ± 0.01	13 ± 0.1	16 ± 0.3
N	2	3	3
log(α_N)	0.3 ± 0.2	0.0 ± 0.1	-0.2 ± 0.1

[a] $k = K_N^{1/N}$

These results are in strict accordance with the binding site sizes obtained in the previous section (Table 5.3). The fitted step-wise binding constants for all decameric sequences under all conditions can be found in Table A5.3. The values of the "average" site binding constant k and the average interaction parameter a_N (N is the maximum number of bound complexes, Chapter 1) have been calculated to gain an insight into the affinity for a single site and to quantify the cooperativity in the system. k is defined here as the proper equilibrium constant for:

$$L + \frac{1}{N}D \rightleftharpoons \frac{1}{N}L_N D \tag{5.8}$$

$$k = \frac{[L_N D]^{1/N}}{[L][D]^{1/N}} = \left(\frac{[L_N D]}{[L][D]}\right)^{1/N} = K_N^{1/N} \tag{5.9}$$

The parameter k represents here the average binding energy ($\langle \Delta G_B \rangle$) for each complex (L) that is bound to the duplex (D) at maximum saturation:

$$\langle \Delta G_B \rangle = \frac{\Delta G_{total}}{N} = -\frac{RTln(K_N)}{N} = -RTln(k) \tag{5.10}$$

The interaction parameter α_i was introduced in Chapter 1, equation (1.70), and corresponds to the ratio between the "average" site binding constant at maximum saturation (k), and the "average" site binding constant upon binding of the first complex to the lattice:

$$\alpha_N = \frac{k}{K_N'/N} \tag{5.11}$$

In the non-cooperative case corresponding to the Scatchard model, α_N will be exactly one. The average binding constant was very close to the value obtained by the non-cooperative Scatchard model at low ionic strength (Table 5.4) indicating that a simple non-cooperative model describes the system quite well. The fact that there was very little cooperativity was confirmed by the value of a_N which did not differ significantly from unity ($\log(\alpha_N) \approx 0$). However, the trend indicates a slightly more positive cooperativity for **G9** ($\log(\alpha_N) = 0.3$) than for **I9** and **A9** ($\log(\alpha_N) = 0.0$ and -0.2, respectively).

An explanation for this might be that the binding was more specific in **I9** and **A9** than in **G9**. According to the hypothesis under investigation, the complex will bind in the terminal steps of the three sequences. Duplex **G9** was only able to bind two complexes, which would be in the two terminal steps in the duplex. The ends of the duplex were identical since **G9** was a palindromic sequence. If no other positions were able to bind a duplex no site-selectivity would be present. Duplexes **I9** and **A9** were also palindromic sequences, however in contrast to **G9** they were able to bind up to three complexes. Two of the sites would again be the identical terminal steps of the duplexes, where the last sites for example could be the central GC step in the duplex. Because of the primary amine group in the minor groove for GC base pairs the binding was expected to be weaker at these sites and site selectivity would be present. Site selective binding can be considered as a type of negative cooperativity because the average affinity per site decreases with increasing saturations. At low saturations the sites with high affinity are unoccupied and free complexes in solution will readily bind to the duplex. At high saturations the unoccupied sites correspond primarily to sites with a low affinity for the complex and further binding will be less preferential. This would result in a negative value of $\log(\alpha_N)$.

Fits of the step-wise binding constants to the emission data derived from titrations at higher ionic strength also confirmed the results found using the Scatchard model, that is, a low cooperativity, however the errors were larger (Figure A5.3). It has been possible to fit the more imprecise absorption data with ReactLab EQUILIBRIA, only, using the Scatchard model (Table A5.4).

5.4.3 NMR Titrations of Λ-9b with G9 and I9

To obtain more direct evidence that the complex in solution is bound to the oligonucleotides in the same position as observed in the crystal structure, ^{1}H NMR (D_2O, 800 MHz, 50 mM potassium phosphate, pH 7.0) experiments were carried out. Absorption and emission spectroscopy give very little structural information about the binding. The finding that the lack of a primary amine group at position 9 significantly increased the binding strength strongly indicated that the binding occurs here as also observed in the crystal structure. However, it can be said with some certainty that the complex was bound next to position 9 it cannot be said whether the intercalations were between base 8 and 9 or between base 9 and 10 (Figure 5.1). On the other hand NMR gives direct insight into the structure of the studied systems in solution like X-ray crystallography does in solid state. Several examples have been presented in the literature where NMR has been used to evaluate the structural

features of DNA with bound compounds, including ruthenium complexes.[212] In addition to gaining insight into the binding position of the compound it might also be possible to gain an insight into the binding mode and the conformation of the studied duplex.[213]

Concentrations of 0.4 mM Λ-**9b** and 0.5 mM decamer were used in the experiments, where the absorption and emission titrations were carried out with a concentration of *ca.* 10 μM of complex. Since excess of duplex was used compared to the concentration of Λ-**9b**, and since the concentration of complex was much higher than the dissociation constant ($k^{-1} >> 10^{-5}$ M) it could be presumed that all complex was bound to DNA. Because of the low cooperativity, it was expected that most of the bound complex corresponded to the situation where a single complex was bound to a decameric sequence of DNA. However, in theory, up to three complexes should be able to bind to each decamer, which complicated the situation. It enabled the presence of three possible forms of oligomeric sequences with bound complex plus the decameric sequence without bound complex.

In Figure 5.10 and Figure 5.11 are shown the recorded ^{1}H NMR spectra for the different conditions. It was clear from the spectra of the mixture of Λ-**9b** and the decameric sequences that the complex binds to DNA. However, proper structural features cannot be

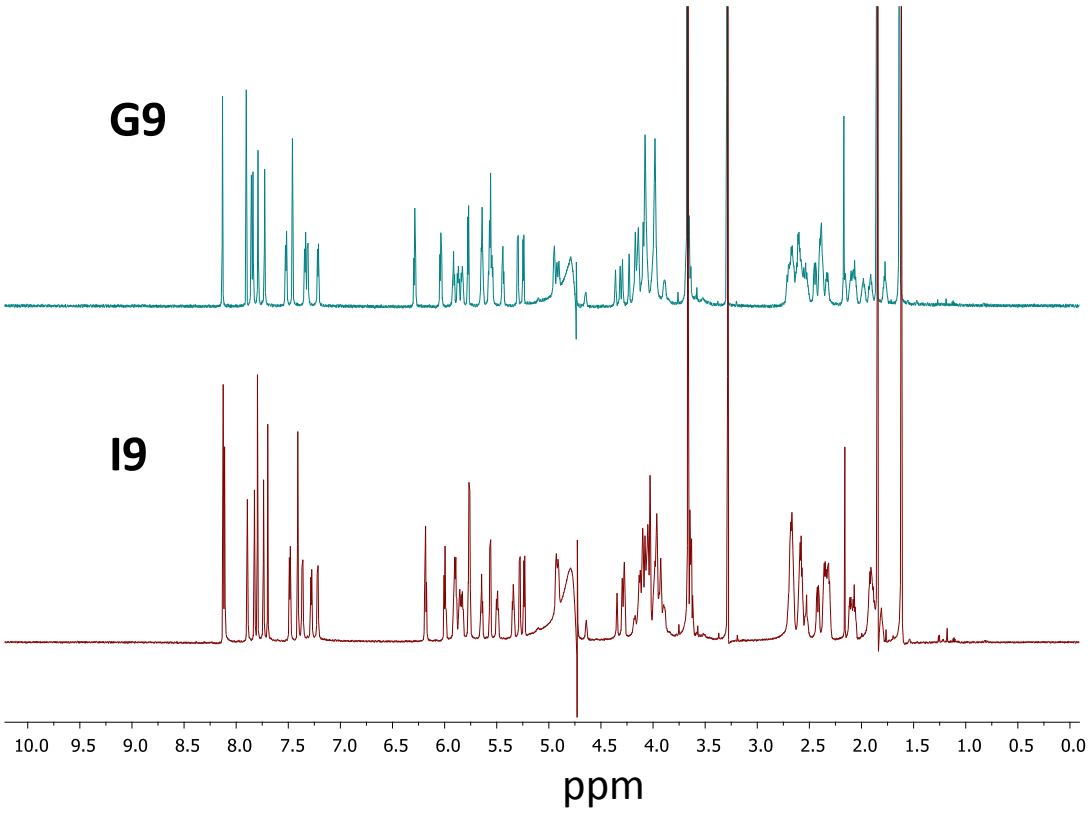

Figure 5.10: *^{1}H NMR (D_2O, 800 MHz, 50 mM potassium phosphate, pH 7.0) spectra of oligomeric sequences **G9** and **I9** (0.5 mM, 1 eq).*

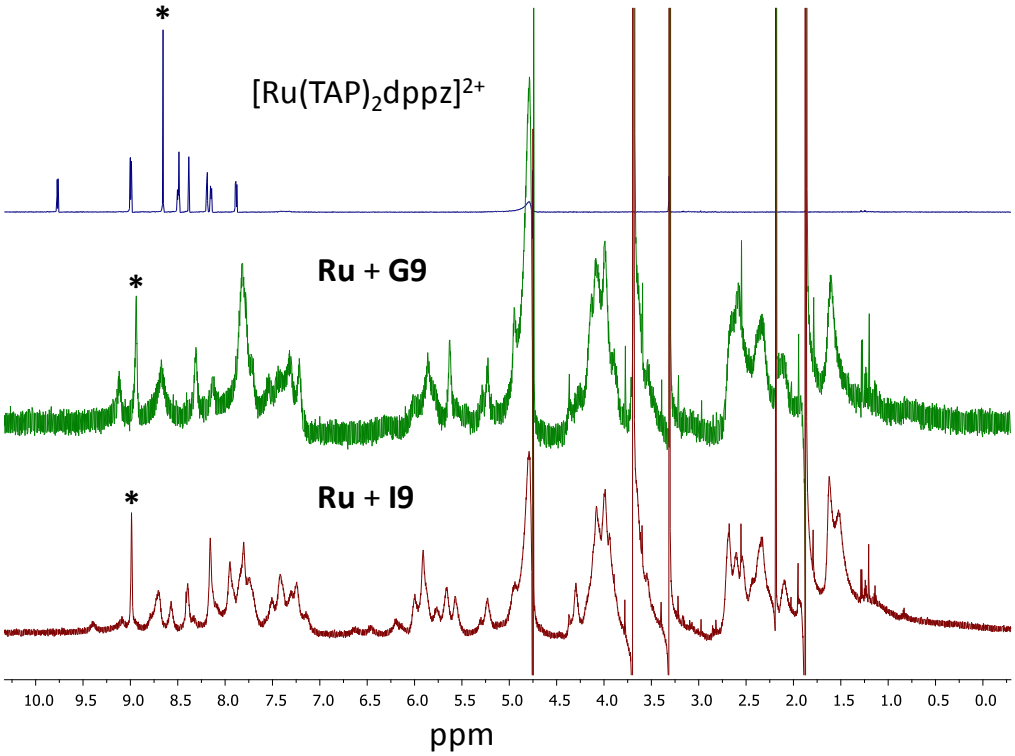

Figure 5.11 *^{1}H NMR (D_2O, 800 MHz, 50 mM potassium phosphate, pH 7.0) spectra of Λ-**9b** (0.4 mM, 0.8 eq) and Λ-**9b** (0.4 mM, 0.8 eq) together with oligomeric sequences **G9** and **I9** (0.5 mM, 1 eq) alone and together. 50 mM potassium phosphate buffered aqueous solution at 25 °C. Spectra at varied temperatures are shown in Figure A5.10 and Figure A5.11.*

obtained from the spectra since these were very noisy and had broad peaks. This might be due to a combination of several factors including the possibility mentioned above of different forms of decamers with two or three complexes bound to a single duplex. Furthermore, for each stoichiometry, the complexes would be able to bind in different ways to a single duplex. The crystal structure indicated the possibility of three different binding sites, and the calculated interaction parameter calculated in the previous section indicated little site specificity in the binding mode. In theory, there may be up to nine different intercalation pockets (Figure 5.14) making the spectrum a superposition of the spectra for several different forms.

The resonances for the spectrum involving Λ-**9b** were slightly sharper in the presence of **I9** than in the presence **G9**. This indicated more specific binding, and it was consistent with studies from the absorption and emission titration experiments. The spectra had narrower resonance peaks for **G9** after increase of temperature up to 45 °C, which was expected to be the result of faster exchange between the different forms (Figure A5.10). The corresponding resonance peaks became sharper at increased temperature in the presence of

I9, however, new resonance peaks also appeared (Figure A5.11). This can be explained by less specific binding at higher temperature, according to Boltzmann's distribution.

5.4.4 NMR Titrations of Λ-9b with d(CCGGTACCGG)$_2$ (TA)

For comparison the sequence d(CCGGTACCGG)$_2$ (duplex **TA**) has also been investigated for site selective binding. The duplex was like **G9**, **I9** and **A9** purchased from AtdBio®. More explicit structural information have been possible to derive from titrations of Λ-**9b** with **TA**. It has been shown that the intercalation pocket at the central TA step binds Λ-**9b** much stronger than any other potential binding sites of the duplex (Figure 5.12).[152,214] A crystal structure of the complex bound to **TA** showed intercalation of three complexes at the decamer, including an intercalation in the TA pocket. A similar crystal structure of Λ-**9b** bound to the same decamer sequence d(CCGGATCCGG)$_2$ (duplex **AT**) with the reverse order of the central step showed no intercalation at the central step. To evaluate the expectation that the complex would primarily bind to the central step in **TA**, an NMR titration experiment was carried out. The result should be compared to the situation in which **G9** or **I9** are used. According to the spectroscopic and NMR titration experiments described above little site specific preferences were observed in these cases.

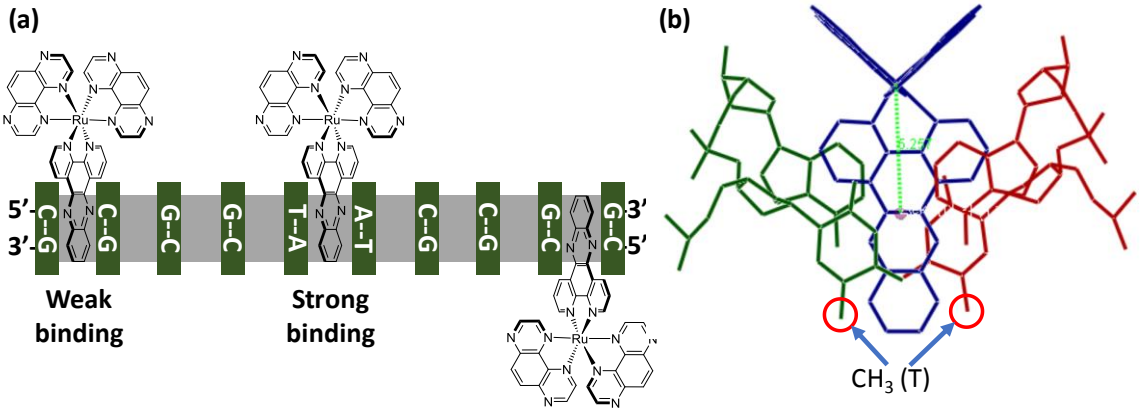

Figure 5.12: *(a) Schematic illustration of site specific binding of Λ-**9b** to oligonucleotid **TA**. (b) An X-ray crystal structure for Λ-**9b** bound the central TA-step.*

Figure 5.13 shows the ^{1}H NMR spectrum of TA in the presence of Λ-**9b**. The spectrum for this mixture was much more structured, and had sharper peaks than the spectra recorded for **G9** and **I9** in the presence of Λ-**9b**. Especially noticeable was the splitting of the signal for the methyl group at thymine at 1.38 ppm. In the presence of Λ-**9b** a signal with the same shift was still present corresponding to duplex with no bound complex or to duplex where the complex binds to a place other than at TA. However, a signal at 1.26 ppm appears slightly downfield, quite well corresponding to intercalation of a complex in the TA pocket.

According to the crystal structure there will be the same change in the chemical shift of two thymine methyl group as a result of symmetry, which also seems to be the case. However, from the location of the methyl groups relative to the aromatic phenazine rings it would be expected that a downfield change in the chemical shift was observed because of the ring current of the ring system. It was expected that a slightly different binding geometry was present in solution which would place the methyl groups in the centre of the neighbouring benzene ring, which would result in the observed upfield change in the spectrum. This could for example be a result of electrostatic interactions with the phosphate backbone.[18] Break of symmetry would not result in splitting of the methyl signal if the energy barrier between the two possible conformations was small since a fast exchange compared to the NMR time scale would be present.

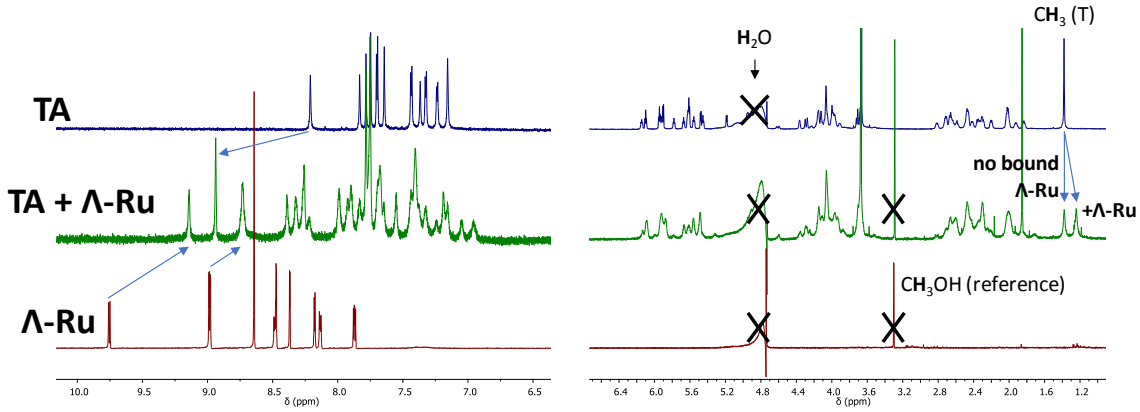

Figure 5.13: *^{1}H NMR (D_2O, 800 MHz) spectra of Λ-**9b** (0.4 mM, 0.8 eq) and the oligomeric sequence **TA** (0.5 mM, 1 eq), alone and together. 50 mM potassium phosphate buffered aqueous solution at 25 °C. Spectra at varied temperatures are shown in Figure A5.12.*

From the relative size of the proton integrals for the two peaks it can be deduced that *ca.* 57% of all **TA** have complexes bound next to T. If all complexes in solution were bound to this step, 80% of all duplexes would display an upfield shift of the methyl signals according to the [duplex]/[Ru] ratio used in the experiment. The reason why only about 60% were bound next to T can be explained by binding to other binding sites. According to the crystal structure two complexes were able to bind in the ends of the duplex, and, consequently, it is likely that about 20% of all complexes were bound here rather than at the preferred central AT step. Presuming three independent binding sites in solution, as seen in the crystal structure for the solid state, the relative strength for the different sites can be estimated. The relative distribution of complexes bound at the TA step (B_{TA}) and one of the terminal CC/GG step (B_{CG}) can be derived from the proton integrals that showed that 57% of all duplexes had a complex bound next to TA:

$$[B_{TA}] = \frac{0.57}{0.8} C_{Ru} = 71\% \times C_{Ru}, \qquad [B_{CG}] = 29\% \times C_{Ru}, \; C_{\boldsymbol{TA}} = \frac{5}{4} C_{Ru}$$

It can be presumed due to symmetry that the two terminal binding sites have the same site binding constant (k_{CG}). The site binding constant for these sites and the one for the central TA step will be defined as:

$$k_{TA} = \frac{[B_{TA}]}{[Ru][TA]}, \qquad k_{CG} = \frac{[B_{CG}]}{[Ru][CG]}$$

[Ru] is the concentration of free unbound complex in solution and [TA] and [CG] are the concentration of unoccupied binding sites at the TA/TA and the CC/GG steps, respectively. The concentration of free unoccupied TA-binding sites is ($C_{\boldsymbol{TA}}$ – [B$_{TA}$]) and the concentration of free unoccupied CG-binding sites is (2 × $C_{\boldsymbol{TA}}$ – [B$_{CG}$]). Since the total concentration of **TA** (C_{TA}) was 0.5 mM and the total concentration of complex (C_{Ru}) was 0.4 mM the relative strength of k_{TA} compared to k_{CG} was:

$$\frac{k_{TA}}{k_{CG}} = \frac{\frac{[B_{TA}]}{[Ru][TA]}}{\frac{[B_{CG}]}{[Ru][CG]}} = \frac{[B_{TA}][CG]}{[B_{CG}][TA]} = \frac{[B_{TA}](2C_{TA} - [B_{CG}])}{[B_{CG}](C_{TA} - [B_{TA}])}$$

$$\frac{k_{TA}}{k_{CG}} = \frac{71\% \times C_{Ru}\left(2 \times \frac{5}{4} \times C_{Ru} - 29\% \times C_{Ru}\right)}{29\% \times C_{Ru}\left(\frac{5}{4} \times C_{Ru} - 71\% \times C_{Ru}\right)} = 10$$

In other words, the concentration of complexes bound at the TA-step is 10 times larger than the concentration at any other site. It was presumed that, of the eight potential binding pockets of TA, only the TA-step and the two terminal sites are able to bind a complex. The actual difference between the concentration of complex bound to the TA-step and the concentration of complex bound to other sites might, for that reason, be larger than 10. In contrast to the mixture of Λ-**9b** and **G9**, the increase of the temperature for Λ-**9b** mixed with **TA** resulted in broadening of the signals. This indicated that the exchange between the different forms was relatively slow, but sufficiently fast to happen within the NMR time scale (~1 s).

5.4.5 Conclusion for Site-specific Binding of Λ-9b to DNA

It has been demonstrated that substitution of guanine for inosine in a DNA decamer significantly enhances the affinity of the decamer for Λ-**9b** from 5.3 × 10^5 M^{-1} to 13 × 10^5 M^{-1}. This is explained by the existence of an NH_2 group in the minor groove of the decamer when guanine is included, resulting in a steric clash at binding. Substitution of a GC base pair with IC or AT had a similar effect on the binding behaviour with a large

increase in the affinity for Λ-**9b** as result of a large increase in the non-electrostatic contribution to the binding energy. This is in good agreement with the fact that neither IC nor AT have NH_2 group in the minor groove. This allows for a deeper intercalation of the **dppz** part of the complex and results in stronger binding because of improved stacking interactions. NMR studies of binding of the complex to **G9** and **I9** showed little site-selectivity, however the spectrum of **I9**, indicated some selectivity.

5.5 Comparison of Binding of the Enantiomers to Oligomeric and Polymeric DNA

The binding site sizes for Λ-**9b** to oligomeric sequences presented in the previous section were larger than what was usually observed for binding of Ru-**dppz** complexes to polymeric DNA.[44,54,80] The reason may be that the studied oligomers were DNA strings rich of GC compared to natural DNA that have a GC content at less than 50%. If the binding of Λ-**9b** to DNA was weak it could result in large binding site sizes. It is likely that AT-rich DNA would give smaller binding site sizes than those seen for natural DNA. It also must be taken into consideration that a simple non-cooperative binding model is usually used to describe the binding, which might give an inaccurate value of the binding site size.

Further, it is necessary to take into consideration that we are working here with small oligomeric sequences of DNA that are in many ways different from polymeric DNA. Some very simple considerations are illustrated in Figure 5.14. It must be kept in mind that a reported binding site size is always a measure of the stoichiometry of the binding and not necessarily the actual size of a ligand (maximum number of complexes bound per duplex are given as the number of base pairs in the sequence divided by *n*). For an intercalator the number of potential binding pockets between base pairs that are present may be more important than the number of bases. This number is always one less than the number of base pairs. A circumstance that also might give an increase in the apparent binding site size is that it is impossible for a non-integer number of complexes to bind to the decamer. If a complex demands four base pairs to bind to the duplex it will only be possible for two complexes to bind, given an effective binding site size of five base pairs.

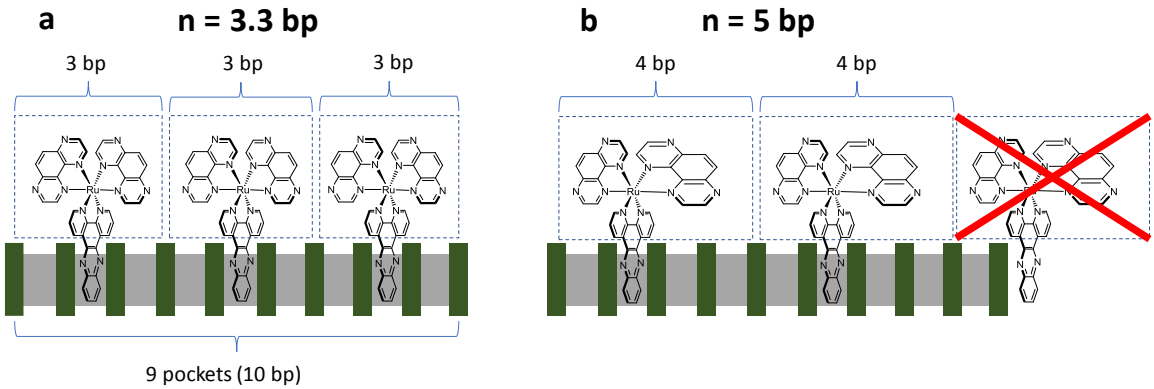

Figure 5.14: *Figure illustrating the possible explanations for the large apparent binding site size observed for decameric sequences compared to what is observed for polymeric DNA duplexes. (a) An actual size of three bp of the complex can give rise to an apparent site size of 3.3 bp. (b) An actual site size of four bp will give an apparent site size of five bp.*

More complex considerations that must be included are that the intrinsic properties of oligomeric and polymeric DNA are in some respects very different. It is difficult to predict, how these differences will affect the binding site size. For example, the degree of hydration of oligomeric and polymeric DNA will be different[215,216] as well as the interactions with ionic species[211] and the stability of the DNA duplex.[217]

5.5.1 Titrations of Δ- and Λ-9b with st-DNA

Titrations experiments with st-DNA were carried out under the same conditions as those used for the studies of binding to **G9**, **I9** and **A9**. The spectroscopic changes in the emission spectra were different for the titrations of Δ- and Λ-**9b**. The delta enantiomer showed, as expected, a gradual decrease in the emission at increased concentration of DNA. This was also seen when the racemic mixture was titrated with ct-DNA[80] and for similar experiments described in Chapter 2 for the **TAP** complex **33b**. On the other hand, the lambda enantiomer showed biphasic behaviour. In the beginning of the titration a steady decrease was observed at increasing concentrations of DNA. However, after a plateau was reached, the emission began to increase. It seemed that the molar emission of bound complex was less quenched at low saturations than at high. This behaviour might be explained by site specific binding with a preferential binding to the AT rich region of DNA. It is known that poly(dG)poly(dC) quenches the emission while poly(dA)poly(dT) enhances emission at binding to complex **9b**.[80]

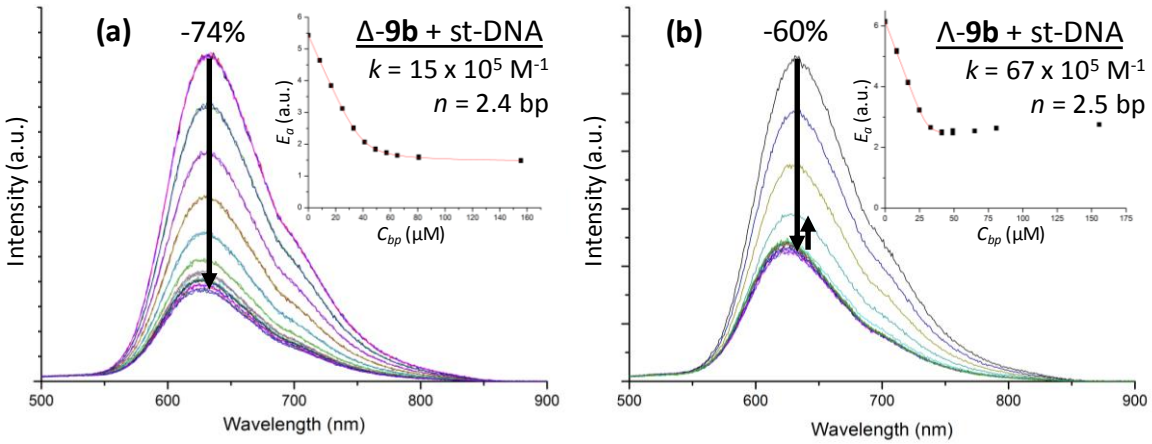

Figure 5.15: *Changes in the emission spectra of Δ-**9b** (a) and Λ-**9b** (b) at titration with st-DNA; 50 mM potassium phosphate aqueous buffer, pH 7.0 and 25 °C, ca. 10 μM complex.*

The recovery of the luminescence was modest, however, this made it a challenge to calculate the binding parameters from the changes in the spectrum, since the fits to the data depended on a linear relation between the fraction of bound complex and the molar emission. The fit in Figure 5.15b was expected to yield a relatively large error. Different values were obtained from the absorption data, which emphasised the problem (Table A5.15). On the other hand, the use of ReactLab EQUILIBRIA in a similar manner as in Chapter 2 for **phen** complex **33a**, was expected to correct for the non-linear behaviour. Two equilibria for fits to the changes in the emission spectrum of Λ-**9b** yielded results that were much more similar to what was obtained from the change in the absorption data (Table A5.15).

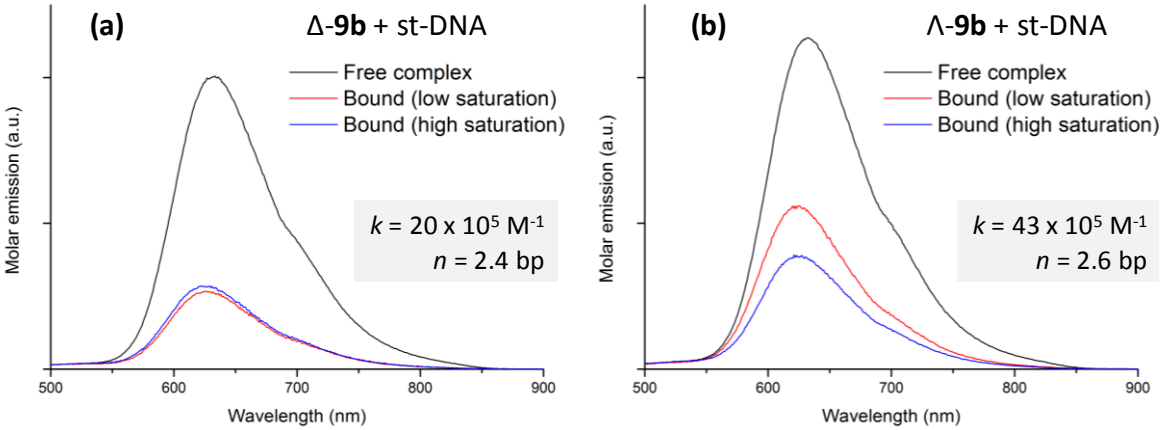

Figure 5.16: *Molar emission spectra of Δ-**9b** (a) and Λ-**9b** (b) as free complex (black) in solution and at binding to st-DNA at low saturation (red) or high saturation (blue); 50 mM potassium phosphate buffer, pH 7.0, 25 °C, ca. 10 μM complex; obtained with ReactLab EQUILIBRIA using two equilibria.*

5.5.2 Electrostatic and Non-Electrostatic Contribution to Binding

The electrostatic and non-electrostatic contributions to the binding were quantified in the same way as done for the binding of Λ-**9b** in Section 5.4.2. Unfortunately, it was only possible to do the quantification for Δ-**9b** using the described method because of the biphasic behaviour of the change in the emission spectrum of Λ-**9b**. A standard titration of Δ-**9b** in potassium phosphate buffered aqueous solution without any KCl present, was carried out until almost all complex was bound to DNA. Afterwards the concentration of KCl was gradually increased, and the Scatchard binding constant for each condition was calculated from the emission. The non-electrostatic contributions to the binding energy was almost unaffected by changes in the ionic strength with a value of -15.6 kJ mol^{-1} at low ionic strength (50 mM K^+).

There is a larger electrostatic contribution to the binding for st-DNA than was observed for the oligomeric sequences (Table 5.1). The higher electrostatic contribution to the binding can be a result of the higher negative charge of DNA resulting in stronger attraction to positively charged species, especially compared to a binding in the end of oligonucleotides where the charge density is lowest. This might explain why a larger binding constant is observed for polymeric DNA. On the other hand, a smaller non-electrostatic contribution was observed for the binding energy for binding to st-DNA than for binding to the oligomeric sequences. This might be result of the disturbance introduced in the helical structure when an intercalator bind to a DNA duplex. The disturbance of polymeric DNA will be on a much larger scale than when an intercalator binds to an oligonucleotide of a finite length.

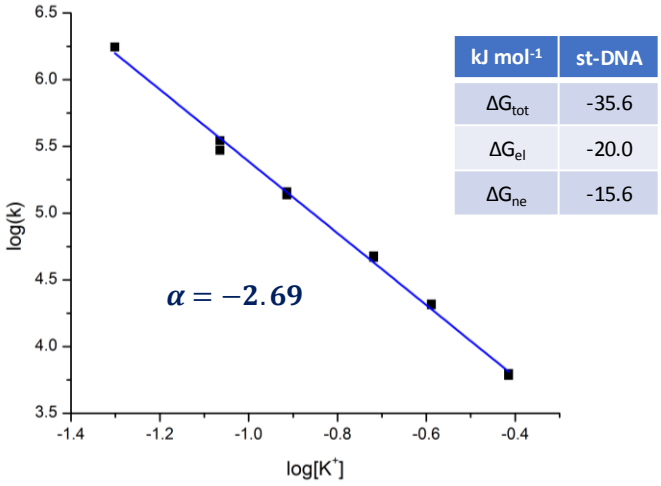

Figure 5.17: *Double logarithmic plots with site binding constants (k/M^{-1}) for affinity of Δ-**9b** for st-DNA and concentration of potassium ions ($[K^+]/M$) as dependent and independent variables, respectively. Linear fits to determine electrostatic (ΔG_{el}) and non-electrostatic (ΔG_{ne}) contributions to the free energy (ΔG_{tot}). 50 mM phosphate buffered aqueous solution at pH 7.0 and 25 °C, ca. 10 μM complex.*

5.5.3 Titrations of Δ- and Λ-9b with Oligonucleotides

To further explore if there was a general trend in the difference between binding to oligomeric and polymeric DNA, titrations of Δ- and Λ-**9b** with two dodecameric DNA sequences have been carried out with the sequence d(CGCGAATTCGCG)$_2$ (duplex **A2T2**) and d(CGCAAATTTGCG)$_2$ (duplex **A3T3**). Both sequences showed similar changes in the absorption spectra as seen for **G9**, **I9** and **A9** with increasing concentration of DNA, with a hypochromic change in the MLCT band at 412 nn (Figure A5.17 and Figure A5.18). However, the changes in the emission were very different. The change in the emission for **A2T2** was similar to what is seen for the titration with st-DNA, with a decrease in the emission with increasing concentration of DNA, but in contrast to *e.g.* **G9** it was not a 100% quenching. The change in the emission for **A3T3** showed even more deviating behaviour with a mixture of increasing and decreasing molar emission through the titrations with Δ- and Λ-**9b**. This behaviour might be explained by site specific binding with preferential binding to the AT rich region of the oligomers. It is known that poly(dG)poly(dC) quenches the emission while poly(dA)poly(dT) enhances emission at binding to **9b**. It was not surprising that **A3T3**, in particular, showed an unusual variation in the emission at binding to **9b**, since this sequence has an AT and GC content of 50%. Site specific binding was also used to explain the biphasic change in the emission spectrum of Λ-**9b** at titration with st-DNA.

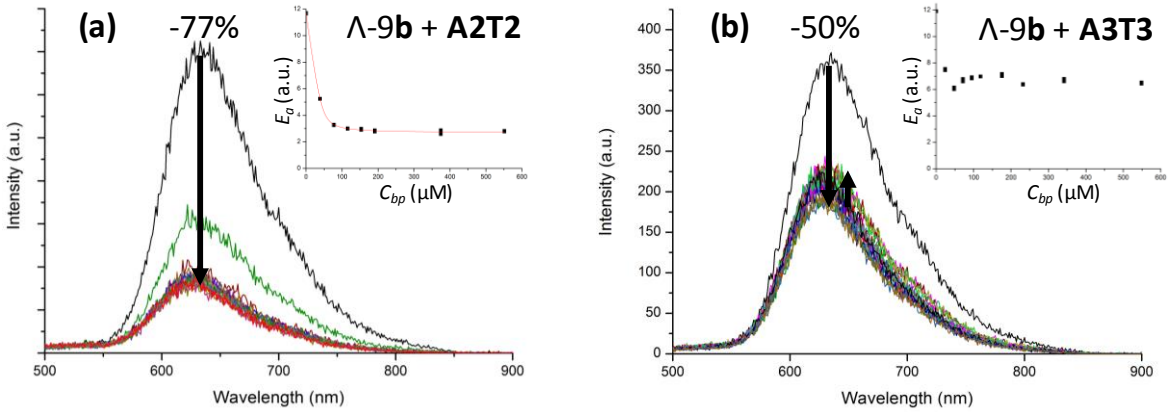

Figure 5.18: *Changes in the emission spectra of Λ-**9b** at titration with (a) **A2T2** and (b) **A3T3**; 50 mM potassium phosphate aqueous buffer, pH 7.0, 25 °C, ca. 10 μM complex.*

5.5.4 Conclusion for Comparison of Binding to DNA

Table 5.5 and Table 5.6 show Scatchard binding parameters calculated from emission or absorption data for the two enantiomers for binding to different oligomeric sequences of DNA. It is striking that all oligomeric sequences show weaker binding than binding with st-DNA. Similar to the observation described previously, most of the cases concerning

binding to oligomers show larger binding sites (Table 5.3 and Table 5.6). Two exceptional cases were the binding of Δ-**9b** to **G9** and **I9** that gave slightly smaller binding site sizes than was obtained for similar binding to st-DNA. It was demonstrated that the electrostatic contribution to the binding energy was higher for polymeric than for oligomeric DNA, which could contribute to the explanation of the different binding behaviour.

Table 5.5: *Scatchard site binding constants for the binding of Δ- and Λ-**9b** to different sequences of DNA in 50 mM potassium phosphate buffer at pH 7.0 and 25 °C.*

k (x 10^5 M^{-1})	G9[a]	I9[a]	A9[a]	A2T2[a]	A3T3[b]	st-DNA[a,d]
Δ-9b	1.1[c]	1.3[c]	-	13	2.7	20
Λ-9b	5.3	13	11	16	3.2	43

[a] Fitted to emission data; [b] fitted to absorption data; [c] calculated from titration data obtained by Dr Poynton. [d] Fitted with ReactLab to correct for non-linear behaviour in the spectroscopic changes.

Table 5.6: *Binding site size for the binding of Δ- and Λ-**9b** to different sequences of DNA in 50 mM potassium phosphate buffer at pH 7.0 and 25 °C.*

n (bp)	G9[a]	I9[a]	A9[a]	A2T2[a]	A3T3[b]	st-DNA[a,d]
Δ-9b	2.1[c]	2.0[c]	-	4.5	3.9	2.4
Λ-9b	4.6	3.2	3.5	5.1	2.7	2.6

[a] Fitted to emission data; [b] fitted to absorption data; [c] calculated from titration data obtained by Dr Poynton. [d] Fitted with ReactLab to correct for non-linear behaviour in the spectroscopic changes.

5.6 Cooperative Binding of Δ-9b to Polymeric DNA (st-DNA)

Spectroscopic titrations of Δ-**9b** with st-DNA have been carried out in order to study cooperativity in the binding to DNA. The choice was to study the Δ-enantiomer since the change in the emission is more easy to use for calculations of binding parameters because of the biphasic nature for the Λ-enantiomer, as described in Section 5.5.1. The biphasic nature made the concentration profile calculated from the relative change in the emission less reliable. This was also the reason why it only was possible to calculate the electrostatic and non-electrostatic contributions to the binding of Δ-**9b** to st-DNA and not to the binding of the Λ-form in Section 5.5.2. The titrations have been done with 50 mM potassium phosphate buffer and 50 mM KCl ($\log[K^+] = -1$). This ionic strength was chosen since it resulted in a moderate strength of the binding constant, which offer the optimal conditions for fits of more

complex binding models. According to the double logarithmic plot shown in Figure 5.17 the value of *k* would be 2.4×10^5 M^{-1} ($10^{5.3}$ M^{-1}) at 100 mM [K^+] (10^{-1} M).

It is often difficult to fit cooperative binding models, since more parameters must be fitted than for a simple non-cooperative binding description.[55] For that reason very precise measurements were made to avoid over-parametrisation. Titrations using more than 30 different concentrations of DNA, have been carried out, and, for each concentration, the emission was given as the average of 16 measurements. This procedure reduced the statistical error to a fourth compared to a procedure in which only one measurement is performed (the size of the error is inversely proportional to the square root of the number of measurements). In the following sections are presented results obtained from titrations using absorption and CD spectroscopy; however, these techniques were not sensitive enough to calculate cooperativity parameters.

5.6.1 Spectroscopic Changes in Spectra of Δ-9b upon Binding to st-DNA

The changes in the absorption and emission spectra at titrations with st-DNA were consistent with those described in Section 5.5.1 at lower ionic strength, however, a plateau was reached at a higher Ru/bp ratio (Figure 5.19). A 15% hypochromic change was observed in the MLCT band at 412 nm, and a 72% decrease was seen for the emission spectrum.

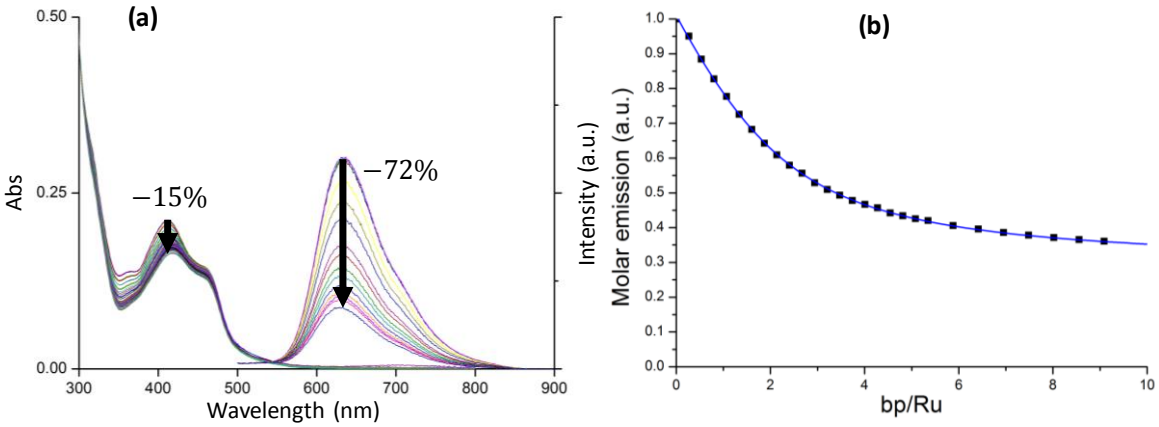

Figure 5.19: *(a) Changes in absorption and emission spectra of Δ-**9b** at titration with st-DNA. (b) Changes in molar emission of Δ-**9b** at titrations with st-DNA; 50 mM potassium phosphate aqueous buffer with 50 mM KCl, pH 7.0, 25 °C, ca. 10 μM complex.*

A gradual change was also observed in the CD spectrum of Δ-**9b** at titration with st-DNA (Figure 5.20). A decrease was observed of the positive signal at 397 nm and of the negative signal at 301 nm. An increase was observed of the positive signal at 262 nm. The large change in the bisignate bands at 262 and 397 nm can be assigned to large interactions between the ancillary **phen** ligands and the chiral sugar-phosphate backbone of DNA. This

was in accordance with the placement of this ligands in the groove when **dppz** intercalated between the base pairs. The CD spectrum of Λ-**9b** was a perfect mirror image of the spectrum of the delta enantiomer (Figure 5.3). The changes in the spectrum for a similar titration had the same sign, *i.e.* the positive band for Λ-**9b** at 300 nm becomes less positive, and the negative band at 260 nm becomes less negative (Figure 5.21). No significant change was observed in the negative band at 415 nm in accordance with little ICD in this region of the spectrum. The change in the CD signal of Δ-**9b** at this wavelength was also relatively small. It was expected that the change would be smaller for the Λ-enantiomer since the band was negative and as a hypochromic change was observed in the absorption spectrum. That no change was observed for the Λ-**9b**, in contrast to Δ-**9b**, can be explained by the negative ICD was cancelled out with the decrease in the absorbance of the MLCT band.

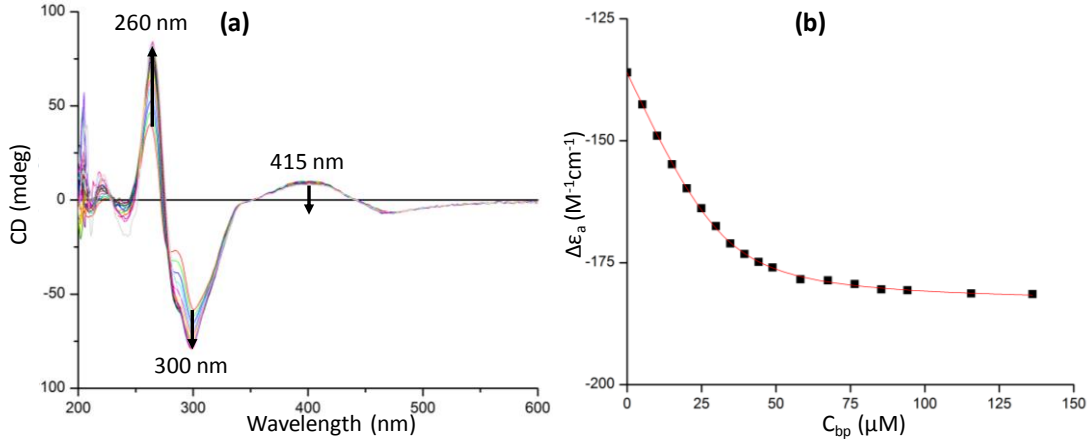

Figure 5.20: *(a) Changes in the CD spectrum of Δ-**9b** at titration with st-DNA. (b) Changes in the molar CD signal at 300 nm of Δ-**9b** at titrations with st-DNA; 50 mM potassium phosphate aqueous buffer with 50 mM KCl, pH 7.0, 25 °C, ca. 10 μM complex.*

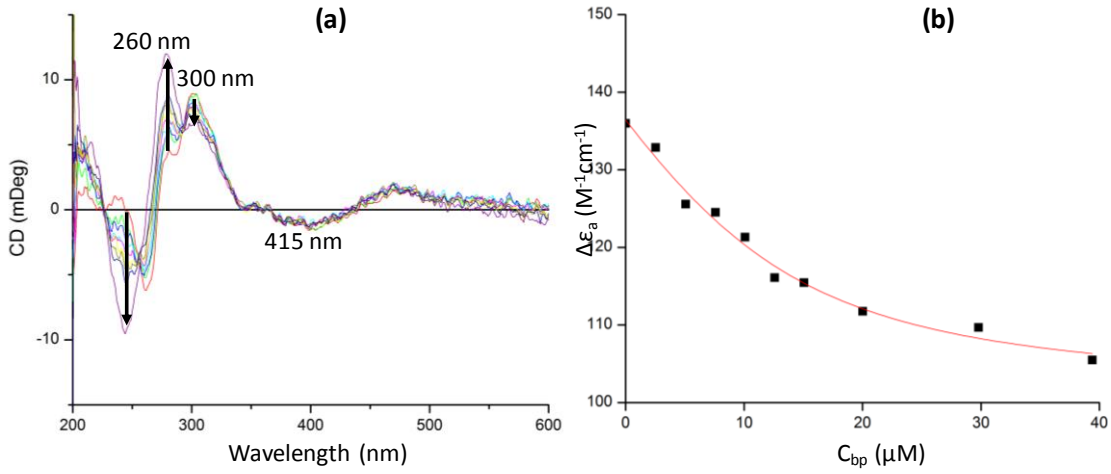

Figure 5.21: *(a) Changes in the CD spectrum of Λ-**9b** at titration with st-DNA. (b) Changes in the molar CD signal at 300 nm of Λ-**9b** at titrations with st-DNA; 50 mM potassium phosphate aqueous buffer with 50 mM KCl, pH 7.0, 25 °C, ca. 3 μM complex.*

5.6.2 Calculation of Binding Parameters

The data have been fitted to several different binding models. This included procedures, in which data have been fitted directly to the molar emission using the Scatchard and the Hill models as well as fitting of the data using the model independent method (Chapter 1). The model independent method has been used to calculate ΔS_B and to construct a Scatchard plot, to which the cooperative MGVH model has been fitted. The data has also been fitted with ReactLab EQUILIBRIA to account for possible non-linear relations between concentration of bound complex and the molar signal.

Non-cooperative Binding Parameters

The modified Bard method introduced in Chapter 1 was used again to calculate the Scatchard binding parameters assuming that there is no cooperativity involved in the binding. The model independent method has been used, also, to estimate the binding constant at zero saturation of DNA. Parameters calculated from absorption and emission data were of a similar size, however, the values calculated from the variations in the emission were more precise. As expected, the binding was strong with a Scatchard binding constant of 2.7 × 10^5 M^{-1} and a model independent binding constant of 0.70 × 10^5 M^{-1} (Figure 5.22). The Scatchard binding site size was 2.0 bp, which is typical in case of intercalation.[4] Compared to the values obtained in buffer, only, the binding site size was a little bit smaller (Table 5.6), however, the Scatchard binding constant was very close to the value predicted from the double logarithmic plot in Figure 5.17 (2.4 × 10^5 M^{-1}).

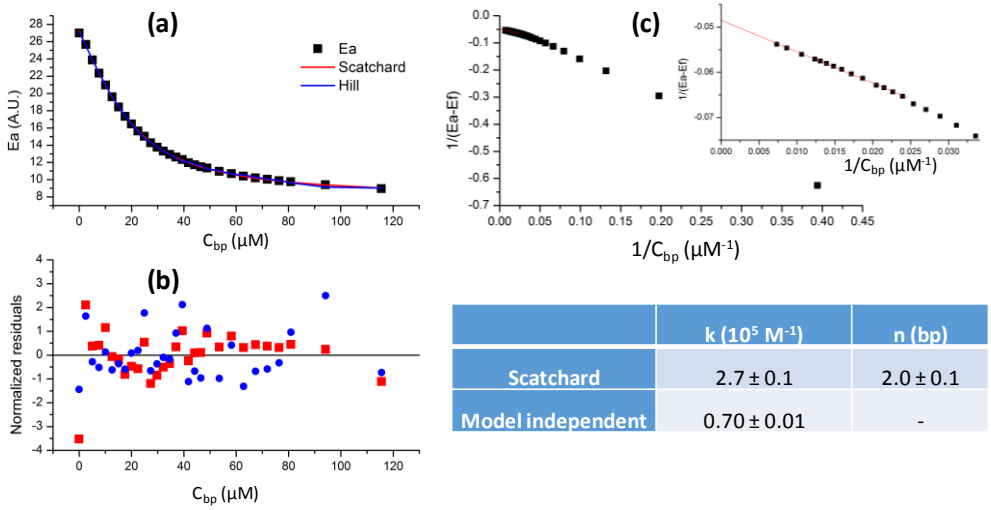

	k (10^5 M^{-1})	n (bp)
Scatchard	2.7 ± 0.1	2.0 ± 0.1
Model independent	0.70 ± 0.01	-

Figure 5.22: *(a) Fit of the Scatchard and the Hill models to the emission data. (b) Normalised residuals for fit to the emission data of the Scatchard and Hill models. (c) Linear fit of the model independent binding constant to emission data. 50 mM potassium phosphate buffer with 50 mM KCl, pH 7.0 and 25 °C. The reported values and errors are the mean and standard error for all replicates. Data obtained from absorption and CD data can be found Table A5.5.*

The Scatchard model seems to fit the data very well with an R^2 close to unity. However, a close look at the residuals indicates small deviations from a perfect fit (Figure 5.22b). Especially in the beginning of the titration with the largest saturation of DNA the deviation was relatively big.

Cooperative Binding Parameters

As mentioned, a fit of the non-cooperative Scatcard model showed small systematic errors when it was fitted to the emission data. Fits using the Hill and the cooperative MGVH models did not show any systematic errors (Figure 5.22 and Figure 1.9). The changes in the molar emission have been fitted directly to the Hill model, as done in case of calculation of the Scatchard binding parameters. The Hill coefficient was 3.0, which indicated positive cooperativity. As mentioned in Chapter 1, a Hill coefficient larger than one corresponds to positive cooperativity. The Hill site binding constant was 3.1×10^5 M^{-1}, very close to the Scatchard binding constant. However, the Hill binding site size was 3.7 bp, almost twice the value obtained with the Scatchard binding model.

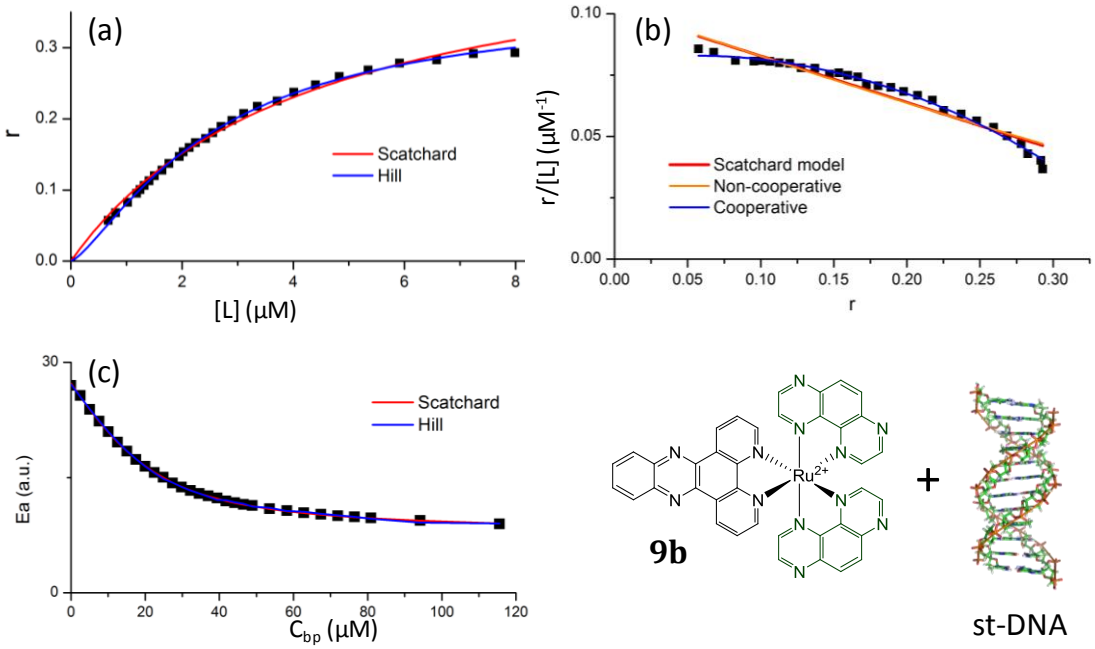

Figure 5.23: *Binding isotherms obtained from luminescence titration of ruthenium complex Δ-[Ru(dppz)TAP$_2$]$^{2+}$ (Δ-**9b**) with salmon testes DNA (st-DNA), 50 mM potassium phosphate buffer with 50 mM KCl. (a) Fit of the Scatchard and the Hill models to a r-plot. (b) Fit of the Scatchard and the McGhee-von Hippel (MGVH, cooperative and non-cooperative) equations to a Scatchard plot. (c) Fit to the molar emission of the Scatchard and Hill models.*

The cooperative and non-cooperative MGVH models have been fitted to a Scatchard plot, which has been constructed as described in Chapter 1. It can be seen that the Scatchard plot shows a negative curvature, which is typical in case of positive cooperativity. Data fitted using the non-cooperative MGVH model yielded results of a slightly worse quality than the linear fit obtained using the Scatchard model. This was expected since the fitted curve for the non-cooperative MGVH model have always a positive curvature.

However, the cooperative MGVH model resulted in a perfect fit to the Scatchard plot with no systematic deviations from the data points (Figure 5.23). The MGVH cooperativity constant (y) was 4.4, which, like the results obtained using the Hill model, indicated positive cooperativity. The site binding constant is 0.7×10^5 M^{-1}, which was the same as the value obtained using the model independent method. This is expected and a good validation of the model, since the MGVH site binding constant is a measure of "isolated" binding to a single base pair. The binding site size is 2.5 bp, which was a little larger than the value obtained using the Scatchard model.

Table 5.7: *Binding parameters obtained from emission data for the binding between Δ-**9b** and st-DNA in 50 mM potassium phosphate buffered solution with 50 mM KCl using different binding models.*

	k (10^5 M^{-1})	n (bp)	R^2
Scatchard	2.7 ± 0.1	2.0 ± 0.1	> 0.99
Hill[a]	3.1 ± 0.4	3.7 ± 0.4	> 0.99
Model independent	0.71 ± 0.01	-	> 0.99
MGVH[b]	0.69 ± 0.07	2.5 ± 0.1	> 0.99

(a) Hill coefficient = 3.0 ± 0.8; (b) y = 4.4 ± 0.4.

It has been seen before that a ruthenium polypyridyl complex showed positive cooperativity at intercalation with DNA. Lincoln *et al.* used a method similar to the MGVH model to calculate positive cooperativity parameters.[33] In their work, cooperativity was explained as local interactions between neighbouring bound complexes. Another explanation of positive cooperativity for the binding of an intercalator is that the intercalator may disturb the helical structure and improve binding at higher saturation in an allosteric manner.[32] For the experiments presented in this thesis can be concluded that positive cooperativity was present. Further studies must be conducted to explain why positive cooperativity was present, such as isothermal titration calorimetry.[45]

Global Analysis for Calculation of Binding Parameters

Global fitting with ReactLab EQUILIBRIA was also used to calculate binding parameters and derive the molar spectra for complex when bound to DNA. One important reason for using the program was that all discussion so far are based on the presumption of a linear relationship between the fraction of bound complex and the molar signals. As shown in Chapter 2 for **phen**, complex **33a**, this assumption is not always fulfilled. It was shown for complex **33a** that a relatively large error in the size of the binding constant can arise when this problem is not addressed. It cannot be excluded that the small deviation of the data from the Scatchard model was a consequence of similar non-linear behaviour (Figure 5.22). For the emission, absorption and CD titrations the data have been fitted to a binding model with two equilibria (Figure 5.24). It was only possible to fit both binding constants using emission data. Using the absorption and CD data a common non-cooperative binding constant has been fitted in a similar manner as done for complex **33a**.

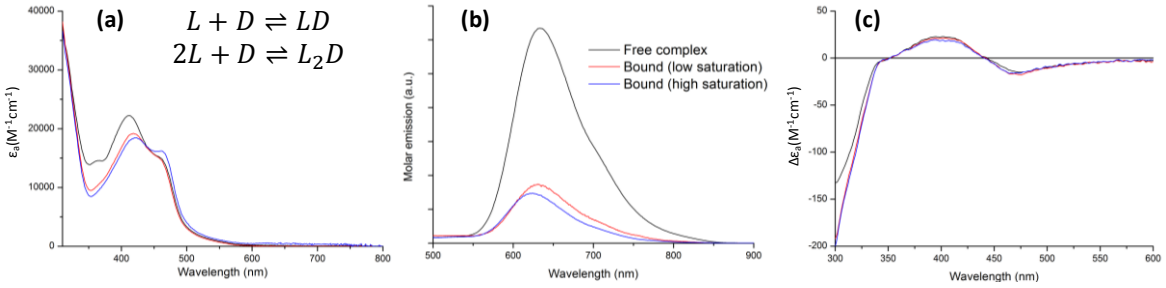

Figure 5.24: *Molar spectra of Δ-**9b** as free complex (black) in solution and at binding to st-DNA at low saturation (red) or high saturation (blue); 50 mM aqueous potassium phosphate buffer with 50 mM KCl, pH 7.0, 25 °C, ca. 10 μM; obtained with ReactLab EQUILIBRIA using two equilibria.*

In Figure 5.24 low saturation corresponds to the molar spectrum of LD ("50% of maximum saturation") while high saturation corresponds to half the molar spectrum of L_2D ("maximum saturation"). It can be seen that in all three cases only minor differences were observed in the molar spectra for high and low saturations indicating that the assumption used so far has been satisfactory. Further, for the emission data it has been possible to fit the binding constant for both equilibria rather than only one common site binding constant. This made it possible to calculate the interaction parameter as:[55]

$$\alpha_2 = \frac{4K_2'}{K_1'}$$

In case the Scatchard model is valid log(α_2) will be exactly zero. However, a value of 1.3 was found which indicates strong positive cooperativity, which was also predicted by the Hill and the MGVH models in the previous section.

***Table 5.8**: Site binding parameters for Δ-**9b** bound st-DNA in 50 mM potassium phosphate buffered solution with 50 mM KCl. The parameters were calculated from absorption, emission and CD data with ReactLab EQUILIBRIA with two equilibria.*

	Absorption	Emission	CD
k (10^5 M^{-1})[a]	2.5 ± 0.4	3.7 ± 0.2	5.0 ± 0.1
n (bp)	2.3 ± 0.3	2.9 ± 0.2	2.8 ± 0.2
log(α_2)	-	1.3 ± 0.7	-

5.6.3 Titrations with Synthetic Homo-polymers of DNA

A final objection against the conclusion made in the previous sections is that natural DNA was treated as a homogenous lattice with identical base pairs. A heterogenous duplex will always, to some extent, show site specific binding at sites where a certain part of the lattice has higher affinity for the DNA binding ligand (Δ-**9b**) than other parts. This will give rise to binding modes that have an appearance of negative cooperativity, since the "average" site binding constant will be higher at low saturation than at high. This was used to explain the difference in cooperativity for **G9**, **I9** and **A9** in Section 5.4.2. It is likely that the positive cooperativity found would be even higher for a homogenous DNA sequence.

To evaluate to what extent the above mentioned effects will have to be taken into considerations, titrations with poly(dG)poly(dC) and poly(dA)poly(dT) were carried out under the same conditions (50 mM potassium phosphate buffer and 50 mM KCl). The st-DNA consists of nearly 50% of each type of base pairs, and the difference in the affinity of the complex for these two sequences will act as a conservative estimate for how large variations there actually were in the affinity for different sites; if the difference was large it would also be expected that the variations of binding affinity to different sites at natural DNA would be large. Consistent with what was seen in the past for similar titrations, for titrations of the lambda enantiomer, and for the titrations with st-DNA, a large decrease in the emission was seen at titrations with poly(dG)poly(dC). On the other hand, an increase in the emission was observed for titrations with poly(dA)poly(dT), which has also been seen in the past.[80]. The AT base pair has a lower oxidation potential than GC, preventing it from

being photo-oxidised by Δ-**9b**. The increase in emission was expected to be a result of protection from oxygen upon intercalation.

The Scatchard binding parameters were calculated from the emission data in the same way as done previously (Table 5.9). Clearly, a huge difference was observed for the binding constant calculated for the two synthetic polymers. The affinity of Δ-**9b** for poly(dA)poly(dT) was more than an order of magnitude larger than for poly(dG)poly(dC), with site binding constant at 74×10^5 M^{-1} and 1.5×10^5 M^{-1}, respectively. As expected, the binding constant for st-DNA was between these two extremes (2.7×10^5 M^{-1}), however it was most similar to the binding constant for poly(dG)poly(dC).

Table 5.9: *Scatchard binding parameters for Δ-$[Ru(TAP)_2dppz]^{2+}$ bound to poly(dG)poly(dC), poly(dA)poly(dT) and st-DNA in 50 mM potassium phosphate buffered solution with 50 mM KCl. Parameters are calculated from emission data, pH 7.0, 25 °C.*

	poly(dG)poly(dC)	poly(dA)poly(dT)	st-DNA
k (10^5 M^{-1})	1.5	74 ± 2	2.7 ± 0.1
n (bp)	2.1	1.8 ± 0.1	2.0 ± 0.1

These results demonstrated clearly that natural DNA cannot be considered as a homogenous lattice. However, since positive cooperativity was reported, the sign of cooperativity can still be considered correct, since site specific binding was expected to contribute negatively to the cooperativity. It is likely that even stronger cooperativity might be observed for a homogenous lattice. The very weak binding for poly(dG)poly(dC) and the very strong binding for poly(dA)poly(dT) made it difficult to derive cooperativity constants under the present conditions. For poly(dG)poly(dC) only very low saturation was obtained, and a very abrupt plateau appeared for poly(dA)poly(dT). It is expected it would be possible to describe cooperativity if the experimental conditions are adjusted, *e.g.* by increasing or decreasing the ionic strength and by doing very precise measurements as was done for st-DNA.

5.6.4 Conclusion for Cooperative Binding of Δ-9b to Natural DNA

The cooperativity of binding of Δ-**9b** to st-DNA has been evaluated with a simple titration experiment, both to get insight into the behaviour of this very important system and to test some new methods and models for the study of DNA binding. The Scatchard model provided a good fit to the data, however, an improvement in the fit was obtained when models suited for describing cooperativity were used. All cooperativity models showed positive

cooperativity with a Hill coefficient of 3.0 and a MGVH cooperativity constant of 4.4. The MGVH model seemed to give reliable results since the binding constant was consistent with a value found using a model independent method. Positive cooperativity was confirmed further by using ReactLab EQUILIBRIA, which is able to account for possible non-linear relations between concentrations of bound complex and molar signals. It was shown by titration with homo-polymers that the complex binds much stronger to poly(dA)poly(dT) than to poly(dG)poly(dT) with Scatchard binding constants of 74×10^5 M^{-1} and 1.5×10^5 M^{-1}, respectively. It was argued that the cooperativity might be even more positive than reported here since specific binding will give a negative contribution to the cooperativity.

5.7 Conclusion and Future Perspectives

In this chapter, specific and cooperativity binding of Δ- and Λ-**9b** to DNA have been evaluated with respect to binding to small oligomeric sequences, synthetic polymers and natural DNA. The binding of Λ-**9b** showed preferential binding from the minor groove. When guanine (duplex **G9**) was substituted with inosine (duplex **I9**) the site binding constant increased from 4.2×10^5 to 13×10^5 M^{-1} (in 50 mM potassium phosphate). This may be explained by the lack of an amine group, found in guanine, however not in inosine, in the minor group. This hypothesis was confirmed by doing similar titration experiments with AT instead of GC (duplex **A9**). This gave a very similar binding constant as obtained for **I9** (16×10^5 M^{-1}). NMR titration experiments was also carried out with **G9** and **I9**. This indicates a complex non-specific binding. NMR studies using a decamer with an AT base pair at the central step showed a much more specific binding. Further studies might well involve titrations of **I9** at higher ionic strengths. This is expected to increase the fraction of **I9** that will intercalate near inosine, since this will result in the largest non-electrostatic binding.

Comparisons of results from titrations of Δ- and Λ-**9b** with different oligomeric sequences of DNA, including **G9**, **I9** and **A9**, showed that, in all cases, the site binding constants were smaller, and the site sizes were in most cases larger than expected. Some simple considerations about possible contributions to these deviations from expected values have been presented. There seemed to be a stronger electrostatic contribution to the binding for polymeric DNA than for oligomers. A suggested explanation for the difference was the poly-electrolytic nature of DNA. Further studies will explore if this is the case in general for both enantiomers.

The binding of Δ-**9b** showed positive cooperativity when emission data from a titration experiment was fitted using the Hill and the MGVH models, and also when the data was treated with ReactLab EQUILIBRIA. It was shown, also, that the Δ-**9b** had a much stronger affinity for poly(dA)poly(dT) than for poly(dG)poly(dC) with a site binding constant that is more than an order of magnitude larger for the former. In future work the methods and the methodology described here will be used to analyse other systems; including studies of the cooperative binding of Δ-**9b** to poly(dG)poly(dC) and poly(dA)poly(dT) and binding modes of Δ-**9b**.

Chapter 6

Functionalisation of AuNPs with Ru(II) Polypyridyl Complexes for Biological Applications

6.1 Introduction

In Chapter 1, work in the Gunnlaugsson group related to the functionalisation of gold nanoparticles (AuNPs) with Ru(II) polypyridyl complexes was introduced.[2] Current work in the group aims to further evaluate these AuNPs potential in biological applications. Synthesis of AuNPs (the same surfactants) with a diameter of *ca*. 15 nm instead of 5 nm have also been achieved in the group.[43] In this chapter, work concerning these two sizes of AuNPs will be described, including optimisation and evaluation of the synthetic procedures and further characterisation. The work involved studies of the stability of the AuNPs in solution, zeta-potential measurements, dynamic light scattering (DLS), scanning and transmission electron microscopy (SEM and TEM), and DNA binding studies using absorbance and emission spectroscopies.

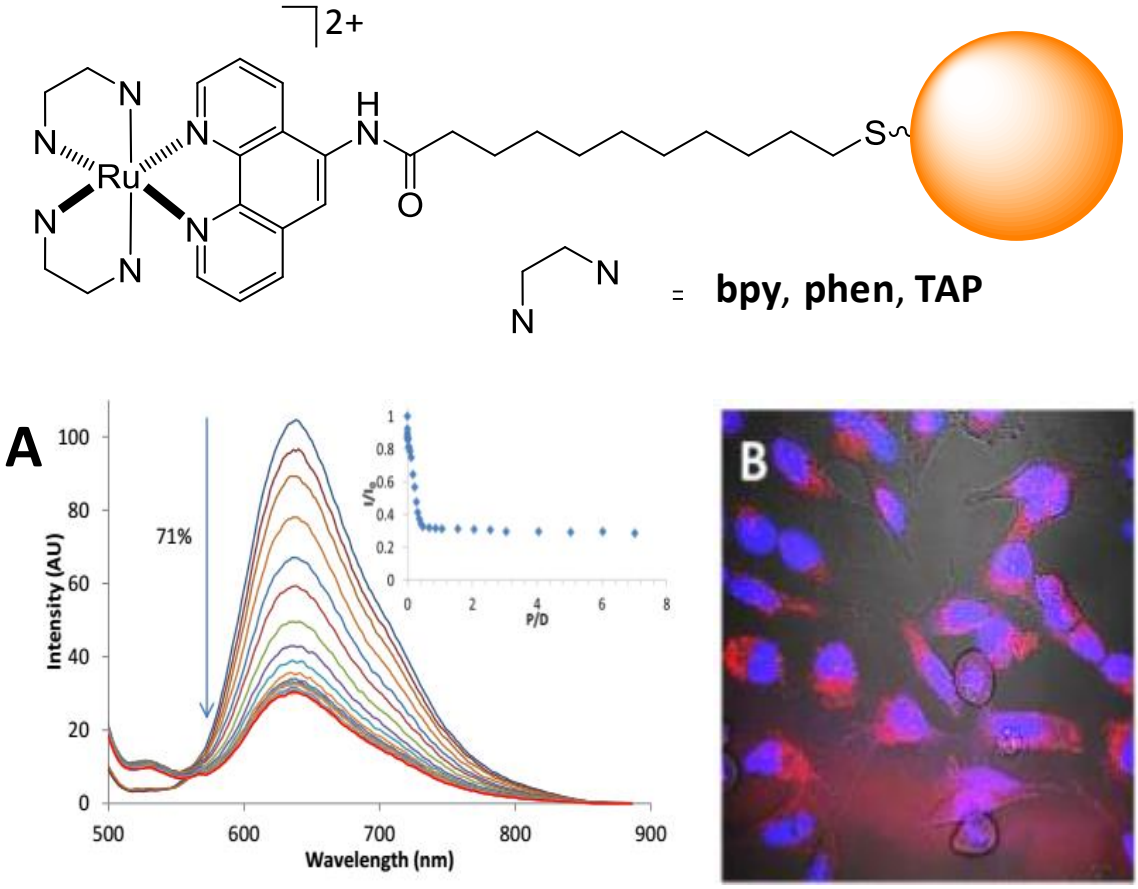

Figure 6.1: *AuNPs synthesis by Dr Elmes, which have ligand* ***54*** *attached to the AuNPs and* ***bpy*** *(****AuNP$_{5nm}$-55****),* ***phen*** *(****AuNP$_{5nm}$-55a****) or* ***TAP*** *(****AuNP$_{5nm}$-55b****) as ancillary ligands. A: Modulation in the emission spectrum at increasing concentration of st-DNA with AuNPs where* ***TAP*** *is the ancillary ligands. B: Cellular uptake and localisation of the AuNPs with* ***bpy*** *as ancillary ligand followed with confocal microscopy.*[2]

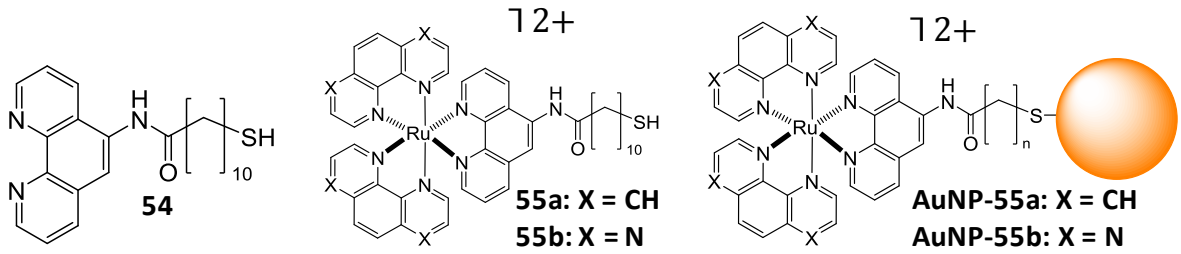

Figure 6.2: *Ru(II) polypyridyl complexes synthesised in the Gunnlaugsson group which have been studied in the project.*

Further work is concerned with expanding the family of Ru(II) polypyridyl functionalised AuNPs to new types and evaluate their potential for biological applications. In Chapter 2, the attempts to use the ligand **mpdppz** as a handle for the functionalisation of AuNPs, were discussed. AuNPs functionalised with Ru(II) polypyridyl complexes containing this ligand were among others expected to have a high affinity for DNA, which could make the corresponding AuNPs good candidates for cellular imaging or DNA targeting cancer agents. Several attempts to convert the methyl group in **mpdppz** to a more reactive functional group in an attempt to attach a linker with a terminal thiol were unsuccessful. The introduction of a thiol group in the ligand was essential for the final step in the functionalisation of AuNPs where the thiol forms a S-Au bond to the gold surface. In this chapter further attempts to use other ligand types as the handle for the functionalisation of AuNPs are reported. Ligand **57** and **58** were two target molecules, which would enable the attachment of the corresponding Ru(II) polypyridyl complexes to the surface of AuNPs with a similar protocol that has already has been used in the Gunnlaugsson group.

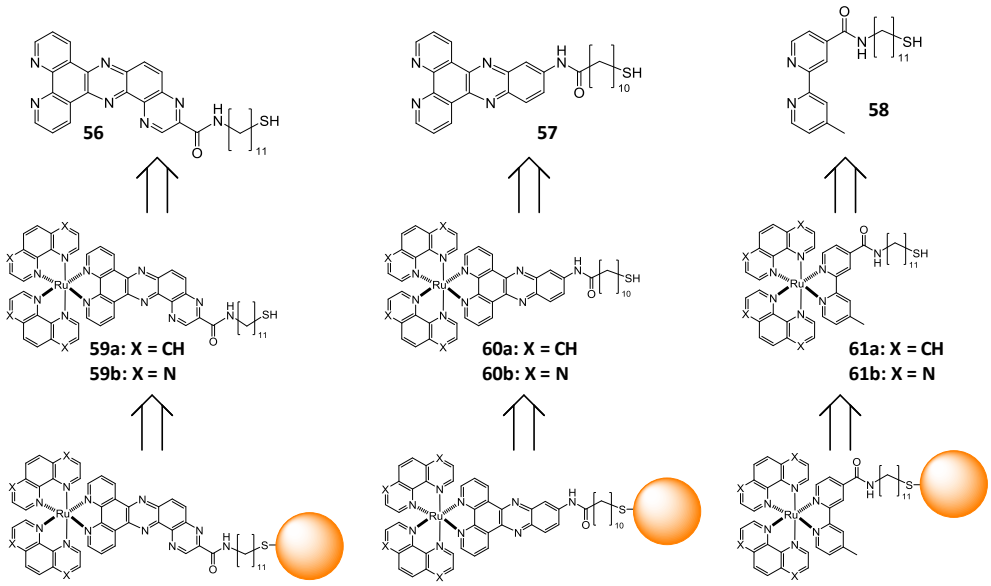

Scheme 6.1: *Retro synthetic scheme for new versions of Ru(II) polypyridyl functionalised AuNPs.*

6.2 Synthesis and Characterisation of Ru(II) Polypyridyl Complexes

The following section describes the syntheses and characterisation of the Ru(II) polypyridyl complexes, with the objective of using the complexes to functionalise AuNPs. In the first section the synthesis of the ligands, which were planned to be used as the "linker" between the Ru(II) polypyridyl complexes and the AuNPs, will be described. This will be followed by a description of work concerning the syntheses of the Ru(II) polypyridyl complexes themselves.

6.2.1 Synthesis of Alkyl Thiol Functionalised Ru(II) Polypyridyl Complexes

The functionalisation of AuNPs was carried out by covalent attachment of the surfactants to the gold surface through the formation of an S-Au bond.[2] In the following work, the synthesis of complexes with alkyl thiol functionalised versions of **phen**, **dppz** and **bpy**, which could act as "linkers" for the attachment to AuNPs, will be described.

Synthesis of Ligand 54 and 66

The synthesis of the "linker" **54** which was based on 1,10-phenanthroline and previously has been synthesised and studied in the group, was performed using the same procedure as the one described by Elmes *et al.* (Scheme 6.2).[2] The final step involved an amide coupling between 5-amino-1,10-phenanthroline (**64**) and a carboxylic acid group of the thiol linker (**65a**). 5-Amino-1,10-phenanthroline was synthesised in two steps. In the first step 5-nitro-1,10-phenanthroline (**63**) was formed using aromatic nitration of the commercially available 1,10-phenanthroline in a mixture of H_2SO_4 and HNO_3. This gave the compound in 67% yield. Reduction of the nitro group, using NH_2NH_2 in EtOH, with 10% Pd/C as catalyst gave the amine as a yellow powder in 50% yield.

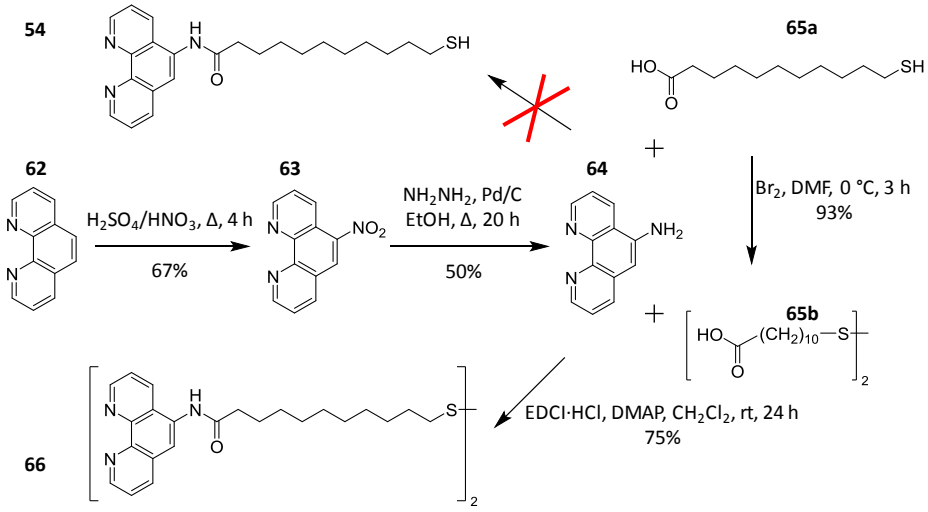

Scheme 6.2: *Synthetic pathway for ligand **66**.*

Several amide coupling attempts were made in CH_2Cl_2 between the amine and 11-mercaptoundecanoic acid, with the hydrochloride salt of 1-ethyl-3-(3-dimethylaminopropyl)carbodiimide (EDCI·HCl) as the coupling agent and with the base 4-dimethylaminopyridine (DMAP) as a catalyst. However, even though this synthetic step has previously been carried out successfully, no product was obtained under the same conditions.[2] The only difference compared to the literature procedure was the use of commercially available 11-mercaptoundecanoic acid, whereas Elmes *et al.* synthesised the compound *prior* to the synthetic step. It was considered possible that the dimeric form with a disulphide bridge between the two units was formed, which could explain the lack of reproducibility. Thus, the carboxylic acid was dimerised *prior* to the amide coupling by stirring the thiol in DMF with Br_2 for three hours, giving the dimeric form in a 93% yield.[218] The formation of the dimer was confirmed by a large increase in the melting point from 49-50 °C[219] to 93-97 °C; however, no significant change in the ^{1}H NMR spectrum (400 MHz, $CDCl_3$) was observed. The coupling with the dimer was successful with 75% yield, which was very similar to the yields obtained previously. The structures of the complexes were confirmed with ^{1}H NMR (400 MHz, DMSO-d_6) spectroscopy by comparison with the litterature.[2] The spectrum showed a characteristic resonance at 10.09 corresponding to the amide proton.

Synthesis of Complex 55a and 55b

The final step in the synthesis of Ru(II) polypyridyl complexes which had **66** as ligand (Scheme 6.3) was carried out at 140 °C under microwave irradiation in a mixture of glycol and H_2O (**phen** complex **55a**) or ethanol and H_2O (**TAP** complex **55b**) after degassing with N_2 to remove dissolved O_2.[2] The products were purified by gradient column chromatography using silica and an ionic mixture of $NaNO_3$ in CH_3CN and H_2O as eluent. The complexes

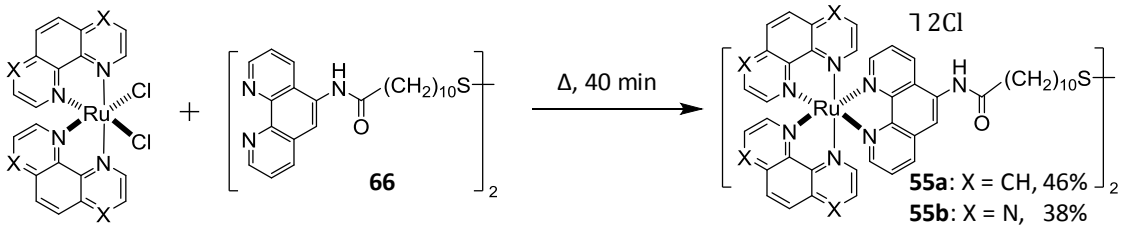

Scheme 6.3: *Syntheses of Ru(II) polypyridyl complexes with **66** as a ligand together with **phen** (**55a**) or **TAP** (**55b**).*

were obtained in 46% and 38% yields for **55a** and **55b**, respectively. The successful formation of the complexes was confirmed using ^{1}H NMR (400 MHz, CD_3OD) spectroscopy and comparison with the literature.[2] Both complexes were very soluble as their chloride salts, and the photophysical properties could be investigated in aqueous solution.

Further attempts were made to synthesise similar complexes with **dppz** as ligands (Scheme 6.4) instead of **phen** or **TAP**. The intention was to synthesise AuNPs with surfactants, which had some of the same properties as Ru(II) complexes with **dppz** as the ligand, such as complex **9b** described in Chapter 5. Such properties included a strong binding to DNA through intercalation with concomitant modulation in the photophysical properties.[80] The synthesis of $[Ru(dppz)_2Cl_2]$ (**67**) was carried out successfully with the same procedure as used to synthesise the corresponding complexes with **phen** or **TAP** as polypyridyl ligands.[220] However, the synthetic step in which the precursor should react with **67** using the **dppz** complex, resulted in no yield.

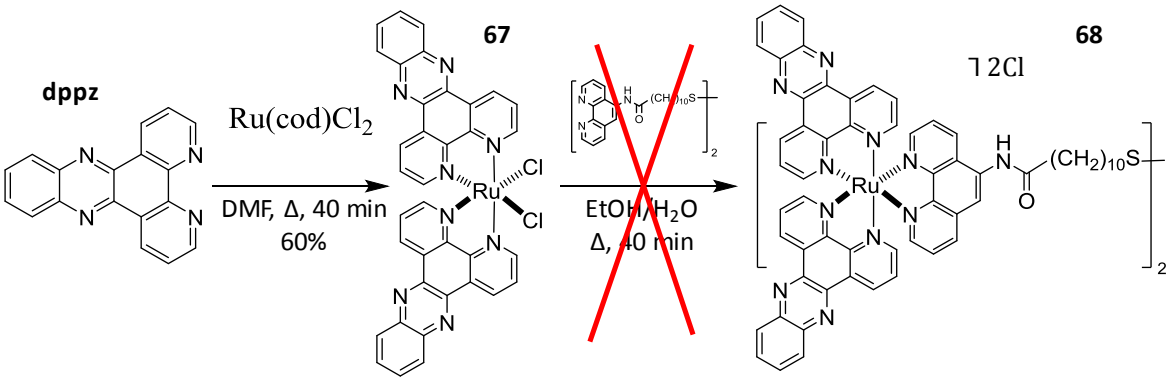

Scheme 6.4: *Attempted synthesis of Ru(II) polypyridyl complex **68** with **66** as a ligand together with **dppz**.*

Synthesis of Ligand 57

As mentioned in Chapter 2, attempts were made to use the ligand **mpdppz** as a precursor for AuNP linking ligands, but with poor results. An alternative molecular design, which was expected to have similar photophysical properties and biological activity was the AuNP linking ligand containing dipyrido[3,2-a:2',3'-c]phenazine-11-amine (**70**) as precursor. It was considered possible to attach an aliphatic linker using an amide coupling in a similar manner to the coupling between **54** with **65b** (Scheme 6.2).

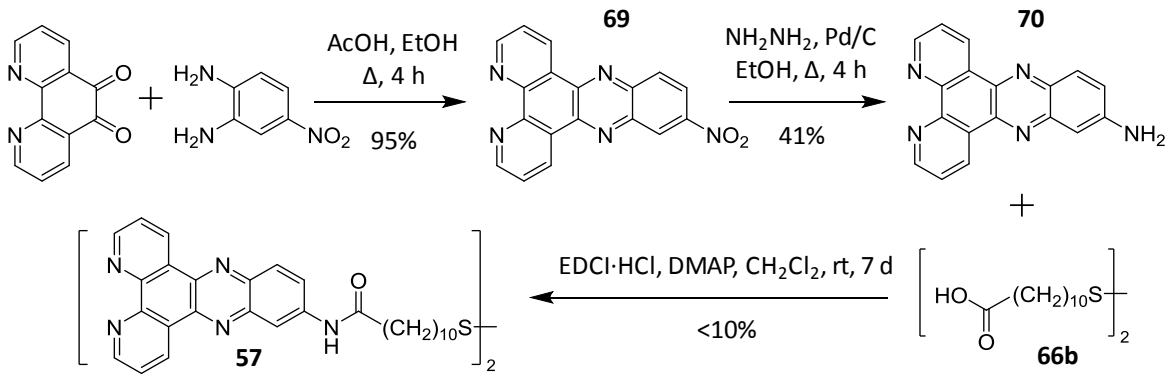

Scheme 6.5: *Synthetic pathway for* ***dppz*** *derivative* ***57****.*

Compound **70** was synthesised in two steps;[221] in the first step, 4-nitro-1,2-phenyldiamine and 1,10-phenanthroline-5,6-dione (**phendione**) were suspended in ethanol and heated with acetic acid for four hours. The precipitate was isolated by centrifugation and washed with ethanol yielding the product as a bright yellow solid in 95% yield. Heating at reflux temperature in EtOH for four hours, with NH_2NH_2 as reducing agent and 10% Pd/C as catalyst, gave the desired amine as a yellow powder in a yield of 41%. The successful synthesis of the compound was confirmed with ^{1}H (400 MHz, DMSO-d_6) and ^{13}C (100 MHz, DMSO-d_6) NMR spectroscopy and HRMS and comparison with the litterature.[221] However, the following amide coupling between the amine and the dimer of 11-mercaptoundecanoic acid (**65b**) was unsuccessful when similar conditions as those for the synthesis of **54** were used. It was expected that delocalisation of the nitrogen lone pair deactivated the amine. Attempts were made to increase the amount of EDCI and DMAP and to use Et_3N as base, which resulted in a small yield according to HRMS. Further attempts using the stronger coupling agent PyBOB with the *N*,*N*-diisopropylethylamine (DIPEA) as base catalyst were made, which gave less than 10% yield according to ^{1}H NMR (400 MHz, DMSO-d_6) spectroscopy.

Synthesis of Ligand 58

It was expected that 4'-methyl-2,2'-bipyridinyl-4-carboxylic acid (**78**) would act as a good precursor for a linking ligand for AuNPs, with similar properties of the corresponding functionalised AuNPs, which has been reported previously (with ligand **66**). As shown in Scheme 6.7, the synthesis involved an amide coupling, similar to the synthetic procedure for **66**. The primary amine was synthesised in five steps.[222] In the first step, potassium phthalimide and 11-bromoundecan-1-ol were suspended in DMF and heated at 60 °C for four hours yielding 11-(*N*-phthalimido)undecane-1-ol as a white solid in 95% yield. The

compound was dissolved in CH_2Cl_2, and Et_3N was added. Mesyl chloride was added at 0 °C, after which the solution was stirred at room temperature for two hours. The product was added to a mixture of thio acetic acid and K_2CO_3 then refluxed in DMF, and after 20 hours 11-(*N*-phthalimido)undecane-1-thio acetate was obtained as a solid in a yield of 90%. This was dissolved in MeOH with H_2SO_4 giving 11-(*N*-phthalimido)undecane-1-thiol in 83% yield after refluxing overnight. Eventually, 11-aminoundecane-1-thiol was synthesised by dissolving the compound in EtOH and by heating it with NH_2NH_2 for three hours giving the amine as a white solid in 93% yield (Scheme 6.6). The structure of the compound was confirmed with ^{1}H NMR (400 MHz, DMSO-d_6) spectroscopy and comparison with the litterature.[222]

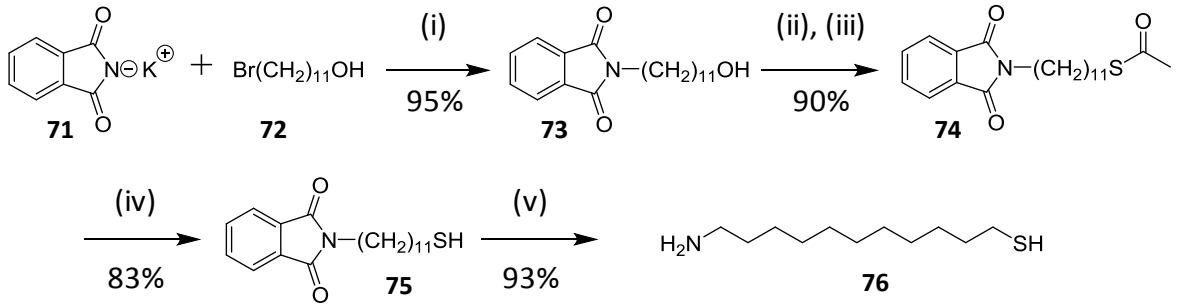

Scheme 6.6: *(i) DMF, Δ, 4 h; (ii) Mesyl chloride, Et_3N, CH_2Cl_2, rt, 2 h; (iii) AcSH, K_2CO_3, DMF, rt, 20 h; (iv) H_2SO_4, EtOH, Δ, 20 h; (v) NH_2NH_2, EtOH, Δ, 3 h.*

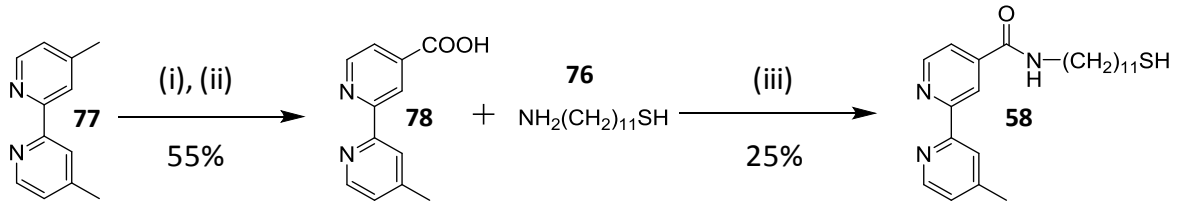

Scheme 6.7: *(i) SeO_2, 1,4-dioxane, Δ, 2 d; (ii) $AgNO_3$, NaOH, EtOH/H_2O, 20 h; (iii) EDCI·HCl, DMAP, CH_2Cl_2, rt, 72 h.*

4'-Methyl-2,2'-bipyridinyl-4-carboxylic acid was synthesised in two steps with an overall yield of 55% (Scheme 6.7).[223] In the first step one of the methyl groups was oxidised to an aldehyde group by refluxing 4,4'-dimethyl-2,2'-bipyridine in 1,4-dioxane for two days with SeO_2 as the oxidising agent. The mixture was filtered through celite, and the filtrate was evaporated to give a yellow solid. This was suspended in EtOH, and $AgNO_3$ and 1 M aqueous NaOH was added. The mixture was left for stirring at room temperature overnight. The carboxylic acid was isolated as a white solid by filtration. As shown in Scheme 6.7 the final step in the synthesis of the ligand was carried out using a similar procedure as for the synthesis of the **54**. The aromatic carboxylic acid and DMAP were suspended in dry CH_2Cl_2,

and EDCI·HCl was added at 0 °C. After one hour, the temperature was increased to room temperature, and the aliphatic amine was added. The reaction mixture was stirred for three days, and the resulting amide was isolated as a white solid in 25% yield. The structure of the compound was confirmed with ^{1}H NMR (400 MHz, DMSO-d_6, Figure 6.3) spectroscopy where a chemical shift of the amide proton was found at 8.87 ppm. HRMS displaying a peak at 399.2379 corresponding to the mass of the molecular ion. A similar yield of 22% was obtained when the dimer of **76** with a disulphide bridge was used in the synthesis.

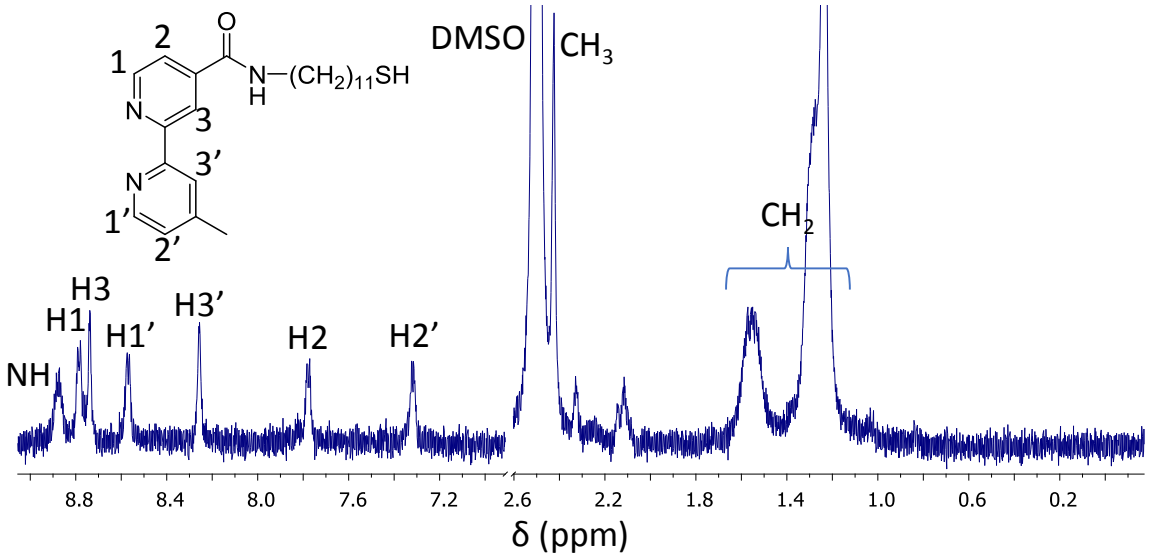

Figure 6.3: *^{1}H NMR (400 MHz, DMSO-d_6) spectrum of **58**. Noise resonances due to low solubility of the compound.*

Synthesis of Complex 61a

The final step in the synthesis of a Ru(II) polypyridyl complex **61a**, with **58** and **phen** as ligands (Scheme 6.8), was carried out under microwave irradiation at 140 °C in a mixture of ethanol and H_2O after degassing with N_2 to remove dissolved O_2. After completion of the reaction the mixture was evaporated at reduced pressure. The resulting residue was dissolved in H_2O (10 mL) and precipitated as the PF_6 salt after addition of solid NH_4PF_6. The chloride form of the complex was obtained by stirring with Cl-resin in methanol for two hours. The products were purified by gradient column chromatography using alumina as solid phase and a mixture of CH_3CN and H_2O as eluent. The complex was obtained in 62% yield. The structure of the complex was confirmed using ^{1}H NMR (400 MHz, CD_3CN) spectroscopy. A peak at 860.2693 was observed with HRMS corresponding to the [M-H] ion. The complex was very soluble as the chloride salt in H_2O, and the photophysical properties were investigated in aqueous solution.

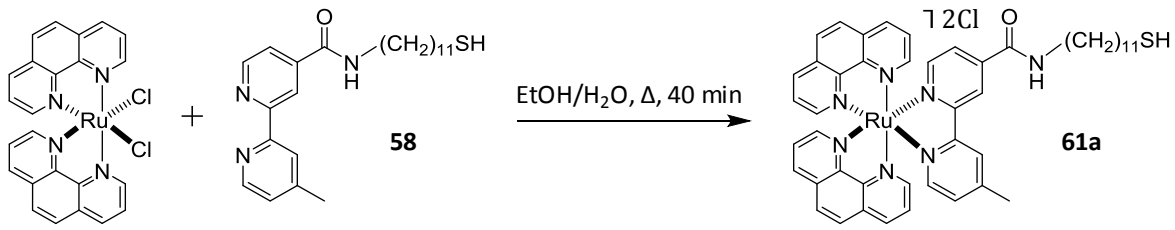

Scheme 6.8: *Syntheses of ruthenium complexes* ***61a*** *with* ***58*** *as a ligand together with* ***phen****.*

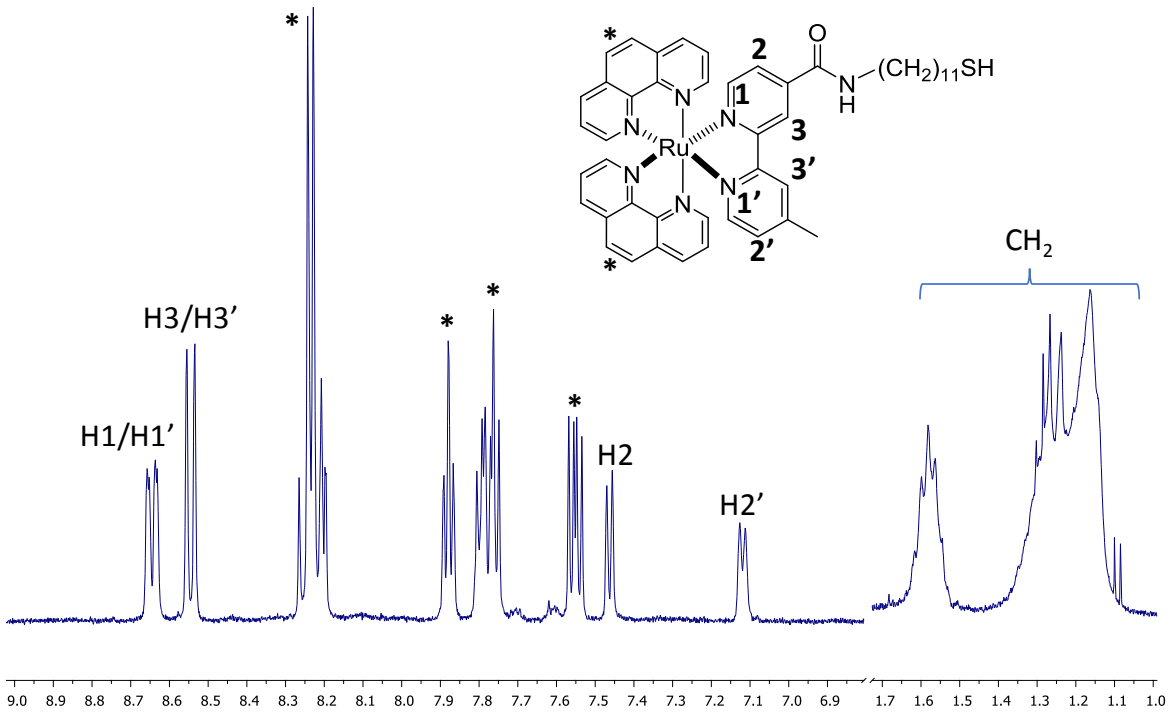

Figure 6.4: *^{1}H NMR (400 MHz, CD_3CN) spectrum of complex* ***61a****.*

6.2.2 Photophysical Characterisation of Synthesised Ru(II) Polypyridyl Complexes

To evaluate the applicability of the complexes in imaging and photo-activated cancer therapy the photophysical properties where evaluated in aqueous solution. The assigned properties were also important with respect to understanding the photophysical properties of the AuNPs functionalised with the corresponding complexes.

Photophysical Characterisation of Complex 55a and 55b

The photophysical properties of the complex **55a** and **55b** were studied in aqueous solution and showed results that were consistent with those obtained by Elmes *et al*.[2] The absorption spectrum of **phen** complex **55a** in aqueous solution showed absorbance maxima at 223 nm, 262 nm, and 450 nm (Figure 6.5a). The bands at 223 nm and 262 nm were characteristic of π-π* intra-ligand transitions of the ancillary **phen** ligands. A luminescence band was observed at 605 nm in H_2O (λ_{exc} = 440 nm). The spectrum of **TAP** complex **55b** in H_2O

showed an absorption band with maximum at 275 nm (Figure 6.5b) characteristic of π–π* intra-ligand transitions of the ancillary **TAP** ligands; and an absorption band at 415 nm attributed to the typical MLCT transition for these kinds of complexes where an electron transfer occurs from the metal centre to the **TAP** ligands.[80] An emission band was observed at 640 nm in H_2O (λ_{exc} = 415 nm).

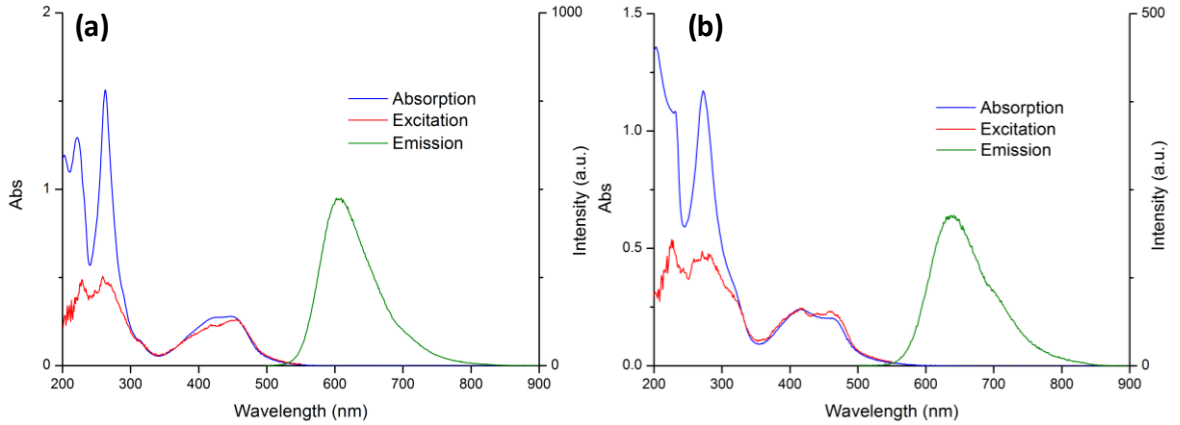

Figure 6.5: *Absorption, emission, and excitation spectra of (a)* ***55a*** *and (b)* ***55b*** *complex with ligand* ***54*** *in aqueous solution. Excitation wavelengths for the emission spectra were 440 nm and 415 nm, and the emission wavelengths for the excitation spectra were 620 nm and 630 nm for complex* ***55a*** *and* ***55b****, respectively.*

Photophysical Characterisation of Complex 61a

The photophysical properties of the new complex **61a** was also studied in aqueous solution and showed results similar to those obtained for **55a** and many other **phen** complexes.[2,54] The absorption spectrum for **55a** in aqueous solution showed absorbance maxima at 263 nm

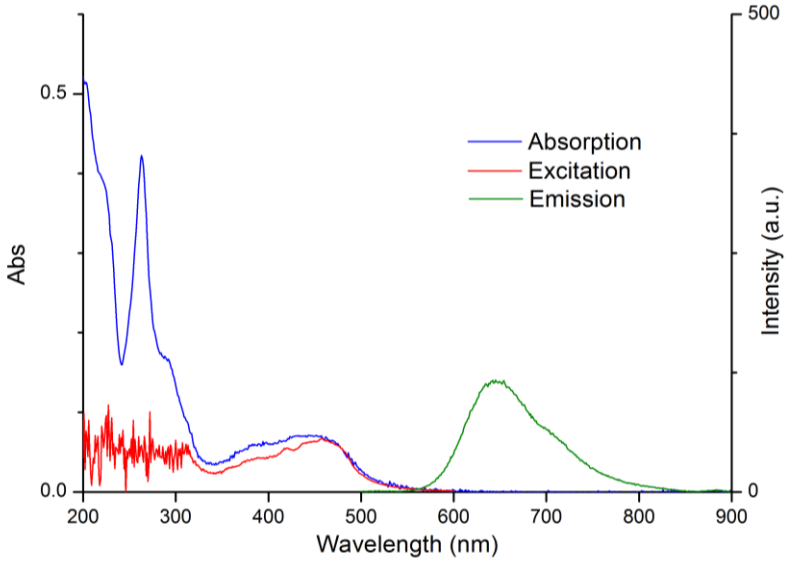

Figure 6.6: *Absorption, emission and excitation spectra of the* ***61a*** *in aqueous solution. Excitation wavelength for the emission spectra was 440 nm, and the emission wavelength for the excitation spectrum was 645 nm.*

and 450 nm, which corresponded to the characteristic π-π* intra-ligand transitions of the ancillary **phen** ligands and MLCT transition from the metal centre to **58** or **phen**, respectively. A luminescence band was observed at 645 nm in H_2O (λ_{exc} = 440 nm). The emission maximum was at a 25 nm longer wavelength than for the corresponding **phen** complex with **58**. This property makes the complex more promising for use in imaging since the transmittance of photons with NIR wavelengths through biological media is higher than at lower wavelengths.

6.3 Synthesis of Ru(II) Polypyridyl Functionalised AuNPs

6.3.1 General Synthetic Procedure

Two conventional methods have been used to synthesise the functionalised AuNPs: the 'citrate' method and the 'Brust-Schiffrin' method according to Scheme 6.9.[224,225] In both methods, $HAuCl_4$ was reduced to give AuNPs stabilised by charged surfactants, which ensures repulsion between individual AuNPs in solution. In 1951, Turkevich reported the citrate method, wherein citrate acted as the reducing agent[224] and as the stabilising surfactant by giving the surface a net negative charge (zeta-potential). The diameter of the AuNPs could be tuned by varying the citrate/Au ratio, to give nanospheres with a diameter between 10 and 150 nm. The 'Brust-Schiffrin' method uses $NaBH_4$ as reducing agent.[225] Tetraoctylammonium bromide (TOAB) acts as a stabilising surfactant by giving the surface a positive charge and facilitate the dissolution of the AuNPs in a range of organic solvents.

In this research project, the 'Brust-Schiffrin' method was used to synthesise AuNPs with a diameter of *ca*. 5 nm.[2,225] An aqueous solution of $HAuCl_4$ was mixed with a solution of TOAB in toluene by vigorously stirring, resulting in the formation of a colourless water layer, and an orange toluene layer when the $HAuCl_4$ units were transferred to the toluene layer. Upon addition of $NaBH_4$, the orange toluene layer turned black immediately upon formation of AuNPs. After one hour the toluene layer with the AuNPs was isolated and stored for future use at room temperature. TOAB acted as the stabilising agent by giving the surface of the AuNPs a positive charge. The solution of the AuNPs in toluene was mixed with an aqueous solution of the appropriate complex giving a biphasic mixture that was stirred vigorously for 16 hours. Successful functionalisation of the AuNPs with an S-Au bond between the complex (**55a** or **61a**) and the gold surface resulted in the transfer of the AuNPs to the water layer, which turned black. The colourless toluene layer was discarded, and solid NH_4PF_6 was added to the H_2O layer resulting in the formation of a dark-red

precipitate of functionalised AuNPs and free unreacted complex that was in excess. The precipitate was isolated by centrifugation, washed with H_2O, and dissolved in MeCN. Upon addition of a saturated solution of tetrabutyl ammonium chloride (TBACl) in MeCN the functionalised AuNPs formed a precipitate in its chloride form. The AuNPs precipitate was isolated by centrifugation, while the supernatant that contained the unreacted complex was discarded. The successful functionalisation was confirmed with absorption spectroscopy to ensure that both the MLCT band of the complex and the SPR band of the AuNP core were present (Section 6.3.2 and 6.4.1).

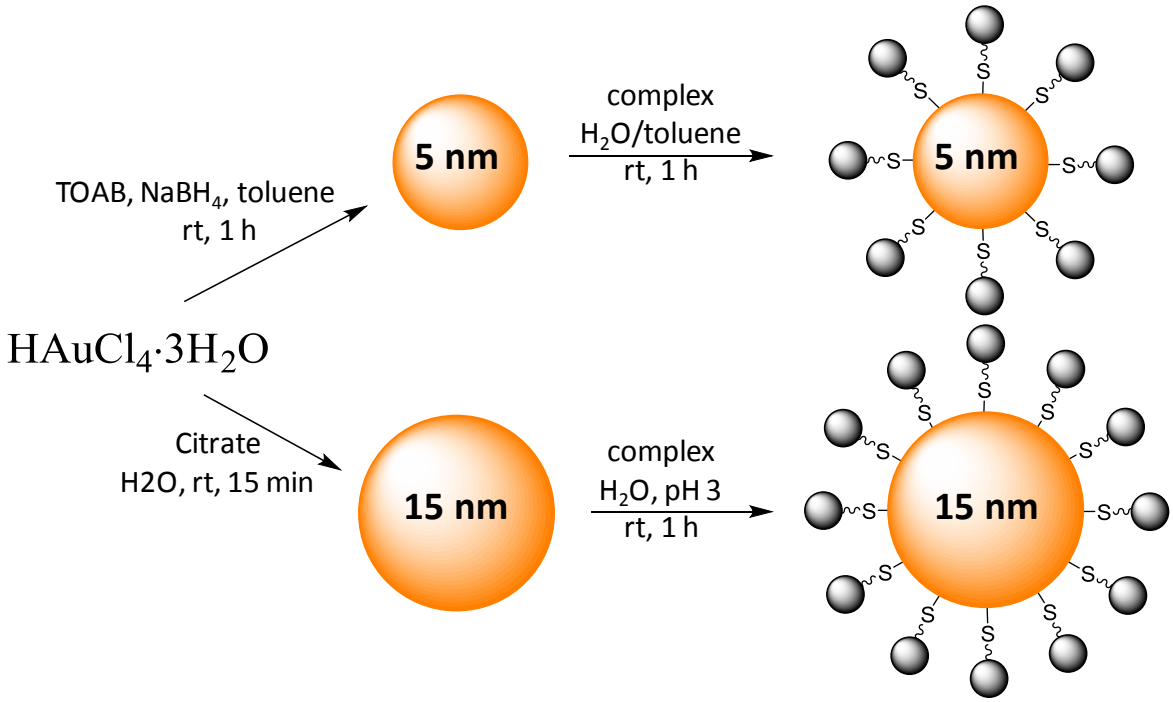

Scheme 6.9: *General synthetic methods used for the formation of AuNPs. Yellow = AuNP, grey = Ru(II) polypyridyl complex (**55a**, **55b** or **61a**).*

The 'citrate' method was used to synthesise AuNPs with a diameter of *ca*. 15 nm. $HAuCl_4$ was dissolved in H_2O, yielding a bright yellow solution, to which an aqueous solution of tri-sodium citrate was added. The solution was heated at reflux for 15 minutes and the solution turned red indicating the successful formation of AuNPs. The citrate acts as both reducing agent and stabilising surfactant by giving the surface a negative charge.[224] A 0.1 M HCl solution was added to the solution of the AuNPs and the pH adjusted to 3. This solution was then mixed with a solution of the appropriate complex (**55b**). The mixture was stirred overnight at room temperature, to adsorb the complexes on the surface by covalent attachment through S-Au bonds. Addition of NH_4PF_6 resulted in the precipitation of functionalised AuNPs, as well as unreacted complex, wherein the former were isolated by

centrifugation and washed with H_2O. The precipitate was dissolved in MeCN and a concentrated solution of TBACl in MeCN was added. This formed a precipitate of the chloride salt of the AuNPs that was isolated by centrifugation while the supernatant containing unreacted complex was discarded. Successful functionalisation was confirmed by absorption spectroscopy to ensure that both the MLCT band of the complexes and the SPR band of the AuNPs was observed.

6.3.2 AuNPs Synthesised with the 'Brust-Schiffrin' Method ($AuNP_{5nm}$)

AuNPs with a diameter of *ca*. 5 nm were functionalised with complex **55a**; the primary purpose of this was to optimise the synthetic procedure. A problem with the method used by Elmes *et al*. was that the same number of moles of complex was used as that of gold atoms in the synthetic step.[2] This quantity of complex was a huge excess of surfactant compared to the fraction of gold atoms that would be expected at the surface of the AuNPs which are capable of making an Au-S bond. Hence, it was decided to find the minimum amount of compound that was needed to achieve the desired functionalisation in order to reduce the cost and the amount of synthetic work that was needed. The degree of functionalisation was evaluated using absorption spectroscopy as described in Section 6.4.1. The 'Brust-Schiffrin' method was also used for the synthesis of AuNPs with complex **61a** as surfactant. This has only been done using a minimum amount of surfactant in the functionalisation step.

6.3.3 AuNPs Synthesised with the Citrate Method ($AuNP_{15nm}$)

Dr Miguel Martínez-Calvo synthesised AuNPs with the same surfactant as that used by Elmes *et al*. (Figure 1.26),[2] however, with a larger diameter.[43] He used the citrate method with four equivalents of citrate relative to $HAuCl_4$.[43] These AuNPs were found to be monodisperse in water with a diameter of *ca*. 15 nm. Similar results were obtained from TEM (*e.g.* 15.8 ± 3.8 nm for **$AuNP_{15nm}$-55b**). The interaction of the AuNPs with DNA was also studied by spectroscopic and microscopic methods, and these results suggested the formation of large self-assembly structures in solution. Larger AuNPs were easier to observe with TEM, facilitating the tracking of the AuNPs after cellular uptake. The larger size of the AuNPs was also expected to make them more suitable for CT scanning because of a greater X-ray attenuation.[126] However, the particles showed lower stability than the smaller AuNPs with a diameter of *ca.* 5 nm.

Further evaluation of the size dependence of the properties of the AuNPs was carried out by repeating the synthesis with three equivalents of citrate, rather than four. The smallest size of AuNPs was observed when the citrate/Au ratio was between three and four

equivalents. At lower ratios, a dramatic increase in the diameter occurred, while a gradual increase in the diameter occurred at higher citrate/Au ratios. In the following sections the properties of AuNPs synthesised using both citrate/Au ratios will be compared. When complex **55b** was used as a surfactant, the greatest stability of the AuNPs was achieved, likely due to the increased hydrophilicity and decreased hydrophobic interactions between the surfactants of the AuNPs.

6.4 Characterisation of AuNPs

Characterisation was carried out for AuNPs with a diameter of *ca*. 5 nm and 15 nm containing different surfactants. The following presents the evaluation of the obtained results after carrying out the relevant adjustment in the synthetic procedures.

6.4.1 Characterisation of $AuNP_{5nm}$-55a

Photophysical characterisation was carried out to ensure the complete functionalisation of AuNPs, which was mentioned in Section 6.3.2.

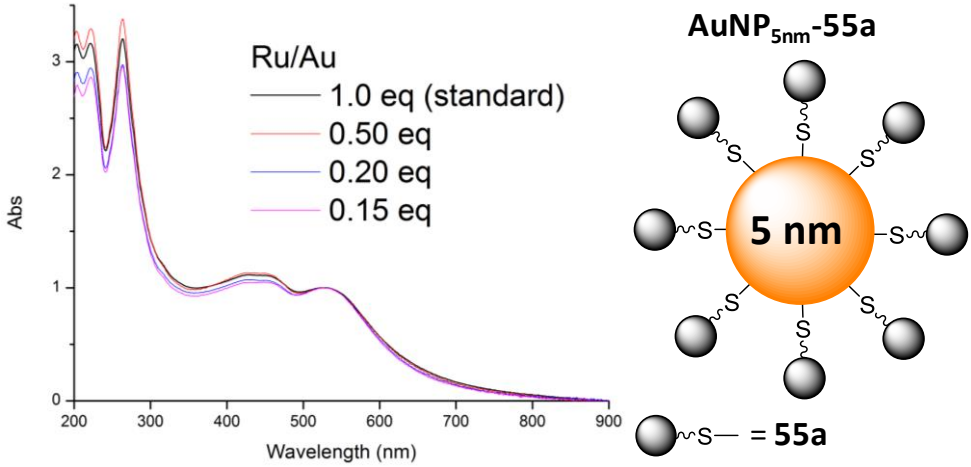

Figure 6.7: *Absorption spectra of* ***AuNP$_{5nm}$-55a*** *in 10 mM aqueous sodium phosphate buffer.*

Photophysical Characterisation

The photophysical properties of AuNPs, which were synthesised by the traditional method introduced by Elmes *et al.* were evaluated in 10 mM sodium phosphate buffered solution together with those synthesised using a lower amount of complex in the functionalisation (Section 6.3.2). Fully functionalised AuNPs were synthesised using the standard protocol, which showed the SPR band maximum at 520 nm with some overlap with the MLCT band at 450 nm of the complex (Figure 6.7). The π-π* intra-ligand transition of the **phen** ligands was observed at *ca*. 260 nm as observed for the free complex, which was in accordance with the results reported in the past.[2]

As shown in Figure 6.7 the normalised absorption spectra of the AuNPs synthesised using the protocols in which a reduced amount of complex was used, have a similar form to AuNPs produced by the standard method. For functionalisation with Ru/Au ratio of 1.0, the observed ratio between the absorbance of the π-π* intra-ligand transition and the SPR band was 3.21 (Table 6.1). When half the amount of complex was used (Ru/Au = 0.50) the normalised absorption spectrum was almost a superimposition of the normal spectrum with a ratio of 3.29 between the two bands. This confirmed the ratio between moles of complex and gold atoms was the same for the functionalised AuNPs as was seen for the standard protocol and that they were fully functionalised. When the concentration of complex was further reduced (Ru/Au = 0.20 and 0.15) the absorbance from the *π-π** transition and the MLCT band decreased relative to the SPR band, which indicated that the AuNPs were not fully functionalised. Taking into consideration the close similarity with the absorption spectrum for the fully functionalised AuNPs it was likely that longer reaction time would result in maximum functionalisation. The summary of the results obtained using different ratios of Ru(II) complex to Au atoms (Ru/Au) is shown in Table 6.1.

Table 6.1: *Results for functionalisation of AuNPs with use of varying amounts of Ru(II) complex* ***55a****.*

Ru/Au (used)	*A(π-π*)/A(SPR)*	*Ru/Au (AuNP) (estimated)*	*Fractional Functionalisation*
1.0	3.21	0.082	100%
0.50	3.29	0.084	100%
0.20	2.97	0.076	90%
0.15	2.96	0.075	90%

Presuming that the 262 nm absorption band arises from only chromophores of the complex, the total concentration of complex at the AuNPs could be estimated from the known molar absorptivity of the complex (ε_{262nm} = 72700 $M^{-1}cm^{-1}$) and the Beer-Lambert law.[2] The ratio between the total concentration of Ru(II) complex and the number of used Au atoms was 0.08 at full functionalisation. When 0.15 equivalent of complex was used, the ratio was 0.75 corresponding to a degree of functionalisation of 90% of maximum functionalisation.

6.4.2 Characterisation of $AuNP_{15nm}$-55b

The difference in the properties of AuNPs synthesised using three and four equivalents of citrate and with the **TAP** complex as surfactant was studied using several techniques. These included measurements of the nanoparticle size using dynamic light scattering (DLS), transmission electron microscopy (TEM) and the zeta potentials to evaluate their stability. The DNA binding properties of the AuNPs will be described in Section 6.5.

Photophysical Characterisation

The photophysical properties of the functionalised AuNPs were evaluated in 10 mM sodium phosphate buffered solution. As can be seen in the normalised spectra shown in Figure 6.8 a small difference in the absorption spectra was observed when the two different methods were used. The SPR band maxima were observed at 539 nm and 534 nm when four and three equivalents of citrate were used, respectively.[226] The red shift in the spectrum of the AuNPs when less citrate was used may be due to the formation of smaller AuNPs. Formation of smaller particles may also explain why the normalised absorbance was stronger for the band at 282 nm corresponding to the π-π* intra-ligand transition of the **TAP** ligands and of the MLCT transition band. Smaller AuNPs result in a larger surface to volume ratio and consequently in a higher degree of functionalisation relative to the total amount of gold atoms.

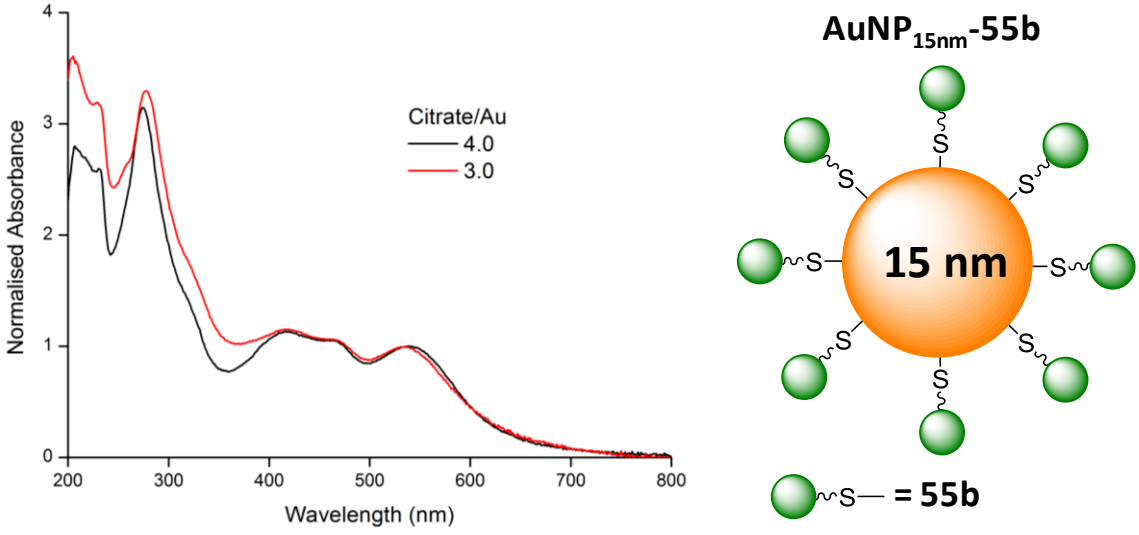

Figure 6.8: *Normalised absorption spectra of* ***$AuNP_{15nm}$-55b*** *synthesised using different strategies; 10 mM aqueous sodium phosphate buffer.*

Stability Studies

The stability of the AuNPs synthesised with the two different methods was evaluated by measuring the absorbance for the SPR bands over the course of 8 hours in 10 mM sodium phosphate buffered solution (pH 7.4). The lack of an observed decrease in the absorbance confirmed that the stability of the AuNPs was relatively high for both methods.

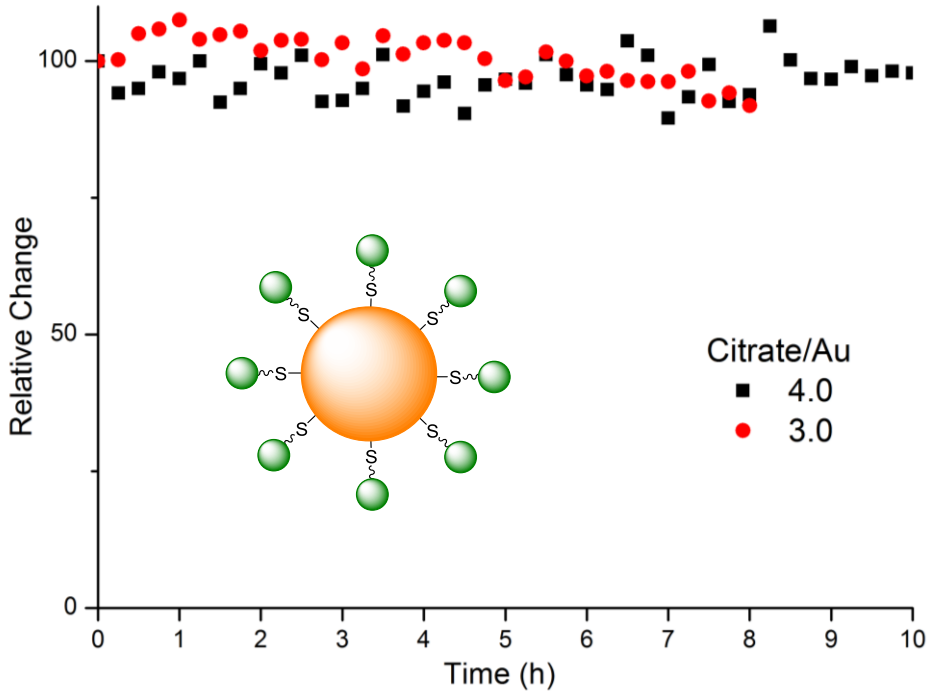

Figure 6.9: *Time dependent absorbance of SPR band of* ***AuNP$_{15nm}$-55b*** *synthesised using different equivalents of citrate; 10 mM aqueous sodium phosphate buffer. Stability was quantified as the relative absorbance compared to the starting point.*

Transmission Electron Microscopy

Transmission electron microscopy (TEM) was used to investigate the AuNPs synthesised using three equivalents of citrate. Similar studies of AuNPs synthesised using four equivalent of citrate have been done in the past by Dr Miguel Martínez-Calvo.[43] TEM was utilised due to the much higher resolution images generated compared to images obtained with optical microscopy.[227] The AuNPs were deposited onto formvar stabilised carbon coated copper grids prior to the TEM imaging. In contrast to the AuNPs synthesised with the traditional method (Figure 6.10a) the TEM images for those synthesised using the new protocol (Citrate/Ru = 3) showed strong aggregation (Figure 6.10b). Due to the high degree of polydispersity the size distribution was not quantified, however the diameter of the individual particles was similar to the sizes obtained with four equivalent of citrate in the past (15.8 ± 3.8 nm).[43]

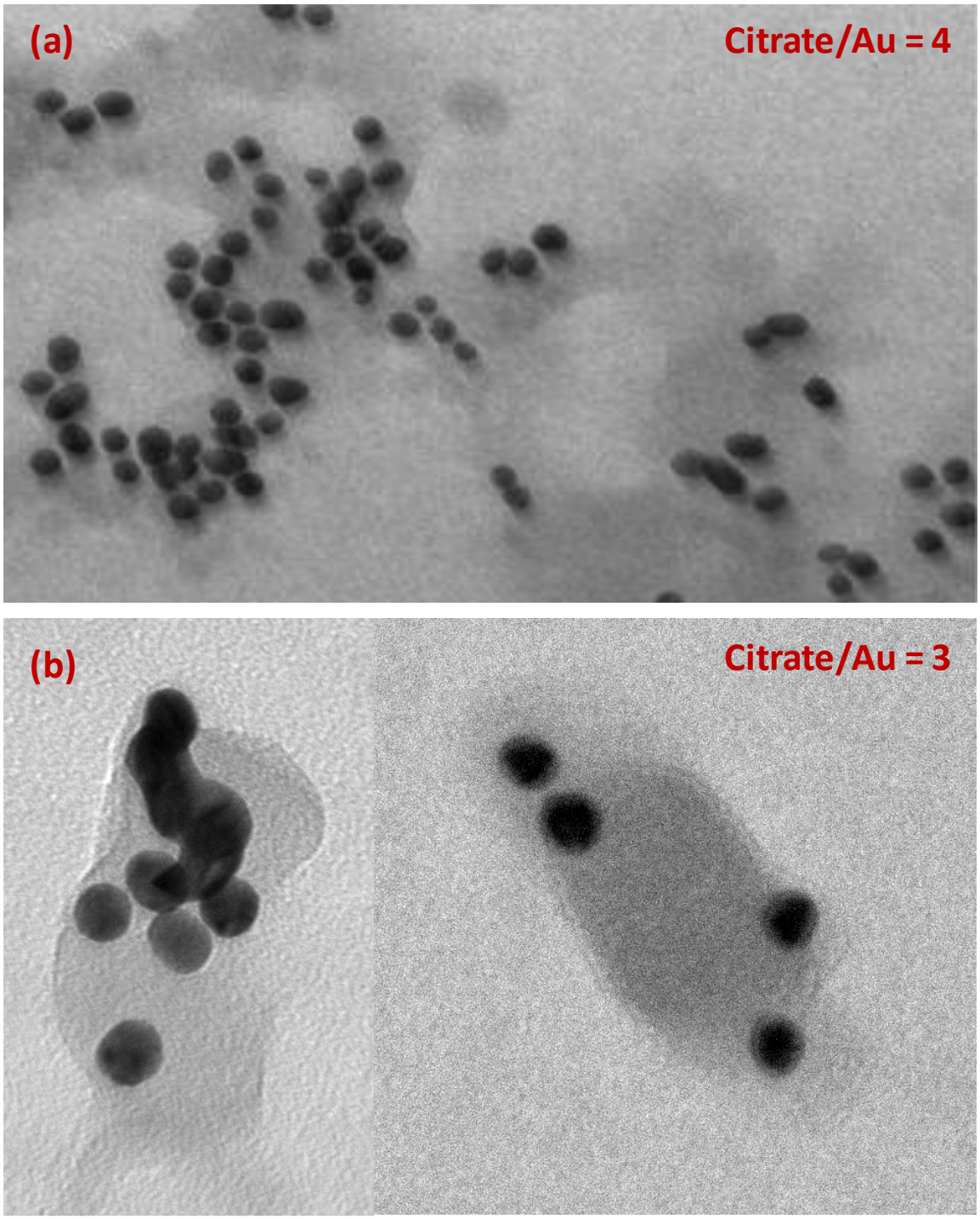

Figure 6.10: *TEM images of* ***AuNP$_{15nm}$-55b*** *synthesised with (a) four and (b) three equivalent of citrate deposition onto formvar stabilised carbon coated copper grids. Diameter ca. 15 nm in both cases.*

Dynamic Light Scattering and Zeta-potential

Dynamic light scattering (DLS) is a technique that can be used to measure the size of the particles in the micro- or nanometre scale.[228] Particles in suspension undergo Brownian motion as a result of bombardment of solvent and solutes driven by thermal energy and leading to random fluctuation. When the light from a laser penetrates the sample the

fluctuation of the intensity of scattered light will depend on the velocity of the particles, which is directly correlated to their size. Analysis of the fluctuation can be used to measure the diameter of the particles. The size is an "effective" diameter, which, in case of functionalised AuNPs in H_2O, includes the gold core, surfactants and strongly associated solutes and solvent molecules. Aggregation of different nanoparticles can also result in larger sizes of the derived diameter. When measured in H_2O the size is called the hydrodynamic diameter.

In addition to measuring hydrodynamic diameters, DLS can also be used to measure the zeta-potential, which represents the charge at the surface of nanoparticles.[229] Just as the hydrodynamic diameter corresponds to the effective size of the particles, the zeta-potential does not necessarily represent the actual charge at the surface of the particle. The measured value also includes contribution from the charge of ionic species that are associated with the surface. For example, a decrease in the zeta-potential will be observed when negatively charged DNA binds to the surface. High positive or negative zeta-potentials are needed to stabilise nanoparticles, since this will result in strong electrostatic repulsion between individual particles, which prevents aggregation.

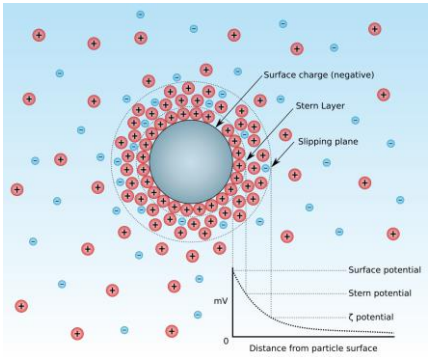

Figure 6.11: *Schematic presentation of Zeta-potential of a nanoparticle.*[1,2]

Dr Martínez-Calvo showed the hydrodynamic diameter of the AuNPs in water was 11 nm using DLS, which was similar to the that observed by TEM (Figure 6.10). However, DLS measurements of the AuNPs synthesised with three equivalent of citrate herein resulted in poor quality of the collected data. DLS is not well suited to study the suspension of particles with large and non-normal size distribution. For that reason it is essential that 'high quality' samples are used. Hence, this technique is unsuited for the study of polydisperse samples, with large variation in the particle diameters. The poor quality of the collected data might be a consequence of the aggregation of AuNPs as observed in TEM (Figure 6.10).

Zeta-potential measurements for both types of AuNPs were carried out in pure water, giving a value of +18.6 ± 0.9 mV when synthesised with four equivalent of citrate, which is typical of AuNPs with a low stability. It was not possible to measure the zeta-potential for AuNPs synthesised with three equivalent of citrate, as a possible consequence of their polydispersity.

6.4.3 Characterisation of $AuNP_{5nm}$-61a

The AuNPs with the new surfactant **61a** were characterised using various techniques; their size was measured using DLS and SEM, and their stability was measured using absorbance spectroscopy and also the corresponding zeta potential.

Photophysical Characterisation and Stability Studies

The photophysical properties of AuNPs were evaluated in pure aqueous solution and under phosphate buffered conditions. The absorbance and emission spectra were similar to spectra of the AuNPs, which was observed for **$AuNP_{5nm}$-55a**. However, the SPR band had a maximum at 546 nm, which corresponded to a redshift of *ca*. 25 nm compared to the spectrum of other AuNPs functionalised with **55a** (Figure 6.7). The π-π* intra-ligand transition band of the **phen** ligands had a maximum at 265 nm, which was the same as that observed for the free complex. The MLCT transition band at *ca*. 440 nm was relatively weak and almost masked by overlap with the SPR band. A very broad emission band with a maximum at 645 nm, which also showed emission up to above 800 nm, was similar to a band for the free complex. The emission in the NIR region make the AuNPs good candidates for imaging because of the better penetration of tissue by light in this region.[230]

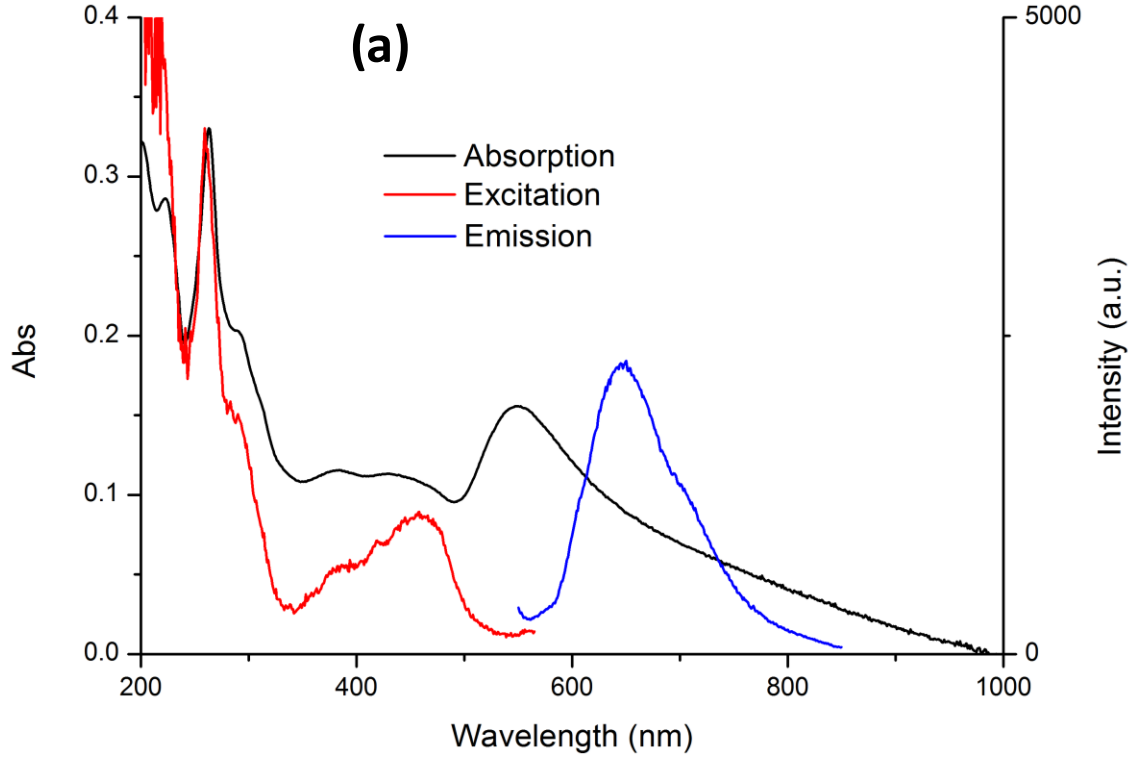

Figure 6.12: *Absorption and emission spectra of* ***$AuNP_{5nm}$-61a*** *in aqueous solution. Excitation wavelength for the emission spectra was 440 nm and emission wavelength was 645 nm.*

The stability of the AuNPs was evaluated by measuring the absorbance of the SPR bands over the course of 24 hours in 10 mM aqueous sodium phosphate buffered solution (pH 7.4) and pure H_2O (Figure 6.13). Surprisingly, in pure H_2O an increase was observed in the absorbance of the SPR, MLCT and π-π* band. This could be due to release of the complex from the AuNPs over time upon nucleation since the relative decrease in absorbance was more pronounced for decreasing wavelengths, where the relative absorption of complex **61a** will be higher compared to absorption of the gold core of the AuNPs. The absorbance of the complex may be lower when attached to the AuNPs due to close proximity of the chromophores of the complexes, which is known to result in a hypochromic effect.[231,232] A concomitant decrease in the absorbance in the NIR region of the spectrum indicated that the AuNPs precipitated out of the solution over time (Figure 6.13). The nucleation of the AuNPs may result in release of the surfactants to the solution that could explain the increase in absorption of the MLCT band. A decrease of *ca.* 5% in the absorbance at 750 nm was observed after 12 hours (Figure 6.13).

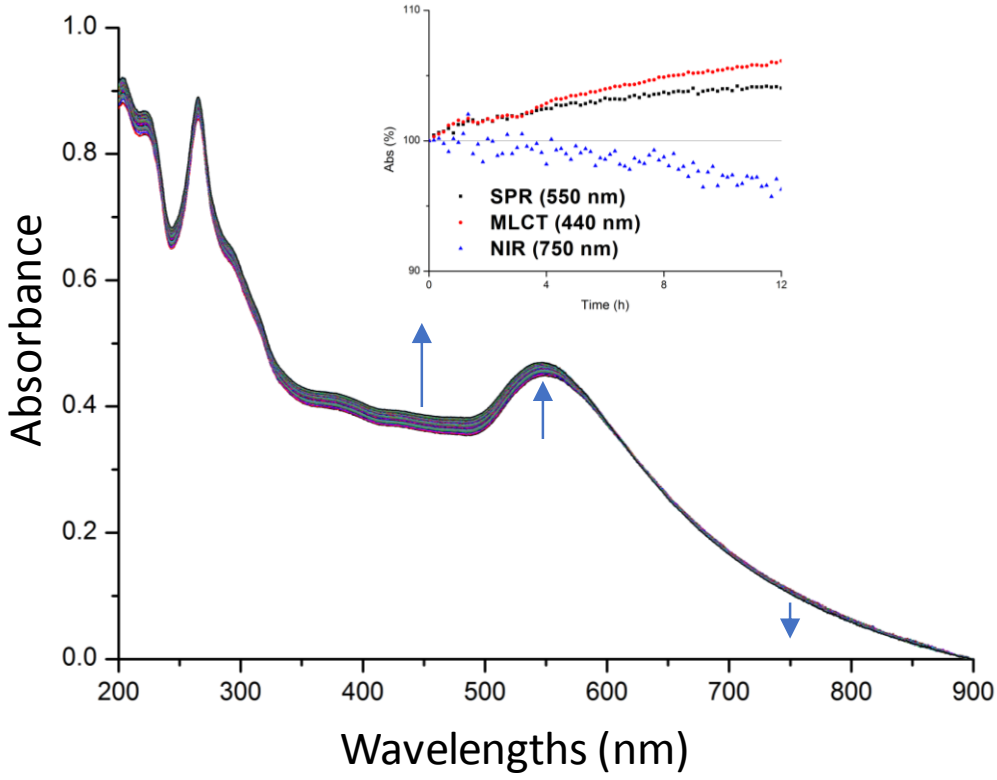

Figure 6.13: *Changes in spectra of* ***AuNP$_{5nm}$-61a*** *in pure deionised water. Insets: Relative change in absorbance at different wavelengths.*

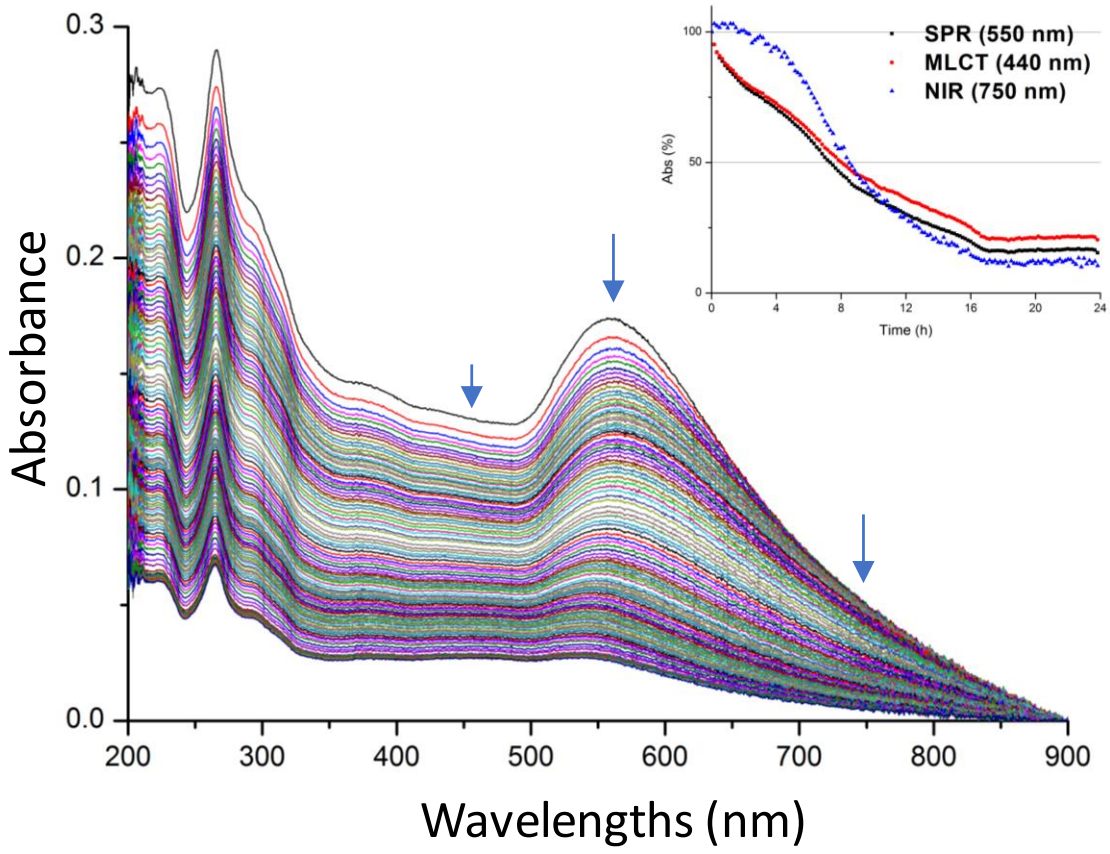

Figure 6.14: *Changes in spectra of* ***AuNP$_{5nm}$-61a*** *in 10 mM sodium phosphate buffered aqueous solution (pH 7.4). Insets: Relative change in absorbance at different wavelengths.*

A relative fast decrease in the absorbance spectrum was observed in phosphate buffer with a large decrease over the course of 24 hours, which was in accordance with low stability of the AuNPs. It is known that the stability of functionalised AuNPs will decrease with increasing ionic strength due to decrease in the zeta-potential.[233] A plateau in the decrease was observed in the absorbance after 16 hours (Figure 6.13). A decrease in the NIR region was expected to be the best measure for the concentration of AuNPs because the complex has no absorbance in this region of the spectrum and the band can be assigned exclusively to absorption of the gold core of the AuNPs. The rate of the decrease was relatively small in the beginning, but accelerated through the first seven hours. This may be due to nucleation of the AuNPs occurring when the aggregates of AuNPs reach a certain size and precipitate out of solution.[234] The observation of the rapid decrease in the absorbance of the MLCT band in the beginning, may be due to interactions between the chromophores of the surfactants of different AuNPs upon aggregation.

Scanning Electron Microscopy

Scanning Electron Microscopy (SEM) imaging of the AuNPs was carried out by Dr Savyasachi A. J. in order to get an insight into the size and morphology of the AuNPs synthesised herein. Similar to TEM, which utilises electrons to image the sample, SEM uses an electron beam to visualise the sample. However, instead of detecting the transmitted electrons through the sample, the SEM imaging is based on the detection of reflected electron.[227] The resulting grey scale picture has a resolution that is lower than TEM images, however, this technique also gives a good insight into the morphology of the AuNPs.

The samples were prepared by dropcasting solutions with different weight percentages (w/w) of AuNPs (0.5%, 0.2% and 0.1%) onto a formvar stabilised carbon coated copper grids. The images showed the aggregation of polydisperse spherical nanoparticles at all concentrations with a diameter of the individual particles between 20 and 50 nm (Figure 6.15). The synthetic procedure used was expected to give AuNPs with a diameter of *ca*. 5 nm, and it was expected that the observed particles were composed of several aggregated AuNPs.

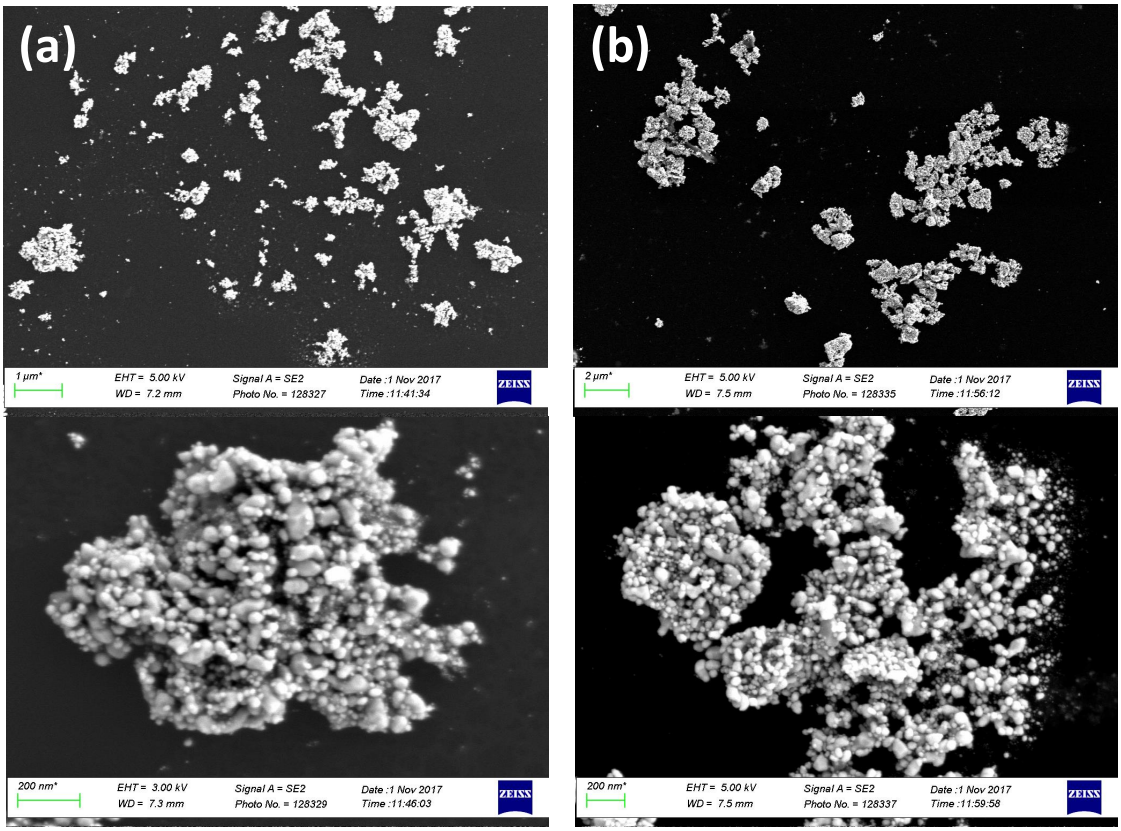

Figure 6.15: *SEM images of* ***AuNP$_{5nm}$-61a*** *after dropcasting solutions onto formvar stabilised carbon coated copper grids with varied w/w: (a) 0.2% and (b) 0.1%.*

Dynamic Light Scattering and Zeta-potential

Attempts made to carry out DLS measurements with **AuNP$_{5nm}$-61a** resulted in poor quality collected data. This was rationalised by the potential polydispersity of the AuNPs. This large size distribution was also observed using SEM. The average zeta-potential was found to be +40.7 ± 0.3 mV, which is a typical value for stable AuNPs which would suggest that the AuNPs were positively charged as a result of the functionalisation with the cationic Ru(II) complex, as expected.

6.5 DNA Binding Interactions of AuNPs

6.5.1 Spectroscopic Titrations AuNP$_{15nm}$-55b with st-DNA

The changes observed in the absorption spectrum of·**AuNP$_{15nm}$-55b** synthesised with the standard method were similar to what was observed by Martínez-Calvo upon titration with st-DNA (Figure 6.16a).[43] Before addition of st-DNA a band with a maximum at 282 nm (attributed to the transitions of the ancillary ligands, π-π*; ε = 50900 $M^{-1}cm^{-1}$), an MLCT band centered at *ca.* 420 nm with a shoulder at 460 nm, and an SPR band with a maximum at *ca.* 535 nm was observed. By addition of st-DNA abrupt changes were observed in the higher energy transitions, as well as in the MLCT band, which underwent a hypochromic change, and a similar effect was observed for the SPR band centered at 535 nm. These changes were similar to those reported for the complex alone upon titration with st-DNA; which were consistent with a strong association of AuNPs with DNA. The site binding constant (*k)* was also determined by fits of these changes using the modified Bard method. A plot of ε_a vs. C_{bp} and the corresponding best fit of the data to the equation is shown in Figure 6.16b. From the changes, *k* of 3.6×10^6 M^{-1} was determined. This is a comparable binding affinity to that seen for other Ru(II) complexes, under similar experimental conditions.[80] The value obtained for the binding site size from the titration was close to unity (0.9 bp), which indicated that the AuNPs were interacting with the DNA through either groove binding or electrostatic interactions, since this value is much lower than the expected value of *ca*. 2.0 commonly seen for interaction by intercalation.[28] This was not surprising given that the conjugation of these complexes to the AuNPs will have an effect on the degree of freedom for the binding to the biomolecule. A dramatic decrease was observed in the band intensity in the emission spectrum, which may be explained by the quenching of the excited state as a result of a photo-oxidation of DNA upon excitation of the complex.[52]

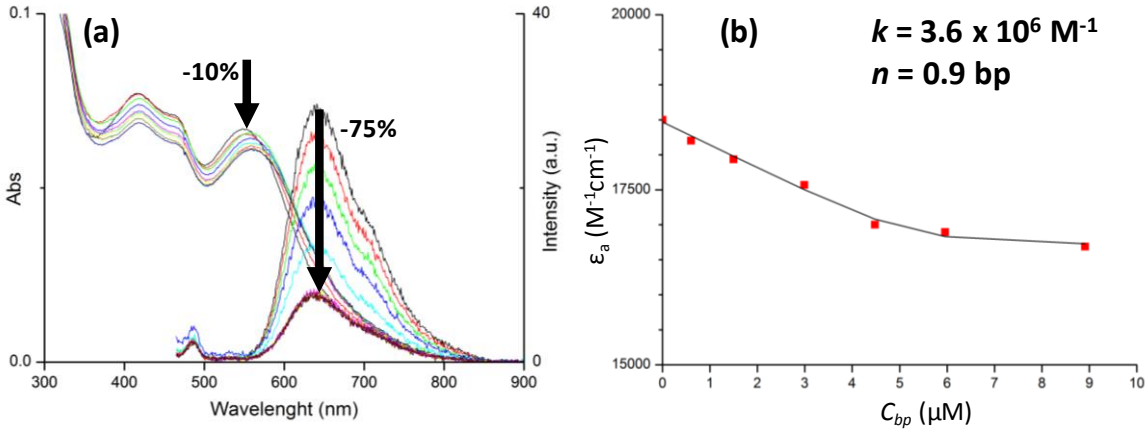

Figure 6.16: *(a) Changes in absorption and emission spectrum of* ***AuNP$_{15nm}$-55b*** *(ca. 20 μM) upon increasing concentration of st-DNA; (b) Fit of Scatchard binding parameters for binding to st-DNA of complex at* ***AuNP$_{15nm}$-55b****; 10 mM sodium phosphate buffer, pH 7.4, 25 °C. AuNPs synthesised with citrate/Au = 4.*

A different result was obtained for the titrations of the AuNPs synthesised with three equivalents citrate. Upon addition of st-DNA to a solution of AuNPs, a precipitate was formed, which resulted in disturbance of the spectrum (Figure A6.1). It was not possible to fit binding parameters to the data. The formation of a precipitate was in accordance with the tendency of AuNPs to form aggregates upon binding to DNA. It has been shown by Dr Martínez-Calvo using DLS and TEM that aggregation is also induced in the AuNPs synthesised with method A upon increase in DNA concentration.[43] Hence, due to the general tendency of the AuNPs synthesised with the method to form aggregates it was not surprising to see the precipitation in the performed titrations.

6.6 Conclusion and Future Perspectives

Based on and inspired by previous work in the Gunnlaugsson group AuNPs functionalised with luminescent Ru(II) polypyridyl complexes **55a**, **55b** and **61a** were synthesised and characterised. The previously studied AuNPs, functionalised with **phen** complex **55a** (**AuNP$_{5nm}$-55a**), were also synthesised with the primary purpose of optimising the synthetic procedure. The synthetic procedure was optimised to make it practically feasible to produce the AuNPs on a large scale . It was shown that similar absorbance spectra was observed for all AuNPs even when only 15% of the usual amount of complex was used in the synthesis, however, with minor variations in the sharpness of the spectra. AuNPs with the same properties as those synthesised with the previously reported procedure,[43] including characterisation of size, stability and zeta-potential. Synthesis of larger AuNPs functionalised with **TAP** complex **55b** was also carried out using an alternative procedure

to that introduced by Dr Martínez-Calvo.[43] The new procedure showed decreased stability and small changes in the photophysical properties of the resulting AuNPs. Upon binding to DNA the AuNPs formed a precipitate most likely due to aggregation and nucleation of the AuNPs.

A new functionalised type of AuNPs with **phen** complex **61a** as surfactant (**AuNP$_{5nm}$-61a**) was also synthesised. Like complex **61a** the AuNPs showed a strong emission in the red and NIR region. The AuNPs were relatively stable in pure aqueous solution with a zeta potential of +40.7. SEM showed aggregation of the AuNPs with spherical clusters of AuNPs with a diameter between 20 and 50 nm. The AuNPs showed a very low stability in 10 mM aqueous sodium phosphate buffer.

Chapter 7

Experimental

7.1 General Methods

All NMR spectra were recorded using an Agilent Technologies 400/54 Premium Shielded spectrometer, which operates at 400 MHz for ^{1}H NMR and 100 MHz for ^{13}C NMR, a Brüker AV-600 spectrometer, operating at 600 MHz for ^{1}H NMR and 150 MHz for ^{13}C NMR, or an Agilent Technologies 800/54 Premium Compact spectrometer, which operates at 800 MHz for ^{1}H NMR and 200 MHz for ^{13}C NMR. Chemical shifts (δ) were referred to relative to the internal solvent signals and reported in ppm.

Electrospray ionisation (ESI) mass spectra were recorded on a Mass Lynx NT V 3.4 with a Waters 600 controller connected to a 996 photodiode array detector using HPLC-grade solvents. All high resolution (HR) masses were reported within ±10 ppm of the expected mass.

Melting points were obtained in an unsealed capillary tube using an Electrothermal 9100 melting point apparatus. Elemental analyses were conducted at the Microanalytical Laboratory, School of Chemistry and Chemical Biology, University College Dublin (UCD).

7.2 Photophysical Measurements

UV-Vis spectroscopy and luminescence measurements were performed in a quartz cell at room temperature. The absorption spectra were recorded using a Varian Cary 50 UV-Visible spectrophotometer. The emission and excitation spectra were recorded on a Varian Cary Eclipse fluorescence spectrophotometer. Circular Dichroism (CD) spectra of DNA were recorded at a concentration corresponding to an optical density of approximately 1.0 for the DNA absorbance (75 μM base pairs) at 260 nm on a Jasco J-810-150S CD spectropolarimeter. Phosphate buffered solutions were made from a 10 mM stock solution of NaH_2PO_4 or 50 mM stock solution of KH_2PO_4 in millipore water in which the pH was adjusted by addition of NaOH or KOH, respectively.

The extinction coefficients were determined in the following manner: Absorption spectra were measured at different concentrations of complex, and absorption maxima were plotted against concentrations. The extinction coefficients were derived from the slope of the best linear fits of these plots. In every case the standard error of the mean value was reported.

7.3 Use of ReactLab EQUILIBRIA to Calculate Parameters for Binding with DNA

ReactLab EQUILIBRIA™ is a commercially available program from Jplus Consulting,[235] which is able to calculate binding constants from global fitting to multivariate data from

spectroscopic titration experiments. The program is designed to study systems with a limited number of equilibria. In the following the protocol will be given for use of the program to fit, in practice, an infinite number of equilibria in case of multivalent binding (Chapter 1). The program uses Microsoft Excel as interface and makes the calculations in MatLab. Some prior knowledge of the program is needed for the understanding of the following (The manual may be found at http://jplusconsulting.com/products/reactlab-equilibria/).

7.3.1 Fit of the Scatchard Binding Parameters

Most of the data was introduced to the program in accordance with the standard procedure. A single 1:1 equilibrium was defined as a binding model (top of 'Main' sheet). The start concentration of complex (L) and the volume in the cuvette were added to the fields for automatic calculation of the concentration (bottom of 'Main' sheet). The model was compiled. The binding site size (n) was defined as an auxiliary ligand. The concentration of binding sites (D) was defined in the field for automatic calculation of the concentration as C_{bp}/n by referring to the field for the value of the fitting parameter (it is important to define the concentration of D after compilation has been carried out). The added volume and the spectra were included in 'Data' sheet in accordance with the standard procedure. The model was fitted using an appropriate start guess of the binding parameters.

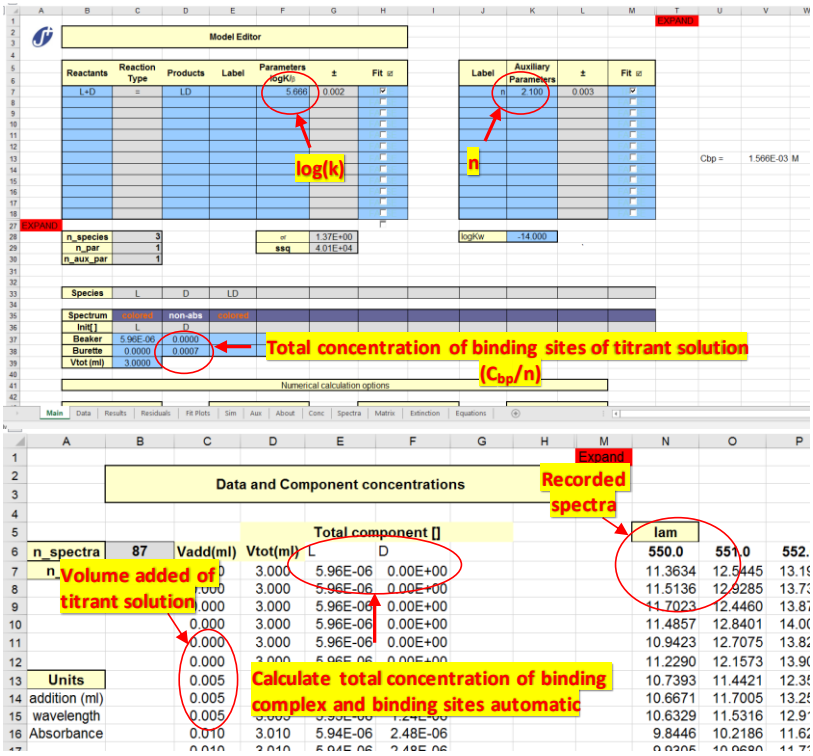

Figure 7.1: *'Main' and 'Data' sheet for fitting of Scatchard binding parameters in ReactLab EQUILIBRIA.*

7.3.2 Fit of Multiple Equilibria

The data were introduced to the program in a manner similar to the one just described for the Scatchard model. Instead of just one equilibrium, several equilibria were defined as binding models (1:1, 1:2, *etc.*). The model was compiled. Instead of defining the concentration of sites D as C_{bp}/n, the concentration of a *cluster* of sites were defined in the field for the automatic calculation of the concentration of D as $C_{bp}/(N \cdot n)$. In this expression N is the number of defined equilibria (N = 3 in the example in Figure 7.2). All logarithmic values for the association constants can be fitted in accordance with normal practice. Alternatively a single site binding constant can be defined as an auxiliary fitting parameter to avoid over parameterization. Instead of initialising the binding parameters for each equilibrium in the usual fashion, the respective fields will have to be defined according to the equation:

$$K_i = Q_i{}' k^i \qquad (7.1)$$

The significance of this equation is that the i complexes bound to a single binding site, D, can bind in $Q_i{}'$ ways, all corresponding to the same energy. Presuming there are N independent binding sites, $Q_i{}'$ will be given as the binomial coefficients $[\binom{N}{i}]$. In that case $\log K_i$ will be given as:

$$logK_i = i \cdot \log(k) + \log\binom{N}{i} \qquad (7.2)$$

This equation corresponds to a fit using the Scatchard model, however with different molar signals for bound L.

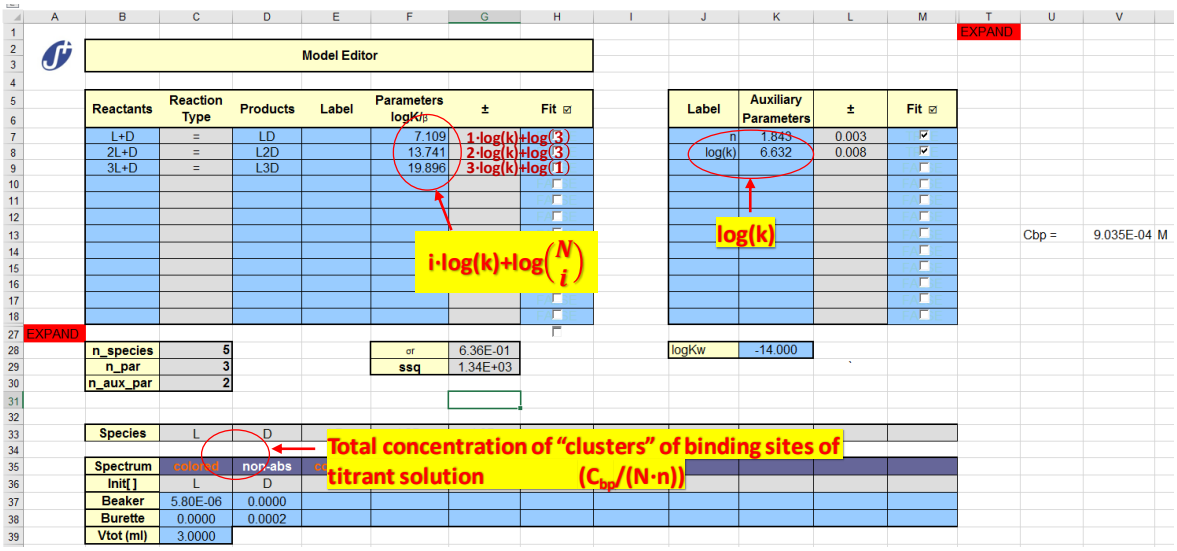

Figure 7.2: *Main sheet for fitting of binding parameters for multiple equilibria in ReactLab EQUILIBRIA in case of multivalent binding with an undefined number of binding sites.*

7.3.3 Fits of the Non-cooperative MGVH Model

The data were fitted to the Scatchard model, as described in Section 7.3.1, to initialise the concentration profile for bound complex. Afterwards, the fields in the 'Main' sheet that do automatic calculations of the concentration of complex and binding sites, were cleared. Instead, the concentrations were defined manually in the 'Data' sheet. Total concentration of complexes (L) had already been calculated before the fitting to the Scatchard model. However, the concentration of binding sites (D) had to be recalculated in accordance with the non-cooperative MGVH model (Chapter 1). For the spectra recorded of solutions with zero concentration of base pairs, D, were set to zero. For all other spectra the concentration was defined from the total concentration of base pairs (C_{bp}) and the concentration of bound ligand, which is calculated in the 'Results' sheet. The data were fitted repeatedly until only a small change occured in the calculated binding parameters between each fit (*ca*. 10 times).

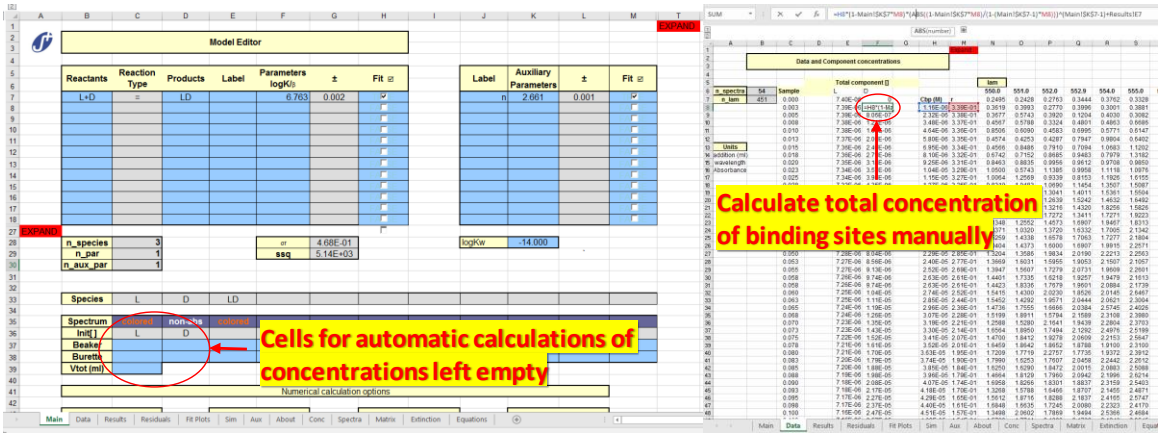

Figure 7.3: *'Main' and 'Data' sheet for fitting of the non-cooperative MGVH binding parameters in ReactLab EQUILIBRIA.*

7.3.4 Fits of the Cooperative MGVH Model

The cooperative MGVH model was fitted using a predefined Excel file with enabled macros. The background for the construction of the template is given in Chapter 1.

7.4 General Biological Procedures

HeLa cells were grown at 37 °C in a humidified atmosphere of 5% CO_2 in a cell culture flask using low-glucose Dulbecco's Modified Eagle Medium supplemented with 10% fetal bovine serum. Confocal laser microscopy experiments were carried out using HeLa cells, seeded at a density of ca. 1×10^5 cells/mL. Cells were incubated for 24 hours before treatment with the required compound. Luminescence was detected using a Leica TCS SP8 X point scanning microscope. The software Leica Application Suite X was used to collect images.

Cell cytotoxicity tests were carried out using HeLa cells, seeded at a density of ca. 25×10^3 cells/mL, and an Alamar Blue cytotoxicity assay.

7.5 Computational Methods used in Molecular Modelling

All quantum mechanical calculations were done with density functional theory (DFT) using the Gaussian 09 Software package.[148] Geometry optimised structures of all compounds were calculated on the basis of the crystal structure if available, or the structures were pre-optimised using the molecular mechanical method MM2 and ChemDraw3D. The quantum mechanical calculations for molecules in solvent were carried out using a solvation model based on density (SMD), which is suitable for calculations of thermodynamic parameters.[185]

7.6 Synthetic Procedures

Commercial reagents were purchased from Sigma-Aldrich Ireland Ltd., Acros Organics or TCI Ltd. Deuterated solvents were purchased from Apollo Ltd., Sigma-Aldrich or VWR International. Silica gel 60 (230-400 mesh ASTM) was used for standard chromatographic separation. A Teledyne ISCO CombiFlash® Rf 200 automatic column chromatography machine was used for automatic column flash chromatography. Reactions in which microwave irradiation was used were carried out using a Biotage® Initiator microwave synthesiser.

Procedure 1: Precursor for Ru(II) Polypyridyl Complexes

The appropriate polypyridyl ligand (**phen**, **TAP** or **dppz**; 2 eq) and $Ru(cod)Cl_2$ (1 eq) were suspended in DMF (10 mL/100 mg $Ru(cod)Cl_2$). The mixture was degassed with nitrogen for 15 minutes and then heated at 140 °C for 40 minutes using microwave irradiation. The mixture was cooled to room temperature, mixed with Me_2CO (25 mL), and left overnight at 15 °C. The product was isolated by filtration as a black solid and washed with cold Me_2CO (10 mL).

Procedure 2: Ru(II) Polypyridyl Complexes

The appropriate polypyridyl ligand (1 eq) and a ruthenium polypyridyl precursor complex ($[Ru(phen)_2Cl_2]$ or $[Ru(TAP)_2Cl_2]$; 1 eq) were suspended in a mixture of ethanol and H_2O (EtOH:H_2O 1:1, 5 mL) or in a mixture of glycol and H_2O (glycol:H_2O 4:1, 10 mL). The exact conditions are stated in the relevant sections. The mixture was sonicated until all ligand was in suspension, then degassed with nitrogen for 15 minutes, and finally heated between

100 and 140 °C using microwave irradiation. The mixture was reacted at 140 °C for 10 to 40 minutes (see the syntheses of appropriate complexes below).

Purification was carried out by column chromatography with either alumina or silica as the solid phase. When neutral alumina was used, the solid was purified using MeCN:H_2O (10:0 to 9:1) as eluent. On the other hand when silica was used, solid NH_4PF_6 (ca. 5 eq) was added to the reaction mixture resulting in the formation of a dark precipitate. The precipitate was isolated by centrifugation and washed with H_2O (10 mL). Purification was achieved through silica gel flash column chromatography using MeCN:H_2O:$NaNO_3$(conc. aq) (40:4:1) as eluent. Solvent from the collected band containing the product was removed at reduced pressure. The resulting solid was dissolved or suspended in water (25 mL) and solid NH_4PF_6 (ca. 5 eq) was added to the solution/suspension. The PF_6-salt of the complex was collected by centrifugation and washed with H_2O (3 × 10 mL). The chloride form of the complex was reformed by stirring a solution of the PF_6-complex in MeOH (50 mL) with Amberlite ion exchange resin (the chloride form) for one hour.

Procedure 3: Ru(II) Polypyridyl Complex with phendione as Ligand[164]

The ligand **phendione** (1 eq) and ruthenium polypyridyl precursor complex ([$Ru(phen)_2Cl_2$]; 1 eq) were suspended in a mixture of ethanol and H_2O (EtOH:H_2O 1:1, 5 mL). The mixture was degassed with nitrogen for 15 minutes and then heated at 140 °C for 30 minutes using microwave irradiation. Upon addition of solid NH_4PF_6 (ca. 5 eq) a dark precipitate was formed. The precipitate was isolated by centrifugation, washed with H_2O (3 × 10 mL) and then purified by trituration by dissolving the compound in MeCN (2 mL) and adding Et_2O (10 mL). The solid was isolated by centrifugation and washed with Et_2O (3 × 10 mL). The chloride form of the complex was reformed by stirring a solution of the PF_6 complex in MeOH (50 mL) in Amberlite ion exchange resin (the chloride form) for one hour.

Procedure 4: Functionalised $AuNP_{5nm}$[2]

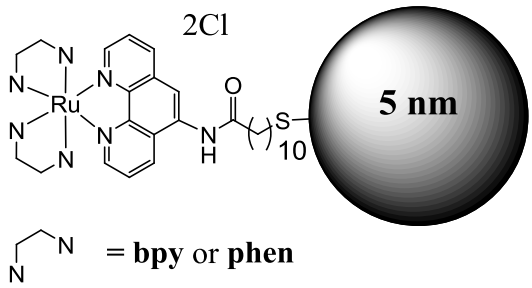

Glassware used in the synthesis was carefully cleaned with *aqua regia* and plenty of water before use. $HAuCl_4$ (100 mg, 254 μmol, 1 eq) was dissolved in H_2O (100 mL) yielding a bright yellow solution. A solution of tetraoctylammonium bromide (TOAB, 360 mg, 658 μmol, 1 eq) in toluene

(25 mL) was added resulting in a colourless water layer and an orange toluene layer. After 10 minutes, a solution of $NaBH_4$ (130 mg, 3.44 mmol, 13 eq) in H_2O (10 mL) was added resulting in a colour shift of the toluene layer to a darker shade. After one hour, the toluene layer containing the TOAB stabilised gold nanoparticles (**AuNP$_{5nm}$**) was isolated and stored for future use.

An aqueous solution (5 mL) of the appropriate Ru(II) complex (50 mg) was mixed with 5 mL of the solution of **AuNP$_{5nm}$** giving a biphasic mixture that was stirred overnight. The two layers were then separated by centrifugation yielding a colourless toluene layer and a dark water layer, which were isolated. Upon the addition of NH_4PF_6 (*ca*. 50 mg) to the aqueous fraction a dark precipitate was formed. The precipitate was isolated by centrifugation, washed with H_2O (3 × 5 mL), and dissolved in MeCN (5 mL). Upon the addition of a saturated solution of tetrabutylammonium chloride (TBACl) in MeCN (2 mL) the corresponding chloride salt of the AuNP was precipitated with unreacted complex staying in solution. This precipitate was then isolated by centrifugation and washed with MeCN (3 × 5 mL). The functionalised AuNPs were isolated as a black powder and dried *in vacuo*.

Procedure 5: Functionalised AuNP$_{15nm}$[43]

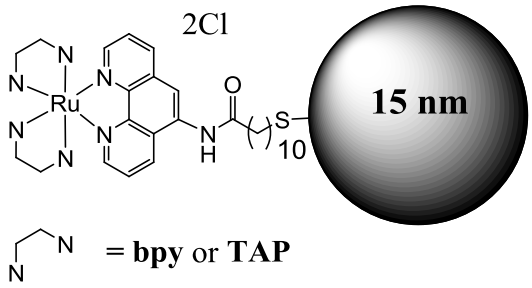

Glassware used in the synthesis was carefully cleaned with *aqua regia* and plenty of water before use. $HAuCl_4 \cdot 3H_2O$ (40 mg, 102 μmol, 1 eq) was dissolved in H_2O (300 mL) yielding a bright yellow solution that was heated at reflux temperature for 15 minutes. A solution of trisodium citrate dihydrate (193 mg, 656 μmol, 6 eq) in water (10 mL) was added, and the solution was heated under reflux for 15 minutes while the colour turned wine red. The solution with the citrate-stabilised gold nanoparticles (**AuNP$_{15nm}$**) was cooled to room temperature and stored for future use.

An aqueous solution (1 mL) of the appropriate complex (0.7 mM) was mixed with 1 mL of the solution of **AuNP$_{15nm}$** after adjustment of pH to 3 for both solutions by addition of diluted HCl. The mixture was stirring overnight at room temperature. Upon the addition of saturated aqueous NH_4PF_6 (1 mL) to the water layer a dark precipitate was formed. The precipitate was isolated by centrifugation, washed with H_2O (3 × 5 mL), and dissolved in MeCN (5 mL). Upon the addition of a saturated solution of tetrabutylammonium chloride

(TBACl) in MeCN (2 mL) the corresponding chloride salt of the AuNP was precipitated with unreacted complex staying in solution. This precipitate was then isolated by centrifugation and washed with Me_2CO (3 × 5 mL). The functionalised AuNPs were isolated as a black powder and dried *in vacuo*.

2-Methyl-6-nitroquinoxaline (34)[136]

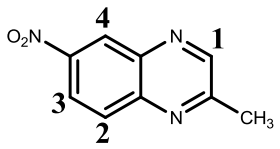

A solution of 4-nitro-1,2-benzenediamine (10.00 g, 64.45 mmol, 1 eq) in ethanol (500 mL) was heated to reflux temperature. Aqueous methylglyoxal (40%, 15 mL, 99 mmol, 1.5 eq) was added, and the resulting solution was heated at reflux for two hours. The reaction mixture was cooled to room temperature. The solvent was removed under reduced pressure, and the resulting solid was dissolved in CH_2Cl_2 (200 mL). This was washed with H_2O (3 × 100 mL). The CH_2Cl_2 phase was filtered through SiO_2 (100 mL), extracting with CH_2Cl_2 (200 mL), and the organic phase was evaporated. The solid was recrystallised three times from isopropanol, the product was isolated as white crystals and dried *in vacuo* (5.32 g, 27.8 mmol, 43%). *m.p.* = 163.0-166.0 °C (Ref.,[236] 168-169 °C). δ_H (400 MHz, DMSO-d_6): 9.06 (s, 1H, H1), 8.85 (d, 1H, J = 2.6 Hz, H4), 8.52 (dd, 1H, *J* = 9.2 Hz, *J* = 2.6 Hz, H3), 8.22 (d, 1H, *J* = 9.2 Hz, H2), 2.78 (s, 3H, CH_3). HRMS (*m/z*-ESI): Found: 188.0462 (M-H. Requires: 188.0460).

2-Methyl-5-amino-6-nitroquinoxaline (35)

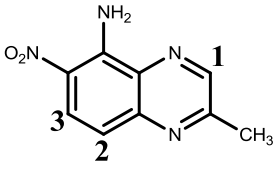

Metallic sodium (1.46 g, 63.4 mmol, 4 eq) was added to anhydrous methanol (250 mL) at room temperature. The sodium reacted with methanol resulting in the formation of hydrogen gas. Hydroxylammonium chloride (2.10 g, 30.2 mmol, 2 eq) was added to the solution. The mixture was stirred for one hour. 2-Methyl-6-nitroquinoxaline (3.00 g, 15.8 mmol, 1 eq) was then added to the colourless reaction mixture, immediately yielding a green-yellow solution. The solution was stirred overnight giving a colour change to a dark mixture. To the mixture, concentrated aqueous NH_4NO_3 (25 mL) was added. The solvent was removed under reduced pressure. The solid was dissolved in CH_2Cl_2 (300 mL) and washed with H_2O (3 × 100 mL). The CH_2Cl_2 layer was dried over $MgSO_4$ before removal of the solvent under reduced pressure. The resulting solid was purified using automatic column chromatography (120 g SiO_2, hexane:EtOAc 100:0 to 70:30). The product 2-methyl-5-amino-6-nitroquinoxaline (**35**) was obtained as a yellow

solid and dried *in vacuo* (0.870 g, 4.26 mmol, 27%). *m.p.* = 182.0-183.0 °C. Calculated for $C_9H_8N_4O_2$: C, 52.94; H, 3.95; N 27.44,. Found: C, 53.05; H, 3.92; N, 26.72. δ_H (400 MHz, DMSO-d_6): 8.82 (s, 1H, H1), 8.42 (s, 2H, NH_2), 8.23 (d, 1H, *J* = 9.6 Hz, H3), 7.07 (d, 1H, *J* = 9.6 Hz, H2), 2.72 (s, 3H, CH_3). δ_C (100 MHz, DMSO-d_6): 158.2 (Cq), 145.1 (Cq), 145.1 (Cq), 143.9, 131.9 (Cq), 126.0, 125.8 (Cq), 114.0, 22.2 (CH_3). ν_{max}(film)/cm^{-1}: 3358 (N-H stretch), 1611 (N-H bend), 1503 (C-NO_2), 1305 (C-NO_2).

2-Methyl-5,6-diaminoquinoxaline (36)[136]

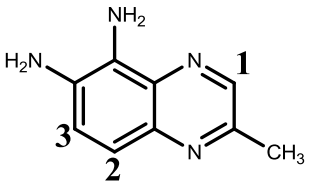

2-Methyl-5-amino-6-nitroquinoxaline (0.87 g, 4.3 mmol, 1 eq) and 10% Pd/C (0.16 g) were suspended in ethanol (100 mL). The mixture was heated at reflux for 30 minutes followed by addition of hydrazine monohydrate (4 mL, 85 mmol, 20 eq). The mixture turned brown. After two hours the hot mixture was filtered through celite (1 cm), and after extraction with CH_2Cl_2 (20 mL) the solvent was removed under reduced pressure. The product 2-methyl-5,6-diaminoquinoxaline (**36**) was obtained as a blood red solid and dried *in vacuo* (0.68 g, 3.9 mmol, 91%). *m.p.* = 177.0-178.0 °C (no literature value). δ_H (400 MHz, DMSO-d_6): 8.50 (s, 1H, H1), 7.19 (d, 1H, *J* = 8.7 Hz, H3), 7.09 (d, 1H, *J* = 8.7 Hz, H2), 5.10 (s, 2H, NH_2), 5.07 (s, 2H, NH_2), 2.57 (s, 3H, CH_3).

1,10-Phenanthroline-5,6-dione (phendione)[139]

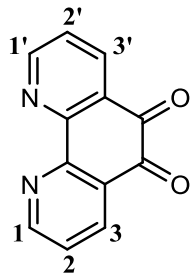

To a mixture of 1,10-phenanthroline (1.03 g, 5.73 mmol) and KBr (5.02 g, 42.2 mmol, 7 eq) concentrated H_2SO_4 (20 mL, 95%, 0 °C) was added dropwise followed by the dropwise addition of cold concentrated HNO_3 (8 mL, 65%). The reaction mixture was heated at 80 °C for one hour followed by heating at 100 °C for a further four hours. The mixture was cooled to room temperature and stirred overnight. The mixture was reheated to 100 °C and purged with nitrogen to remove bromine gas. After cooling to room temperature, the mixture was poured over ice (1 L), then 6 M NaOH (50 mL) was added. This was followed by addition of $NaHCO_3$ until pH of the mixture was between 5 and 7. The precipitate was removed by filtration, and the filtrate was extracted using CH_2Cl_2 (4 × 100 mL). The combined CH_2Cl_2 layers were washed with H_2O (3 × 100 mL), and the solvent was evaporated leaving a brown-yellow solid. The final product was obtained as a yellow solid by recrystallisation from methanol and dried *in vacuo* (0.88 g, 4.2 mmol, 73%). *m.p.* > 250 °C (Ref.,[139] > 250 °C). δ_H (400 MHz, $CDCl_3$): 9.10 (dd, 2H, *J* = 4.7 Hz, *J* =

1.8 Hz, H1/H1'), 8.48 (dd, 2H, *J* = 7.9 Hz, *J* = 1.8 Hz, H3/H3'), 7.58 (dd, 2H, *J* = 7.9 Hz, *J* = 4.7 Hz, H2/H2'). δ_C (100 MHz, $CDCl_3$): 178.8 (CO), 156.5, 153.0 (Cq), 137.4, 128.2 (Cq), 125.7. HRMS (*m/z*-ESI): Found: 211.0501 (M+H. Requires: 211.0508). ν_{max}(film)/cm^{-1}: 1684 (C=O stretch)

N-Methyl-1,8-phen-5,6-dionium iodid (45b)[166]

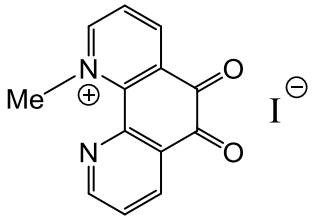

phendione (99 mg, 0.47 mmol, 1 eq) and MeI (0.25 mL, 4.0 mmol, 8.5 eq) were suspended in dry MeCN (2.5 mL) in a sealed microwave vessel, and the mixture was protected from light. The compounds were solubilised by heating to 80 °C. A very dark red precipitate where isolated after 24 hours by centrifugation and washed with MeCN (3 × 10 mL) and Me_2CO (3 × 10 mL). The dark-red powder was dried *in vacuo* yielding the product as the iodide salt (120 mg, 0.341 mmol, 72%). Calculated for $C_{13}H_9N_2O_2I$: C, 44.34; H, 2.58; N 7.96,. Found: C, 44.16; H, 2.11; N, 7.70. δ_H (400 MHz, DMSO-d_6): 9.34-7.86 (m, 6H, Ar), 5.12-7.42 (m, 3H, CH_3). δ_C (100 MHz, DMSO-d_6): 152.9, 149.7, 143.1, 136.7, 127.5, 89.4, 53.4. HRMS (*m/z*-ESI): Found: 225.0672 (M. Requires: 225.0659). ν_{max}(film)/cm^{-1}: 1687 (C=O stretch).

3-Methylpyrazino[2,3-*h*]dipyrido[3,2-*a*:2',3'-*c*]phenazine (mpdppz)

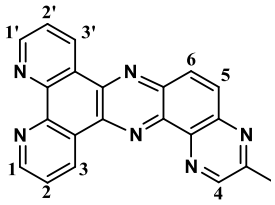

2-Methyl-5,6-diaminoquinoxaline (74 mg, 0.43 mmol, 1 eq) and 1,10-phenanthroline-5,6-dione (94 mg, 0.45 mmol, 1 eq) were suspended in a mixture of EtOH and H_2O (1:1, 25 mL). The mixture was heated in a high-pressure tube at 140 °C overnight followed by cooling to room temperature. The suspension was filtered, and the grey filter mass was washed with CH_2Cl_2 (25 mL) leaving the product as a white solid that was dried *in vacuo* (137 mg, 0.393 mmol, 92%). *m.p.* > 250 °C. Calculated for $C_{21}H_{12}N_6 \cdot 2.25H_2O$: C, 64.84; H, 3.12; N, 21.60. Found: C, 64.84; H, 3.41; N, 21.99. δ_H (400 MHz, $CDCl_3$/TFA): 10.69 (d, 1H, *J* = 7.3 Hz, H1/H1'), 10.16 (d, 1H, *J* = 8.0 Hz, H1/H1'), 9.77 (s, 1H, H4), 9.40 (bs, 2H, H3/H3'), 8.95 (d, 1H, *J* = 9.3 Hz, H5/H6), 8.79 (d, 1H, *J* = 9.3 Hz, H5/H6), 8.38 (bs, 2H, H2/H2'), 3.27 (s, 3H, CH_3). δ_C (100 MHz, $CDCl_3$/TFA): 158.3 (qC), 150.5, 148.9, 145.2, 144.7 (qC), 142.1, 141.8 (qC), 140.4 (qC), 140.3 (qC), 140.0 (qC), 139.9, 138.5 (qC), 136.6 (qC), 136.4, 129.6 (qC), 129.2, 129.2 (qC), 128.1 (qC), 127.9 (qC), 21.0 (CH_3). ν_{max} (film)/cm^{-1}: 1392 and 1367 (C-N stretches). HRMS (*m/z*-ESI): Found: 349.1202 (M+H. Requires: 349.1196).

3-(Carboxylic acid)pyrazino[2,3-*h*]dipyrido[3,2-*a*:2',3'-*c*]phenazine (37)

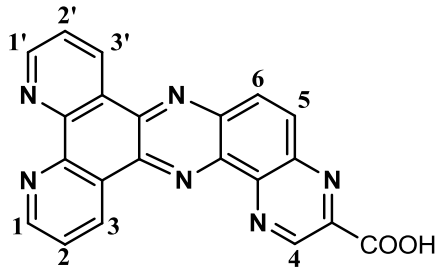

3-Methylpyrazino[2,3-*h*]dipyrido[3,2-*a*:2',3'-*c*]phenazine (100 mg, 287 μmol, 1 eq) was suspended in H_2O (10 mL), and $KMnO_4$ (99 mg, 626 μmol, 2 eq) was added yielding a dark-violet solution. The mixture was heated slowly to reflux temperature in an open microwave tube, at which gas was formed. After no more gas was formed the tube was sealed and the heating was continued at 140 °C for five hours by microwave irradiation. The mixture was cooled to room temperature and filtered. The bright yellow filtrate was acidified to pH 1 by addition of concentrated HCl. The product was obtained as a yellow precipitate that was isolated by filtration, washed with H_2O (5 mL), and dried *in vacuo* (8 mg, 21 μmol, 7%). *m.p.* > 250 °C. δ_H (400 MHz, $CDCl_3$/TFA): 10.77 (d, 1H, *J* = 7.9 Hz, H1/H1'), 10.28 (s, 1H, H4), 10.18 (d, 1H, *J* = 7.9 Hz, H1/H1'), 9.43 (bs, 2H, H3/H3'), 8.91 (d, 1H, *J* = 9.4 Hz, H5/H6), 8.77 (d, 1H, *J* = 9.4 Hz, H5/H6), 8.40 (bs, 2H, H2/H2'). δ_C (100 MHz, $CDCl_3$/TFA): 167.0 (COOH), 150.7, 148.6, 146.2, 145.4 (Cq), 144.7 (Cq), 144.2, 142.3, 141.0 (Cq), 140.4 (Cq), 140.2 (Cq), 139.8, 139.5 (Cq), 135.2 (Cq), 133.2 (Cq), 129.8, 129.3, 128.2, 127.8. HRMS (*m/z*-ESI): Found: 379.0958 (M+H. Requires: 379.0943).

[Ru(phen)$_2$mpdppz]Cl$_2$ (33a)

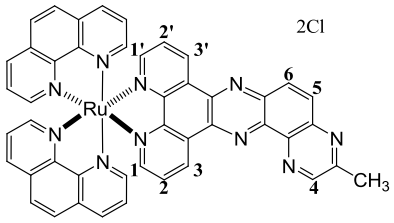

Complex **33a** was synthesised according **Procedure 2** (ethanol and H_2O as solvent, reaction time 40 min) using **mpdppz** (217 mg, 623 μmol, 1 eq) and [Ru(phen)$_2$Cl$_2$] (311 mg, 584 μmol, 1 eq). Purification was achieved through alumina gradient column chromatography yielding the product as an orange powder (217 mg, 246 μmol, 42%). *m.p.* > 250 °C. δ_H (400 MHz, CD_3CN): 9.86 (d, 1H, *J* = 8.1 Hz, H1/H1'), 9.70 (d, 1H, *J* = 8.1 Hz, H1/H1'), 9.15 (s, 1H, H4), 8.63 (bs, 2H, **phen**), 8.61 (bs, 2H, **phen**), 8.58 (d, 1H, *J* = 9.4 Hz, H5/H6), 8.47 (d, 1H, *J* = 9.4 Hz, H5/H6), 8.27 (bs, 5H, **phen**), 8.26-8.22 (m, H, **phen**), 8.16 (d, 2H, *J* = 5.2 Hz, H3/H3'), 8.05 (d, 2H, *J* = 5.2 Hz, **phen**), 7.85-7.80 (m, 2H, H2/H2'), 7.68-7.63 (m, 4H, **phen**), 2.89 (s, 3H, CH_3). δ_C (100 MHz, CD_3CN): 158.4 (Cq), 155.5, 155.4, 154.3, 154.2, 154.0, 151.6 (Cq), 151.6 (Cq), 148.9 (Cq), 148.9 (Cq), 148.8 (Cq), 145.6 (Cq), 145.0 (Cq), 142.4 (Cq), 141.1 (Cq), 140.3 (Cq), 139.4 (Cq), 138.0, 138.0, 137.9, 135.2, 134.4, 132.2, 132.1, 132.1, 132.1, 131.6 (Cq), 131.2 (Cq), 129.1,

129.1, 128.2, 128.1, 126.9, 126.9, 126.9, 22.8 (CH_3). Calculated for $C_{45}H_{28}N_{10}RuCl_2 \cdot 1.20NaCl \cdot 0.79NaPF_6$: C, 49.91; H, 2.60; N, 12.93; Cl, 10.47. Found: C, 49.91; H, 2.69; N, 13.21; Cl, 10.47. ν_{max}(film)/cm^{-1}: 1392 and 1367 (C–N stretches). HRMS (*m/z*-ESI): Found: 810.1567 (M. Requires: 810.1542).

[Ru(TAP)$_2$mpdppz]·2Cl (33b)

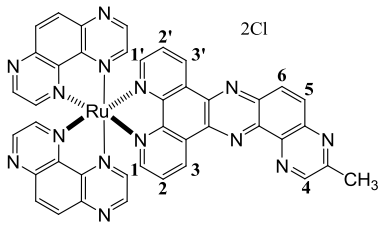

Complex **33b** was synthesised according to **Procedure 2** (ethanol and H_2O as solvent, reaction time 10 min) using **mpdppz** (105 mg, 301 μmol, 1 eq) and [Ru(TAP)$_2$Cl$_2$] (154 mg, 287 μmol, 1 eq). Purification was achieved through alumina gradient column chromatography yielding the product as an orange powder (34 mg, 39 μmol, 13%). *m.p.* > 250 °C. δ_H (400 MHz, CD_3CN): 9.99 (dd, 1H, *J* = 8.3 Hz, *J* = 1.1 Hz, H1/H1'), 9.82 (dd, 1H, *J* = 8.3 Hz, *J* = 1.3 Hz, H1/H1'), 9.16 (s, 1H, H4), 9.00-8.97 (m, 4H, **TAP**), 8.63 (s, 4H, **TAP**), 8.60 (d, 1H, *J* = 9.5 Hz, H5/H6), 8.50 (d, 1H, *J* = 9.5 Hz, H5/H6), 8.32-8.30 (m, 2H, H3/H3'), 8.26-8.23 (m, 4H, **TAP**), 7.94-7.89 (m, 2H, H2/H2'), 2.90 (s, 3H, CH_3). δ_C (100 MHz, CD_3CN): 158.4, 155.5, 155.4, 154.3, 154.2, 154.0, 151.6, 151.6, 148.9, 148.9, 148.8, 145.6, 145.0, 142.4, 141.1, 140.3, 139.4, 138.0, 138.0, 137.9, 135.2, 134.4, 132.2, 132.1, 132.1, 132.1, 131.6, 131.2, 129.1, 129.1, 128.2, 128.1, 126.9, 126.9, 126.9, 22.8 (CH3). Calculated for $C_{45}H_{28}N_{10}RuCl_2$+1.3NaCl: C, 53.86; H, 3.33; N, 13.96%. Found: C, 53.68; H, 3.33; N, 13.83%; Cl. υ_{max}(film)/cm^{-1}: 3059 (aromatic C–H stretch), 1426 and 1361 (C–N stretches). HRMS (*m/z*-MALDI): Found 810.1542: (M. Requires: 810.1567).

[Ru(phen)$_2$phendione]·2Cl (45a)[44]

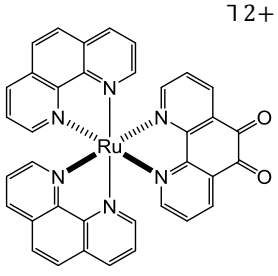

[Ru(phen)$_2$phendione]·2Cl was synthesised according to **Procedure 3** using **phendione** (25 mg, 119 μmol, 1 eq) and [Ru(phen)$_2$Cl$_2$] (51 mg, 111 μmol, 1 eq) yielding the product as an orange powder (47 mg, 70 μmol, 63%). *m.p.* > 250 °C. δ_H (400 MHz, CD_3CN): 8.66 – 7.39 (22H, Ar). δ_C (100 MHz, D_2O): 176.06-124.80 (Ar). HRMS (*m/z*-ESI): Found: 672.0845 (M. Requires: 672.0848). Calculated for $C_{45}H_{28}N_{10}RuCl_2 \cdot 5H_2O$: C, 51.93; H, 3.87; N, 10.09%. Found: C, 51.74; H, 3.35; N, 9.97%.

[Ru(TAP)$_2$dppz]·2Cl (9b)[80]

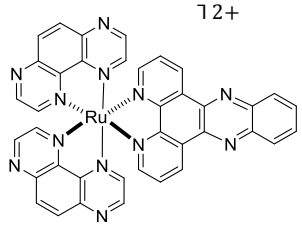

The complex was synthesised according to **Procedure 2** (ethanol and H_2O as solvent, reaction time 40 min) using **dppz** (187 mg, 662 μmol, 1 eq) and [Ru(TAP)$_2$Cl$_2$] (239 mg, 446 μmol, 1 eq). Purification was achieved through alumina gradient column chromatography. The complex was purified further by solubilising it in water followed by precipitation by addition of NH_4PF_6. The chloride form was regenerated from Amberlite and dried under high vacuum to yield a red-brown solid (104 mg, 127 μmol, 28%). *m.p.* > 250 °C. δ_H (800 MHz, D_2O): 9.75 (d, *J* = 8.3, 1.2 Hz, 2H) , 8.99 (d, *J* = 7.7, 3.0 Hz, 2H), 8.97 (d, *J* = 3.0 Hz, 2H), 8.64 (s, 4H), 8.49 (m, 4H), 8.37 (d, *J* = 3.0 Hz, 2H), 8.17 (dd, *J* = 5.4, 1.2 Hz, 2H), 8.13 (dd, *J* = 6.5, 3.0 Hz, 2H), 7.87 (dd, *J* = 8.3, 5.4 Hz, 2H). δ_C (100 MHz, CD_3CN): 153.1, 150.9, 150.5, 150.4, 150.2, 149.8, 146.6, 146.5, 143.9, 143.4, 143.3, 140.7, 136.0, 133.9, 133.8, 133.8, 132.1, 130.7, 128.6.

Dithiobis(undecanoic acid) (65b)[218]

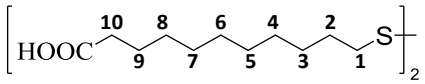

11-Mercaptoundecanoic acid (1.003 g, 4.59 mmol, 1 eq) was added to DMF (15 mL), and the mixture was cooled to 0 °C. Bromine (0.142 mL, 0.439 g, 2.75 mmol, 0.6 eq) was added dropwise, and the reaction mixture was stirred for three hours. The solvent was removed at reduced pressure giving a brown solid that was suspended in a concentrated aqueous solution of $NaHSO_3$ (25 mL). The precipitate was isolated by centrifugation and washed with 1 M HCl (25 mL) and H_2O (2 × 25 mL) yielding the product as a white solid that was dried *in vacuo* (0.925 g, 2.13 mmol, 93%). *m.p.* = 93-97 °C (Ref.,[237] 97-100 °C). δ_H (400 MHz, $CDCl_3$): 11.01 (bs, 1H, -OH), 2.70 (t, 2H, *J* = 7.4 Hz, H1), 2.36 (t, 2H, *J* = 7.1 Hz, H10), 1.66 (m, 4H, H2/9), 1.42 – 1.26 (bs, 12H, H3/4/5/6/7/8).

Dithiobis(*N*-(1,10-phenanthrolin-5-yl)undecanamide) (66b)[2]

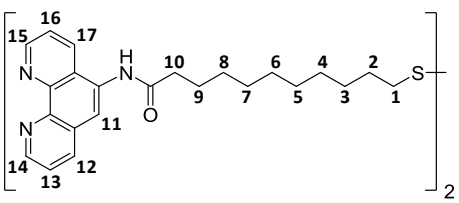

5-Amino-1,10-phenanthroline (55 mg, 282 μmol, 1 eq) was added to dry CH_2Cl_2 (10 mL) before the solution was cooled to 0 °C. Dithiobis(undecanoic acid) (50 mg, 115 μmol, 0.4 eq) was added followed by addition of the hydrochloride salt of 1-ethyl-3-(3-dimethylaminopropyl)carbodiimide (EDCI·HCl, 108 mg, 563 μmol, 2 eq) and 4-dimethylaminopyridine (DMAP, 18 mg, 147 μmol, 0.5 eq). The

mixture was stirred at 0 °C for one hour before being allowed to reach room temperature and then stirred for a further 24 hours. The reaction mixture was evaporated under reduced pressure to give an oil, before H_2O (25 mL) was added causing precipitation of a white solid which was isolated by centrifugation and washed with H_2O (10 mL). The resulting solid was redispersed in MeCN (10 mL) and collected by suction filtration yielding the product as a bright grey solid that was dried *in vacuo* (83 mg, 105 µmol, 75%). *m.p.* = 75 °C (Ref.,[2] 88-90 °C). δ_H (400 MHz, DMSO-d_6): 10.09 (s, 1H, N-H), 9.11 (dd, 1H, *J* = 4.2 Hz, *J* = 1.3 Hz, H15), 9.02 (dd, 1H, *J* = 4.2 Hz, *J* = 1.5 Hz, H14), 8.60 (dd, H, *J* = 8.5 Hz, *J* = 1.3 Hz, H17), 8.43 (dd, 1H, *J* = 8.1 Hz, *J* = 1.5 Hz, H12), 8.16 (s, 1H, H11), 7.81 (dd, 1H, *J* = 8.5 Hz, *J* = 4.2 Hz, H16), 7.72 (dd, 1H, *J* = 8.1 Hz, *J* = 4.2 Hz, H13), 2.66 (t, 2H, H10, *J* = 7.1 Hz), 2.51 (t, 2H, H1), 1.68 (m, 2H, H9), 1.59 (m, 2H, H2), 1.42–1.21 (m, 12H, H3/4/5/6/7/8).

[Ru(phen)$_2$(11-mercapto-*N*-(1,10-phenanthrolin-5-yl)undecanamide)]Cl$_2$ (55a)[2]

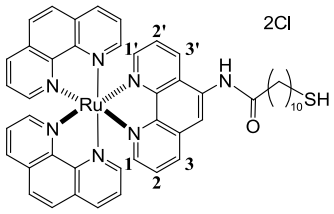

Complex **19** was synthesised according to **Procedure 2** (glycol and H_2O as solvent, 140 °C, 40 min reaction time) using **17** (67 mg, 169 µmol, 1 eq) and [Ru(phen)$_2$Cl$_2$] (90 mg, 169 µmol, 1 eq). Purification was achieved through alumina gradient column chromatography yielding the product as an orange powder (73 mg, 79 µmol, 46%). *m.p.* > 250 °C (Ref.,[2] 115-120 °C). δ_H (400 MHz, CD_3OD): 8.74 (d, 1H, *J* = 8.1 Hz, H1/H1'), 8.70 (m, 4H, **phen**), 8.62 (d, 1H, *J* = 8.5 Hz, H1/H1'), 8.49 (s, 1H, H4), 8.32 (s, 4H, **phen**), 8.15 (m, 3H, **phen** and H3/H3'), 8.10 (m, 2H, **phen**), 8.06 (d, 1H, *J* = 5.5 Hz, H3/H3'), 7.73 (m, 5H, **phen** and H2/H2'), 7.68 (m, 1H, H2/H2'), 2.65 (m, 4H, CH_2CO and CH_2S), 1.82 (m, 2H, CH_2), 1.64 (m, 2H, CH_2), 1.48 (m, 2H, CH_2), 1.34 (m, 10H, CH_2).

[Ru(TAP)$_2$(11-mercapto-*N*-(1,10-phenanthrolin-5-yl)undecanamide)]Cl$_2$ (55b)[2]

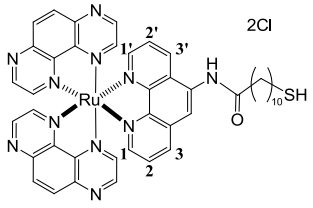

Complex **20** was synthesised according to **Procedure 2** (ethanol and H_2O as solvent, 140 °C, 40 min reaction time) using **17** (135 mg, 340 µmol, 1 eq) and [Ru(TAP)$_2$Cl$_2$] (185 mg, 340 µmol, 1 eq). Purification was achieved through alumina gradient column chromatography yielding the product as an orange powder (135 mg, 131 µmol, 38%). *m.p.* > 250 °C (Ref.,[2] 115-120 °C). δ_H (400 MHz, CD_3OD): 9.04 (d, 2H, *J* = 5.3 Hz, **TAP**), 9.03 (d, 2H, *J* = 5.3 Hz, **TAP**), 8.85 (d, 1H, *J* = 8.6 Hz, H1/H1'), 8.72 (d, 1H, *J* = 7.9 Hz, H1/H1'), 8.67 (bs, 2H, **TAP**), 8.65 (bs, 2H, **TAP**), 8.54 (s, 1H, H4), 8.43 (m, 2H, **TAP**), 8.30 (m, 3H, **TAP**, H3/H3'), 8.20 (d, 1H,

J = 5.4 Hz, H3/H3'), 7.83 (dd, 1H, *J* = 8.6 Hz, *J* = 5.2 Hz, H2/H2'), 7.76 (dd, 1H, *J* = 8.3 Hz, *J* = 5.2 Hz, H2/H2'), 2.65 (bs, 4H, CH_2SH, CH_2CO), 1.80 (m, 2H, CH_2), 1.64 (m, 2H, CH_2), 1.32 (bs, 10H, CH_2).

Dipyrido[3,2-*a*:2',3'-*c*]phenazine-11-nitro (69)[221]

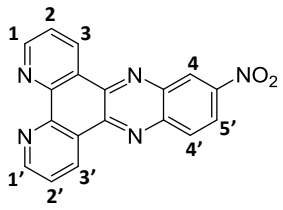

4-Nitro-1,2-phenylenediamine (0.439 g, 2.87 mmol, 1 eq) and 1,10-phenanthroline-5,6-dione (0.586 g, 2.79 mmol, 1 eq) were suspended in EtOH (30 mL) and acetic acid (0.5 mL) was added. The mixture was heated at reflux temperature for four hours followed by cooling to room temperature. The suspension was filtered, and the residue was washed with cold EtOH (10 mL) and Et_2O (2 × 10 mL) leaving the product as a bright yellow solid that was dried *in vacuo* (0.864 g, 2.64 mmol, 95%). *m.p.* > 250 °C (Ref.,[238] 328 °C). δ_H (400 MHz, $CDCl_3$): 9.56 (dd, 2H, *J* = 8.0, 1.8 Hz, H3/H3'), 9.30 (dd, 2H, *J* = 4.9, 1.7 Hz, H1/H1'), 9.20 (d, 1H, *J* = 2.5 Hz, H4'), 8.64 (dd, 1H, *J* = 9.3, 2.5 Hz, H5), 8.44 (d, 1H, *J* = 9.3 Hz, H4), 7.80 (dd, 2H, *J* = 8.1, 4.4 Hz, H2/H2'). HRMS (*m/z*-ESI): Found: 328.0844 (M+H. Requires: 238.0834).

Dipyrido[3,2-*a*:2',3'-*c*]phenazine-11-amine (70)[221]

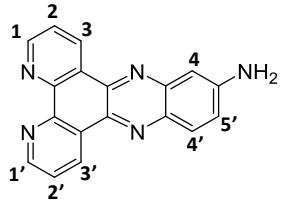

Dipyrido[3,2-a:2',3'-c]phenazine-11-nitro (116 mg, 0.354 mmol) and 10% Pd/C (185 mg) were suspended in absolute ethanol (75 mL). Hydrazine monohydrate (10 mL, 10 g, 200 mmol, 500 eq) was added over 20 minutes. The mixture was heated at reflux temperature for four hours. The hot mixture was filtered, and the filtrate was evaporated to a small volume, forming some precipitate that was isolated by centrifugation. The residue was washed with cold EtOH (5 mL, -15 °C) yielding the product as a yellow solid that was dried *in vacuo* (43 mg, 0.145 mmol, 41%). *m.p.* > 250 °C (Ref.,[239] > 330°C). δ_H (400 MHz, DMSO-d_6): 9.50 (dd, 1H, *J* = 8.1, 1.7 Hz, H3/H3'), 9.42 (dd, 1H, *J* = 8.1, 1.7 Hz, H3/H3'), 9.17 (dd, 1H, *J* = 4.4, 1.7 Hz, H1/H1'), 9.11 (dd, 1H, *J* = 4.3, 1.7 Hz, H1/H1'), 8.06 (d, 1H, *J* = 9.1 Hz, H4'), 7.89 (m, 2H, H2/H2'), 7.50 (dd, 1H, *J* = 9.1, 2.3 Hz, H5), 7.15 (d, 1H, *J* = 2.3 Hz, H4), 6.35 (s, 2H, NH_2). δ_C (100 MHz, DMSO-d_6): 151.8, 151.7, 150.7, 147.6, 146. 4, 144.8, 140.2, 137.2, 135.3, 132.9, 131.8, 130.0, 127.6, 127.1, 125.2, 124.2, 124.1, 103.1. HRMS (*m/z*-ESI): Found: 298.1092 (M+H. Requires: 298.1087).

11-(*N*-Phthalimido)undecan-1-ol (73)[222]

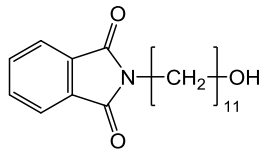

11-Bromoundecanol (5.73 g, 22.8 mmol, 1 eq) and potassium phthalimide (4.13 g, 22.8 mmol, 1 eq) were suspended in dry DMF (100 mL) and heated at 60 °C for four hours. The solvent was evaporated under reduced pressure to form a suspension, which was resuspended in $CHCl_3$ (25 mL) and filtered through a celite bed (1 cm). The filtrate was evaporated under reduced pressure to yield the desired product as a white solid, which was dried *in vacuo*. (6.74 g, 21 mmol, 95%). *m.p.* = 81-83 °C (Ref.,[222] 85-86 °C). δ_H (400 MHz, $CDCl_3$): 7.84 (dd, 2H, *J* = 5.5, 3.03 Hz), 7.70 (dd, 2H, *J* = 5.5, 3.03 Hz), 3.67 (t, 2H, *J* = 7.3 Hz, CH_2OH), 3.63 (t, 2H, *J* = 6.6 Hz, CH_2N), 1.66 (m, 2H,), 1.55 (m, 2H,), 1.41-126 (m, 14H, CH_2).

1-[11-(*N*-Phthalimido)]undecyl thioacetate (74)[222]

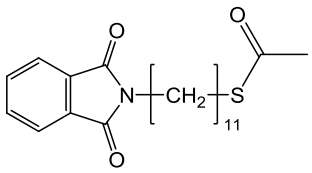

11-(*N*-Phthalimido)undecan-1-ol (7.20 g, 22.7 mmol, 1 eq) and Et_3N (9.0 mL, 5.9 g, 65 mmol, 3 eq) were dissolved in dry CH_2Cl_2 (100 mL). The mixture was cooled to 0 °C and mesyl chloride (4.0 mL, 5.9 g, 62 mmol, 3 eq) was added slowly. The mixture was heated to room temperature and left stirring for two hours. CH_2Cl_2 (200 mL) was added, and the mixture was washed with 0.5 M HCl (2 × 200 mL), brine (200 mL) and conc. aqueous $NaHCO_3$ (2 × 200 mL). The organic layer was dried over $MgSO_4$ for 20 min and evaporated to an oil which was added to a mixture of AcSH (1.9 mL, 2.1 g, 27 mmol, 1.2 eq) and K_2CO_3 (4.8 g, 34 mmol, 1.5 eq) in dry DMF (100 mL) and stirred at room temperature overnight. The dark brown suspension was evaporated to give an oil, $CHCl_3$ (200 mL) was added, and the mixture was washed with brine (2 × 200 mL), 0.5 M HCl (2 × 200 mL), conc. aqueous $NaHCO_3$ (2 × 200 mL) and, again, brine (200 mL). The organic layer was dried over $MgSO_4$ for at least 20 min under vigorously stirring and evaporated to an oil that solidified upon drying *in vacuo* (7.73 g, 20 mmol, 90%). *m.p.* = 78.0-79.0 °C (Ref.,[222] 78 °C). δ_H (400 MHz, $CDCl_3$): 7.84 (dd, 2H, *J* = 5.5, 3.0 Hz), 7.70 (dd, 2H, *J* = 5.5, 3.0 Hz), 3.67 (t, 2H, *J* = 7.3 Hz, CH_2N), 2.85 (t, 2H, *J* = 6.6 Hz, CH_2S), 1.66 (m, 2H), 1.54 (m, 2H,), 1.41-125 (m, 14H, CH_2). δ_C (100 MHz, DMSO-d_6): 196.2, 168.6, 134.0, 132.3, 123.3, 30.8, 29.6, 29.6, 29.6, 29.5, 29.3, 29.2, 28.9, 28.7, 27.0.

11-(*N*-Phthalimido)undecane-1-thiol (75)[222]

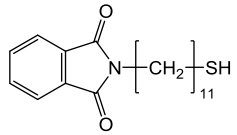

1-[11-(*N*-Phthalimido)]undecyl thioacetate (3.00 g, 7.92 mmol, 1 eq) was dissolved in MeOH (50 mL) with concentrated sulphuric acid (0.3 mL). The mixture was refluxing overnight and evaporated to an oil which was dissolved in CH_2Cl_2 (50 mL). The mixture was washed with brine (50 mL), conc. aqueous $NaHCO_3$ (50 mL) and, finally, brine (50 mL). The organic layer was dried over $MgSO_4$ for at least 20 min under vigorously stirring and evaporated to an oil that was solidified by drying *in vacuo* (2.21 g, 6.61 mmol, 83%). *m.p.* = 41.0-42.0 °C (no literature value found). δ_H (400 MHz,): 7.83 (dd, 2H, *J* = 5.5, 3.0 Hz), 7.70 (dd, 2H, *J* = 5.5, 3.0 Hz), 3.67 (t, 2H, *J* = 7.3 Hz, CH_2N), 2.85 (dt, 2H, *J* = 7.2, 2.8 Hz, CH_2S), 1.66-1.57 (m, 4H, CH_2), 1.37-125 (m, 14H, CH_2).

11-Aminoundecane-1-thiol (76)[240]

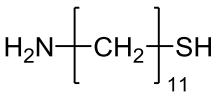

11-(*N*-Phthalimido)undecane-1-thiol (0.413 g, 1.24 mmol, 1 eq) was dissolved in EtOH (20 mL), and $NH_2NH_2{\cdot}H_2O$ (0.25 mL, 0.25 g, 5.0 mmol) was added. The solution was heated to reflux temperature and left stirring for three hours. The mixture was cooled to room temperature and filtered. The white residue was extracted with EtOH (20 mL), and 1 M NaOH (20 mL, aq) was added to the combined filtrate. The mixture was evaporated to 20 mL followed by extraction with CH_2Cl_2 (2 × 20 mL). The combined CH_2Cl_2 layers were washed with brine (20 mL) and dried over $MgSO_4$ for at least 20 min under vigorously stirring. The solvent was removed at reduced pressure yielding the product as a white solid, which was dried *in vacuo* (0.235 g, 1.16 mmol, 93%). *m.p.* = 75 °C (decompose, Ref.,[240] 191-192 °C). δ_H (400 MHz, $CDCl_3$): 2.51 (2H, *bs*, NH_2), 1.65-1.57 (m, 4H, CH_2N, CH_2S), 1.42-1.26 (m, 18H, CH_2).

4'-Methyl-2,2'-bipyridinyl-4-carboxylic acid (78)[223]

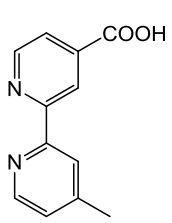

4,4'-Dimethyl-2,2'-bipyridine (3.03 g, 16.4 mmol, 1 eq) and SeO_2 (2.22 g, 19.9 mmol, 1.2 eq) were dissolved in 1,4-dioxane (120 mL). The mixture was heated at reflux for two days, and the hot mixture was filtered through a celite bed (1 cm). The filtrate was evaporated at reduced pressure. The yellow solid was suspended in EtOH (50 mL), and $AgNO_3$ (3.38 g, 19.9 mmol, 1.2 eq) was added. 1 M NaOH (75 mL) was added dropwise over one hour, and the mixture was stirred at room temperature overnight. The black mixture was evaporated to 25 mL under reduced pressure, and the suspension was filtered through a sintered glass funnel. The black residue was extracted with H_2O (25 mL) and 0.1 M NaOH

(25 mL). The combined filtrate was washed with CH_2Cl_2 (3 × 100 mL), and pH of the aqueous layer was adjusted to 3.5 by adding conc. HCl. The mixture was left at 4 °C overnight. A white precipitate was isolated by filtration through a sintered glass funnel, washed with H_2O (25 mL), and dried *in vacuo* (1.94 g, 9.06 mmol, 55%). *m.p.* > 250 °C (Ref.,[241] 280 °C). δ_H (400 MHz, DMSO-d_6): 13.75 (bs, 1H, OH), 8.85 (d, 1H, J = 4.5 Hz, H1), 8.81 (s, 1H, H3), 8.56 (d, 1H, J = 4.5 Hz, H1'), 8.26 (s, 1H, H3'), 7.85 (d, 1H, J = 4.5 Hz, H2), 7.32 (d, 1H, J = 4.5 Hz, H2'), 2.42 (s, 3H, CH_3).

Ligand 58

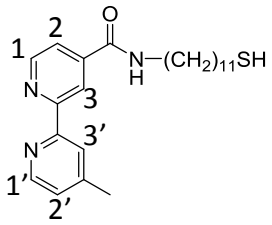

4'-Methyl-2,2'-bipyridinyl-4-carboxylic acid (225 mg, 1.05 mmol, 1 eq) and DMAP (269 mg, 2.20 mmol, 2 eq) were suspended in dry CH_2Cl_2 (20 mL). The mixture was cooled to 0 °C, and EDCI·HCl (692 mg, 3.50 mmol, 3 eq) was added. The mixture was stirred at 0 °C for one hour before being allowed to reach room temperature. 11-Aminoundecane-1-thiol (223 mg, 1.10 mmol, 1 eq) was added, and the mixture was stirred for three days. The mixture was filtered, and the filtrate was washed with brine (2 × 50 mL). The CH_2Cl_2 layer was evaporated giving a solid which was suspended in CH_3CN (10 mL). The precipitate was isolated by centrifugation and washed with H_2O (3 × 10 mL) and CH_3CN (3 × 10 mL) yielding the product as white solid that was dried *in vacuo* (106 mg, 266 µmol, 25%). *m.p.* = 100.5-101.5 °C. δ_H (400 MHz, DMSO-d_6): 8.87 (bs, 1H, NH), 8.78 (bs, 1H, H1), 8.74 (bs, 1H, H3), 8.57 (bs, 1H, H1'), 8.26 (bs, 1H, H3'), 7.77 (bs, 1H, H2), 7.32 (bs, 1H, H2'), 3.42 (s, 3H, CH_3), 1.55 (m, 4H, CH_2N and CH_2S), 1.30-1.20 (m, 18H, CH_2). HRMS (*m/z*-ESI): Found: 399.2379 (M. Requires: 399.2344).

Complex 61a

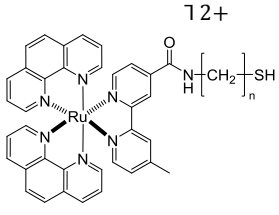

The complex was synthesised according to **Procedure 2** (ethanol and H_2O as solvent, reaction time 40 min) using **58** (107 mg, 268 µmol, 1 eq) and [Ru(phen)$_2$Cl$_2$] (142 mg, 268 µmol, 1 eq). After the end of the reaction some black precipitate was removed by centrifugation, and the supernatant was evaporated at reduced pressure. The resulting residue was dissolved in H_2O (10 mL) and precipitated as the PF_6-salt at addition of NH_4PF_6. The chloride form of the complex was recovered by stirring with Cl-resin in methanol for two hours. Purification was achieved through alumina gradient column chromatography yielding the product as an orange powder (155 mg, 166 µmol, 62%). *m.p.* >

250 °C. δ_H (400 MHz, CD_3CN): 8.64 (m, 2H, H1, H1'), 8.54 (d, 2H, J = 8.2 Hz, H3, H3'), 8.23 (m, 8H, **phen**), 7.88 (m, 2H, **phen**), 7.77 (m, 4H, **phen**), 7.55 (m, 2H, **phen**), 7.46 (d, 1H, *J* = 8.2 Hz, H2), 7.12 (d, 1H, *J* = 8.2 Hz, H2'). HRMS (*m/z*-MALDI): Found: 860.2693 (M-H. Requires: 860.2685).

Chapter 8

References

1. B. M. a. c. t. S. b. M. O. w. b. L.-M. i. b. u. http://en.wikipedia.org/wiki/File:Zeta_Potential_for_a_particle_in_dispersion_medium.png by Larryisgood., CC BY-SA 3.0, https://commons.wikimedia.org/w/index.php?curid=18238739.
2. R. B. P. Elmes, K. N. Orange, S. M. Cloonan, D. C. Williams and T. Gunnlaugsson, *J. Am. Chem. Soc.*, 2011, **133**, 15862-15865.
3. C. A. Puckett and J. K. Barton, *J. Am. Chem. Soc.*, 2007, **129**, 46-47.
4. L.-M. Tumir, M. Radić Stojković and I. Piantanida, *Beilstein J. Org. Chem.*, 2014, **10**, 2930-2954.
5. J. P. Celli, B. Q. Spring, I. Rizvi, C. L. Evans, K. S. Samkoe, S. Verma, B. W. Pogue and T. Hasan, *Chem. Rev.*, 2010, **110**, 2795-2838.
6. S. M. Cloonan, R. B. P. Elmes, M. Erby, S. A. Bright, F. E. Poynton, D. E. Nolan, S. J. Quinn, T. Gunnlaugsson and D. C. Williams, *J. Med. Chem.*, 2015, **58**, 4494-4505.
7. L. Zeng, P. Gupta, Y. Chen, E. Wang, L. Ji, H. Chao and Z.-S. Chen, *Chem. Soc. Rev.*, 2017, **46**, 5771-5804.
8. V. Biju, *Chem. Soc. Rev.*, 2014, **43**, 744-764.
9. A. E. Friedman, J. C. Chambron, J. P. Sauvage, N. J. Turro and J. K. Barton, *J. Am. Chem. Soc.*, 1990, **112**, 4960-4962.
10. S. S. Kelkar and T. M. Reineke, *Bioconjugate chemistry*, 2011, **22**, 1879-1903.
11. A. Gilman and F. S. Philips, *Science*, 1946, **103**, 409-436.
12. S. Neidle, *Principles of nucleic acid structure*, Academic Press, 2010.
13. J. D. Watson and F. H. Crick, *Nature*, 1953, **171**, 737-738.
14. A. Rich, *Gene*, 1993, **135**, 99-109.
15. *By Original uploader was Richard Wheeler (Zephyris) at en.wikipedia - Originally from en.wikipedia; description page is/was here., GFDL,* https://commons.wikimedia.org/w/index.php?curid=2117121.
16. L. H. Hurley, *Nat. Rev. Cancer*, 2002, **2**, 188-200.
17. B. Rosenberg, L. Vancamp, J. E. Trosko and V. H. Mansour, *Nature*, 1969, **222**, 385-386.
18. M. H. Hao and S. C. Harvey, *Macromolecules*, 1992, **25**, 2200-2208.
19. B. G. Feuerstein, N. Pattabiraman and L. J. Marton, *Proc. Natl. Acad. Sci. U.S.A.*, 1986, **83**, 5948-5952.
20. S. K. Kim and B. Nordén, *FEBS J.*, 1993, **315**, 61-64.
21. B. Hyrup and P. E. Nielsen, *Bioorganic Med. Chem.*, 1996, **4**, 5-23.
22. X. Villalobos Alberú, 2015.
23. G. F. Deleavey and M. J. Damha, *Chem. Biol.*, 2012, **19**, 937-954.
24. D. A. Braasch and D. R. Corey, *Biochemistry*, 2002, **41**, 4503-4510.
25. K. M. Vasquez, L. Narayanan and P. M. Glazer, *Science*, 2000, **290**, 530-533.
26. A. Ray and B. Nordén, *FASEB J.*, 2000, **14**, 1041-1060.
27. L. Betts, J. A. Josey, J. M. Veal and S. R. Jordan, *Science*, 1995, **270**, 1838-1845.
28. Y. Kubota, K. Kubota and S. Tani, 2000.
29. J. Woynarowski, M. McHugh, R. D. Sigmund and T. A. Beerman, *Mol. Pharmacol.*, 1989, **35**, 177-182.
30. A. Banerjee, P. Majumder, S. Sanyal, J. Singh, K. Jana, C. Das and D. Dasgupta, *FEBS open bio.*, 2014, **4**, 251-259.
31. J. D. McGhee and P. H. von Hippel, *J. Mol. Biol.*, 1974, **86**, 469-489.
32. Y. D. Nechipurenko, *Biophysics*, 2014, **59**, 6-15.
33. J. Andersson, L. H. Fornander, M. Abrahamsson, E. Tuite, P. r. Nordell and P. Lincoln, *Inorg. Chem.*, 2012, **52**, 1151-1159.

34. M. Trieb, C. Rauch, B. Wellenzohn, F. Wibowo, T. Loerting, E. Mayer and K. R. Liedl, *J. Biomol. Struct. Dyn.*, 2004, **21**, 713-724.
35. G. Scatchard, *Ann. N. Y. Acad. Sci.*, 1949, **51**, 660-672.
36. A. V. Hill, *J. Physiol.*, 1910, **40**, 4-7.
37. C. P. Woodbury, *Introduction to macromolecular binding equilibria*, CRC Press, 2007.
38. T. L. Hill, *Cooperativity theory in biochemistry*, Springer, 1985.
39. W. Bujalowski, *Chem. Rev.*, 2006, **106**, 556-606.
40. E. Q. Adms, *J. Am. Chem. Soc.*, 1916, **38**, 1503-1510.
41. J. Wyman, *J. Mol. Biol.*, 1965, **11**, 631-644.
42. L. K. von Krbek, C. A. Schalley and P. Thordarson, *Chem. Soc. Rev.*, 2017, **46**, 2622-2637.
43. M. Martínez-Calvo, K. N. Orange, R. B. Elmes, B. la Cour Poulsen, D. C. Williams and T. Gunnlaugsson, *Nanoscale*, 2016, **8**, 563-574.
44. C. Hiort, P. Lincoln and B. Nordén, *J. Am. Chem. Soc.*, 1993, **115**, 3448-3454.
45. A. K. Mårtensson and P. Lincoln, *Dalton Trans.*, 2015, **44**, 3604-3613.
46. J. A. Schellman, *Biopolymers*, 1975, **14**, 999-1018.
47. I. Langmuir, *J. Am. Chem. Soc*, 1918, **30**, 1361-1403.
48. I. M. Klotz, F. M. Walker and R. B. Pivan, *J. Am. Chem. Soc.*, 1946, **68**, 1486-1490.
49. P. W. Atkins and R. S. Friedman, *Molecular quantum mechanics*, Oxford university press, 2011.
50. E. Di Cera, *Chem. Rev.*, 1998, **98**, 1563-1592.
51. S. Lifson, *J. Chem. Phys.*, 1964, **40**, 3705-3710.
52. J. P. Hall, F. E. Poynton, P. M. Keane, S. P. Gurung, J. A. Brazier, D. J. Cardin, G. Winter, T. Gunnlaugsson, I. V. Sazanovich, M. Towrie, C. J. Cardin, J. M. Kelly and S. J. Quinn, *Nat. Chem.*, 2015, **7**, 961-967.
53. S. Banerjee, J. A. Kitchen, S. A. Bright, J. E. O'Brien, D. C. Williams, J. M. Kelly and T. Gunnlaugsson, *Chemical Communications*, 2013, **49**, 8522-8524.
54. B. C. Poulsen, S. Estalayo-Adrián, S. Blasco, S. A. Bright, J. M. Kelly, D. C. Williams and T. Gunnlaugsson, *Dalton Trans.*, 2016, **45**, 18208-18220.
55. P. Thordarson, *Chem. Soc. Rev.*, 2011, **40**, 1305-1323.
56. B. Gole, A. K. Bar and P. S. Mukherjee, *Chem. Eur. J.*, 2014, **20**, 2276-2291.
57. T. M. Lohman and W. Bujalowski, *Methods Enzymol.*, 1991, **208**, 258-290.
58. M. R. Panman, P. Bodis, D. J. Shaw, B. H. Bakker, A. C. Newton, E. R. Kay, D. A. Leigh, W. J. Buma, A. M. Brouwer and S. Woutersen, *Phys. Chem. Chem. Phys.*, 2012, **14**, 1865-1875.
59. M. T. Carter, M. Rodriguez and A. J. Bard, *J. Am. Chem. Soc.*, 1989, **111**, 8901-8911.
60. D. Schmechel and D. Crothers, *Biopolymers*, 1971, **10**, 465-480.
61. A. Wolfe, G. H. Shimer Jr and T. Meehan, *Biochemistry*, 1987, **26**, 6392-6396.
62. R. O'Gorman, J. Rosenberg, O. Kallai, R. Dickerson, K. Itakura, A. Riggs and K. Matthews, *J. Biol. Chem.*, 1980, **255**, 10107-10114.
63. J. N. Weiss, *FASEB J.*, 1997, **11**, 835-841.
64. A. Zasedatelev, G. Gurskii and M. Vol'kenshtein, *Mol. bio.*, 1971, **5**, 194-198.
65. G. Gurskii, A. Zasedatelev and M. Vol'kenshtein, *Mol. Biol.*, 1972, **6**, 385-393.
66. B. Perlmutter-Hayman, *Acc. Chem. Res.*, 1986, **19**, 90-96.
67. J. G. Vos and J. M. Kelly, *Dalton Trans.*, 2006, **41**, 4869-4883.
68. C. Moucheron, A. Kirsch-De Mesmaeker and J. M. Kelly, *J. Photochem. Photobiol.*, 1997, **40**, 91-106.

69. P. Atkins and J. De Paula, *Atkins' physical chemistry*, Oxford University Press, 2014.
70. H. Takeda, K. Koike, T. Morimoto, H. Inumaru and O. Ishitani, *Adv. Inorg. Chem.*, 2011, **63**, 137-186.
71. J. M. Kelly, D. J. McConnell, C. OhUigin, A. B. Tossi, A. Kirsch-De Mesmaeker, A. Masschelein and J. Nasielski, *ChemComm*, 1987, **24**, 1821-1823.
72. R. B. P. Elmes, Trinity College Dublin., 2011.
73. F. E. Poynton, J. P. Hall, P. M. Keane, C. Schwarz, I. V. Sazanovich, M. Towrie, T. Gunnlaugsson, C. J. Cardin, D. J. Cardin and S. J. Quinn, *Chem. Sci.*, 2016, **7**, 3075-3084.
74. F. E. Poynton, *Spectroscopic Investigations into the Excited-state Processes and Reactivity of Ruthenium(II) Polypyridyl Complexes, PhD thesis*, 2017.
75. J. M. Kelly, A. B. Tossi, D. J. McConnell and C. OhUigin, *Nucleic Acids Res.*, 1985, **13**, 6017-6034.
76. P. Lincoln and B. Nordén, *J. Phys. Chem. B*, 1998, **102**, 9583-9595.
77. E. Amouyal, A. Homsi, J.-C. Chambron and J.-P. Sauvage, *Dalton Trans.*, 1990, 1841-1845.
78. J. G. Vos and J. M. Kelly, *Dalton Trans.*, 2006, 4869-4894.
79. J. P. Hall, D. Cook, S. R. Morte, P. McIntyre, K. Buchner, H. Beer, D. J. Cardin, J. A. Brazier, G. Winter and J. M. Kelly, *J. Am. Chem. Soc.*, 2013, **135**, 12652-12659.
80. I. Ortmans, B. Elias, J. M. Kelly, C. Moucheron and A. Kirsch-DeMesmaeker, *Dalton Trans.*, 2004, **4**, 668-676.
81. F. E. Poynton, S. A. Bright, S. Blasco, D. C. Williams, J. M. Kelly and T. Gunnlaugsson, *Chem. Soc. Rev.*, 2017, **46**, 7706-7756
82. C. A. Puckett and J. K. Barton, *J. Am. Chem. Soc.*, 2007, **129**, 46-47.
83. M. R. Gill, J. Garcia-Lara, S. J. Foster, C. Smythe, G. Battaglia and J. A. Thomas, *Nat. Chem.*, 2009, **1**, 662-667.
84. M. R. Gill, D. Cecchin, M. G. Walker, R. S. Mulla, G. Battaglia, C. Smythe and J. A. Thomas, *Chem. Sci.*, 2013, **4**, 4512-4519.
85. A. K. Gorle, M. Feterl, J. M. Warner, L. Wallace, F. R. Keene and J. G. Collins, *Dalton Trans.*, 2014, **43**, 16713-16725.
86. www.who.int/, www.who.int/).
87. M. M. Morelock, L. L. Choi, G. L. Bell and J. L. Wright, *J. Pharm. Sci.*, 1994, **83**, 948-952.
88. L. Ouyang, Z. Shi, S. Zhao, F. T. Wang, T. T. Zhou, B. Liu and J. K. Bao, *Cell. Prolif.*, 2012, **45**, 487-498.
89. M. Triesscheijn, P. Baas, J. H. Schellens and F. A. Stewart, *The oncologist*, 2006, **11**, 1034-1044.
90. Z. Zhou, J. Song, L. Nie and X. Chen, *Chem. Soc. Rev.*, 2016, **45**, 6597-6626.
91. L.-L. Bao, J. Bian, Y.-J. Yan, L.-J. Zhang, D. F. O'Shea and Z.-L. Chen, *Biomed. Pharmacother.*, 2017, **88**, 1220-1226.
92. A. E. O'Connor, W. M. Gallagher and A. T. Byrne, *Photochemistry and photobiology*, 2009, **85**, 1053-1074.
93. S. I. Moriwaki, J. Misawa, Y. Yoshinari, I. Yamada, M. Takigawa and Y. Tokura, *Photodermatology, photoimmunology & photomedicine*, 2001, **17**, 241-243.
94. C. B. By Jeff Dahl at en.wikipedia, https://commons.wikimedia.org/w/index.php?curid=17301313.
95. P. D. By Fvasconcellos - Own work, https://commons.wikimedia.org/w/index.php?curid=1084569.

96. https://www.graphpad.com/support/faqid/1356/.
97. R. E. Doherty, I. V. Sazanovich, L. K. McKenzie, A. S. Stasheuski, R. Coyle, E. Baggaley, S. Bottomley, J. A. Weinstein and H. E. Bryant, *Sci. Rep.*, 2016, **6**, 22668-22676.
98. B. S. Howerton, D. K. Heidary and E. C. Glazer, *J. Am. Chem. Soc.*, 2012, **134**, 8324-8327.
99. A. N. Hidayatullah, E. Wachter, D. K. Heidary, S. Parkin and E. C. Glazer, *Inorg. Chem.*, 2014, **53**, 10030-10032.
100. J. Tröger, *Adv. Synth. Catal.*, 1887, **36**, 225-245.
101. M. Spielman, *J. Am. Chem. Soc.*, 1935, **57**, 583-585.
102. C. S. Wilcox, *Tetrahedron Lett.*, 1985, **26**, 5749-5752.
103. J. C. Adrian Jr and C. S. Wilcox, *J. Am. Chem. Soc.*, 1989, **111**, 8055-8057.
104. A. P. Hansson, P.-O. Norrby and K. Wärnmark, *Tetrahedron Lett.*, 1998, **39**, 4565-4568.
105. C. Bailly, W. Laine, M. Demeunynck and J. Lhomme, *Biochem. Biophys. Res. Commun.*, 2000, **273**, 681-685.
106. E. Yashima, M. Akashi and N. Miyauchi, *Chem. Lett.*, 1991, **20**, 1017-1020.
107. O. Van Gijte, A. Tatibouet, M. Demeunynck, J. Lhomme and A. Kirsch-De Mesmaeker, *Tetrahedron Lett.*, 1997, **38**, 1567-1570.
108. C. Bresson, M. Luhmer, M. Demeunynck, A. Kirsch-De Mesmaeker and F. Pierard, *Tetrahedron Lett.*, 2004, **45**, 2863-2866.
109. E. B. Veale, D. O. Frimannsson, M. Lawler and T. Gunnlaugsson, *Org. Lett.*, 2009, **11**, 4040-4043.
110. E. B. Veale and T. Gunnlaugsson, *J. Org. Chem.*, 2010, **75**, 5513-5525.
111. S. Banerjee, S. A. Bright, J. A. Smith, J. Burgeat, M. Martinez-Calvo, D. C. Williams, J. M. Kelly and T. Gunnlaugsson, *J. Org. Chem.*, 2014, **79**, 9272-9283.
112. R. B. Elmes, M. Erby, S. A. Bright, D. C. Williams and T. Gunnlaugsson, *Chem. Commun.*, 2012, **48**, 2588-2590.
113. J. Guo, K. Rahme, Y. He, L.-L. Li, J. D. Holmes and C. M. O'Driscoll, *Int. J. Nanomed.*, 2017, **12**, 6131-6152.
114. S. Comby, E. M. Surender, O. Kotova, L. K. Truman, J. K. Molloy and T. Gunnlaugsson, *Inorg. Chem.*, 2013, **53**, 1867-1879.
115. http://www.nanospectra.com/technology/aurolasetherapy.html.
116. V. Torchilin, *Adv. Drug Deliv. Rev.*, 2011, **63**, 131-135.
117. H. Maeda, J. Wu, T. Sawa, Y. Matsumura and K. Hori, *J. Control. Release*, 2000, **65**, 271-284.
118. C. Ayala-Orozco, C. Urban, S. Bishnoi, A. Urban, H. Charron, T. Mitchell, M. Shea, S. Nanda, R. Schiff and N. Halas, *J. Control. Release*, 2014, **191**, 90-97.
119. K. A. Fitzgerald, K. Rahme, J. Guo, J. D. Holmes and C. M. O'Driscoll, *J. Mater. Chem. B*, 2016, **4**, 2242-2252.
120. D. C. Hone, P. I. Walker, R. Evans-Gowing, S. FitzGerald, A. Beeby, I. Chambrier, M. J. Cook and D. A. Russell, *Langmuir*, 2002, **18**, 2985-2987.
121. M. E. Wieder, D. C. Hone, M. J. Cook, M. M. Handsley, J. Gavrilovic and D. A. Russell, *Photochem. Photobiol. Sci.*, 2006, **5**, 727-734.
122. E. M. Surender, S. Comby, B. L. Cavanagh, O. Brennan, T. C. Lee and T. Gunnlaugsson, *Chem*, 2016, **1**, 438-455.
123. K. Sokolov, M. Follen, J. Aaron, I. Pavlova, A. Malpica, R. Lotan and R. Richards-Kortum, *Cancer Res.*, 2003, **63**, 1999-2004.

124. Y. Zhao, B. Pang, H. Luehmann, L. Detering, X. Yang, D. Sultan, S. Harpstrite, V. Sharma, C. S. Cutler and Y. Xia, *Adv. Healthc. Mater.*, 2016, **5**, 928-935.
125. S. S. Kelkar and T. M. Reineke, *Bioconjugate Chem.*, 2011, **22**, 1879-1903.
126. S. Gao, L. Zhang, G. Wang, K. Yang, M. Chen, R. Tian, Q. Ma and L. Zhu, *Biomaterials*, 2016, **79**, 36-45.
127. C. R. Mayer, E. Dumas and F. Sécheresse, *J. Colloid Interface Sci.*, 2008, **328**, 452-457.
128. R. M. Clegg, *Laboratory Techniques in Biochemistry and Molecular Biology*, 2009, **33**, 1-57.
129. S. Zeng, D. Baillargeat, H.-P. Ho and K.-T. Yong, *Chem. Soc. Rev.*, 2014, **43**, 3426-3452.
130. P. J. Debouttière, S. Roux, F. Vocanson, C. Billotey, O. Beuf, A. Favre-Réguillon, Y. Lin, S. Pellet-Rostaing, R. Lamartine and P. Perriat, *Adv. Funct. Mater.*, 2006, **16**, 2330-2339.
131. G. J. Ryan, S. Quinn and T. Gunnlaugsson, *Inorg. Chem.*, 2008, **47**, 401-403.
132. G. J. Ryan, F. E. Poynton, R. B. Elmes, M. Erby, D. C. Williams, S. J. Quinn and T. Gunnlaugsson, *Dalton Trans.*, 2015, **44**, 16332-16344.
133. R. B. P. Elmes, M. Erby, S. M. Cloonan, S. J. Quinn, D. C. Williams and T. Gunnlaugsson, *Chem. Commun.*, 2011, **47**, 686-688.
134. M. Triesscheijn, P. Baas, J. H. M. Schellens and F. A. Stewart, *Oncologist*, 2006, **11**, 1034-1044.
135. G. L. Douaron, F. Schmidt, M. Amar, H. Kadar, B. Séon-Méniel, L. Ferrié, D. Touboul, A. Brunelle, R. Raisman-Vozari and B. Figadère, *Planta Med.*, 2012, **78**, CL20.
136. X. Hui, F. Schmidt, M. A. Fakhfakh, X. Franck and B. Figadere, *Heterocycles*, 2007, **72**, 353-361.
137. S. Knapp, J. Ziv and J. D. Rosen, *Tetrahedron*, 1989, **45**, 1293-1298.
138. R. Nasielski-Hinkens, J. Kotel, T. Lecloux and J. Nasielski, *Synth. Commun.*, 1989, **19**, 511-514.
139. J. Ettedgui, Y. Diskin-Posner, L. Weiner and R. Neumann, *J. Am. Chem. Soc.*, 2010, **133**, 188-190.
140. C. A. Obafemi and W. Pfleiderer, *Helvetica chimica acta*, 1994, **77**, 1549-1556.
141. R. Nasielski-Hinkens, M. Benedek-Vamos and D. Maetens, *J. Heterocycl. Chem.*, 1980, **17**, 873-876.
142. T. Doi, H. Nagamiya, M. Kokubo, K. Hirabayashi and T. Takahashi, *Tetrahedron*, 2002, **58**, 2957-2963.
143. B. Zhang and L.-H. Guo, *Biosens. Bioelectron.*, 2012, **37**, 112-115.
144. J. P. Hall, D. Cook, S. R. Morte, P. McIntyre, K. Buchner, H. Beer, D. J. Cardin, J. A. Brazier, G. Winter and J. M. Kelly, *J. Am. Chem. Soc.*, 2013, **135**, 12652-12659.
145. A. T. R. Williams, S. A. Winfield and J. N. Miller, *Analyst*, 1983, **108**, 1067-1071.
146. K. Nakamaru, K. Nishio and H. Nobe, *Sci. Rep. Hirosaki Univ.*, 1979, **26**, 57-62.
147. K. Nakamaru, *Bull. Chem. Soc. Jpn.*, 1982, **55**, 1639-1640.
148. Gaussian 09, Revision D.01, M. J. Frisch, G. W. Trucks, H. B. Schlegel, G. E. Scuseria, M. A. Robb, J. R. Cheeseman, G. Scalmani, V. Barone, B. Mennucci, G. A. Petersson, H. Nakatsuji, M. Caricato, X. Li, H. P. Hratchian, A. F. Izmaylov, J. Bloino, G. Zheng, J. L. Sonnenberg, M. Hada, M. Ehara, K. Toyota, R. Fukuda, J. Hasegawa, M. Ishida, T. Nakajima, Y. Honda, O. Kitao, H. Nakai, T. Vreven, J. A. Montgomery, Jr., J. E. Peralta, F. Ogliaro, M. Bearpark, J. J. Heyd, E. Brothers, K. N. Kudin, V. N. Staroverov, T. Keith, R. Kobayashi, J. Normand, K. Raghavachari, A.

Rendell, J. C. Burant, S. S. Iyengar, J. Tomasi, M. Cossi, N. Rega, J. M. Millam, M. Klene, J. E. Knox, J. B. Cross, V. Bakken, C. Adamo, J. Jaramillo, R. Gomperts, R. E. Stratmann, O. Yazyev, A. J. Austin, R. Cammi, C. Pomelli, J. W. Ochterski, R. L. Martin, K. Morokuma, V. G. Zakrzewski, G. A. Voth, P. Salvador, J. J. Dannenberg, S. Dapprich, A. D. Daniels, O. Farkas, J. B. Foresman, J. V. Ortiz, J. Cioslowski, and D. J. Fox, Gaussian, Inc., Wallingford CT, 2013.

149. E. Tuite, P. Lincoln and B. Nordén, *J. Am. Chem. Soc.*, 1997, **119**, 239-240.
150. P. M. Keane, J. P. Hall, F. E. Poynton, B. C. Poulsen, S. P. Gurung, I. P. Clark, I. V. Sazanovich, M. Towrie, T. Gunnlaugsson, S. J. Quinn, C. J. Cardin and J. M. Kelly, *Chem. Eur. J.*, 2017, **23**, 10344 – 10351.
151. C. M. Dupureur and J. K. Barton, *J. Am. Chem. Soc.*, 1994, **116**, 10286-10287.
152. H. Niyazi, J. P. Hall, K. O'sullivan, G. Winter, T. Sorensen, J. M. Kelly and C. J. Cardin, *Nat. Chem.*, 2012, **4**, 621-628.
153. B. Nordén and T. Kurucsev, *J. Mol. Recogn.*, 1994, **7**, 141-155.
154. B. Nordén, A. Rodger and T. Dafforn, *Linear Dichroism and Circular Dichroism: A Textbook on Polarized-Light Spectroscopy*
155. G. Cohen and H. Eisenberg, *Biopolymers*, 1969, **8**, 45-55.
156. S. Satyanarayana, J. C. Dabrowiak and J. B. Chaires, *Biochemistry*, 1992, **31**, 9319-9324.
157. C. Deegan, B. Coyle, M. McCann, M. Devereux and D. A. Egan, *Chem. Biol. Interact.*, 2006, **164**, 115-125.
158. S. Arounaguiri, D. Easwaramoorthy, A. Ashokkumar, A. Dattagupta and B. G. Maiya, *J. Chem. Sci.*, 2000, **112**, 1-17.
159. T. F. Silva, P. Smoleński, L. M. Martins, M. F. C. Guedes da Silva, A. R. Fernandes, D. Luis, A. Silva, S. Santos, P. M. Borralho and C. M. Rodrigues, *Eur. J. Inorg. Chem.*, 2013, **2013**, 3651-3658.
160. L. N. Dovigo, A. C. Pavarina, A. P. D. Ribeiro, I. L. Brunetti, C. A. d. S. Costa, D. P. Jacomassi, V. S. Bagnato and C. Kurachi, *Photochem. Photobiol.*, 2011, **87**, 895-903.
161. S. Banerjee, P. Prasad, A. Hussain, I. Khan, P. Kondaiah and A. R. Chakravarty, *Chem. Commun.*, 2012, **48**, 7702-7704.
162. T. A. Dahll, P. Bilski, K. J. Reszka and C. F. Chignell, *Photochem. Photobiol.*, 1994, **59**, 290-294.
163. L. Zhang, K. Lei, J. Zhang, W. Song, Y. Zheng, S. Tan, Y. Gao, Y. Xu, J. Liu and X. Qian, *Med. Chem. Comm.*, 2016, **7**, 1171-1175.
164. C. A. Goss and H. D. Abruna, *Inorg. Chem.*, 1985, **24**, 4263-4267.
165. I. Meistermann, G. V. Kalayda, A. C. Hotze and J. Reedijk, *Tetrahedron Lett.*, 2004, **45**, 2593-2596.
166. G. Hilt, B. Lewall, G. Montero, J. H. P. Utley and E. Steckhan, *Liebigs Ann.-Recl.*, 1997, 2289-2296.
167. I. J. Villar-Garcia, A. Abebe and Y. Chebude, *Inorg. Chem. Commun.*, 2012, **19**, 1-3.
168. EP1964927A1, 2008.
169. S. Er, C. Suh, M. P. Marshak and A. Aspuru-Guzik, *Chem. Sci.*, 2015, **6**, 885-893.
170. K. Moon, J. Grindstaff, D. Sobransingh and A. E. Kaifer, *Angew. Chem.*, 2004, **43**, 5496-5499.
171. R. E. Morris, R. E. Aird, P. S. Murdoch, H. Chen, J. Cummings, N. D. Hughes, S. Parsons, A. Parkin, G. Boyd, D. I. Jodrell and P.J. Sadler, *J. Med. Chem.,* 2001, **44**, 3616-3621.

172. C. Xu, B. Bailly-Maitre and J. C. Reed, *J. Clin. Invest.*, 2005, **115**, 2656.
173. J. O'brien, I. Wilson, T. Orton and F. Pognan, *FEBS J.*, 2000, **267**, 5421-5426.
174. R. R. Allison and C. H. Sibata, *Photodiagn. Photodyn.*, 2010, **7**, 61-75.
175. A. Hergueta-Bravo, M. E. Jiménez-Hernández, F. Montero, E. Oliveros and G. Orellana, *J. Phys. Chem. B*, 2002, **106**, 4010-4017.
176. R. B. P. Elmes, *Diquaternerised and Ru(II) Based Polypyridyl Conjugates as Biological Probes and Ptototherapeutic Agents, PhD Thesis*, 2011.
177. A. Michaeli and J. Feitelson, *Photochem. Photobiol.*, 1994, **59**, 284-289.
178. B. A. Albani, B. Peña, K. R. Dunbar and C. Turro, *Photochem. Photobiol. Sci.*, 2014, **13**, 272-280.
179. D. T. Richens, *Chem. Rev.*, 2005, **105**, 1961-2002.
180. I. Rosenthal, J. Z. Sostaric and P. Riesz, *Ultrason. Sonochem.*, 2004, **11**, 349-363.
181. S. Banerjee, J. A. Kitchen, S. A. Bright, J. E. O'Brien, D. C. Williams, J. M. Kelly and T. Gunnlaugsson, *Chem. Commun.*, 2013, **49**, 8522-8524.
182. I. Slowing, B. G. Trewyn and V. S. Y. Lin, *J. Am. Chem. Soc.*, 2006, **128**, 14792-14793.
183. S. Tardito, C. Isella, E. Medico, L. Marchio, E. Bevilacqua, M. Hatzoglou, O. Bussolati and R. Franchi-Gazzola, *J. Biol. Chem.*, 2009, **284**, 24306-24319.
184. F. Caruso, M. Rossi, A. Benson, C. Opazo, D. Freedman, E. Monti, M. B. Gariboldi, J. Shaulky, F. Marchetti and R. Pettinari, *J. Med. Chem.*, 2012, **55**, 1072-1081.
185. A. V. Marenich, C. J. Cramer and D. G. Truhlar, *J. Phys. Chem. B*, 2009, **113**, 6378-6396.
186. S. Banerjee, E. B. Veale, C. M. Phelan, S. A. Murphy, G. M. Tocci, L. J. Gillespie, D. O. Frimannsson, J. M. Kelly and T. Gunnlaugsson, *Chem. Soc. Rev.*, 2013, **42**, 1601-1618.
187. J. M. Kelly, F. E. Poynton, T. Gunnlaugsson, *Manuscript in preparation*, 2018.
188. J. A. Rothwell, A. J. Day and M. R. Morgan, *J. Agric. Food Chem.*, 2005, **53**, 4355-4360.
189. D. K. Weber, M.-A. Sani, M. T. Downton, F. Separovic, F. R. Keene and J. G. Collins, *J. Am. Chem. Soc.*, 2016, **138**, 15267-15277.
190. F. R. Svensson, M. Matson, M. Li and P. Lincoln, *Biophys. Chem.*, 2010, **149**, 102-106.
191. S. Estalayo-Adrián, J. M. Kelly and T. Gunnlaugsson, *Manuscript in preparation*, 2017.
192. J. Zhong, L. Li, X. Zhu, S. Guan, Q. Yang, Z. Zhou, Z. Zhang and Y. Huang, *Biomaterials*, 2015, **65**, 43-55.
193. A. Arzumanov, A. P. Walsh, V. K. Rajwanshi, R. Kumar, J. Wengel and M. J. Gait, *Biochemistry*, 2001, **40**, 14645-14654.
194. L. F. R. Gebert, M. A. E. Rebhan, S. E. M. Crivelli, R. Denzler, M. Stoffel and J. Hall, *Nucleic Acids Res.*, 2014, **42**, 609-621.
195. H. Han and L. H. Hurley, *Trends. Pharmacol. Sci.*, 2000, **21**, 136-142.
196. R. Hänsel-Hertsch, M. Di Antonio and S. Balasubramanian, *Nat. Rev. Mol. Cell Biol.*, 2017, **18**, 279-284.
197. O. Domarco, D. Lötsch, J. Schreiber, C. Dinhof, S. Van Schoonhoven, M. García, C. Peinador, B. Keppler, W. Berger and A. Terenzi, *Dalton Trans.*, 2017, **46**, 329-332.
198. A. V. Hill, *Biochem. J.*, 1913, **7**, 471-476.
199. A. F. Riggs, *J. Exp. Biol.*, 1998, **201**, 1073-1084.

200. J. M. Kelly, P. Keane, J. Hall, F. E. Poynton, B. C. Poulsen, S. Gurung, I. Clark, I. Sazanovich, M. Towrie and T. Gunnlaugsson, *Chem. Eur. J.*, 2017.
201. N. C. Fletcher and F. Richard Keene, *Dalton Trans.*, 1998, **14**, 2293-2302.
202. N. C. Fletcher and F. Richard Keene, *Dalton Trans.*, 1999, **5**, 683-690.
203. N. Berova, P. L. Polavarapu, K. Nakanishi and R. W. Woody (Eds.). (2012). *Comprehensive chiroptical spectroscopy, applications in stereochemical analysis of synthetic compounds, natural products, and biomolecules* (Vol. 2). John Wiley & Sons.
204. M. Kubista, B. Aakerman and B. Norden, *Biochemistry*, 1987, **26**, 4545-4553.
205. B. Bosnich, *Inorg. Chem.*, 1968, **7**, 2379-2386.
206. M. Ardhammar, P. Lincoln, A. Rodger and B. Nordén, *Chem. Phys. Lett.*, 2002, **354**, 44-50.
207. S. Mason, *Inorg. Chim. Acta.*, 1968, **2**, 89-109.
208. R. V. Person, K. Monde, H. u. Humpf, N. Berova and K. Nakanishi, *Chirality*, 1995, **7**, 128-135.
209. W. Kuhn, *J. Chem. Soc. Faraday Trans.*, 1930, **26**, 293-308.
210. J. R. Lakowicz, "Quenching of fluorescence." In *Principles of fluorescence spectroscopy*, pp. 257-301, Springer US, 1983.
211. M. T. Record, T. M. Lohman and P. De Haseth, *J. Mol. Biol.*, 1976, **107**, 145-158.
212. J. G. Collins, A. D. Sleeman, J. R. Aldrich-Wright, I. Greguric and T. W. Hambley, *Inorg. Chem.*, 1998, **37**, 3133-3141.
213. P. Waywell, V. Gonzalez, M. R. Gill, H. Adams, A. J. Meijer, M. P. Williamson and J. A. Thomas, *Chem. Eur. J.*, 2010, **16**, 2407-2417.
214. P. M. Keane, F. E. Poynton, J. P. Hall, I. V. Sazanovich, M. Towrie, T. Gunnlaugsson, S. J. Quinn, C. J. Cardin and J. M. Kelly, *Angew. Chem.*, 2015, **127**, 8484-8488.
215. G. G. Privé, U. Heinemann, S. Chandrasegaran, L. S. Kan, M. L. Kopka and R. E. Dickerson, *Science*, 1987, **238**, 498-504.
216. S. Pramanik, S. Nagatoishi, S. Saxena, J. Bhattacharyya and N. Sugimoto, *J. Phys. Chem. B*, 2011, **115**, 13862-13872.
217. B.-Y. Pan, L. Zhang, S.-X. Dou and P.-Y. Wang, *Biochem. Biophys. Res. Commun.*, 2009, **388**, 137-140.
218. M. R. Lockett, M. F. Phillips, J. L. Jarecki, D. Peelen and L. M. Smith, *Langmuir*, 2008, **24**, 69-75.
219. US2973379, 1961.
220. L. Wang, H. Yin, M. A. Jabed, M. Hetu, C. Wang, S. Monro, X. Zhu, S. Kilina, S. A. McFarland and W. Sun, *Inorg. Chem.*, 2017, **56**, 3245-3259.
221. J. E. Jones, R. L. Jenkins, R. S. Hicks, A. J. Hallett and S. J. Pope, *Dalton Trans.*, 2012, **41**, 10372-10381.
222. L. S. Wong, S. J. Janusz, S. Sun, G. J. Leggett and J. Micklefield, *Chem. Eur. J.*, 2010, **16**, 12234-12243.
223. T. Banerjee, S. Rawalekar, A. Das and H. N. Ghosh, *Eur. J. Inorg. Chem.*, 2011, **2011**, 4187-4197.
224. J. Turkevich, P. C. Stevenson and J. Hillier, *Faraday Discuss.*, 1951, **11**, 55-75.
225. M. Brust, M. Walker, D. Bethell, D. J. Schiffrin and R. Whyman, *J. Am. Chem. Soc.*, 1994, 801-802.
226. K.-S. Lee and M. A. El-Sayed, *J. Phys. Chem. B*, 2006, **110**, 19220-19225.
227. D. B. Williams and C. B. Carter, in *Transmission electron microscopy*, Springer, 1996, pp. 3-17.

228. B. J. P. Berne, R. Dynamic Light Scattering: with applications to chemistry, biology, and physics; Dover Publications: Mineola, N.Y., 2000.
229. S. Honary and F. Zahir, *Trop. J. Pharm. Res.*, 2013, **12**, 265-273.
230. M. K. G. Jayakumar, N. M. Idris and Y. Zhang, *Proc. Natl. Acad. Sci. USA PNAS*, 2012, **109**, 8483-8488.
231. J. Marmur and P. Doty, *J. Mol. Biol.*, 1962, **5**, 109-118.
232. P. Mukerjee and K. J. Mysels, *Journal of the American Chemical Society*, 1955, **77**, 2937-2943.
233. K. Makino, T. Yamada, M. Kimura, T. Oka, H. Ohshima and T. Kondo, *Biophys. Chem.*, 1991, **41**, 175-183.
234. K. Matusita, T. Komatsu and R. Yokota, *J. Mater. Sci.*, 1984, **19**, 291-296.
235. http://jplusconsulting.com/).
236. CS104455, 1961.
237. S. Borsley and E. R. Kay, *Chem. Commun.*, 2016, **52**, 9117-9120.
238. P. Aguirre, R. López, D. Villagra, I. Azocar-Guzman, A. Pardey and S. Moya, *Appl. Organomet. Chem.*, 2003, **17**, 36-41.
239. C.-S. Choi, T. Mutai, S. Arita and K. Araki, *Perkin Trans.*, 2000, 243-247.
240. D. J. Yoo, K.-S. Lee, A. R. Kim and K. S. Nahm, *Hwahak Konghak*, 2011, **49**, 330-337.
241. R. F. Khairoutdinov, L. V. Doubova, R. C. Haddon and L. Saraf, *J. Phys. Chem. B*, 2004, **108**, 19976-19981.

Appendices

Appendix 1 - 6

Appendix 1:

Cellular Uptake of Positively Charged Compounds

According to Boltzmann's distribution law the relative difference between the populations of two states with a difference in energy of ΔE will be given as:

$$p_i = e^{-\Delta E/k_B T}$$

For an animal cell the membrane potential will typically be -60 mV, which corresponds to an energy difference of -1.92×10^{-20} J for two states of the Ru(II) polypyridyl complex with two positive charges. If the membrane potential makes the only contribution to the distribution of the complex, this will, according to Boltzmann's distribution law at equilibrium, give approximately 89 times higher concentration inside the cells ($[Ru^{2+}]_{in}$) than outside ($[Ru^{2+}]_{out}$):

$$\frac{[Ru^{2+}]_{in}}{[Ru^{2+}]_{out}} = e^{-1.92E-20/(k_B \times 310K)} = 89$$

The difference can be smaller or larger, depending on other properties of the system such as affinity for biomolecules inside cells (*e.g.* DNA) or proteins in the extracellular medium (*e.g.* albumin). Furthermore, the cellular uptake will also depend on the ability of the compound to penetrate the cell membrane, however this is a kinetic consideration.

Appendix 2:

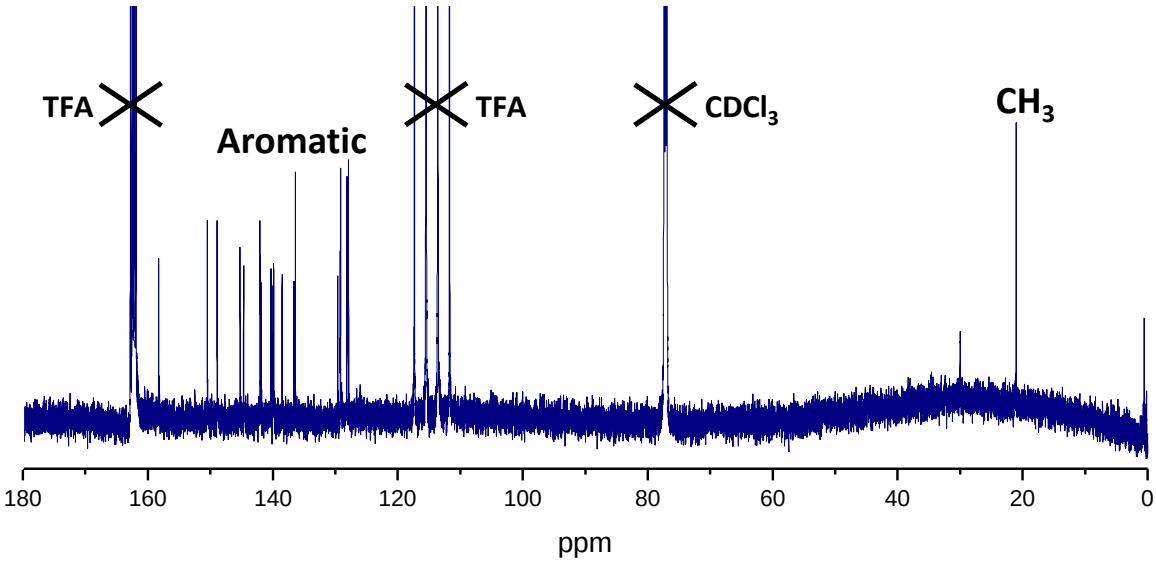

Figure A2.1: *^{13}C NMR (100 MHz, $CDCl_3$ with TFA) spectrum of ligand* ***mpdppz****.*

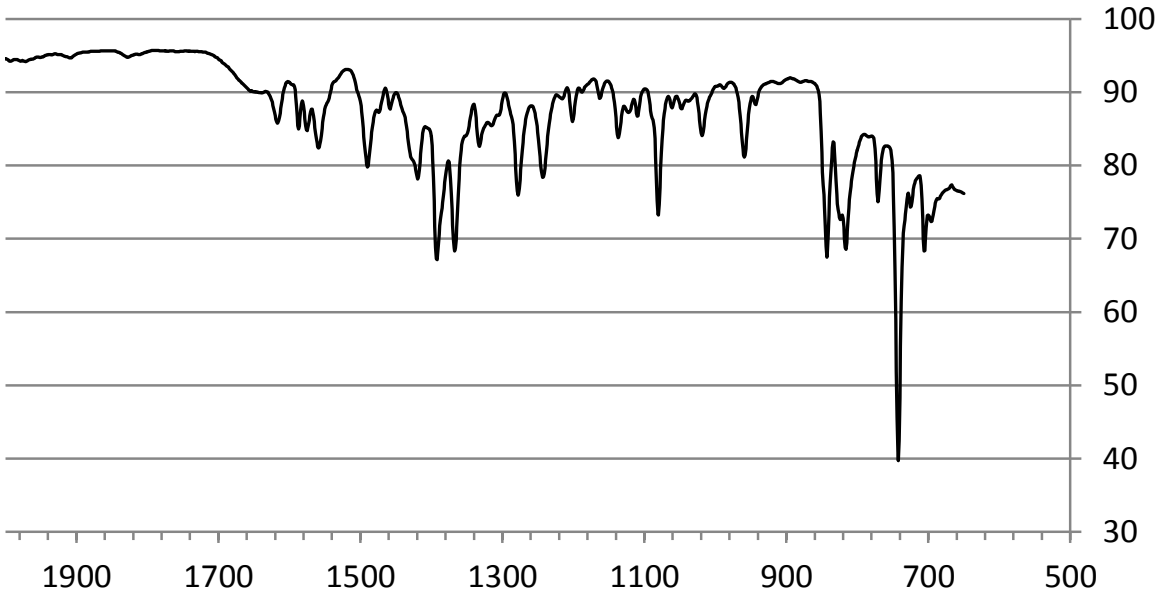

Figure A2.2: *IR spectrum of ligand* ***mpdppz****.*

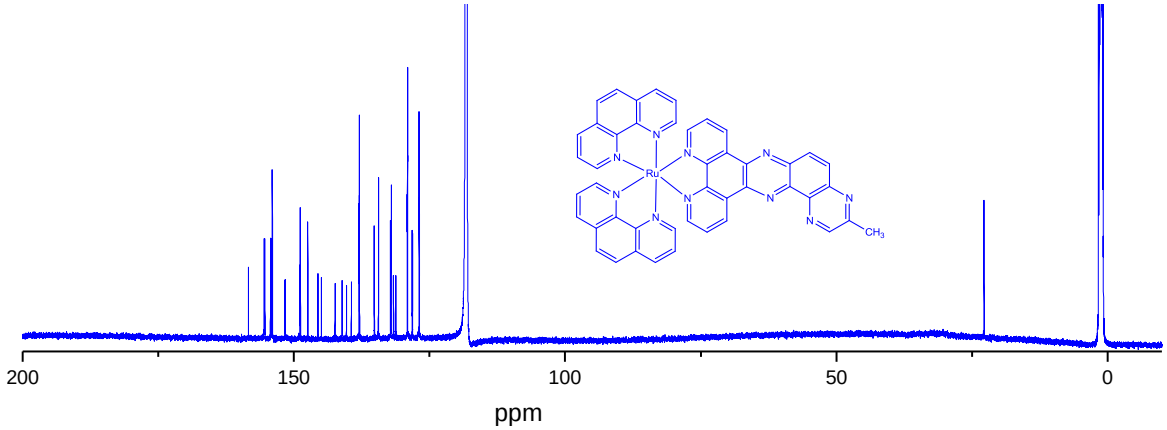

Figure A2.3: *^{13}C NMR (100 MHz, CD_3CN) spectrum of complex* ***33a****·2Cl.*

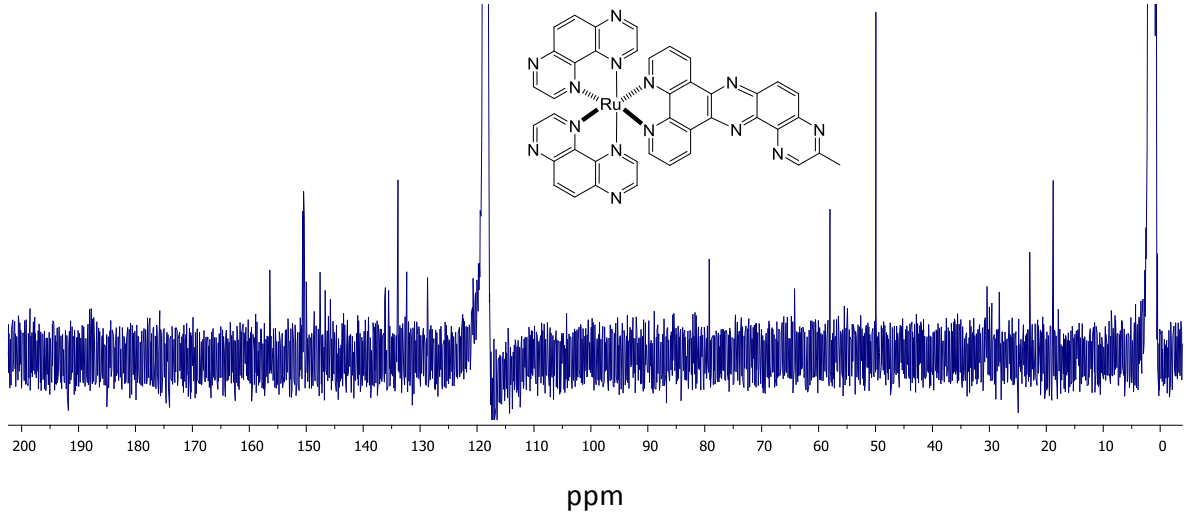

Figure A2.4: *^{13}C NMR (100 MHz, CD_3CN) spectrum of complex* ***33b****·2Cl.*

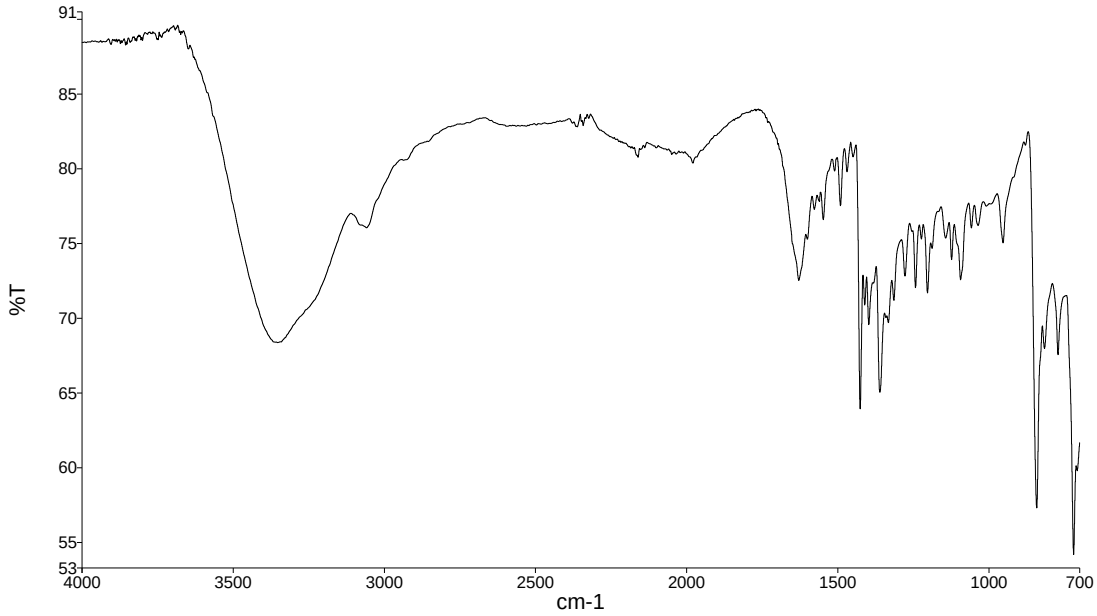

Figure A2.5: *IR spectrum of complex* ***33a****·2Cl.*

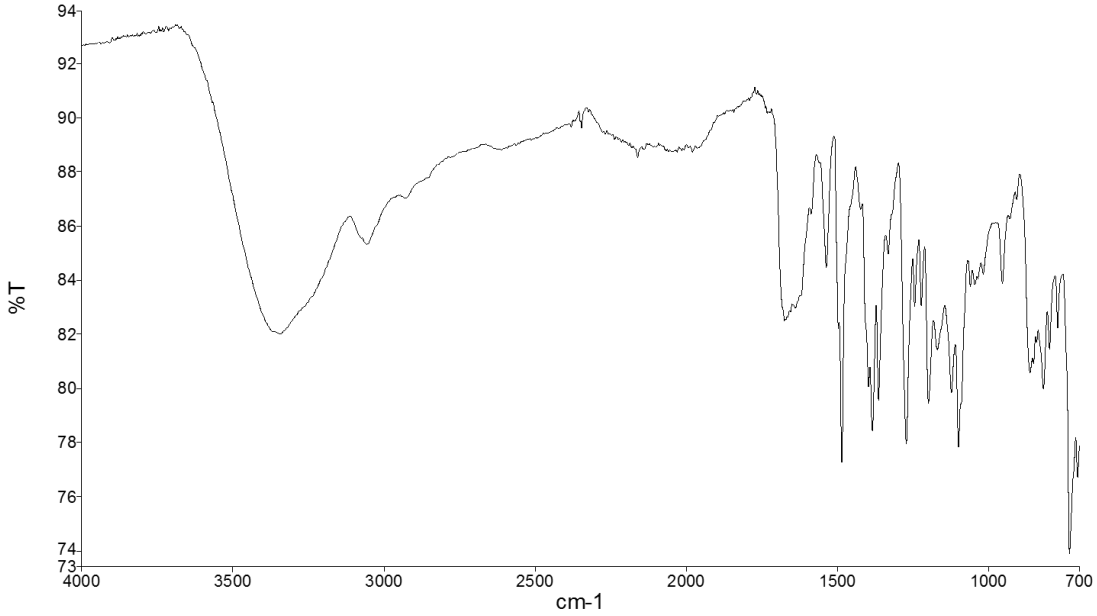

Figure A2.6: *IR spectrum of complex* ***33b****·2Cl.*

Table A2.1: *Scatchard site binding constants (k) and site size (n) for the binding of* ***33a*** *and* ***33b*** *to st-DNA with varied ionic strength at 25 °C. Calculated with the program OriginPro from absorption data. The reported values and errors are the mean and standard error for all replicates.*

	k **(10^6 M^{-1})**		***n*** **(#bp)**	
	33a	**33b**	**33a**	**33b**
Buffer only[a]	3.9 ± 0.2	13 ± 2	1.7 ± 0.1	1.7 ± 0.1
160 mM NaCl[b]	1.5 ± 0.4	0.68 ± 0.07	2.3 ± 0.1	1.7 ± 0.1

[a] *10 mM sodium phosphate buffer, pH 7.4;* [b] *Buffer and 160 mM NaCl.*

Table A2.2: *Scatchard site binding constants (k) and site size (n) calculated from absorption spectra with ReactLab EQUILIBRIA for the binding of* ***33a*** *and* ***33b*** *to st-DNA with varied ionic strength at 25 °C. The reported values and errors are the mean and standard error for all replicates.*

	k **(10^6 M^{-1})**		***n*** **(#bp)**	
	33a	**33b**	**33a**	**33b**
Buffer only[a]	6 ± 2	15 ± 5	2.0 ± 0.1	2.0 ± 0.1
160 mM NaCl[b]	4 ± 1	0.7 ± 0.1	2.8 ± 0.1	2.0 ± 0.1

[a] *10 mM sodium phosphate buffer, pH 7.4;* [b] *buffer and 160 mM NaCl*

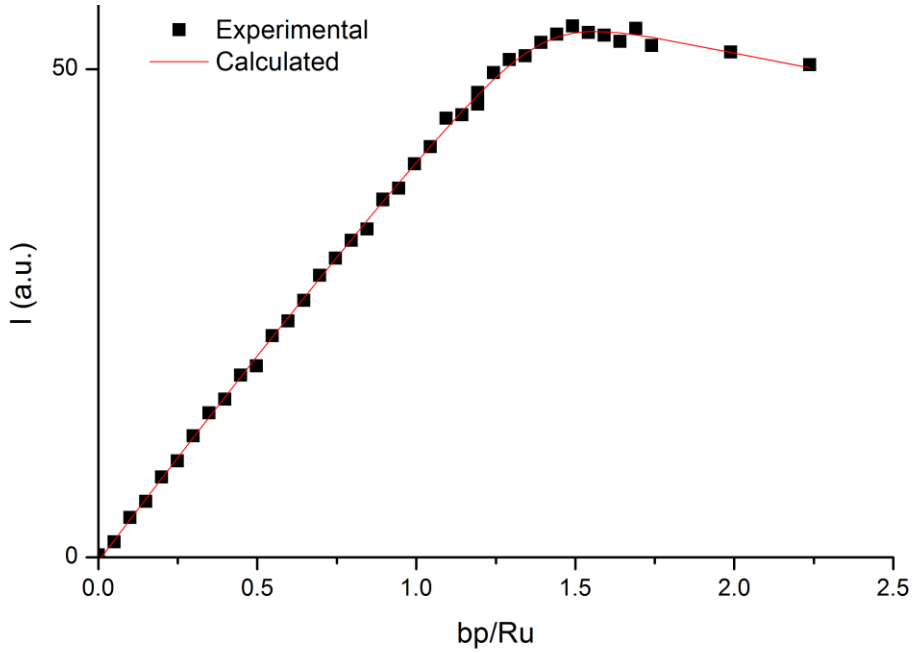

Figure A2.7: *Observed change in the emission of* ***33a*** *upon increasing concentration of st-DNA in 10 mM aqueous sodium phosphate buffered solution and change predicted by ReactLab EQUILIBRIA with two equilibria (non-cooperative).*

Table A2.3: *Non-cooperative MGVH site binding constants (k) and site size (n) calculated from absorption spectra with ReactLab EQUILIBRIA for the binding of* ***33a*** *and* ***33b*** *to st-DNA with varied ionic strength at 25 °C. The reported values and errors are the mean and standard error for all replicates.*

	k **(10^6 M^{-1})**		***n*** **(#bp)**	
	33a	**33b**	**33a**	**33b**
Buffer only[a]	13 ± 3	25 ± 10	1.8 ± 0.1	1.9 ± 0.1
160 mM NaCl[b]	4.7 ± 1.2	0.70 ± 0.08	2.5 ± 0.1	2.0 ± 0.1

[a] 10 mM sodium phosphate buffer, pH 7.4; [b] buffer and 160 mM NaCl

Appendix 3

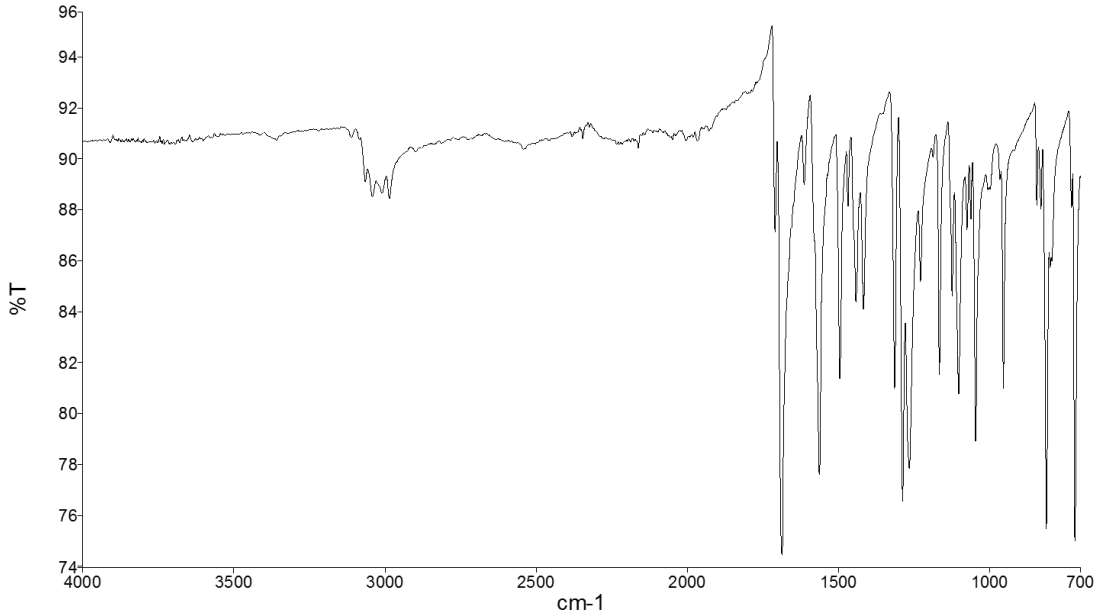

Figure A3.1: *IR spectrum of compound* ***45b·I****.*

Appendix 4

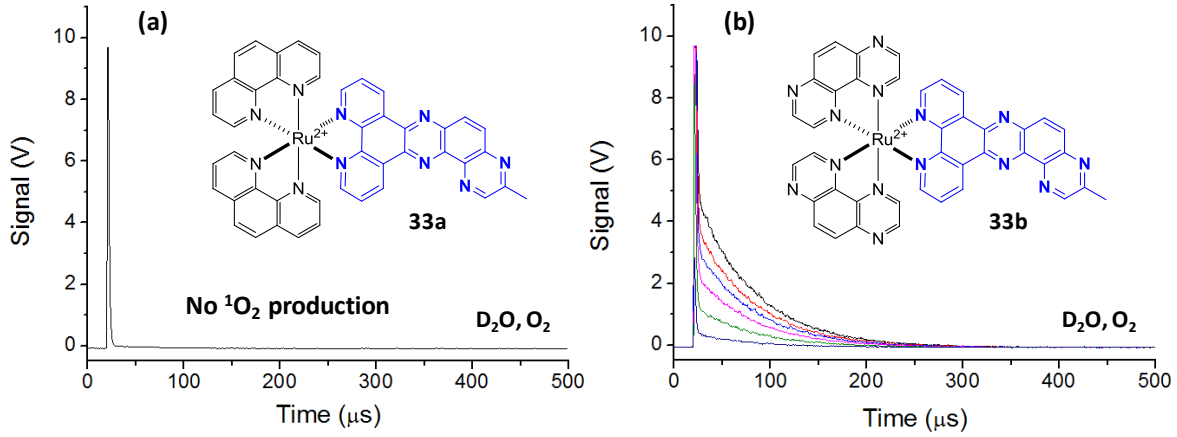

Figure A4.1: *Decay for the decrease in the emission (λ_{exc} = 1260 nm) over time at different time points after excitation (λ_{exc} = 532 nm). (a) Complex **33a**. (b) Complex **33b**. D_2O saturated with O_2. The excitations have been performed with varied laser strength corresponding to different curves.*

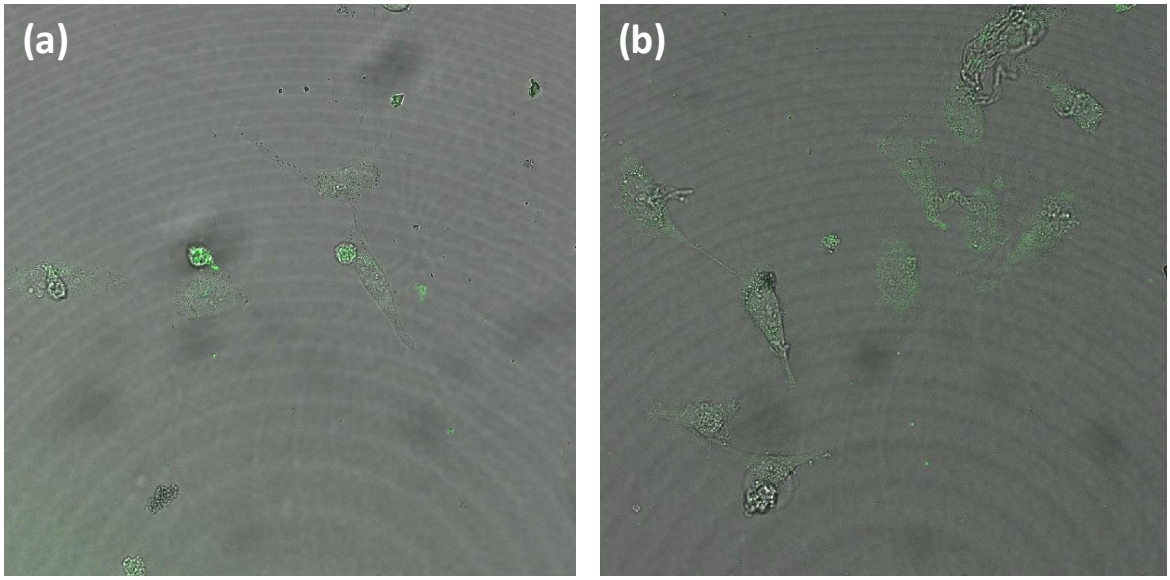

Figure A4.2: *Confocal images of HeLa cells treated with 5 μM of Tröger's base **50** (a) and **52** (b) after 24 hours incubation.*

Appendix 5:

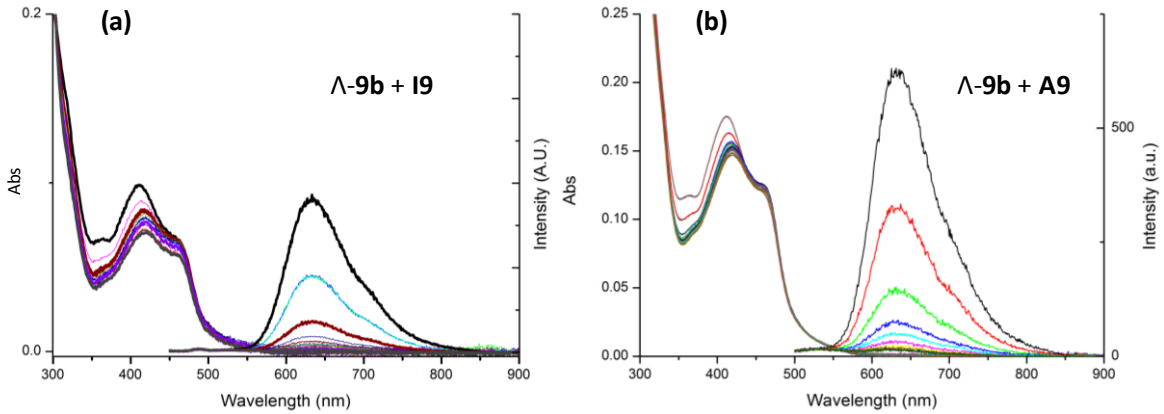

Figure A5.1: *Changes in absorption and emission spectra of Λ-**9b** at titration with **I9** (a) and **A9** (b); 50 mM potassium phosphate buffer, pH 7.0, 25 °C.*

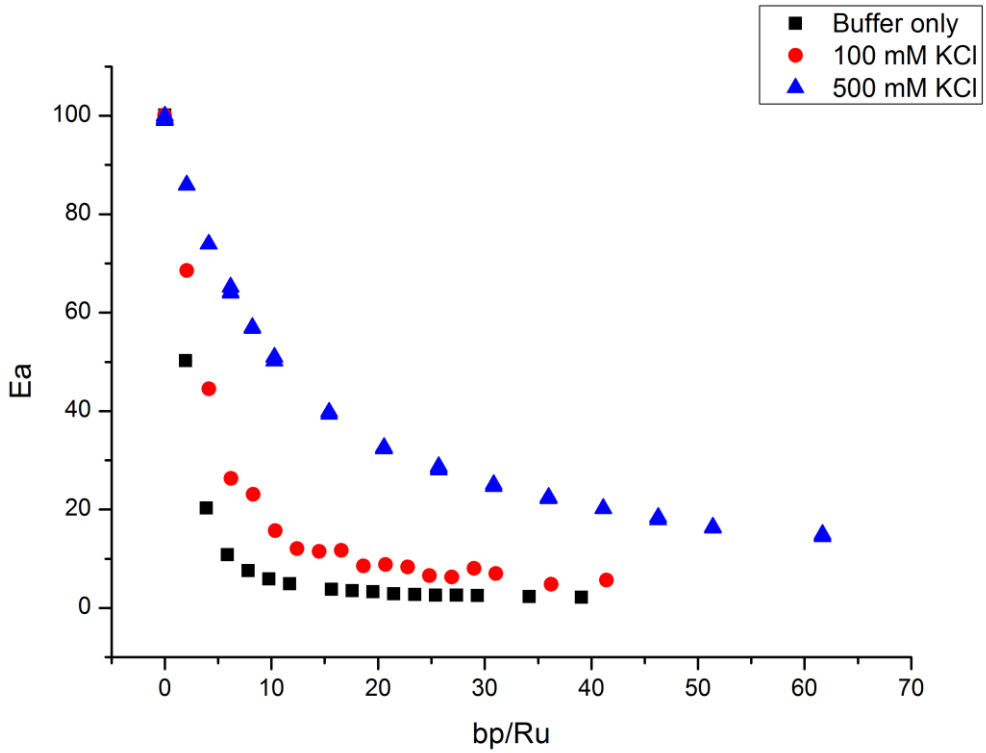

Figure A5.2: *Changes in molar emissions of Λ-**9b** at titrations with **I9** at varied ionic strengths.*

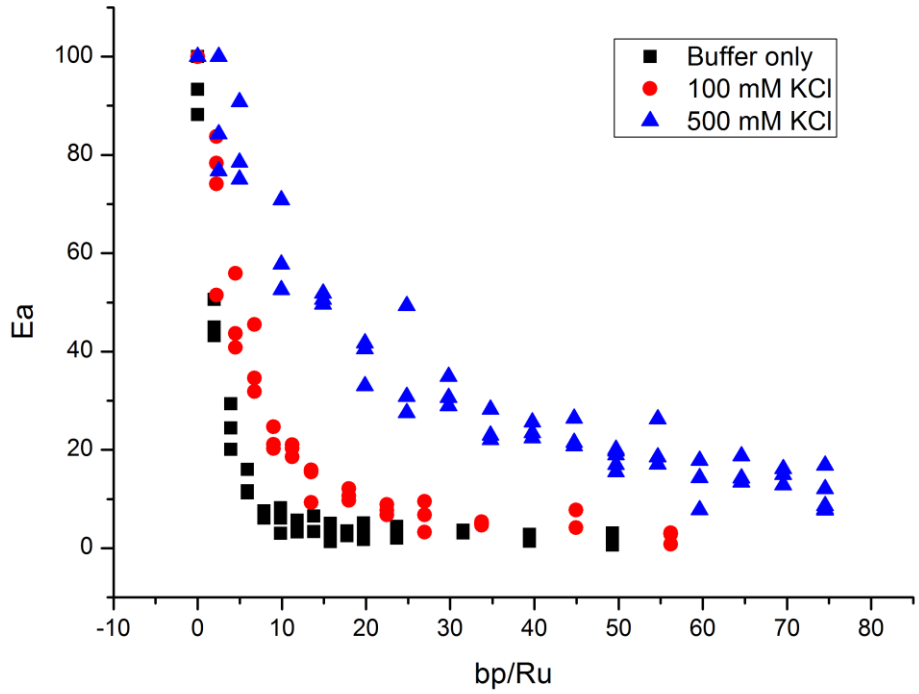

Figure A5.3: *Changes in molar emissions of Λ-**9b** at titrations with **A9** at varied ionic strengths.*

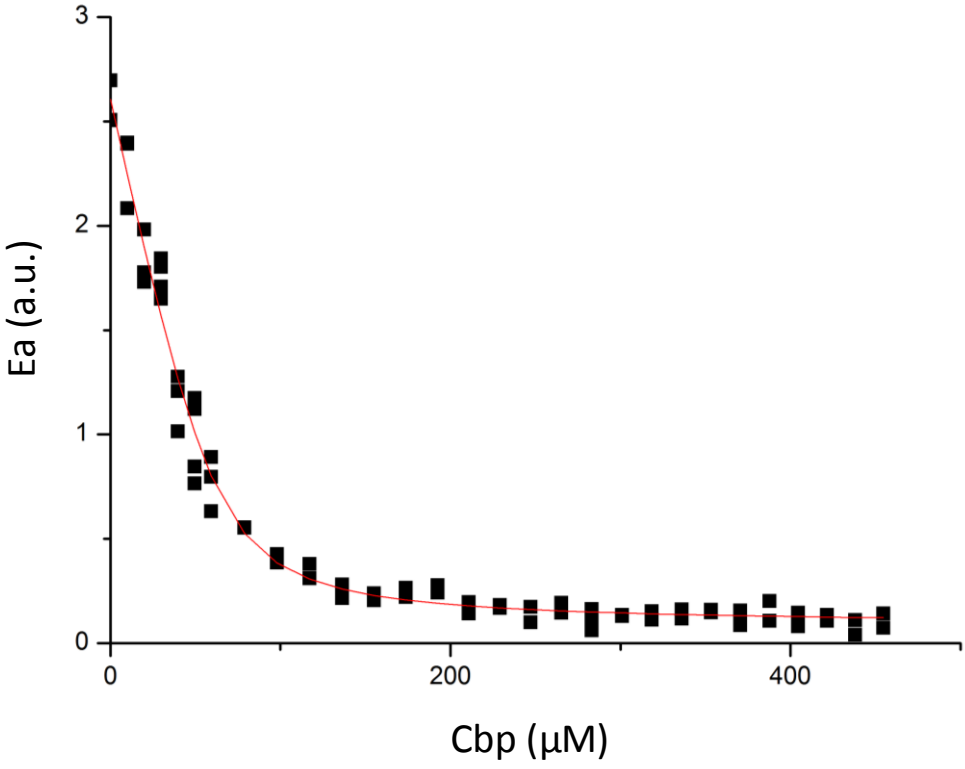

Figure A5.4: *Fit of Scatchard binding parameters in equation (1.46) to data obtained from emission titration of Λ-**9b** with **G9**. 50 mM potassium phostphate buffer, pH 7.0, 25 °C.*

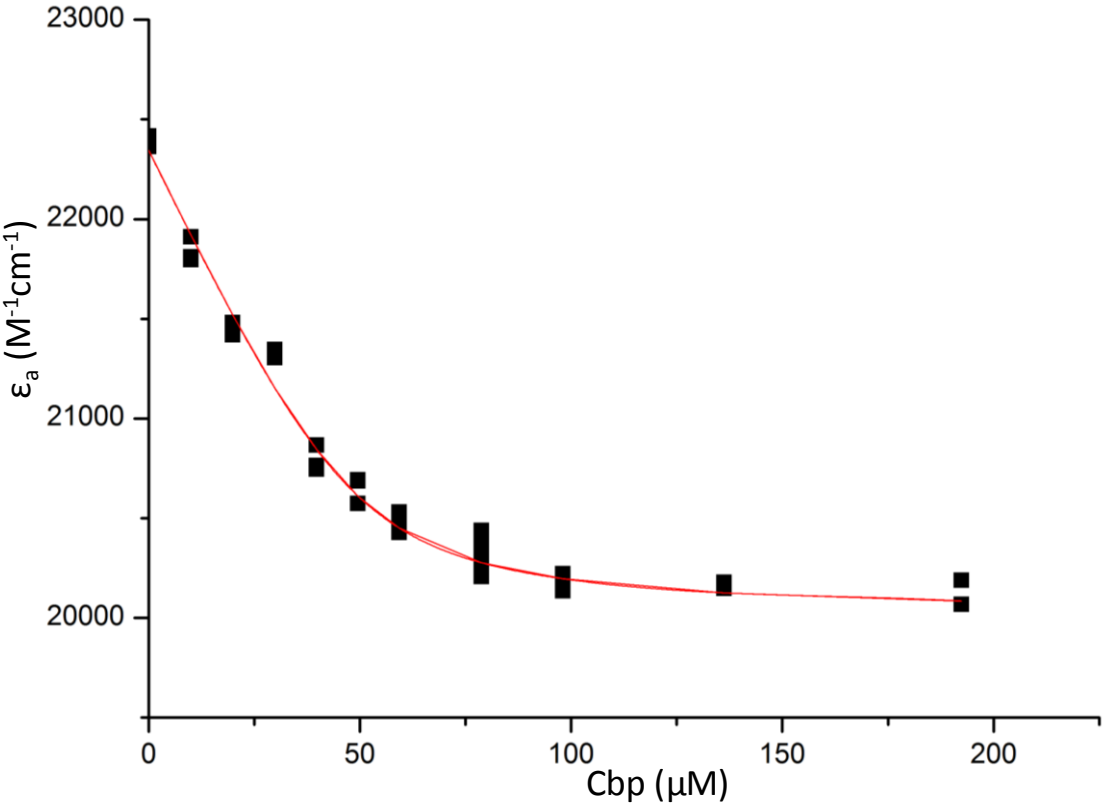

Figure A5.5: *Fit of Scatchard binding parameters in equation (1.46) to data obtained from absorption titration of Λ-**9b** with **G9**. 50 mM potassium phostphate buffer, pH 7.0, 25 °C.*

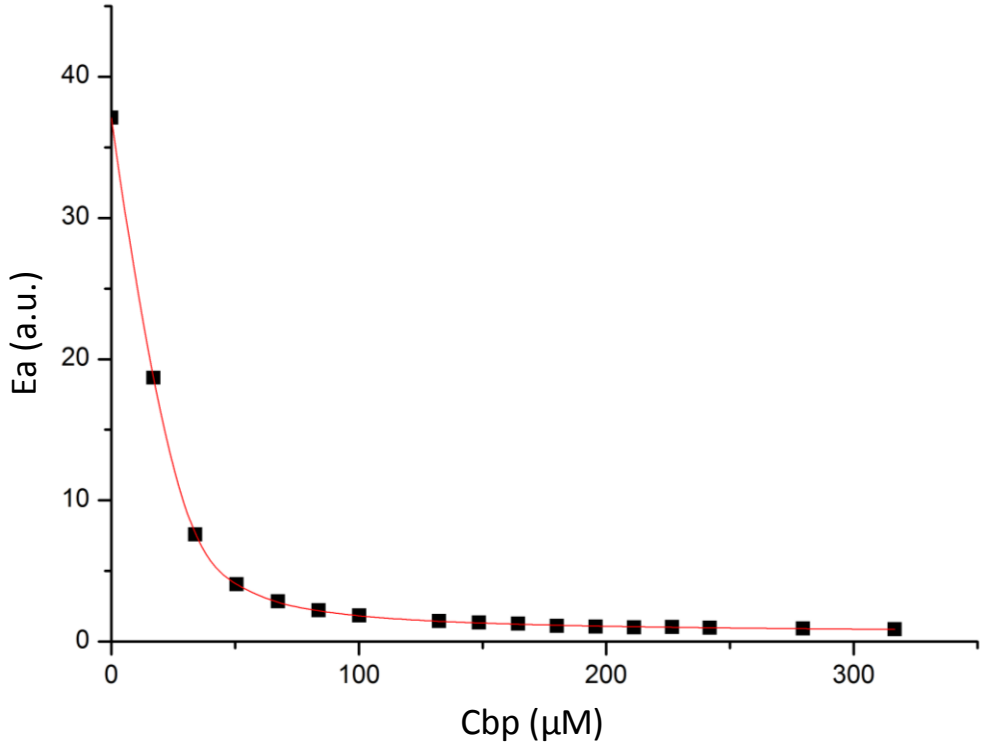

Figure A5.6: *Fit of Scatchard binding parameters in equation (1.46) to data obtained from absorption titration of Λ-**9b** with **I9**. 50 mM potassium phostphate buffer, pH 7.0, 25 °C.*

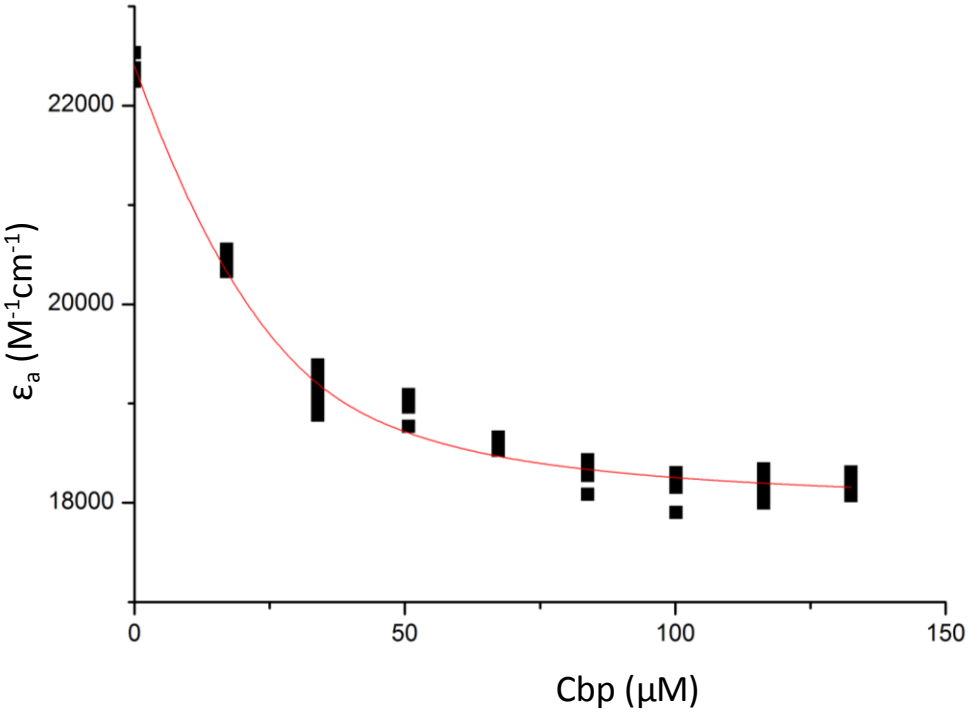

Figure A5.7: *Fit of Scatchard binding parameters in equation (1.46) to data obtained from absorption titration of Λ-**9b** with **I9**. 50 mM potassium phostphate buffer, pH 7.0, 25 °C.*

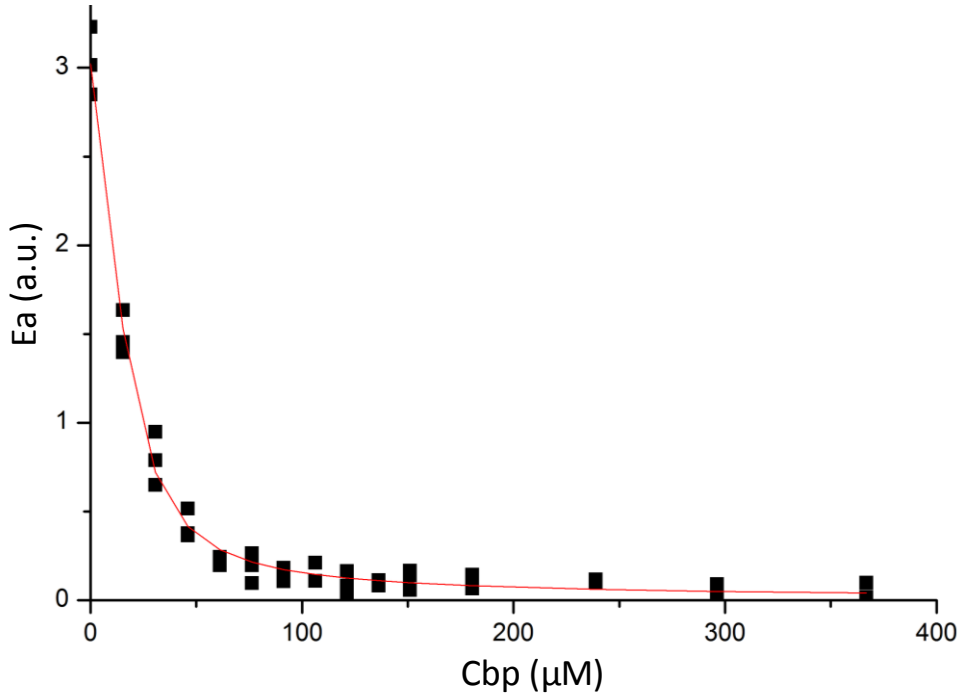

Figure A5.8: *Fit of Scatchard binding parameters in equation (1.46) to data obtained from emission titration of Λ-**9b** with **A9**. 50 mM potassium phostphate buffer, pH 7.0, 25 °C.*

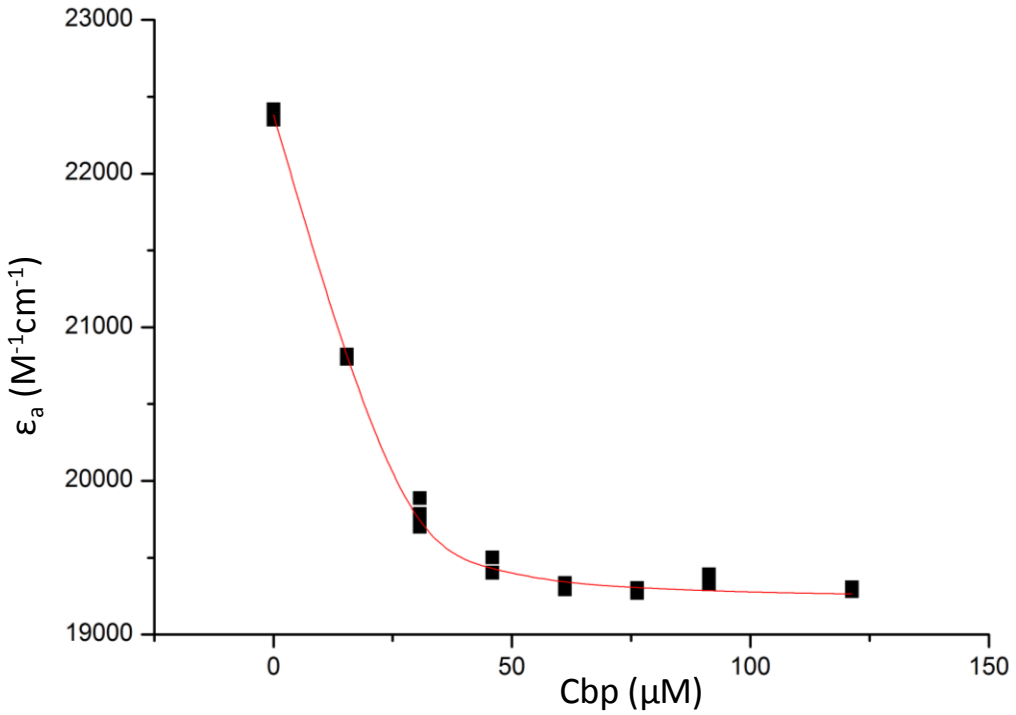

Figure A5.9: *Fit of Scatchard binding parameters in equation (1.46) to data obtained from absorption titration of Λ-**9b** with **A9**. 50 mM potassium phostphate buffer, pH 7.0, 25 °C.*

Table A5.1: *Site binding constants calculated from absorption data for the binding of Λ-**9b** to oligomeric sequences of DNA in 50 mM potassium phosphate buffer at pH 7.0 and 25 °C with varied concentration of KCl. The reported values and errors are the mean and standard error for all replicates.*

k (x 10^5 M^{-1})	G9	I9	A9
0 mM KCl	5.8 ± 1.0	12 ± 3	35 ± 10
100 mM KCl	2.3 ± 0.7	1.5 ± 0.5	2.2 ± 0.4
500 mM KCl	0.3	1.8 ± 0.5	1.9 ± 0.8

Table A5.2: *Binding site sizes calculated from absorption data for the binding of Λ-**9b** to oligomeric sequences of DNA in 50 mM potassium phosphate buffer at pH 7.0 and 25 °C with varied concentration of KCl. The reported values and errors are the mean and standard error for all replicates.*

n (bp)	G9	I9	A9
0 mM KCl	5.2 ± 1.8	3.4 ± 0.3	5.6 ± 1.9
100 mM KCl	10.5 ± 2.5	4.6 ± 0.5	5.2 ± 0.3
500 mM KCl	10*	7.9 ± 0.2	13 ± 3

** Fixed value.*

Table A5.3: *Step-wise binding constants from emission data for Λ-[Ru(TAP)$_2$(dppz)]$^{2+}$ (**Ru**) in the presence of {TCGGCGCCGA}$_2$ (**G9**), {TCGGCGCCIA}$_2$ (**I9**) and {TTGGCGCCAA}$_2$ (**A9**). Fitted with the program ReactLab EQUILIBRIA. In 50 mM K-phosphate buffer in H$_2$O (pH 7). K_i is equilibrium constant for $Ru + Ru_{i-1}D \rightleftharpoons Ru_iD$. <K> is the equilibrium constant for $Ru + \frac{1}{N}D \rightleftharpoons \frac{1}{N}Ru_ND$ where N is the maximum number of bound ligands (geometric average of K_i: $k = {K_N}^{1/N} = \left(\prod_{i=1}^{N} {K_i}'\right)^{1/N}$).*

	0 mM KCl	**100 mM KCl**	**500 mM KCl**
	{TCGGCGCCGA}$_2$ (**G9**)		
K_1' **(M^{-1})**	(4 ± 1) x10^5	(3 ± 2) x10^5	0.03 x10^5
K_2' **(M^{-1})**	(5 ± 3) x10^5	(0.9 ± 0.6) x10^5	-
k **(M^{-1})**	(4.2 ± 0.1) x10^5	(1.6 ± 0.1) x10^5	0.03 x10^5
	{TCGGCGCCIA}$_2$ (**I9**)		
K_1' **(M^{-1})**	(41 ± 9) x10^5	(12 ± 1) x10^5	(1.7 ± 0.2) x10^5
K_2' **(M^{-1})**	(9 ± 2) x10^5	(4 ± 1) x10^5	(0.4 ± 0.1) x10^5
K_3' **(M^{-1})**	(7 ± 2) x10^5	(3 ± 2) x10^5	(0.8 ± 0.1) x10^5
k **(M^{-1})**	(13 ± 1) x10^5	(5 ± 2) x10^5	(0.8 ± 0.1) x10^5
	{TTGGCGCCAA}$_2$ (**A9**)		
K_1' **(M^{-1})**	(47 ± 8) x10^5	(12 ± 3) x10^5	(1.8 ± 0.1) x10^5
K_2' **(M^{-1})**	(9 ± 2) x10^5	(2.0 ± 0.7) x10^5	(0.3 ± 0.2) x10^5
K_3' **(M^{-1})**	(2.1 ± 0.5) x10^5	-	-
k **(M^{-1})**	(9 ± 1) x10^5	(4.8 ± 0.3) x10^5	(0.74 ± 0.01) x10^5

Table A5.4: *Non-cooperative site binding constants calculated from absorption data with ReactLab EQUILIBIRIA for the binding of Λ-**9b** to oligomeric sequences of DNA in 50 mM potassium phosphate buffer at pH 7.0 and 25 °C with varied concentration of KCl. The reported values and errors are the mean and standard error for all replicates.*

k (x 10^5 M^{-1})	**G9**	**I9**	**A9**
0 mM KCl	0.83 ± 0.05^{2eq}	4.6 ± 0.5^{3eq}	17 ± 5^{3eq}
100 mM KCl	0.5 ± 0.1^{2eq}	2.7 ± 1.0^{2eq}	1.0 ± 0.1^{2eq}
500 mM KCl	-	2.0 ± 0.6^{1eq}	1.0 ± 0.1^{1eq}

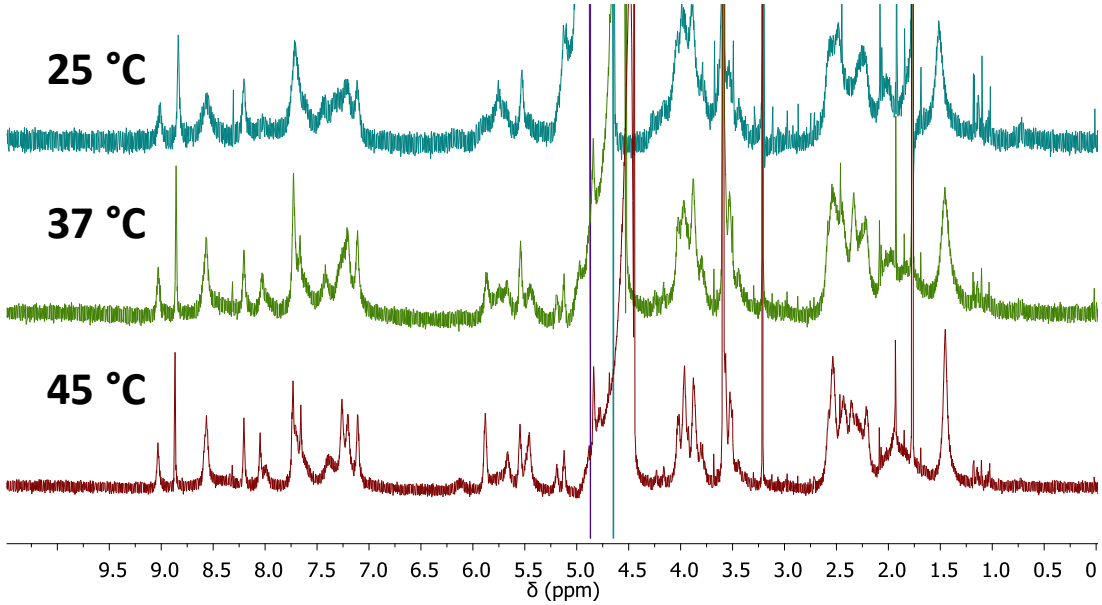

Figure A5.10: *^{1}H NMR spectra (D_2O, 800 MHz) of Λ-**9b** (0.4 mM) together with DNA duplex **G9** (0.5 mM) at varied temperature. 50 mM potassium phosphate buffer, pH 7.0.*

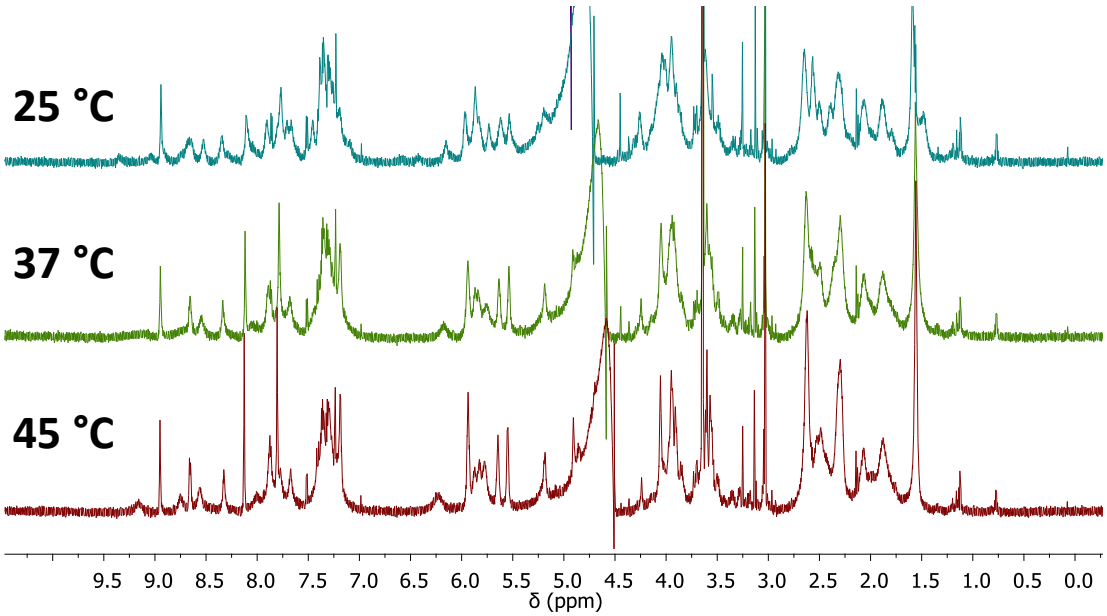

Figure A5.11: *^{1}H NMR spectra (D_2O, 800 MHz) of Λ-**9b** (0.4 mM) together with DNA duplex **I9** (0.5 mM) at increasing temperature. 50 mM potassium phosphate buffer, pH 7.0.*

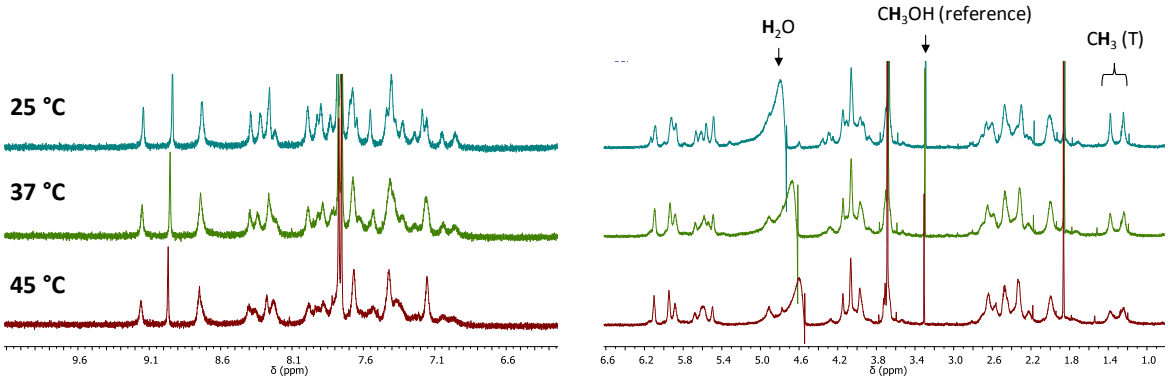

Figure A5.12: *^{1}H NMR spectra (D_2O, 800 MHz) of Λ-**9b** (0.4 mM) together with DNA duplex **TA** (0.5 mM) at increasing temperature. 50 mM potassium phosphate buffer, pH 7.0.*

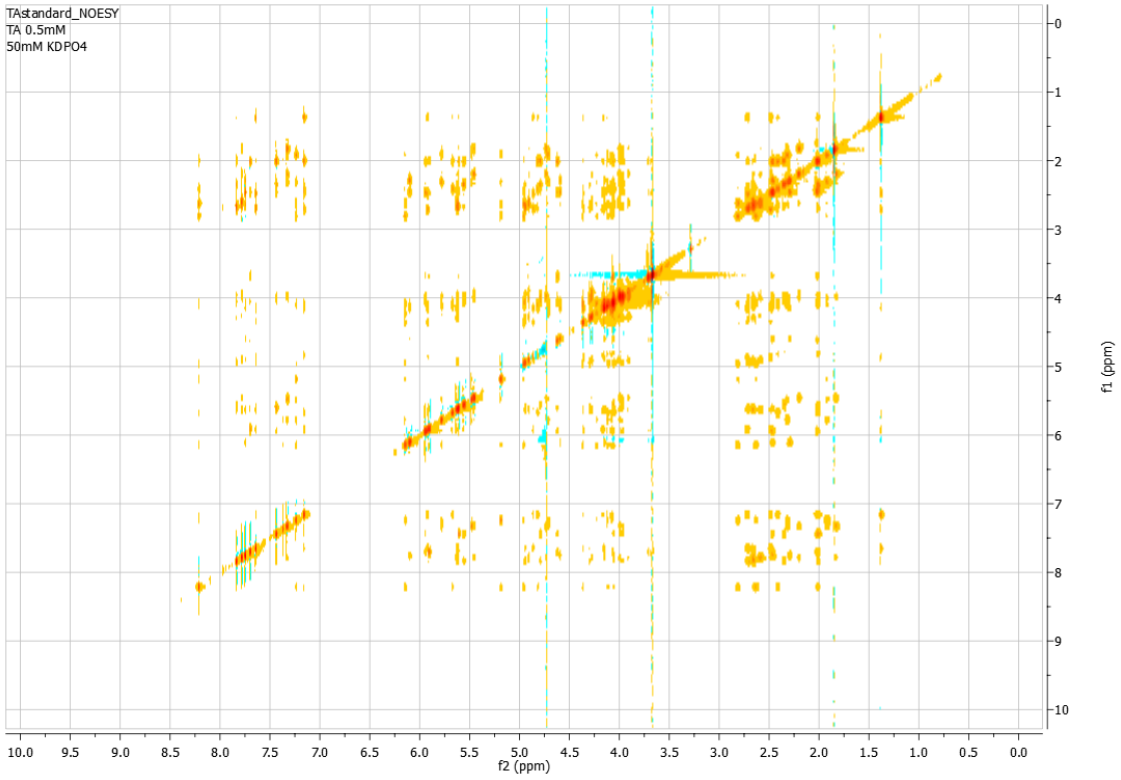

Figure A5.13: *NOESY spectrum (D_2O, 800 MHz) of **TA** (0.5 mM). 50 mM potassium phosphate buffer, pH 7.0, 25 °C.*

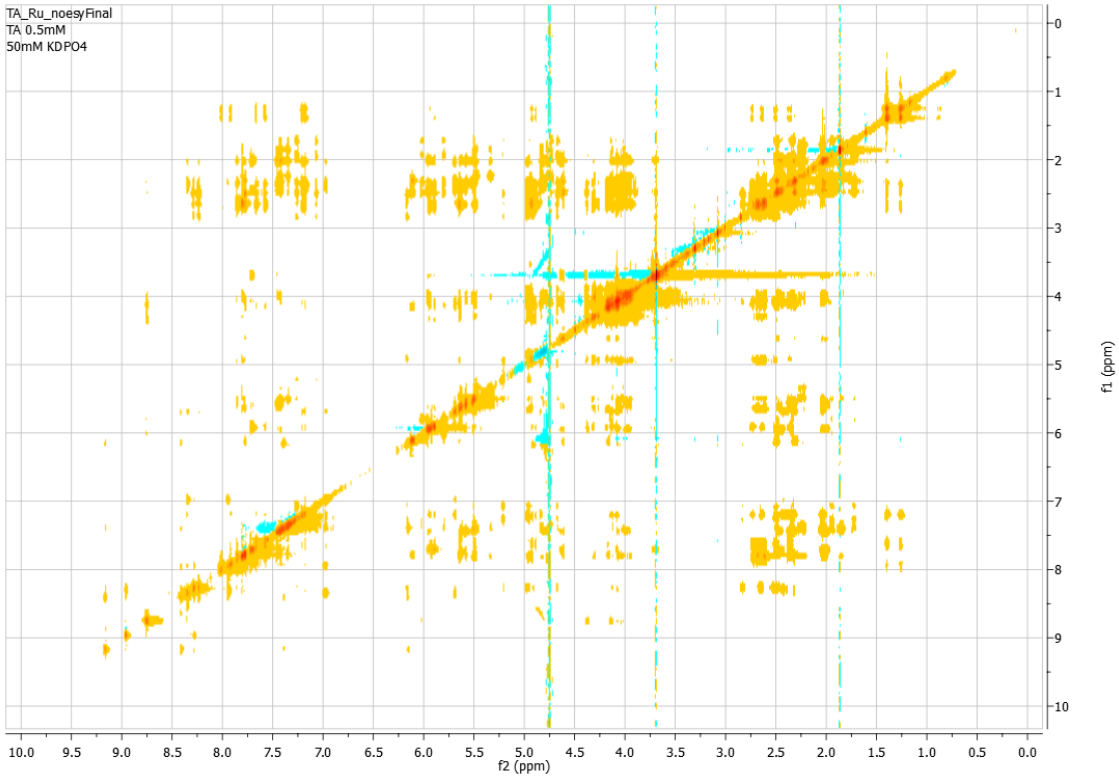

Figure A5.14: *NOESY spectrum (D_2O, 800 MHz) of Λ-**9b** (0.4 mM) together with DNA duplex **TA** (0.5 mM). 50 mM potassium phosphate buffer, pH 7.0, 25 °C.*

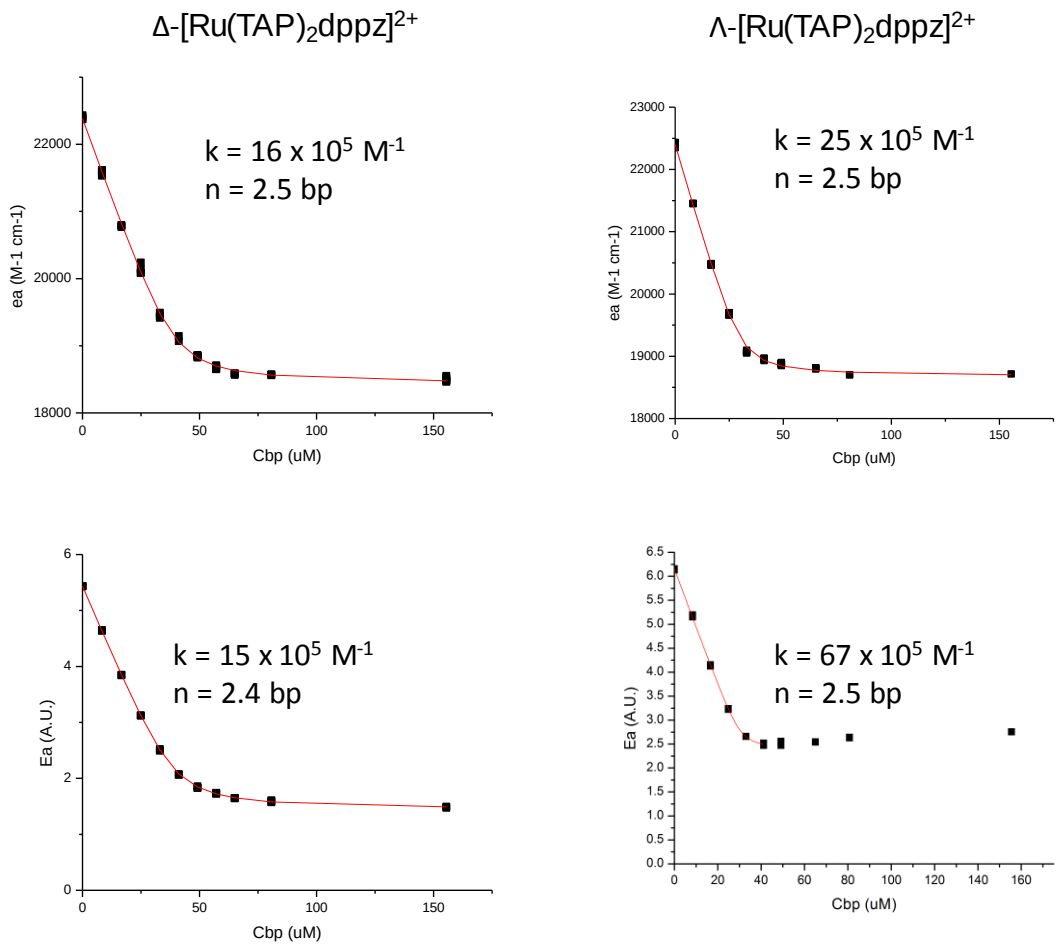

Figure A5.15: *Titration curves for titration of Δ- and Λ-**9b** with st-DNA: apparent molar absorbance (e_a) or emission (E_a) plotted against concentration of DNA base pairs (C_{bp}). 50 mM potassium phosphate buffer, 25 °C.*

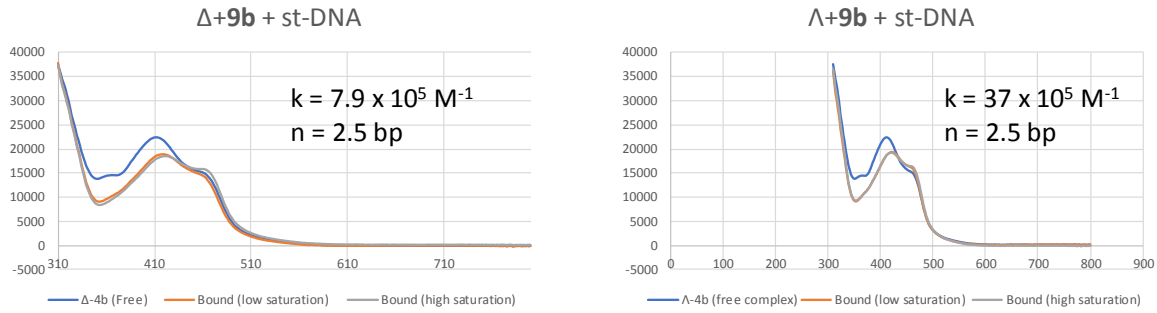

Figure A5.16: *Molar absorption spectra of Δ-**9b** (a) and Λ-**9b** (b) as free complex in solution and at binding to st-DNA at low saturation or high saturation; 50 mM potassium phosphate buffer, pH 7.0, 25 °C; obtained with ReactLab EQUILIBRIA using two equilibria (non-cooperative fit).*

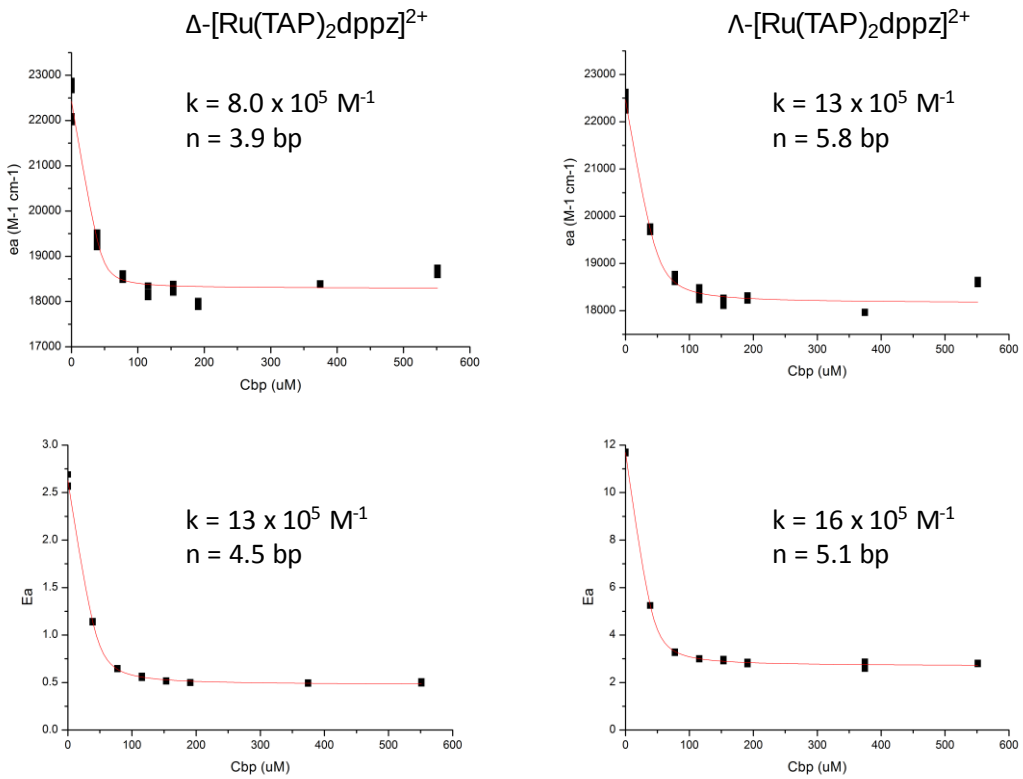

Figure A5.17: *Titration curves for titration of Δ- and Λ-**9b** with oligo **A2T2**: apparent molar absorbance (e_a) or emission (E_a) plotted against concentration of DNA base pairs (C_{bp}). 50 mM potassium phosphate buffer, 25 °C.*

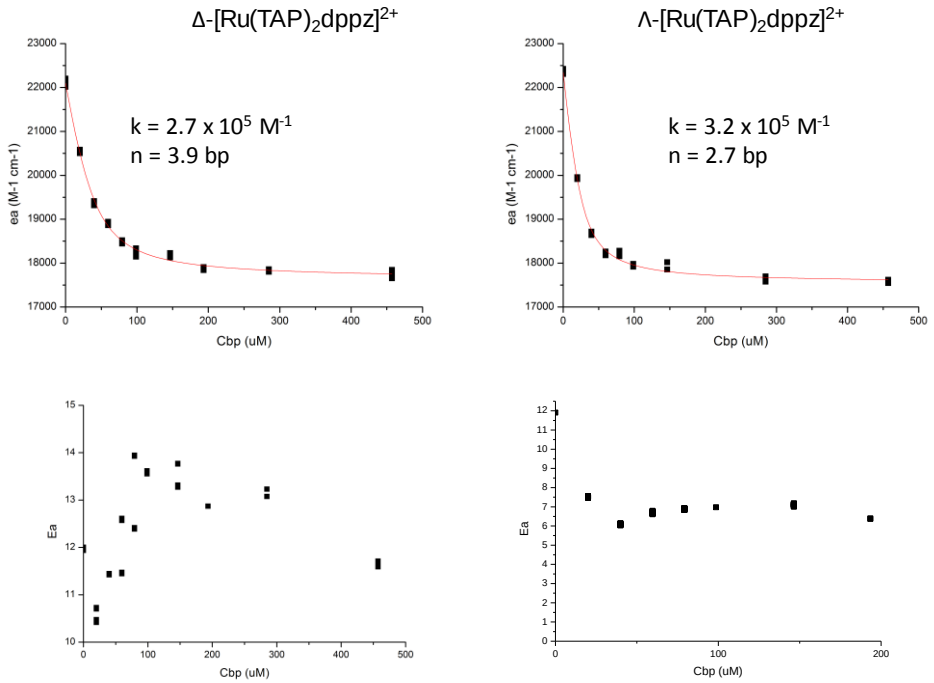

Figure A5.18: *Titration curves for titration of Δ- and Λ-**9b** with oligo **A3T3**: apparent molar absorbance (e_a) or emission (E_a) plotted against concentration of DNA base pairs (C_{bp}). 50 mM potassium phosphate buffer, 25 °C.*

Table A5.5: *Scatchard site binding parameters for Δ-**9b** bound st-DNA in 50 mM potassium phosphate buffered solution with 50 mM KCl. The parameters are calculated from absorption, emission and CD data.*

	Absorption	Emission	CD
k **(10^5 M^{-1})**	3.5 ± 0.6	2.7 ± 0.1	5.5 ± 0.1
n **(bp)**	2.0 ± 0.1	2.0 ± 0.1	2.5 ± 0.1

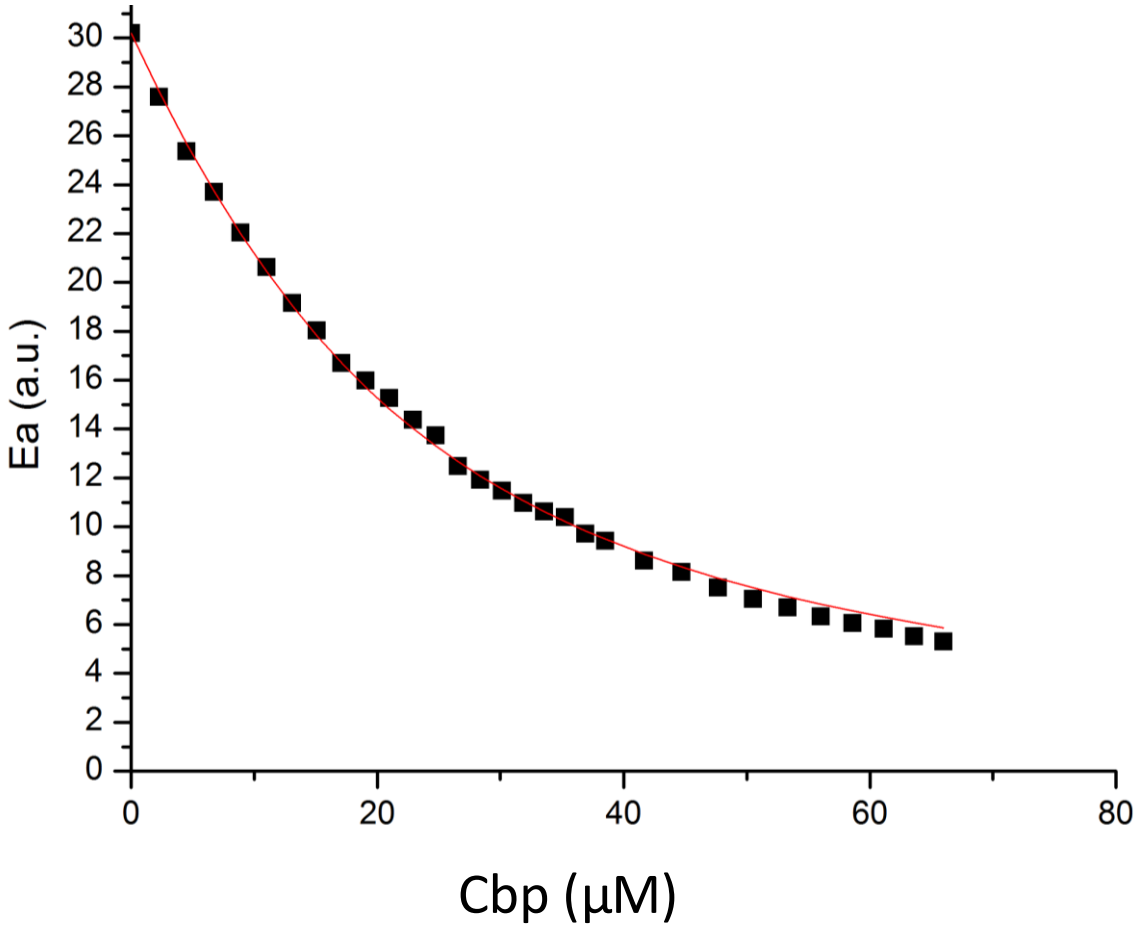

Figure A5.19: *Titration curves for titration of Δ-**9b** with poly(dG)poly(dC): apparent molar emission (E_a) plotted against concentration of DNA base pairs (C_{bp}). 50 mM potassium phosphate buffer + 50 mM KCl, 25 °C.*

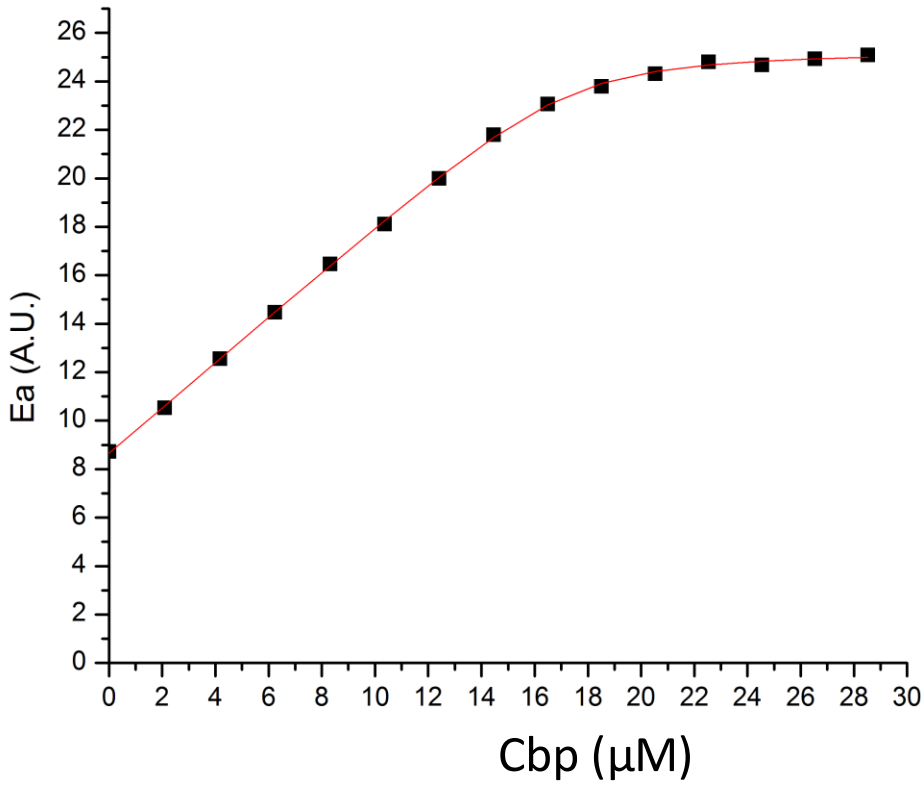

Figure A5.20: *Titration curves for titration of Δ-**9b** with poly(dA)poly(dT): apparent molar emission (E_a) plotted against concentration of DNA base pairs (C_{bp}). 50 mM potassium phosphate buffer + 50 mM KCl, 25 °C.*

Appendix 6

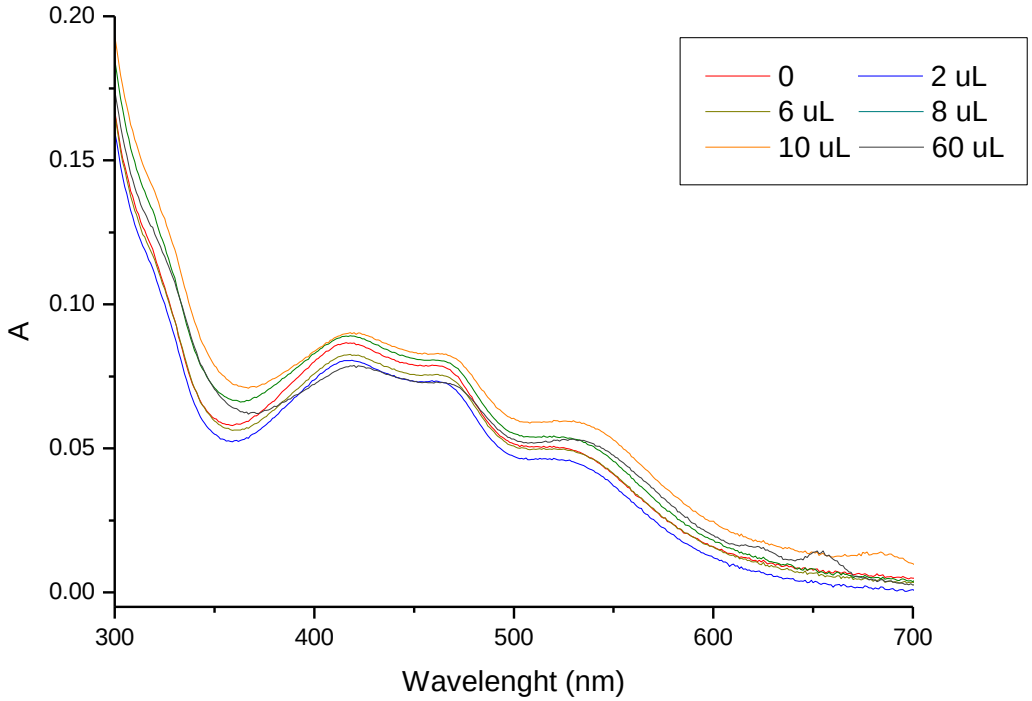

Figure A6.1: *Changes in absorption spectrum of* ***AuNP$_{15nm}$-55b*** *(ca. 20 μM) upon increasing concentration of st-DNA for AuNPs synthesised with citrate/Au = 3.*

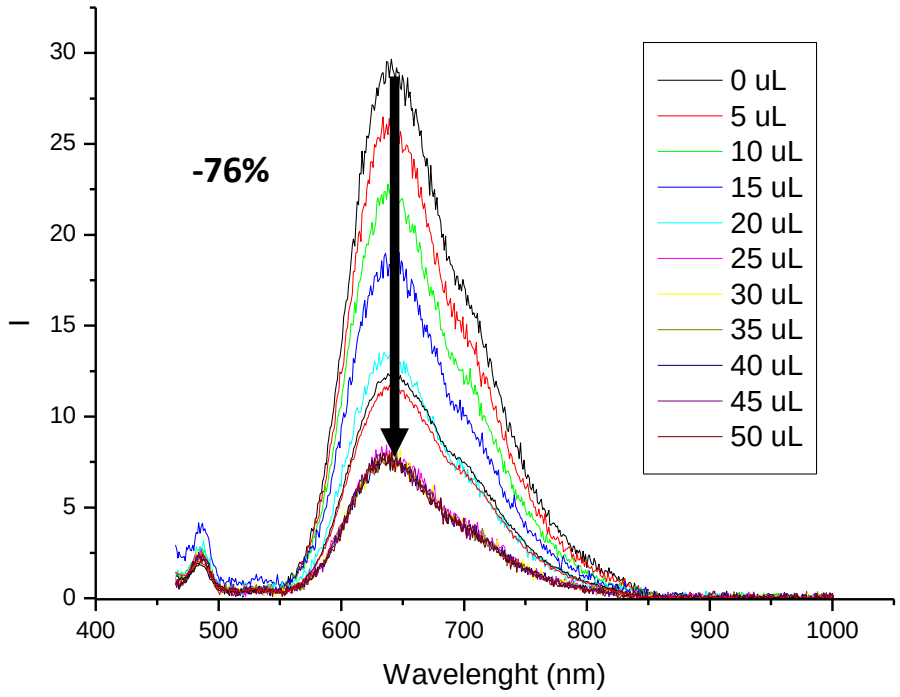

Figure A6.2: *Changes in emission spectrum of* ***AuNP$_{15nm}$-55b*** *(ca. 20 μM) upon increasing concentration of st-DNA for AuNPs synthesised with citrate/Au = 3.*